LIGHT-SHEET FLUORESCENCE MICROSCOPY FOR BIOMEDICINE

Persephone B. Poulton

A Thesis Submitted for the Degree of PhD
at the
University of St Andrews

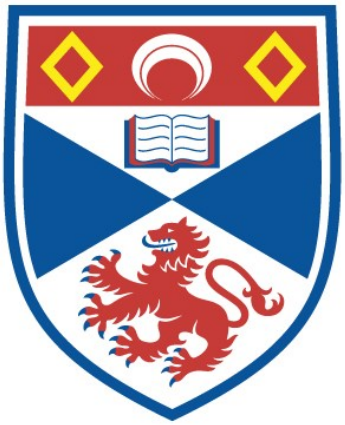

2023

Light-Sheet Fluorescence Microscopy for Biomedicine

By

Persephone B. Poulton

A thesis submitted to
the University of St Andrews
for the degree of
DOCTOR OF PHILOSOPHY

University of
St Andrews

Optical Manipulation Group
School of Physics and Astronomy
J.F. Allen Building
University of St Andrews
September 2022

ABSTRACT

The research motivation behind this Thesis is to expand the information that can currently be extracted from an *ex vivo* biological sample via light-sheet fluorescence microscopy (LSFM) by enhancing the achievable resolution at an increased penetration depth. LSFM has already been used considerably for various biomedical research applications. During this Thesis, I will explain why and in which contexts LSFM is a favoured technique compared to other currently available biomedical imaging tools. I will show how exotic beam shaping with Airy and Bessel-like beams can be implemented with LSFM to enhance the depth of quality, sub-cellular data available from complex biological samples (increasing the specificity and reach of the illumination to increase contrast in images). I will consider how the use of non-linear fluorescence excitation can improve upon the axial sectioning ability of LSFM with beam shaping in biological samples whilst exploiting the lowered attenuation of near infra-red illumination in biological tissues compared to visible illumination for linear fluorescence excitation. There are always fundamental limits to what we can achieve with optical microscopy. The guiding wish is to get a little bit closer to reaching these absolute physical limits with new, practical microscope designs aimed at medical microscopy applications.

DEDICATION

For Marc

ACKNOWLEDGMENTS

Funding

This work was supported by the M Squared - St Andrews Biophotonics Nexus Prosperity grant [grant number EP/R004854/1]; and the Resonant and shaped photonics for understanding the physical and biomedical world [grant number EP/P030017/1].

Candidate's declaration

I, Persephone Beatrice Poulton, do hereby certify that this thesis, submitted for the degree of PhD, which is approximately 38,000 words in length, has been written by me, and that it is the record of work carried out by me, or principally by myself in collaboration with others as acknowledged, and that it has not been submitted in any previous application for any degree. I confirm that any appendices included in my thesis contain only material permitted by the 'Assessment of Postgraduate Research Students' policy.

I was admitted as a research student at the University of St Andrews in September 2018.

I, Persephone Beatrice Poulton, received assistance in the writing of this thesis in respect of language, grammar, spelling and syntax, which was provided by Dr Philip Wijesinghe and Dr Caroline Poulton.

I received funding from an organisation or institution and have acknowledged the funder(s) in the full text of my thesis.

Date Signature of candidate

Supervisor's declaration I hereby certify that the candidate has fulfilled the conditions of the Resolution and Regulations appropriate for the degree of PhD in the University of St Andrews and that the candidate is qualified to submit this thesis in application for that degree. I confirm that any appendices included in the thesis contain only material permitted by the 'Assessment of Postgraduate Research Students' policy.

Date Signature of supervisor

Permission for publication

In submitting this thesis to the University of St Andrews we understand that we are giving permission for it to be made available for use in accordance with the regulations of the University Library for the time being in force, subject to any copyright vested in the work not being affected thereby. We also understand, unless exempt by an award of an embargo as requested below, that the title and the abstract will be published, and that a copy of the work may be made and supplied to any bona fide library or research worker, that this thesis will be electronically accessible for personal or research use and that the library has the right to migrate this thesis into new electronic forms as required to ensure continued access to the thesis.

I, Persephone Beatrice Poulton, have obtained, or am in the process of obtaining, third-party copyright permissions that are required or have requested the appropriate embargo below.

The following is an agreed request by candidate and supervisor regarding the publication of this thesis:

Printed copy

No embargo on print copy.

Electronic copy

No embargo on electronic copy.

Date Signature of candidate

Date Signature of supervisor

Underpinning Research Data or Digital Outputs

Candidate's declaration

I, Persephone Beatrice Poulton, understand that by declaring that I have original research data or digital outputs, I should make every effort in meeting the University's and research funders' requirements on the deposit and sharing of research data or research digital outputs.

Date Signature of candidate

Permission for publication of underpinning research data or digital outputs

We understand that for any original research data or digital outputs which are deposited, we are giving permission for them to be made available for use in accordance with the requirements of the University and research funders, for the time being in force.

We also understand that the title and the description will be published, and that the underpinning research data or digital outputs will be electronically accessible for use in accordance with the license specified at the point of deposit, unless exempt by award of an embargo as requested below.

The following is an agreed request by candidate and supervisor regarding the publication of underpinning research data or digital outputs:

No embargo on underpinning research data or digital outputs.

Date Signature of candidate

Date Signature of supervisor

Personal acknowledgements

I am grateful to my supervisor, Kishan, for this once-in-a-lifetime opportunity and for helping me to grow as a student and as a person. Thank you to the rest of the OMG group; Stella, Philip, Holly, Morgan, Fiona, George, Saba, Mingzhou, Manuel, Yoshi, Georgina, Jonny, Adria, Graham, Nico, Lewis, Josephine, Madhu, Paloma, Soraya, Federico, Hyeonwoo and Alistair. I will miss you all very much, thank you for the good times. I'm especially grateful to Stella, Philip, George, Graham, and Hyeonwoo for their assistance with my learning and research projects. Saba's knowledge of nonlinearities in fibre optics has been invaluable and Kofi's pep talks are unrivalled. Cheers to Laura and Graham for lending me their books and Graham for all his help in general. Thank you to my mum, Caroline, and to Philip, for all of their painstaking proof-reading. I owe you! Thank you Jim, Deirdre, Khushi and Ashray for your kindness and hospitality while I was working away from home. Thanks to UKRI and the Engineering and Physical Sciences Research Council for sponsoring my PhD journey and to Minick of St Andrews for providing the freshest of test samples for my microscopes. Thanks to my family Caroline, Brodyn and Darius. No words are big enough, but I love you. Thanks for your courage through these difficult 4 years and for backing me to the hilt. Thank you Shin and Kitana too for all the love and support. Thank you Neenoo, my loudest cheerleader. Thanks to my Sparents; Richenda, Steve, Carla and Iain for your confidence and for taking me under your respective wings. Cheers to Euan for providing the ultimate thesis-writing attire. Thank you Marina for showing me the finish line and Ruth, because she would've been there too. To the leading ladies; Holly, Hannah, Emma, Shannon, Tanya, Sinéad, Gemma, Rachel and Andrea; what a team. I hope you know how important you are. To Stella, Roberto and your hilarious bambini Sophia and Leo, and to Philip, Kofi and Akosua; thanks for the much-needed serotonin boosts and all the delicious research fuel. Thank you Anmol, Struan, Aaron and 'Tina. Thank you Natasha for reminding me to breathe. And finally, I saved my biggest thank you for Marc. You're the best. You have made so many sacrifices for me to be me here, and I might not have made it without your constant compassion and faith. I couldn't be happier to be moving onto the next chapter with you.

Contents

Page

1 Introduction . . . 1
- 1.1 Motivation . . . 1
  - 1.1.1 Imaging without harm . . . 2
- 1.2 Aims . . . 4
- 1.3 Thesis outline . . . 5
  - 1.3.1 Overview . . . 5
  - 1.3.2 Chapter contents . . . 5

2 Background . . . 7
- 2.1 Image theory . . . 7
  - 2.1.1 The need for contrast . . . 7
  - 2.1.2 Field of view . . . 8
  - 2.1.3 Sectioning data in 3D . . . 9
- 2.2 Biomedical imaging . . . 9
- 2.3 Optical imaging and light-tissue dynamics . . . 12
  - 2.3.1 Scattering . . . 13
  - 2.3.2 Absorption . . . 15
  - 2.3.3 The therapeutic window . . . 16
  - 2.3.4 Fluorescence . . . 17
  - 2.3.5 Multi-photon fluorescence . . . 20
  - 2.3.6 Pulsed Sources . . . 22
  - 2.3.7 Gaussian beams . . . 27
  - 2.3.8 The diffraction limit . . . 30
  - 2.3.9 Nyquist sampling . . . 33
  - 2.3.10 Microscope geometries . . . 33
  - 2.3.11 Characterising an optical microscope . . . 34
  - 2.3.12 Tissue clearing . . . 36

2.4 A directory of selected imaging techniques . . . 36
2.4.1 Non-optical imaging examples . . . 37
2.4.2 Optical imaging examples . . . 40
2.4.3 Comparisons . . . 50
2.5 Light-sheet fluorescence microscopy (LSFM) . . . 50
2.6 Exotic beam shaping . . . 55
2.6.1 Airy beam . . . 56
2.6.2 Bessel beam . . . 59
2.6.3 Deconvolution . . . 62
2.7 Summary . . . 62

3 Bench-top light-sheet microscopy for histopathology with Airy beam shaping . . . 64
3.1 Overview . . . 64
3.2 Gold standard histopathology . . . 65
3.2.1 Current practices . . . 65
3.2.2 Histopathology as an application of LSFM . . . 69
3.3 Building an open-top light-sheet (OTLS) microscope . . . 70
3.3.1 Illumination . . . 71
3.3.2 Creating the light-sheet . . . 74
3.3.3 Open-top geometry . . . 74
3.3.4 Airy beam shaping . . . 77
3.3.5 Detection . . . 79
3.3.6 Overview of OTLS . . . 84
3.4 Methods . . . 86
3.4.1 Sample preparation . . . 86
3.4.2 Post-processing . . . 88
3.5 Biological test samples . . . 91
3.6 Results . . . 95
3.6.1 Gaussian vs Airy OTLS . . . 95
3.6.2 Airy mode OTLS with deep learning for human tissue analysis . . . 96
3.6.3 Airy OTLS with deep learning for imaging cleared samples . . . 99
3.7 Summary . . . 100

4 Towards clinical use: optimising tissue analysis with OTLS . . . 106
4.1 Introduction . . . 106

4.2 Setup . . . 107
4.3 Methods . . . 107
4.4 On-site testing . . . 109
4.5 Results: human tissue imaging . . . 110
4.5.1 Overview . . . 110
4.5.2 Tissue Imaging Summary . . . 123
4.6 OTLS redevelopment based on end-user feedback . . . 125
4.6.1 Spatial resolution . . . 125
4.6.2 Two-colour imaging . . . 127
4.6.3 Sample and system preservation . . . 130
4.6.4 User-friendliness . . . 131
4.6.5 Proposed OTLS for future studies (version 3) . . . 132
4.7 Discussion . . . 135
4.8 Conclusion . . . 135

5 Multi-photon light-sheet microscopy with Bessel beam shaping . . . 137
5.1 Introduction . . . 137
5.1.1 Why would we want to use multi-photon excitation for biological samples? 137
5.2 Why Bessel beams for multi-photon LSFM? . . . 139
5.3 Possible alternative methods for Bessel-like beam shaping in a prototype LSFM setup . . . 143
5.3.1 Aims and experimental design . . . 144
5.4 Meta-surfaces for Bessel-like beam generation . . . 146
5.4.1 Optical design of BBG meta-surfaces . . . 146
5.4.2 Experimental setup (part I) . . . 147
5.4.3 Methods (part I) . . . 150
5.4.4 Experimental setup (part II) . . . 152
5.4.5 Methods (part II) . . . 153
5.4.6 Experimental results . . . 154
5.4.7 Discussion . . . 157
5.5 Bessel-beam generating fibre optics . . . 158
5.5.1 Optical design . . . 158
5.5.2 Experimental setup . . . 159
5.5.3 Methods . . . 161
5.5.4 Experimental results . . . 167

5.5.5 Discussion . . . 182
5.6 Two-photon LSFM with BBG fibre optics . . . 182
5.6.1 Setup . . . 183
5.6.2 Methods . . . 184
5.6.3 Results . . . 187
5.7 Chapter Summary . . . 189

6 Conclusions . . . 190
6.1 Chapter 3 . . . 190
6.2 Chapter 4 . . . 192
6.3 Chapter 5 . . . 194
6.4 Acknowledgments . . . 197
6.4.1 Chapter 2 . . . 197
6.4.2 Chapter 3 . . . 197
6.4.3 Chapter 4 . . . 198
6.4.4 Chapter 5 . . . 198

Appendices

A First Appendix . . . 200

B User guide for compact OTLS . . . 201

References . . . 271

List of Figures

2.1 A compromise between depth of penetration and image resolution: comparing key medical imaging techniques. 11

2.2 Cartoon showing possible photon-sample interactions. 12

2.3 Rayleigh and Mie scattering. 14

2.4 Jablonski diagram portraying one photon excitation. 18

2.5 Jablonski diagram portraying two and three photon excitation. 21

2.6 A comparison between pulsed and continuous wave laser illumination. 22

2.7 A cartoon explaining pulse dispersion and pre-compensation. 25

2.8 Example setup: resizing a single mode Gaussian beam using a Keplerian telescope. 27

2.9 Detecting fluorescence using an objective lens. 30

2.10 Objective lenses and the relationship between NA, WD and lens diameter. . 32

2.11 Basic schematic diagram of a brightfield microscope used for routine diagnostic imaging in healthcare. 42

2.12 Schematic diagram of a confocal fluorescence microscope. A pinhole is used to section information in depth. 45

2.13 Confocal fluorescence microscopy revisited: a close-up of how the sample is irradiated using this method. 46

2.14 A visual description of structured illumination microscopy. 47

2.15 Comparing penetration depth the photon and two photon sources through biological tissue. 49

2.16 Collinear geometry vs orthogonal geometry which is used for LSFM. 51

2.17 Light sheet fluorescence microscopy. Cartoon of optical sectioning in a sample. 52

2.18 Sample mounting example for LSFM. 54

2.19 Airy beam propagation compared to Gaussian beam propagation with an example optical setup for each case. 57

2.20 Cartoon of a light-sheet with 1D Airy beam shaping. 58

2.21 Bessel beam shaping with an axicon lens. 60

2.22 Bessel beam shaping using an annulus. 61

2.23 A simulated Bessel beam compared to a simulated Gaussian beam with the same numerical aperture. 61

3.1 Schematic diagram of compact a open-top light-sheet microscope. 72

3.2 Aberrations at a refractive index boundary in an imaging system. 75

3.3 Cartoon of a solid immersion lens used to facilitate open-top LSFM. 76

3.4 Comparing the beam shapes in the OTLS design using Gaussian mode and Airy mode. 78

3.5 The cross-sectional intensity distribution of a Gaussian beam propagating over a distance of 1000μm. 79

3.6 The cross-sectional intensity distribution of an Airy beam (NA identical to Gaussian case) propagating over a distance of 1000μm. 80

3.7 Comparing the modulation transfer functions of Gaussian and Airy beams propagating over a distance of 1000μm. 81

3.8 OTLS volumetric data geometry using the compact system. 84

3.9 Model and final design of compact OTLS for histopathology applications. . . 85

3.10 The architecture of the generative adversarial network used to post-process images from the OTLS setup. 91

3.11 Porcine tissue imaged using the OTLS to test setup calibration for thick tissue samples. 92

3.12 Test samples 2 and 3: beef muscle fibrils stained in Acridine Orange and imaged using OTLS. Figure shows the effect of improper freezing for sample preservation. 93

3.13 Sample imaged using OTLS: fatty beef tissue stained with AO is shown. Selective nuclear staining has worked in this example. 93

3.14 Beef revisited: comparing Gaussian and Airy mode of the LSFM prior to human tissue imaging trials. 94

3.15 Phantom bead sample used to measure the point spread function of the OTLS across the FoV. 102

3.16 Comparing cancerous and healthy colorectal tissue imaged using Gaussian OTLS and Airy OTLS with deep learning post-processing. 103

3.17 Cancerous and healthy human breast tissue imaged using Gaussian OTLS and Airy OTLS with deep-learning post-processing. 104

3.18 Cleared mouse brain tissue imaged using OTLS. This data can be used to better understand an animal model of Alzheimer's disease in humans. . . . 105

4.1 Flow chart describing experimental method during scoping exercise using OTLS in a research hospital. 108

4.2 A transparent, autofluorescent, blood orange segment used as a calibration test for OTLS imaging of thick tissue samples. 109

4.3 Human heart epicard fat imaged using Gaussian OTLS. Image shows signal attenuation in depth. 112

4.4 Unfixed human heart epicard fat imaged using Gaussian OTLS. 113

4.5 Close up inspection of nuclei in human heart epicard fat imaged using Gaussian OTLS. 115

4.6 Human heart tissue from a left ventricle imaged using Gaussian OTLS. . . . 116

4.7 Human endometrium tissue, fixed in formaldehyde before it was stained with acridine orange and imaged using Gaussian OTLS. 117

4.8 Cartoon of issues that can occur when staining thick, fixed tissue samples for OTLS microscopy. 118

4.9 Human breast tissue imaged using Gaussian OTLS. Successive frames of volumetric data set show topology of the irregular sample surface. 119

4.10 Fatty unfixed breast tissue stained with AO and imaged using Gaussian OTLS. 120

4.11 Unfixed stomach tissue stained with AO and imaged using Gaussian OTLS. 121

4.12 Unfixed human kidney thick tissue section stained with acridine orange and imaged using Gaussian OTLS. 122

4.13 Fixed human kidney slide-mounted section stained with hematoxylin and eosin and imaged using Gaussian OTLS. 123

4.14 Diagrams of custom parts: immersion chamber and sample mount for re-developed OTLS for pathology applications. 126

4.15 Emission and absorption of dyes intended for false H&E staining of samples that would be imaged using two-colour OTLS. 128

4.16 Schematic overview of proposed new design of adapted OTLS for pathology applications. 133

5.1 Revisiting optical sectioning using non-linear fluorescence excitation. 138

5.2 Comparing propagation-invariant Bessel and Airy beam propagation with Gaussian beam propagation. The intensity profiles are inspected for OPE, 2PE and 3PE cases. 139

5.3 Cross-sectional intensity profiles from data in previous figure. 140

5.4 Inspection of the modulation transfer function associated with each 1D intensity profile in the previous figure. 141

5.5 Using peak intensity with propagation distance as a comparison for each beam shape. 142

5.6 Axial resolution of Gaussian, Airy and Bessel beams compared at different propagation distances. 143

5.7 Meta-surface for Bessel-like beam generation at 1064nm. 147

5.8 Experimental setup for characterising Bessel-beams generated using meta-surfaces. 148

5.9 Photograph eta-surface mounted in the setup. 150

5.10 An example of an intensity profile created using a BBG meta-surface 151

5.11 Optical setup for rescaling the metasurface output profiles in 3D. 153

5.12 Optical setup for rescaling the metasurface output profiles in larger optical setup for beam characterisation. 154

5.13 Cross-sectional intensity profiles from the Bessel-like output at different propagation lengths. 155

5.14 Cross-sectional profiles measured after down-scaling telescope. 156

5.15 Diagrams of fibre optic with Bessel-beam generator integrated into the tip. 159

5.16 Experimental setup for characterisation of the BBG fibre optics. 160

5.17 Close-up of setup used to measure the intensity profile from each BBG fibre optic in 3D. 162

5.18 Objective losses at 920nm for fibre coupling setup. 168

5.19 Objective losses at 1320nm for fibre coupling setup. 168

5.20 Coupling efficiency 780HP fibre with Chameleon at 920nm 170

5.21 Coupling efficiency 780HP fibre with Opera-F at 920nm 171

5.22 Coupling efficiency of 47cm of FG105LCA at 820nm with 140fs pulsed illumination. 172

5.23 Coupling efficiency of 1m of FG050LGA at 920nm with 100fs pulsed illumination.172

5.24 Coupling efficiency of 40cm of SMF-28 with CSF tip at 1320nm with 100fs pulsed illumination. 173

5.25 Change in shape of pulse in time before fibre-coupling objective and after 1m of 780-HP fibre. 174

5.26 Spectrum from Opera-F source (centred on 1320nm) measured before and after 40cm of SMF-28. 175

5.27 Spectrum from Opera-F source (centred on 1320nm) measured before and after 40cm of SMF-28 using visible-NIR Thorlabs spectrometer. 176

5.28 Spectrum from Opera-F source (centred on 920nm) measured before and after 40cm of SMF-28 using visible-NIR Thorlabs spectrometer. 177

5.29 Spectra from before and after 1m, 2m and 3m of 780-HP SMF using pulsed illumination at 920nm. 178

5.30 Graph showing the effect of changing SMF length with respect to the spectrum at the output. Spectra are blue-shifted and broadened with respect to the input spectrum. 179

5.31 Cross-sectional intensity profiles measured through the BBG fibre output at different propagation distances. 180

5.32 An example of a cross-sectional intensity profile at some distance from the BBG fibre output. 181

5.33 Comparing the central lobe diameter with propagation distance for simulated Bessel beams and BBG fibre outputs. 182

5.34 Optical setup for 2PE fibre-integrated Bessel beam shaping with LSFM. . . 183

5.35 Custom-made cuvette mount for fibre-based BBG LSFM system. 184

5.36 Looking for evidence of two photon excitation of fluorescent beads using a BBG fibre to deliver illumination. 187

5.37 20μm beads imaged using 2PE and fibre-integrated Bessel beam shaping with LSFM. 188

List of Tables

3.1 Standard process of collecting samples for medical microscopy purposes. . . . 67

3.2 A table showing the resolution of Gaussian and Airy beams compared over 1 mm propagation distance. 82

4.1 Key properties of the revised compact OTLS design. 134

5.1 Table of lasers used for Bessel beam fibre testing and their key characteristics. 163

5.2 Fibre types used to compose fibre optics with integrated Bessel beam shaping at the output. 167

5.3 Pulse duration, τ, measured before and after lengths of SFM and MMF using illumination at 820, 920 and 1320nm. 174

Nomenclature

Physics Constants

$1p$	One photon
$2p$	Two photons
$3p$	Three photons
α	Alpha factor (Airy)
μ	Frequency
ω	Beam radius size (Gaussian)
ω_0	Beam waist size (Gaussian)
ϕ	Gouy phase
θ	Angle of divergence
θ_G	The divergence angle of a focused Gaussian beam
$_{ex}$	Excited
$_{ground}$	Ground
$_{vib}$	Vibrational

A_0 Initial amplitude

b Confocal parameter for a Gaussian beam

c Speed of light in a vacuum

D Diameter

d_x/d_y Lateral resolution

d_z Axial resolution

E_0 Ground energy level

E_1 Excited energy level

E_G Energy field of a Gaussian beam

h Planck's constant

I Intensity

i_x/i_y Pixel dimension

k Wave number

M Magnification

M_T Total magnification

n Refractive index

n_x/n_y Number of pixels in a particular dimension

N_{Pixels} Number of pixels (per unit length) required to satisfy Nyquist sampling

n_{sc} Average number of scattering lengths

P_{avg} Average power

P_{peak} Peak power

R Radius of curvature

r Radius

S_0 Ground energy state

t Time

X, Y, Z Dimensions in Cartesian space

Z_R Rayleigh Range (Gaussian)

List of Abbreviations

$2D$ Two-dimensional

$2PE$ Two Photon Excitation

$3D$ Three-dimensional

$3PE$ Three Photon Excitation

AI Artificial Intelligence

AO Acridine Orange

BBG Bessel Beam-Generating

CW Continuous Wave

DL Deep Learning

DoF Depth of Focus

FCM Fluorescence Confocal Microscopy

$FFPE$ Formalin-Fixed Paraffin-Embedded

$FIJI$ FIJI Is Just ImageJ

FOV Field Of View

FS Frozen Section

FSA Frozen Section Analysis

GAN Generative Adversarial Network

$H\&E$ Hematoxylin and Eosin

IR Infra-Red

LED Light Emitting Diode

$LSFM$ Light Sheet Fluorescence Microscopy

LSM Light Sheet Microscopy

MRI Magnetic Resonance Imaging

$MUSE$ Microscopy with Ultraviolet Surface Excitation

NA Numerical Aperture

NIR Near Infra-Red

NLM Non-Linear Microscopy

OCT Optical Coherence Tomography

OPE One Photon Excitation

$OTLS$ Open-Top Light Sheet

PBS Phosphate-Buffered Saline

RI Refractive Index

$sCMOS$ Scientific Complementary Metal-Oxide Semiconductor

SHG Second Harmonic Generation

SIM Structured Illumination Microscopy

SNR Signal to Noise Ratio

$SPIM$ Selective Plane Illumination Microscopy

SPM Self Phase Modulation

SR Super Resolution

$STED$ Stimulated Emission Depletion microscopy

THG Third Harmonic Generation

UV Ultra-Violet

WD Working Distance

Chapter One

Introduction

1.1 Motivation

Biological matter is arguably the most complex in the known universe [1]. Biological tissues (in plants and animals) rely on a multitude of developmental and repair processes which constantly change in response to their unique environments [2–4]. Biological tissues are fragile and have finite life-spans. Environmental pressure or the natural ageing of organisms over time can lead to tissue damage or disease. The understanding of these processes, which typically originate or are regulated on a sub-cellular scale, underpins our knowledge of many macroscopic behaviours in tissues, organs or in the entire organism. Deeper understanding helps us to develop new preventative and curative medicine to prolong and improve the quality of human, plant and animal life [5–8]. To aid discovery, it is essential to develop new imaging and measurement methods targeting the sub-cellular scale. We require sub-cellular information about many kinds of samples and processes. This information is often needed in the form of wide-angle images so that processes or features can be contextualised within their surroundings. Information can be located on or near a sample surface or much deeper within. Sometimes, repeated imaging over time is required to investigate developing biological processes. In these cases, the temporal resolution of an imaging method is important as well as its spatial resolution.

1.1.1 Imaging without harm

There is a distinction between imaging biological tissue for research purposes and imaging tissue to aid medical care. In the first case, it is often acceptable to image destructively; i.e. to destroy or deform the sample or to permanently alter its function in some way. Medical imaging requires a different approach. We would like to gather information about a patient without causing undue harm or discomfort. Often, multiple, non-destructive, analyses of the same tissue sample are required. These stipulations can add an additional layer of complexity to the creation of new imaging methods.

"Do no harm" is one of the sentiments of the Hippocratic oath which physicians must take before they are granted a licence to practice their skills on patients [9]. In reality, it can be very difficult to maintain this stipulation during day-to-day care. For example, chemotherapy can often be a very harmful, distressing treatment. However, it is still useful in that it can increase the number of quality life years available to a patient in the future. Similarly, it is deemed acceptable to excise small samples of functional tissue for destructive imaging if there is a risk that malignant sub-cellular changes would be detected. In these cases, detection of changes allows appropriate treatment to be sought (ideally before the local changes become macroscopic and/or possibly life-altering [10]). In other cases, destructive imaging allows doctors to assess the effectiveness of a treatment and to determine if further treatments will be required or not.

Any tools that the scientific community develop for use in the medical sector must facilitate routine tasks whilst minimising harm or damage to patients. "Label-free" imaging is preferred for *in vivo* detection. This means that there is no need to introduce foreign material into a sample to enhance image contrast[1] (more on the need for contrast to come in chapter 2). Better still, medical imaging methods would be label-free, non-invasive *and* non-destructive. In other words, there will be no tangible effect on the patient at all (including

[1]Many contrast-enhancing agents are damaging to biological material [11]

physical and psychological discomfort).

Imaging tools used for biomedical research (rather than healthcare) can generally afford to be more destructive than this. However, research can also require the imaging of live samples over time. Accurately modelling living tissue is difficult if we are constrained to observe cells outside of their natural environment (in a Petri dish, for example). We have tools to "freeze" tissue in time using fixation methods, but this inevitably changes the state of the cells before the fixed samples are imaged. Fixed cells are no longer living, making continuous observation of processes impossible using the same sample. Sometimes fixed tissue imaging is repeatable and the same preserved sample can be imaged again and again. Other times, fixed samples can be further altered by the act of capturing information about them, making them unimageable in the future. For each research or medical application, we can choose from a selection of current biomedical imaging techniques based on the answers to these questions:

1. What is the nature of the sample?
2. What would we like to know about it?
3. Can it be imaged *in vivo*?
4. Which imaging methods will work without destroying the information that we need?
5. Will the biological imaging method bring harm or discomfort to the organism that it grew from? If so, is potential the harm/discomfort deemed to be an acceptable sacrifice based on the value of the information[2]?

[2]This is a question of ethics. Generally the level of "acceptable sacrifice" is based on species and the reason for the sacrifice. Human culture tends to place the greatest value in human life, therefore we often use biological models based in other organisms (e.g. mice) to model human biological processes that we wish to better understand. These models can be studied (imaged) destructively within our moral architecture, if it is anticipated that doing so will have some significant benefit.

6. Will the sample need to be imaged again in the future?

7. How much time and money are available?

Choosing the right imaging method for each application is about finding a compromise between the characteristics of imaging methods (for example, spatial resolution) and any potential adverse effects to the subject. For the purposes of this Thesis I will divide all imaging methods into two families; optical and non-optical imaging. Optical methods (which use light to probe for information) are generally favoured for medical microscopy applications, whereas certain non-optical imaging methods are popular for medical, non-destructive, imaging of inaccessible areas of the human body. Chapter 2 will consider key methods from each family currently used for medical and research-motivated imaging, looking at the capability and suitable applications of each.

1.2 Aims

The main focus of this research is the betterment of a particular optical imaging method called light-sheet fluorescence microscopy (LSFM). I wanted to explore ways in which LSFM could be adapted to image deeper below the surface of intact biological samples whilst maintaining sub-cellular resolution in all three spatial dimensions. I experiment using LSFM techniques with a view to extend the range and quality of what can currently be imaged within the constraints of medical microscopy for pathology, and for *in situ* endoscopic medical imaging applications.

1.3 Thesis outline

1.3.1 Overview

Reflecting my research aims, this Thesis is an explanation of how I used a range of optical components and methods to create two novel light-sheet fluorescence microscopy systems. Each of these microscopes were prototype systems designed to meet selected demands set by modern biomedical applications. Specifically, I describe ways in which we can see deeper into a volumetric biological sample whilst maintaining sub-cellular resolution.

1.3.2 Chapter contents

Chapter 2 lays out some key techniques and background physics which underpin light propagation through biological tissue and aspects of fluorescence microscope design. Fluorescence microscopy is contextualised within a broader range of optical and non-optical imaging methods which are currently available for biomedical applications. Chapter 2 also notes common practices in histopathology (the study of disease in tissue) as this is the target application of one of the new LSFM designs. Non-linear fluorescence imaging, Airy and Bessel beam shaping, post-processing methods, and the delivery and collection of light using fibre optics are each discussed to provide a basis for LSFM adaptations which are described in later chapters.

Chapter 3 outlines in detail the design and construction of an "open-top" light-sheet fluorescence microscope for applications in histopathology. This open-top light-sheet (OTLS) geometry allows imaging of samples of arbitrary shape and thickness. Chapter 3 describes how Airy beam shaping can be utilised to increase the depth from which we can acquire high resolution fluorescence images from intact samples. Chapter 3 also includes a section on data post-processing with deep learning (DL) using an adversarial generative network (GAN). Experimental results show how DL can improve the resolution and signal to noise

ratio (SNR) throughout a volumetric data set. These methods were evaluated with fresh human tissue samples (breast and colon, cancerous and benign) to illustrate the potential utility in histopathology applications. The maximum imaging depths using Gaussian and exotic Airy beams for light-sheet (LS) illumination are compared in this chapter. Cleared mouse brain samples were imaged to further explore how LSFM, Airy beam shaping, and DL post-processing can be implemented harmoniously in one microscopy method. I describe how doing so can increase the attainable dimensions of high-resolution, volumetric data from intact samples when the constraints set by scattering sample media are reduced/removed.

Chapter 4 describes a scoping exercise undertaken via a collaboration with the Albert Einstein Institute in New York, where we trialled a compact LSFM design in a real clinical environment. A range of fresh and fixed human tissues were studied. Pros and cons of use of this technology in a clinical setting are considered. I summarise our experimental findings and the valuable feedback from pathologists who used the system. Points of note were folded into my new proposed design of the microscope, which addresses some of the issues that we faced. This redeveloped design is described at the end of chapter 4.

Chapter 5 explores two novel ways in which Bessel beams can be generated for non-linear fluorescence microscopy applications. I evaluate these methods and compare them to the more traditional approach of Bessel-beam shaping using an annulus. I consider non-linear effects in microscope design choices. Following this analysis, a new LSFM for biomedical applications is unveiled: a multi-photon fibre-based microscope with in-built Bessel beam illumination. I explain the capability and potential applications of this microscope. Initial experimental results using this design to image fluorescent bead phantoms with two-photon excitation are presented.

Chapter 6 contains concluding remarks and a short discussion of potential future avenues of investigation in this vein.

Chapter Two

Background

2.1 Image theory

2.1.1 The need for contrast

Let's take a moment to define an image. An image is a two-dimensional (2D) form of spatial information about a subject. Across this area, an image shows how one or more variables change relative to position. To construct an image, we need a method for differentiating a target feature from its background. In other words, we require contrast. This can be accomplished in a number of ways. For optical imaging techniques, contrast is generally produced through absorption, fluorescence and phase-altering processes. Definitions and examples of these effects used in practice are given in sections 2.3 and 2.4.2. For non-optical techniques (see examples in section 2.4.1), we can use many different kinds of sensor (e.g. force, temperature, vibration, magnetism etc) to build up an image, provided that there is some method of isolating measurements from individual locations. The spacing of discrete measurement sites represents the resolution or "pixel size" of an image.

Resolution is inherently linked to the recovery of spatial frequencies from an object, and the contrast of an image. A small pixel size does not necessarily improve the resolution if the signal to noise ratio (SNR) of measurements is too small to register changes from one pixel to the next. Generally speaking, contrast and high resolution become more difficult to achieve

with increasing imaging depth. This is because our measurement techniques must penetrate through more material in order to access the information, and more material can add noise and reduce contrast. Deep imaging of biological samples is particularly difficult to achieve. Animal tissues are often highly inhomogeneous. External detectors must have the means to bypass multiple obstructions and access a specific internal site without gathering irrelevant information from features elsewhere. Organic features can be difficult to model accurately prior to imaging, adding further complexity. The alternative to through-tissue imaging is to make incisions to directly access a measurement site. This option has its own problems which need to be considered on a case-by-case basis. "Penetration depth" is a term used to describe the distance between the surface of an intact sample and the deepest possible layer of information that we can access using a particular imaging technique whilst maintaining adequate contrast. The achievable penetration depth for imaging depends on the interaction between the probing mechanism and the sample itself. The spatial scale of the information that we require is normally a limiting factor. A good rule of thumb for biological imaging is: the higher the resolution, the shallower the penetration depth.

2.1.2 Field of view

The field of view (FoV) is another key image parameter. Some biological processes can only be understood when information is collected over a wide area at a single point in time. The FoV is dependent on both the probing mechanism and the detection mechanism. In other words; over what area have we managed to produce sufficient contrast, and over what area can we detect that contrasting information?[1] The FoV can be linked to the temporal efficiency (area imaged per unit time) of an imaging method. In general, methods able to

[1]In the context of illumination for optical fluorescence imaging, FoV refers to the area over which the illumination is sufficiently focused for fluorescence to occur. The FoV can also be used to describe the dimensions of the area captured by a detector array inside a camera. Note that these two FoVs are not always the same in an optical imaging setup.

acquire wide FoV images in a single acquisition require less imaging time than small FoV methods would need to view the same area.

2.1.3 Sectioning data in 3D

Some form of sectioning is required for volumetric imaging. If the sample itself is 2D, the edges of the sample form the "section", or the depth resolution of the image. We may stack successive sectioned images of a sample together to form a volumetric data set. In this case, 2D pixels become 3D voxels. Optical sectioning can be achieved through selectively applied illumination. Selective detection can also be used to improve the depth sectioning of an imaging system. If the penetration depth of a method is a similar length to the desired depth resolution, that method has inherent sectioning built into it for surface-level imaging of a 3D sample.

2.2 Biomedical imaging

For the purposes of this broad overview, I will group biomedical imaging into three subcategories based on application type. First, day-to-day medical imaging methods (for example magnetic resonance imaging (MRI), computed tomography (CT) scanning and ultrasound (US)) are targeted at minimally invasive assessment of disease, change or injury observable on a supercellular scale (for example; bone fractures, multi-cellular growths (tumours), fetuses, fluid build-up). Each of these non-optical imaging tools occupy a niche in diagnostic medicine which is determined by the unique properties of the method. Further information on each of these methods is provided in section 2.4.

Second, subcellular information can be required for diagnostic purposes. I will refer to this category as medical microscopy. The resolution of nuclei and other subcellular features is conveniently on the same scale as that of the resolution of many optical microscopy methods [12]. We can exploit the dimensions of an optical probe (i.e. a wavelength) to measure

features on the order of the diffraction-limited (or pixel-limited) resolution of an optical imaging system. This comes at the cost of lowered penetration depth as visible to light is strongly scattered in most human tissues [13, 14]. The interactions that occur between light and biological tissue are discussed in section 2.3.

The last category comprises of imaging tools for biomedical research. Imaging for biomedical research is a broad family of methods which can include both optical and non-optical imaging methods. This group is often used to study mechanisms on the scale of diffraction-limited resolution or smaller (although biomedical research can also cover lower resolution studies). Optical detection can be "upgraded" in certain situations so that light can be used to capture information that is smaller than the diffraction limit. These methods are known as super resolution (SR) imaging methods. Alternatively, there are non-optical options for even smaller resolution applications. For example, scanning electron microscopy (SEM) [15–18] can resolve features well below the optical diffraction limit (on the scale of nanometres, or even angstroms, rather than microns) [19–21]. Modern SEM can provide shallow volumetric information, however this is generally limited to 10s of nanometres below a sample surface [22].

In summary, all biomedical imaging techniques all have a fundamental limit in resolution and volume that can be imaged in a single acquisition [23–25]. Figure 2.1 summarises the typical trade-off that techniques make between penetration depth and resolution. Each imaging method referenced here is explained in more detail in the directory of imaging methods (section 2.4). For medical microscopy, optical imaging methods are most commonly used. The next section sheds light on why this is the case. 2.3 describes how light interacts with biological tissue and how these interactions can facilitate and hinder our use of it as a probing mechanism.

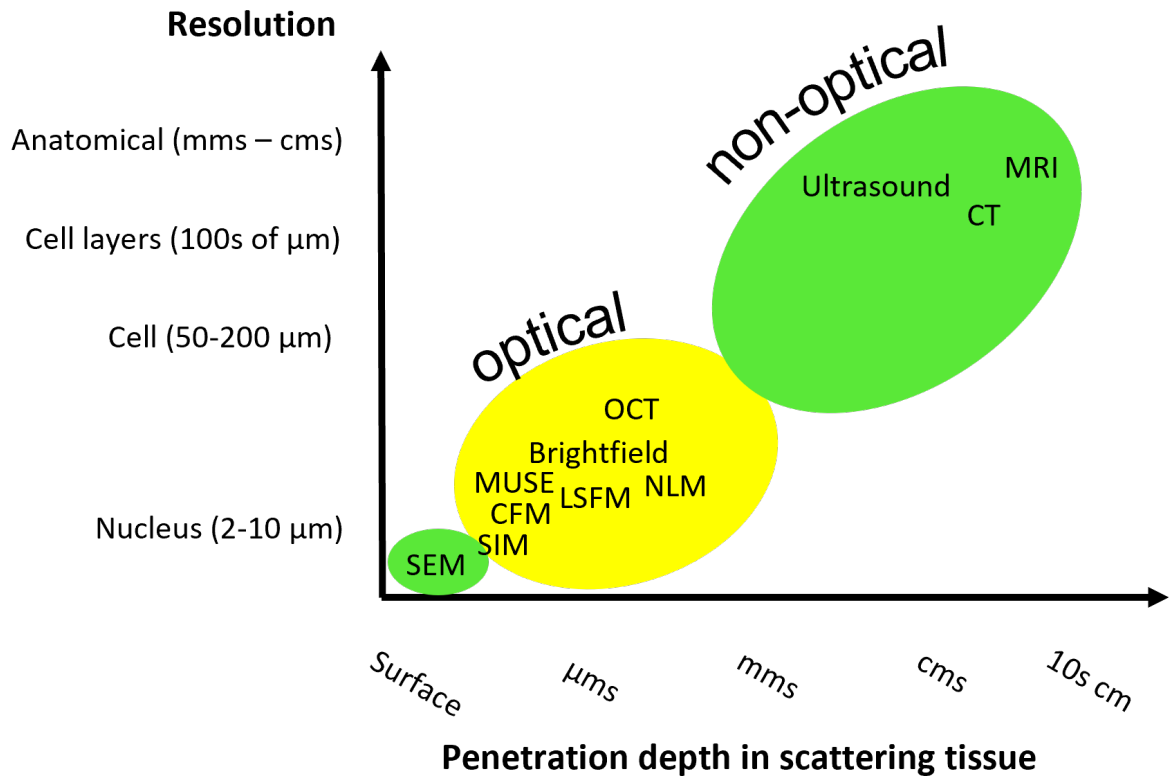

Figure 2.1 The penetration depth of optical methods for medical microscopy (inside the yellow circle) is fundamentally limited by attenuation of light in tissue. Non-optical techniques are highlighted in green. In general, low penetration depth SR resolution methods (like SIM and SEM) are most applicable in biomedical research applications. Ultrasound, MRI and CT are non-invasive medical imaging tools that are used to visualise mesoscopic and microscopic features some depth below the surface of particular human tissue types. Descriptions of all methods in this figure can be found in sections 2.4 and 2.5.

2.3 Optical imaging and light-tissue dynamics

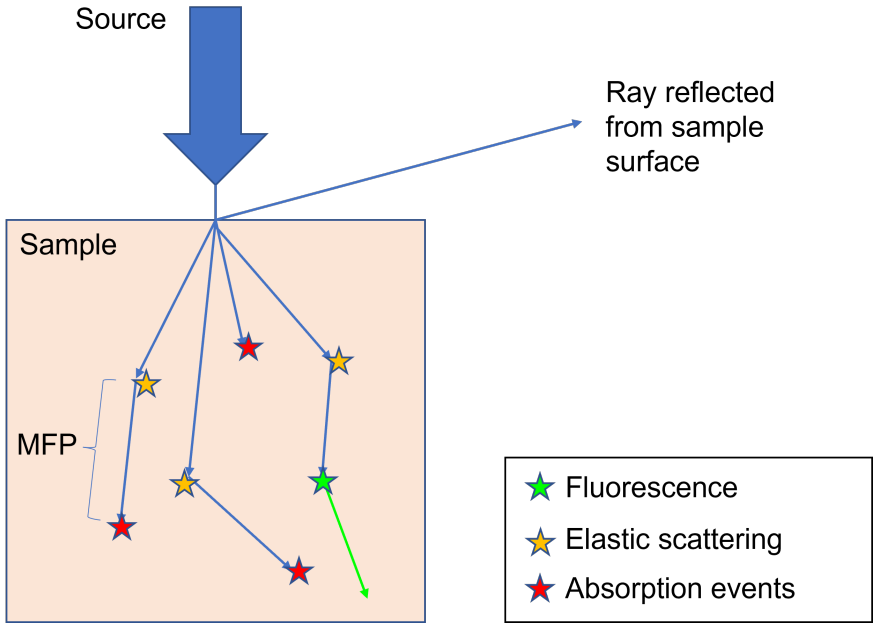

Figure 2.2 Cartoon showing possible photon-sample interactions. Some photons travel several mean free paths (MFPs) before being absorbed by the sample. A special case of absorption is also shown here - some of the energy from the incident (blue) is re-released in the form of a lower energy (green) photon. Elastic scattering of visible light is more likely to occur in tissue samples.

A thorough understanding photon-tissue interactions is required to engineer functional optical microscope designs for medical applications. To this end, let us consider the journey of an average photon. A photon released from a light source will maintain constant energy and travel in a straight line until one of the following events occurs:

1. The photon donates its energy to promote an electron within an atom to a different energy state (it is absorbed).

2. The photon undergoes elastic scattering. Its trajectory is altered but its wavelength is not. Energy is conserved.

3. The photon undergoes inelastic scattering. Some energy is lost to or gained from an external mechanism. The wavelength changes and the photon may have an altered

trajectory.

Elastic scattering, absorption and fluorescence are represented in 2.2.

Key definitions

We need some terms to describe where and when these events might occur. The average propagation distance of a photon through a medium can be modelled using the mean free path (MFP), an "extinction coefficient", and a probability distribution that describes likely scattering angles. The MFP is the average distance that a photon travels before interacting with a sample in some way. The photon travels linearly between interactions. The distance between interaction locations is selected from a probability distribution centered on the MFP. On arrival, the photon will either be absorbed or scattered. There is a second probability distribution associated with this "decision". The extinction coefficient expresses the likelihood that a photon will be absorbed by the sample [26]. This illumination and sample-dependent coefficient is inversely proportional to the average number of scattering lengths (n_{sc}) that each photon can travel inside a sample before absorption occurs. n_{sc} is linked to the penetration depth of an optical imaging method, although the total distance travelled is *not* equivalent to the penetration depth.

2.3.1 Scattering

Scattering is an event that can occur when photons meet atomic structures and refractive index boundaries. Scattering can be elastic (energy conserved) or inelastic (photon loses some energy to the material). Both elastic and inelastic scattering events can lead to the dispersal of light through a biological medium. The frequency and nature of scattering events in a sample depends on the wavelength of the illumination and the contents of the sample.

Linear scattering

We can estimate the angular dependence of linear scattering for each wavelength and the average particle size in a medium. Figure 2.3 shows a representation of scattering in the Rayleigh regime (where the particles are much smaller than the incident wavelength λ_0) and in the Mie regime (where particle sizes are similar or large compared to λ_0).

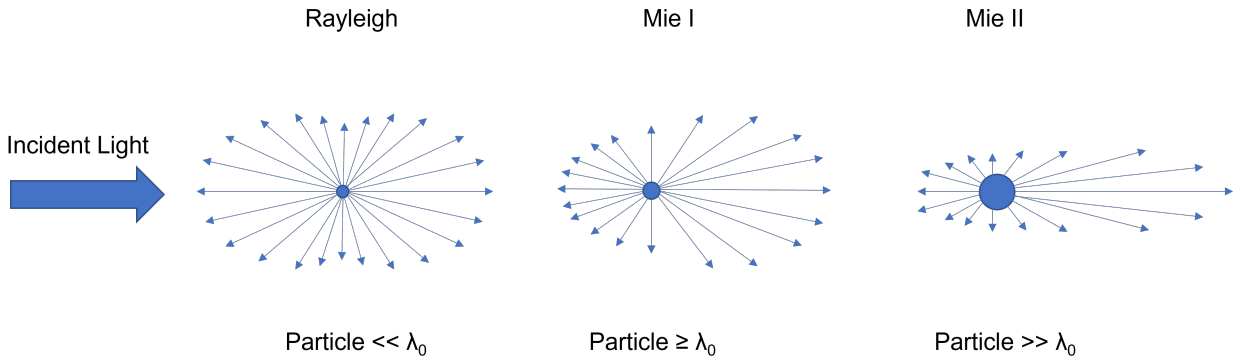

Figure 2.3 Directional scattering distributions are dependent on the relative size of the illumination and the scattering particle. Two regimes, Rayleigh and Mie scattering, are used to describe the likely scattering angles when the particle size « λ and when the particle size $\geq$ or » λ. Adapted from [27].

This dependence of scattering angle on incident wavelength is relevant to our aim of increasing the penetration depth of an optical imaging method. Rayleigh scattering often occurs when we use illumination in the visible range. This leads to significant back-scattering of photons propagating into tissue. For reflection-based imaging methods, this is a positive feature. For example, optical coherence tomography (OCT) utilises interference between incident and back-scattered light to calculate the depth of features inside a sample. OCT is explained further in section 2.4. For fluorescence-based imaging (see sections 2.3.4 and 2.4.2), back-scattering can present problems. It has the effect of dispersing light laterally through a sample and hindering propagation of illumination at depth. This reduces contrast throughout the sample, as there is out-of-focus signal near the surface and very little total signal at depth (signal falls below the noise level).

If we select a longer illumination wavelength (e.g. in the near infra-red (NIR)), we can

shift the scattering pattern towards the Mie regime. Mie scattering is also represented in figure 2.3. Mie scattering favours movement of photons in the forward direction and tends to increase the signal at depth whilst reducing out-of-focus illumination.

For highly structured samples (for example a layer of water on top of a planar sheet of glass) we can use Snell's law (see equation 2.1) to calculate expected refraction angles analytically. Refraction is linear scattering of electromagnetic waves due to changes in the propagation medium. In this case, we shift from a particulate model towards a wave-based model of light and can implement geometric optics for modelling. Refraction of light occurs where there are changes in refractive index (RI). RI (n(λ)) is also a wavelength-dependent material parameter.

$$n_1 sin(\theta_1) = n_2 sin(\theta_2) \tag{2.1}$$

Equation 2.1 Snell's law of refraction. n_1 and n_2 are the refractive indices (RI) of medium 1 and medium 2 respectively. A ray travels in a straight line through medium 1 towards medium 2. θ_1 is the angle between the ray trajectory and the normal of the RI interface. θ_2 is the refracted ray angle [28].

Total internal reflection (TIR) can occur when rays strike a surface at an angle equal to or smaller than the critical glancing angle θ_c, which is defined by equation 2.2 [29, 30].

$$\theta_c = sin^{-1}(\frac{n_2}{n_1}) \tag{2.2}$$

Equation 2.2 The critical angle, θ_c, is the angle at which an incident ray will undergo total internal reflection when it strikes a boundary between two refractive indices. This equation is only valid when the RI of the propagation medium, n_1, is greater than the RI of the material that the ray reflects from (n_2) [29].

2.3.2 Absorption

When a photon is completely absorbed, its energy is fully donated to some external mechanism (a molecule, for example). The original photon can no longer contribute to the elec-

tromagnetic field, however the energy from it can stimulate processes which then go on to produce more photons [31]. Unlike scattering, absorption does not lead to out-of-focus illumination. Absorption is an important part of generating fluorescence, which is discussed in sections 2.3.4 and 2.3.5. In order to use fluorescence as a contrast agent we must expect and encourage some absorption of incident light [32]. However, if too much absorption occurs, the illumination will have a low n_{sc} value in that sample. The illumination will not penetrate below the surface layers, and imaging will be limited to the surface only. The sample may also be damaged by excessive energy deposition.

2.3.3 The therapeutic window

"Therapeutic windows" are ranges of wavelengths where the total attenuation of light due to scattering and absorption in human tissue is lower than average. In human skin, absorption (due to melanin) is the dominant force in optical attenuation in the UV region [33–35]. Elsewhere, scattering typically dominates. Water, a primary component of human cells has reduced absorption in the NIR [33, 36, 37]. This is the first optical window (650-950 nm) [37]. Absorption of light is minimised when the chemical compounds present (e.g. water and hemoglobin) simultaneously have a dip in absorption spectra. The higher the concentration of the compound, the greater impact its absorption spectrum and scattering properties has on total attenuation.

In modern medicine and biomedical research of human disease, volumetric tissue imaging techniques are often limited to use illumination wavelengths within a therapeutic window)[2]. The specificity of optical window predictions can be improved for a particular tissue type by including more of the chemical compounds present and their relative concentrations. We can use knowledge of the absorption and scattering properties of tissue to specialise an optical

[2]Some naturally transparent human tissues (for example the cornea) do exist. There are also some naturally transparent animal models for human tissues. We can employ "tissue clearing" techniques to render opaque samples transparent for biomedical research purposes. See section 2.3.12 for further information.

imaging method for different types of tissue sample. It is worth noting that absorption and scattering affect both the incident light and any fluorescent response generated within samples.

2.3.4 Fluorescence

Illumination may be used to excite fluorescent molecules inside a sample [38–41]. These can be man-made fluorophores or naturally autofluorescent molecules. Typically, these molecules are sensitive to a particular window of wavelengths at which incident photon energy may be absorbed. A photon of the correct energy is absorbed by the molecule. After some time interval, a second photon may be released from the molecule with less energy and a longer wavelength than the incident photon (see equation 2.4). For fluorescence microscopy, a certain threshold of incident photons must be reached for this effect to become imageable above the noise floor. The likelihood of incident photon absorption occurring is defined using the absorption cross section, $\sigma(\lambda)$, which is different for each fluorescent molecule[3].

Equation 2.3 describes the relationship between the local fluorescence intensity, $I_f(b)$, and the illumination intensity, $I_{ex}(b)$, for the simple case of illumination in a solution of fluorescent molecules. A is a dimensionless coefficient describing the fraction of total available light that is absorbed (the absorption coefficient). γ is the absorption coefficient per mole of the fluorescent material per cm. κ is the quantum efficiency of photon generation; i.e. the ratio between photons absorbed and photons emitted as fluorescence. *C(b)* is the local concentration of the solution in Mcm^{-3} and L (cm) is the thickness of the material that the illumination passes through.

Let's look at what this means diagrammatically.

[3]If there are more incident photons, the total probability of fluorescence occurring increases. The intensity of the incident beam is therefore very important

$$I_f(b) = I_{ex}(b)A\gamma\kappa C(b)L \tag{2.3}$$

Equation 2.3 Equation for local fluorescence intensity in a fluorescent medium based on general parameters. The absorption coefficient, A, is equal to the total attenuation coefficient minus the contribution to attenuation due to scattering. Repeated scattering events will reduce the incident intensity $I_{ex}(b)$ in line with the dominant scattering regime (Rayleigh or Mie). Adapted from [42].

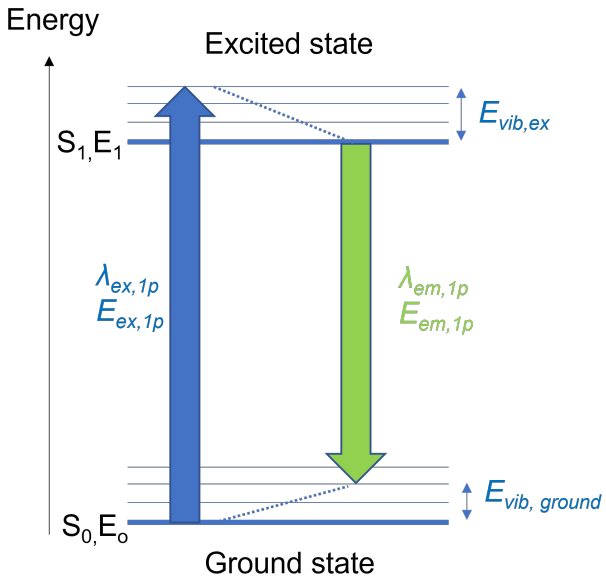

Figure 2.4 A Jablonski representation of one photon excitation (OPE) of an arbitrary fluorescent molecule. S_0 is the ground electronic energy state and S_1 is an excited electronic energy state. Above S_0 and S_1, there are additional energy sub-levels corresponding to vibronic states where an electron may also reside. Vibrational ("non-radiative") transitions ($E = E_{vib}$) give the emitted photon (with energy $E_{em,1p}$) a lower energy and longer wavelength ($\lambda_{em,1p}$) than the incident photon (energy $E_{ex,1p}$, wavlength $\lambda_{ex,1p}$). Excited energy levels have an associated lifetime which is the length of time an electron is likely to stay there before energy is lost by non-radiative decay or by release of a photon. In this diagram, the green arrow represents a longer photon wavelength (lower energy transition) than the blue arrow (a higher energy transition). Equation 2.4 shows the relationship between wavelength and energy of a photon. λ and E have subscripts $_{1p}$ to indicate that this cycle is due to OPE. Adapted from [43].

When it comes to predicting excitation and photon emission energies, we must consider each fluorophore type separately. They each have unique molecular properties which may

be understood with a Jablonski diagram like the one shown in figure 2.4. Without external excitation, an electron naturally rests in the first "ground state" (S_0) of the molecule (or one of the associated vibronic levels). Radiation from an external electromagnetic field can be applied to donate extra energy to the system. If the incident photon energy, E_{ex}, matches the energy gap between the ground state and a higher energy state, the photon can be absorbed by the electron. The electron is then in an "excited state" (S_1) of the molecule. This is "one photon" excitation (OPE), so called because a single photon has been absorbed. Typically, the electron loses some energy ($E_{vib,ex}$) by vibrational decay and descends to a slightly lower energy level after some time. From here, the electron energy may further decay back down to a vibrational ground state ($E = E_0 + E_{vib,ground}$). When this happens, a second photon is emitted. Fluorescent photons have an energy, E_{em}, equal to $E_{ex} - E_{vib}$, where E_{vib} is the total energy lost to during vibrational "non radiative" transitions. Fluorescence therefore has a longer wavelength than the incident field and a lower energy. This spectral change is known as the Stokes shift. Equation 2.4 relates photon energy to wavelength and frequency.

$$E = \frac{hc}{\lambda} = h\nu \tag{2.4}$$

Equation 2.4 The Planck-Einstein relation [44]. Photon energy, E, is related to the wavelength, λ), and the spectral frequency, ν, of the wave packets. h is Planck's constant and c is the speed of light in a vacuum.

Sources for generating one photon fluorescence

Many laser and LED devices are available for OPE applications. They must produce photons at a rate which is sufficient to generate enough contrast for imaging. One photon fluorescence is a linear response (see equation 2.3), therefore the fluorescence increases linearly with increasing illumination intensity. It is not practical to measure this trend all the way down to $I_{ex}(b) = 0Wcm^{-2}$ as no imaging system can completely eliminate noise. The illumination must provide sufficient power to overcome the noise floor level. Continuous wave (CW) laser

sources are often used for OPE imaging systems. These sources output photons constantly over time. Figure 2.6) shows a comparison between a CW laser output and a non-continuous source of the same average power.

2.3.5 Multi-photon fluorescence

It is also possible to use "multi-photon" excitation (MPE) to induce a fluorescent response. MPE is useful for increased optical sectioning ability and for seeing deeper into biological tissue, as will be discussed in section 2.4. This kind of excitation is more difficult to achieve than OPE. With two photon excitation (2PE) and three photon excitation (3PE), two or three identical photons are absorbed simultaneously by a fluorophore to excite an electron to a higher energy level[4] 2PE is less likely to occur than OPE, 3PE is less likely than 2PE and so on. The intensity of the fluorescent response I_f varies with $I_{ex}(b)$ to the power of the fluorescence excitation order, n [47, 48]. Multi-photon excitation (MPE) may also represented in a Jablonski diagram. Figure 2.5 shows the same fluorophore depicted in figure 2.4, this time absorbing multiple incident photons at once. The excited electron, as with the one photon case, undergoes some energy reduction via non-radiative transitions. The electron then makes a further transition back to a ground state and in doing so releases a photon with energy $E_{em,2p}$ or $E_{e,3p}$. Equation 2.4 may be modified to form 2.5 for the absorbed energy in 2PE and 3PE cases. It is important to note that in most cases, $E_{em,1p} \approx E_{em,2p} \approx E_{em,3p}$, however these energies are not always identical. Indeed, $E_{ex,1p}, 2 \times E_{ex,2p}$ and $3 \times E_{ex,3p}$ are also slightly different in many cases [49]. This is because the likelihood of absorption, $\sigma(\lambda, n)$, varies with the wavelength of the incident light *and* the order of excitation n [46, 49–52]. There may be a shift in the absorption peak when multi-photon excitation is used. A shift in the emission spectrum follows from this.

[4]Multi-photon absorption normally occurs when incident photons are of equal energy, however it is also possible that "non-degenerate" absorption will occur and two photons of different wavelengths will each donate their energy to the same electron [45, 46].

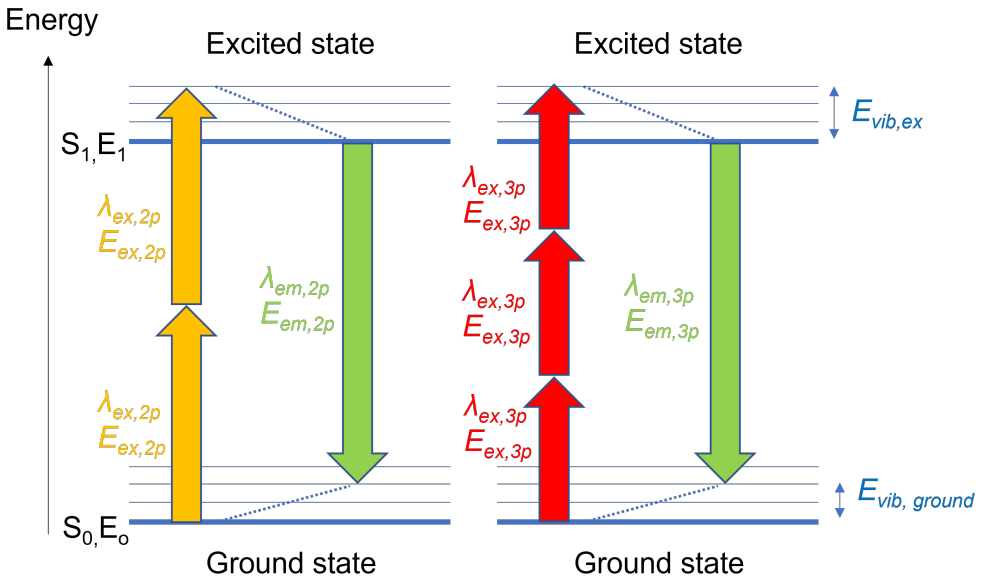

Figure 2.5 A Jablonski representation of two and three photon excitation (left and right respectively). 2PE occurs when two incident photons strike the molecule at the same time. These photons each have an energy equal to half of the energy gap between the ground state and an excited state. 3PE is a similar process but it is even less likely as three identical photons must be present at the same time for the molecule to absorb them together. Adapted from [43].

$$E_{nPE} = \frac{hc}{n\lambda} = \frac{h\nu}{n} \tag{2.5}$$

Equation 2.5 Total absorbed energy, E_{nPE}, is related to the combined energy of multiple (identical) incident photons. n is is order of excitation, or the number of photons that were absorbed simultaneously. λ is the wavelength of the illumination.

Manufactured fluorescence and natural "autofluorescence"

Fluorescence events involving one or multiple absorbed photons can occur in natural endogenous compounds in a tissue. This is known as "autofluorescence". Autofluorescence can be useful for label-free imaging (relevant to *in vivo* studies) however autofluorescence images often lack contrast. To enhance or implement the fluorescent response from samples, we may add fluorescent dyes which selectively attach to the features we would like to image.

Targeted fluorescence imaging (with one or multiple photon excitation) is widely used in medicine and in biomedical research [51, 53–59]. Contrast-enhancing agents which bind to antibodies are a powerful tool for medical microscopy and biomedical research [60]. This kind of imaging is often *ex vivo* as many fluorescent dyes are harmful to humans. It is important to match the illumination wavelength carefully to the excitation wavelength of the fluorescent molecules. This maximises the contrast and helps to avoid excessive exposure to radiation. High incident optical power can cause photo-bleaching [61], fluorophore saturation [50, 62] and photodamage [63] inside a sample.

2.3.6 Pulsed Sources

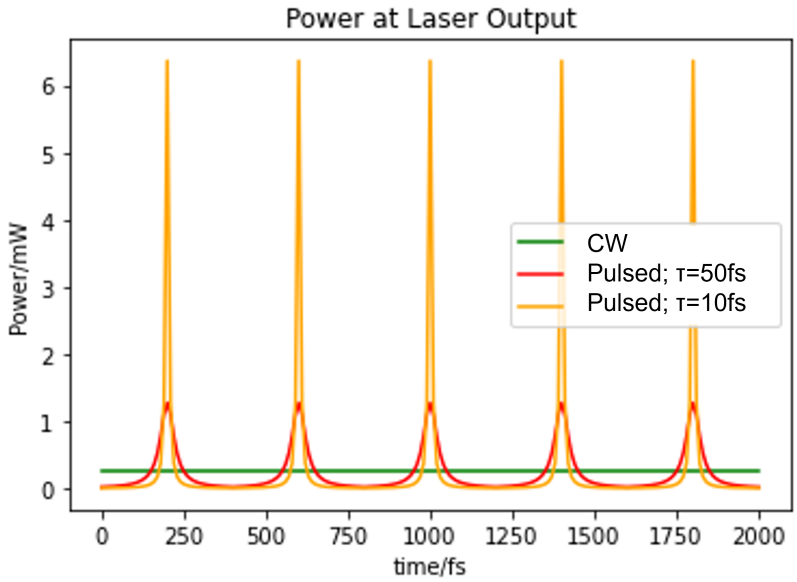

Figure 2.6 Continuous wave illumination vs pulsed illumination. P_{Avg} of the CW source is 0.4 mw, which is also P_{Peak} in this case. The pulsed lasers also have an average optical power of 0.4 mW. Both pulsed sources have a pulse interval of 400 fs. By reducing the pulse duration, τ, by a factor of 5, the peak power is increased from 1.3 mW to 6.4 mW. These pulses have a Lorentzian profile in time, but other pulse shapes are also possible.

We can increase the likelihood of MPE occurring by increasing the number of incident photons which arrive in the same place at the same time. For this, pulsed illumination

is used. Continuous wave (CW) lasers generate a constant flow of photons in time. In chapters 3 and 4, I discuss how optics can be used to manipulate light from a CW source to focus rays to pass within a small volume, thus increasing the photon flux or the optical intensity. Pulsed sources take this idea further by grouping output photons into small bundles in time. A "pulse" is a burst of photons released within a short time interval. The duration of the pulse is called τ. For MPE, we generally require τ to be in the order of 10s of femtoseconds or shorter [64]. Using ultrashort pulses dramatically increases the odds of MPE occurring in a fluorophore at the beam focus. The shorter the pulses, the higher the peak optical power (P_{peak}) for the same number of incident photons. Equations 2.6 and 2.7 are useful for estimating the energy and power deposited by pulsed lasers. Figure 2.6 shows a representation of such laser pulses and compares the situation to a CW source of the same average optical power (P_{avg}). Pulse shapes can typically be fitted using some general function (e.g. sech^2, Lorentzian etc) [65–67]. By curve-fitting the pulses we can estimate the pulse duration (τ) with a full width half maximum (FWHM) measurement, for example. The pulse interval, T, is the time interval between successive peaks. Repetition frequency, f_{rep}, is equal to $\frac{1}{T}$.

$$E_{pulse} = P_{peak} \times \tau \tag{2.6}$$

Equation 2.6 The energy contained within each pulse (E_{pulse}) from the source can be approximated using this expression, which assumes that the pulses are top hat functions in time. The approximation may be improved if the shape of the pulse in time is known.

$$P_{avg} = E_{pulse} \times T \tag{2.7}$$

Equation 2.7 The average power is the rate that energy is transferred during a complete pulse cycle with cycle length T. This expression is valid if the source produces one pulse per cycle.

CW and pulsed sources typically output a small bandwidth of frequencies [68]. CW

sources are more monochromatic and can have bandwidths of $<$ 1nm [69], whereas for ultrashort pulsed sources bandwidths of $>$10 nm are common. This has implications for a non-linear effect called dispersion (see the next section for details). In order to achieve MPE for fluorescence microscopy, short pulse durations must be preserved during energy transfer between the source output and the focal plane inside a fluorescent sample.

Dispersion

The refractive index (RI), n, is a medium specific function which can vary with temperature, optical intensity and wavelength amongst other things. For a CW beam propagating through a uniform medium with $RI = n(\lambda)$, this is not so crucial. Some wavelengths travel slower than others, but the overall intensity, $I(t)$, after some propagation distance is not altered very much as all wavelengths arrive continuously. However, for a pulse of light containing multiple wavelengths, $RI = n(\lambda)$ means that some parts of a pulse are slowed more than others. Group velocity dispersion (GVD) can dramatically change the peak intensity of a pulse after propagation through a dispersive medium. The peak intensity is high only if the pulse duration is kept short. A representation of pulse GVD through a medium is shown in figure 2.7. Pulse durations are always finite rather than infinitely short because they are transform-limited. That is it say, a duration of 0 seconds corresponds to an infinite energy, and this is not physically possible.

In glass, short wavelengths are slowed more than long wavelengths. Let's assume that a short pulse is made up of multiple wavelengths, and that each wavelength contributes to the intensity, $I(t)$, throughout the pulse duration before a dispersive glass element. As the pulse propagates through the glass, the short wavelengths are slowed more compared to the long wavelengths and this leads to a broadening of the pulse in time. The pulse thus becomes "positively chirped" (as shown in 2.7). If we change the initial pulse so that short wavelengths are at the front of the propagating wave bundle, then we give them a "head start" so that the faster, long wavelengths catch up with the short and the pulses become narrowed. This is

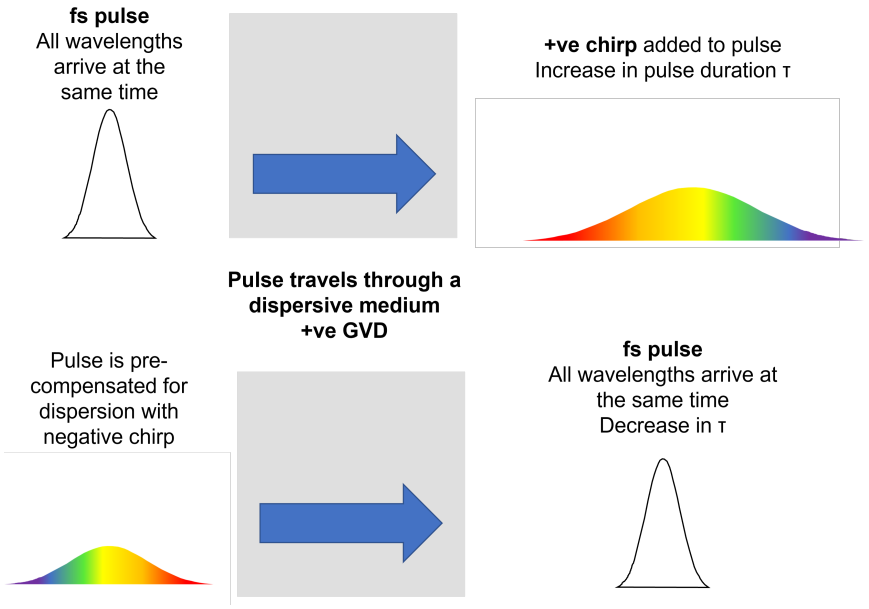

Figure 2.7 A cartoon explaining pulse dispersion and pre-compensation. The y axis is intensity (A.U.), the x axis is time and the colours represent wavelength. White represents all wavelengths contributing to the intensity at that point in time. Without pre-compensation, pulses arrive at the end point with a chirp due to group velocity dispersion (GVD). In this figure the grey regions represent some dispersive media with $RI = n(\lambda)$. A pre-compensated negatively chirped pulse undergoes GVD too. In this case, the blue end of the pulse travels more slowly through the medium than the red end, allowing the back end of the pulse to "catch up" with the front by the time the pulse reaches its destination. The wavelengths arrive in a short fs burst. The pulse duration, τ has decreased through the medium. Pre-compensation requires prior knowlegde of the optical setup and initial pulse properties.

called dispersion compensation using a "negative chirp''. To compensate for pulse dispersion in each unique setup, we must have a clear understanding of dispersive properties throughout the specific optical path to ensure that the pulses arrive at their destination in a temporally compressed form. Dispersion through a fibre optic is given in units of $ps.nm^{-1}.km^{-1}$. This unit of measurement relies on being able to accurately fit a function to the pulses to get a reliable value for the pulse duration at spatial intervals.

Other non-linear effects

GVD considers the temporal distribution of a laser pulse. Pulses may also be described in frequency space, but this spectral distribution is not altered directly by GVD. However, other non-linear effects do affect the spectrum. In fact, we have already discussed one such process (multi-photon absorption) in section 2.3.5. The following non-linear behaviours are particularly relevant to studies described in this Thesis.

- Multi-photon fluorescence
- 2nd and 3rd harmonic generation (2HG and 3HG)
- Self-phase modulation (SPM)
- Self-steepening

2HG and 3HG can occur when material is exposed to illumination at some resonant wavelength λ. Absorption of incident photons occurs as described in sections 2.3 and 2.3.5. However, with non-linear harmonic generation, electrons excited into a higher energy level (S_1) undergo no vibrational decay to lower energy levels and instead the full energy of the absorbed photon is conserved and re-emitted as a photon with $2\times$ (2HG) or $3\times$ (3HG) the energy.

SPM [70–72] and self-steepening are non-linear effects associated with pulsed illumination in single mode fibre (SMF) optics. Ultrashort pulses can self-focus via the optical Kerr effect [73], where the refractive index of a medium varies with incident optical intensity (which varies significantly with ultrashort pulses). The varying refractive index causes phase shifts in the pulse, which also shifts the frequencies in Fourier space. There is an increased likelihood of SPM with small SMF fibre core diameters [74]. SPM can lead to spectral broadening and symmetrical oscillatory patterns about the central wavelength [72, 75].

Self-steepening [76–78] causes the central wavelength of illumination to shift, normally towards shorter wavelengths. It has been noted previously in ultrashort laser experiments

with SMFs [79]. Self-steepening also occurs due to the rapidly changing optical intensity of an ultrashort pulse. The refractive index experienced by the centre of the pulse, where intensity is strongest, is different from the intensity experienced by the leading and trailing edges [78].

These non-linear effects, and others, may found in fibre optics when they are irradiated with very high peak powers from pulsed sources. Non-linear effects can be increased with fibre length, mode field diameter (MFD), average intensity as well as peak intensity.

2.3.7 Gaussian beams

This section is provided as a reference point for LSFM with beam shaping, which will be covered in section 2.6. Gaussian beams are common to all forms of optical imaging, although the use of shaped light for biomedical research has steadily been increasing in recent years[80].

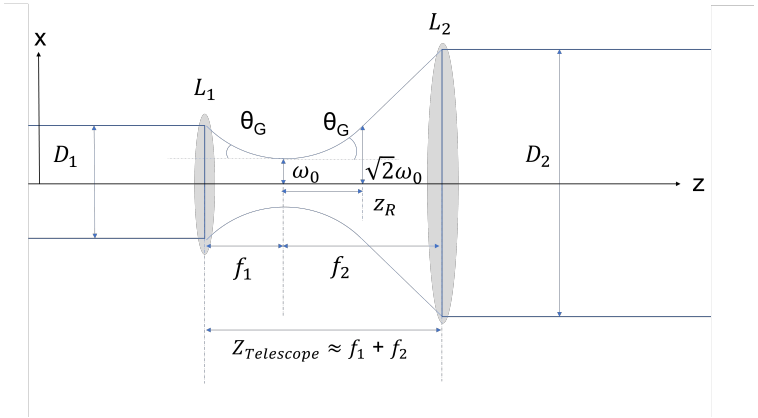

Figure 2.8 Diagram of a collimated Gaussian beam that has been focused and recollimated with a wider diameter using a two lens telescope (L_1 and L_2, with focal lengths f_1 and f_2 respectively). ω_0 is the radius at the beam waist. θ_G is the angle of far-field divergence of rays propagating out from the focal plane of the Gaussian beam. Z_R, the Rayleigh range, denotes the distance which a Gaussian beam propagates before the cross-sectional area has doubled in size compared to the beam waist. D_1 is the diameter of the incoming collimated beam and D_2 is the diameter of the collimated beam post expansion. Not drawn to scale.

Figure 2.8 shows a schematic diagram of a Gaussian beam, where the solid blue line at the beam edge represents the point in the field where the beam intensity has dropped to

$\frac{1}{e^2}$ of the maximum intensity value. The region between lenses L_1 and L_2 is labelled key parameters which are widely used to describe a focused Gaussian beam. The cross-sectional beam radius between the lenses, ω_0, is given by equation 2.9 where λ is the wavelength and the other parameters are attributed to the geometry shown in figure 2.8. In the context of fluorescence microscopy, the focused spot size (of the illumination) is directly linked to the resolution of the instrument.

Equation 2.8 describes the electric field of a Gaussian beam. A_0 is a scaling factor equal to the square root of the maximum intensity at $E(r{=}0,z{=}0,t{=}0)$ ($I \propto |E|^2$). r is the radial axis in cylindrical coordinates. ν is the frequency of the illumination and $e^{i\nu t}$ represents time-dependent oscillations of the electric field. The first exponent describes the characteristic distribution of a Gaussian function, rotationally symmetric about the optical axis at propagation distance z. k is the wavenumber in z ($k{=}2\pi/\lambda$).

$$E_G(r,z,t) = A_0 e^{i\nu t} \frac{\omega_0}{\omega(z)} \exp \frac{-r^2}{\omega(z)^2} \exp -i(kz + \frac{kr^2}{2R(z)^2} - \phi(z)) \tag{2.8}$$

Equation 2.8 Gaussian beam propagation. The electric field of a Gaussian beam E_G away from the focus with initial (maximal) field amplitude A_0. i is the imaginary number $\sqrt{-1}$. Adapted from [81].

The beam waist radius at any given position in z is given by equation 2.9.

$$\omega(z) = \omega_0 \sqrt{1 + (\frac{\lambda z}{\pi \omega_0^2})^2} \tag{2.9}$$

Equation 2.9 The Gaussian beam radius, ω, scales with propagation distance, z, and is symmetrical about the focal plane and about the optical axis ($\omega(z) = \omega(-z)$ and $\omega_x(z) = \omega_y(z)$). Adapted from [81].

The distance at which the beam area has doubled ($\omega(z) = \sqrt{2}\omega_0$) is called the Rayleigh range, or Z_R. Z_R is given in equation 2.10 and shown in figure 2.8[5].

[5]The confocal parameter 'b' is sometimes used to describe the total length of Rayleigh range on both

$$Z_R = \frac{\pi\omega_0^2}{\lambda} = \frac{k\omega_0^2}{2} \tag{2.10}$$

Equation 2.10 The Rayleigh range of a Gaussian beam, Z_R, is dependent on the wavelength of light, λ, and the beam waist radius, ω_0. This is related to the wavenumber, k. Adapted from [81].

Wavefronts are always perpendicular to the direction of propagation. At the focus of a Gaussian beam, the wavefront is planar, however on either side a curve develops due to diffraction. The radius of curvature (ROC), $R(z)$ of the wavefronts at any given point is given by equation 2.11.

$$R(z) = z + \frac{Z_R^2}{z} \tag{2.11}$$

Equation 2.11 Radius of curvature, $R(z)$, may be calculated using the known Rayleigh range of the Gaussian beam. Adapted from [81].

$\phi(z)$ is the Gouy phase for Gaussian beam propagation [81]. It describes how the phase of the beam evolves as a Gaussian beam propagates. $\phi(z)$ is given in equation 2.12.

$$\phi(z) = \arctan(\frac{z}{Z_R}) \tag{2.12}$$

Equation 2.12 The Gouy phase, $\phi(z)$, for Gaussian beam propagation [81].

Equation 2.13 is a useful approximation for the far field divergence angle, θ_G, of a Gaussian beam given the beam waist radius, ω_0, and the wavelength, λ.

sides of the focus ($b = 2 \times Z_R$). This region of the beam is considered to have a focusing power acceptable for fluorescence imaging with Gaussian illumination provided that the beam waist has similar dimensions to the target feature size.

$$\theta_G = \frac{\lambda}{\pi\omega_0} \tag{2.13}$$

Equation 2.13 The far field divergence of a Gaussian beam may be calculated with knowledge of the focused spot size and wavelength. Note the similarity between this expression and equation 2.14. [81]

2.3.8 The diffraction limit

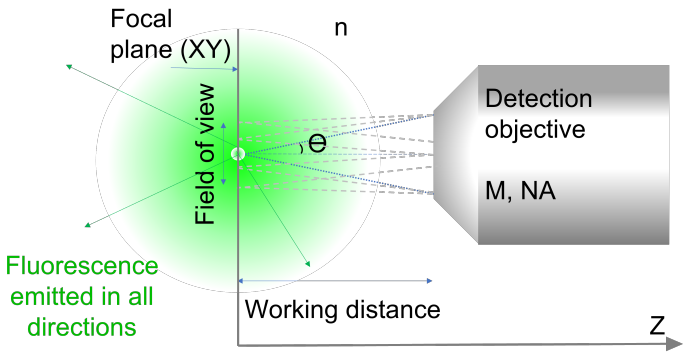

Figure 2.9 A detection objective with some magnification (M) and numerical aperture (NA) captures a cone of light emitted by a fluorescing point source suspended in a medium with refractive index (RI) (n). A cone of light is collected from each point within the field of view of the objective lens. Successive optics in a detection system combine focusing power to produce some total magnification, M_T, which increases the scale of the image of the sample section. The working distance (WD) is the distance between the edge of the objective lens and the focal plane. The focal plane normal is parallel to the optical axis of the detection pathway. The area of the focal plane that the objective can detect a signal from is FoV. The maximum detectable angle of a fluorescent photon trajectory is θ.

Gaussian beams have traditionally been focused into fluorescent samples in order to generate a response which can then be imaged. We now turn our attention to the detection of fluorescent signals. The smallest resolvable spot of light has a diameter, d, which is defined by the Abbe diffraction limit (equation 2.14) [82, 83]. This limit is due to the natural diffraction of light waves as they propagate. d is dependent upon the wavelength of light emitted from that spot and the NA of the detection objective (see figure 2.9 and equation 2.15). Imaging techniques that surpass the "diffraction-limited" resolution set by the Abbe criterion are

known as "super resolution" (SR) methods [84–89][6]. θ and the refractive index (RI) of the medium, n, dictate the numerical aperture (NA) of the objective via the relationship given in equation 2.15.

$$d_{x,y} = \frac{\lambda}{2NA} \tag{2.14}$$

Equation 2.14 The Abbe criterion [82]. The diffraction-limited spot size, d, corresponds to the smallest resolvable feature in an fluorescence image. λ is the wavelength of the emission and NA the numerical aperture of the detection optics (equation 2.15). x and y are Cartesian spatial dimensions in the focal plane. In most cases, $d_x = d_y$ although not always.

$$NA = n \sin \theta \tag{2.15}$$

Equation 2.15 The numerical aperture (NA) of an optical component. n is the RI of the medium and θ is the angle of the light cone collected from the sample. A large angle θ is needed for high resolution fluorescence detection.

Wide-field detection is signal capture that happens over an entire area simultaneously. Without some kind of scanning, the field of view (FoV) of a wide-field imaging is limited by the choice of detection optics (see figure 2.9). A high NA objective has a stronger focusing power and this usually means it will have a smaller FoV. This point is illustrated in figure 2.10.

Wide-field imaging differs to point-scanning detection methods (e.g confocal microscopy; see section 2.4.2) which capture signal from a sample one spatial coordinate at a time.

[6] An example of one such technique is structured illumination microscopy (SIM), which is discussed in section 2.4

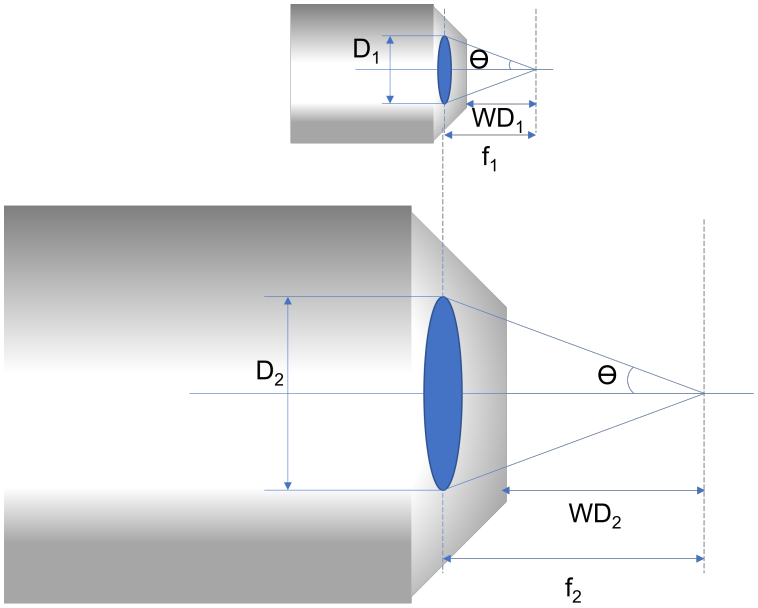

Figure 2.10 High NA objectives are constrained by short working distances (WD)s unless the lens geometry is scaled up to compensate. This cartoon represents a scaled-up objective lens used to increase the working distance without affecting the numerical aperture. Larger optics are heavy, bulky and not practically suited to many optical setups.

High-NA objectives require a large lens aperture diameter in order to capture a wide angular range of rays. The NA is intrinsically linked to the resolution of the objective (see equation 2.14). Figure 2.10 shows how this relationship places constraints on the working distance (WD) of an objective with a limited aperture diameter. For practical imaging setups, short WD objectives are therefore used for high-resolution imaging close to the surface of samples (within the WD of the objective). For imaging at depth, a longer WD objective is required. This necessitates acceptance of lowered resolution in most cases. The geometry of epifluorescence microscopy (an example of which is in figure 2.12) places strict constraints on axial resolution and lateral resolution that can be achieved with a high magnification objective (see section 2.3.8 for more details).

N.B. Physicists tend to use a scale bar to show the magnification of an image relative to the pixel size, however it is also common to see image magnification quoted as factor (e.g. 50×) in an image caption (particularly in the biomedical sciences). In the latter case, further

information is needed to find the true resolution of the image (especially digital images).

2.3.9 Nyquist sampling

In order to make full use of the optical (diffraction-limited) resolution of a wide-field imaging system, the Nyquist sampling condition (equation 2.16) must be satisfied [90]. If it is not, the system will instead have pixel-limited resolution (i_x). This is given by equation 2.17). The FoV of an array of pixels at the end of an optical detection pathway is given by equation 2.18.

$$\frac{N_{pixels}}{d_{x,y}} \geq 2 \tag{2.16}$$

Equation 2.16 The Nyquist sampling rate [91]. In each dimension, the sampling rate, N_{pixels}, required to fully resolve a diffraction limited spot is at least two pixels per diffraction limited length $d_{x,y}$ (equation 2.14).

$$i_x = \frac{d_x}{M_T} \tag{2.17}$$

Equation 2.17 The object in focus is relayed through optics with a particular magnification, M_T, and the image is re-focused onto an array of detectors (pixels), each with dimensions i_x. Typically, camera pixels are square, in which case $i_x = i_y$.

$$FOV_x = i_x \times n_x \tag{2.18}$$

Equation 2.18 The FoV in x is the real distance along x sampled by each pixel, i_x, multiplied by the number of pixels in the x direction, n_x. The same relationship applies for the FoV in the perpendicular y dimension.

2.3.10 Microscope geometries

Many geometries are possible for optical microscopy systems. Most commonly used are collinear geometries - in this case illumination and detection are coaxial with one an-

other. Examples include confocal epifluorescence microscopy and brightfield microscopy (transmission-based). These examples are both described in section 2.4 Alternatively, decoupled illumination and detection pathways are possible, as is the case with light-sheet fluorescence microscopy which displaces one path by 90° to the other (see section 2.5 for details). "Open-top" imaging geometries can be used when we want to image large or irregular samples from below. Open-top optical imaging systems are designed so that all illumination and detection optics are situated below an imaging platform, which samples can be placed on top of.

Medical microscopes often involve fibre-based geometries to allow more flexibility to image hard-to-reach places. Fibre optics are a mature technology now widespread in their use across multiple sectors. Their principal purpose is to deliver or collect light from a remote source with minimal losses. In medicine, fibre optics are used for endoscopic procedures (minimally invasive internal examination). The main body of a fibre microscope may be kept at the processing end to keep the volume of equipment inserted into a patient to a minimum.

2.3.11 Characterising an optical microscope

Point spread function (PSF)

The PSF is an important term in microscopy. It describes the intensity profile of an imaged point-like object in the microscope's focus, or the impulse response function of the system. Ideal optical imaging systems have a spatially-invariant PSF. However, in practice optical aberrations will always occur, particularly away from the optical axis. Accidental aberrations and deliberate optical design features can impact the PSF (a function of position) across the entire FoV.

The PSF is independently affected by both the illumination beam and the detection optics. The PSF of a microscope is independent of the sample being imaged, although the way the sample is mounted and any mounting media present *can* effect the PSF. Equation 2.19

describes the PSF of a co-axial Gaussian fluorescence microscope, or a Gaussian epifluorescence system capturing fluorescent signals using the same objective lens used for illumination delivery. Note the similarity to equation 2.8. The electric field due to the illumination is multiplied by the collection profile of the detection optics, which in the case epifluorescence microscopy are one and the same. The factor, p, in the exponent refers to the order of excitation of the fluorescence being detected (for OPE $p = 1$). If illumination and detection optics are decoupled (as they are for LSFM), each set of optics must be considered separately to calculate the resultant PSF for that imaging system.

$$PSF_{Gaussian}(r,z) = [A_0 \frac{\omega_0}{\omega(z)} \exp \frac{-r^2}{\omega(z)^2} \exp -i(kz + \frac{kr^2}{2R(z)^2} - \phi(z))]^{2p} \tag{2.19}$$

Equation 2.19 The point spread function of an ideal Gaussian beam epifluorescence microscope. The illumination objective is identical in every way to the detection objective, therefore the square of the intensity distribution is equivalent to the PSF for OPE. Adapted from [81] and [92].

The PSF tells us about the intensity of the illumination deposited at that point in the FoV and the predicted intensity of the signal that could be collected there. However, contrast also contributes to the data quality. If the signal to noise ratio (SNR) is low, the resolution will be negatively impacted.

Modulation transfer function (MTF)

The modulation transfer function (MTF) is a number between 0 and 1 which varies with spatial frequency. Spatial frequency describes the sharpness of features. The higher the spatial frequency, the greater the associated contrast-dependent resolution. A perfect imaging system would have an MTF of 1 for all possible spatial frequencies present in all parts of the object plane. The MTF incorporates the effect of contrast into the predicted overall image quality. To calculate it, we take the Fourier transform (FT) of the PSF with respect to spatial frequency. As with the PSF, the MTF changes with excitation order p. The MTF

is therefore also affected by any optical aberrations in the system. Aberrations can lead to a reduction in contrast of microscope images.

$$MTF_{(z=z_1)} = FT\{PSF\} \tag{2.20}$$

Equation 2.20 The modulation transfer function (MTF) is the Fourier transform of the PSF in frequency space. For volumetric imaging systems, the MTF can be calculated for each penetration depth z. Adapted from [81, 93].

2.3.12 Tissue clearing

Light in complex heterogeneous tissue is susceptible to scattering from refractive index boundaries between features. This is hard to get around in non-destructive, *in vivo* fluorescence imaging, however tissue clearing can be performed on excised samples to prepare whole volumes of tissue with a uniform refractive index and lowered scattering properties. Tissue clearing is often combined with bleaching techniques to remove pigments which add to the total attenuation of light via absorption. Optically transparent samples open up a range of possibilities for volumetric fluorescence imaging studies in biomedicine [57].

2.4 A directory of selected imaging techniques

This section aims to describe the landscape of current biomedical imaging methods. Some are more suited to point-of-care diagnostics and others are used more broadly in biomedical research. First, three common non-optical methods commonly used for medical imaging are presented. These methods facilitate deep tissue imaging, however resolution limits information capture to anatomical and mm-scale features. At the other end of the resolution scale, I discuss a fourth non-optical method which facilitates surface-level imaging of structures such as bacteria and viruses far smaller than the diffraction limit of light. Finally, I'll present several optical imaging techniques which occupy the middle ground in resolution and pene-

tration depth. Figure 2.1) summarises the spread of current biomedical imaging capability in a penetration depth-resolution plot.

2.4.1 Non-optical imaging examples

Magnetic resonance imaging (MRI)

MRI is a non-invasive, non-destructive medical imaging method that can access low resolution 3D data from soft tissue anywhere in the human body [94]. During an MRI scan, a strong, continuous external magnetic field is applied around the region of interest. Spinning protons in hydrogen atoms making up water and fat inside a patient have their own small magnetic field and they become aligned with the larger, external magnetic field. This alignment is disrupted using a second (radiofrequency) pulse matched to the precessional frequency of the protons. Resonances in the magnetic field occur. Once the radiofrequency pulse has ended, there is a relaxation time during which the proton spins realign with the external field and electromagnetic energy is released [95]. This energy release is localised to successive 3D pixels ("voxels") to build up a volumetric data set of the tissue. The resolution of modern MRI imaging for healthcare is 2-5mm for each "slice" through the body and 2-3mm for in-plane resolution within each slice [96]. Although it is possible to resolve a cell using MRI, this requires an enormous magnetic field (9T) and is only practical for a small volume sample (8 hours to accurately locate and resolve the signal from a single *Paramecium* cell)[97]. MRI is typically used for anatomical imaging in medicine [23, 97, 98]. Modern MRI scanners for medical applications use a magnetic field strength in the range of 0.5-3T [99]. Imaging can take up to 90 minutes depending on the area being examined [100], however imaging time is normally 15-19 minutes [101]. Patients must lie still for the duration of the procedure. MRI cannot be used on patients with metal transplants, cardiac or neural transplants and some find the loud noise of the scanner intolerable.

Computed tomography (CT)

Like MRI, CT scans can provide non-invasive volumetric data sets for medical diagnostics. Instead of manipulating and measuring magnetic fields, the CT method measures attenuation of X-rays through the body in different orientations to build a tomographic reconstruction of the bones and soft tissues. Biological features are resolvable by their relative transmissivity of the X-ray radiation, although intraveneous injections of contrast media are widely administered prior to imaging to enhance the contrast of these measurements [102]. Resolution increases with the (potentially harmful) radiation dose that each patient is exposed to. Generally, CT images for medical diagnostics have a spatial resolution of 0.5-0.625mm [103, 104]. The signal to noise ratio (SNR) of CT images tends to be lower than the SNR of MRI images [103], however CT scans are usually more tolerable for patients. The FoV in both cases can match the dimensions of the whole human body.

Ultrasound

Ultrasound medical imaging uses the acoustic back-scattering of high-frequency longitudinal (sound) waves to image deep tissue in real-time [105]. Like MRI and CT imaging, it is a non-invasive method for gathering diagnostic information from living tissue. The word "ultrasound" means sounds which are $\geq$20kHz (above the upper limit of human hearing). Ultrasound imaging does not require the use of radiation like CT, however, ultrasonic frequencies can cause heating in some circumstances. Ultrasonic waves generated outside the patient can propagate well through liquid-filled human organs (for example a full bladder, uturus) or through small organs close to the surface (e.g. a gallbladder [106]. Typically, medical ultrasound images are generated using sound waves between 3-10MHz [105] to maximise depth and resolution whilst keeping heating damage and imaging time to a minimum. The depth is limited by the transmission of the acoustic waves through tissue, which can be highly inhomogeneous. Higher ultrasonic frequencies lead to higher resolution, however, this

also leads to a greater attenuation of the signal in depth.

Ultrasound was initially developed during World War 1 to detect submarines more than 1km away. In this case, sonar at 38kHz was used to perform long-range measurements through relatively inhomogeneous seawater [81, 107]. The spatial resolution of medical ultrasound images can range between 0.02-1cm [105, 108, 109]. The FoV is highly sample dependent. Air (e.g. inside the lungs) and bones is strongly attenuating to ultrasound waves, however more than 10cms in depth can be imaged through the front of the abdominal cavity or through other areas where there is limited sonic impedance [108, 110]. A gel is used to couple the sound waves in between the detector/transmitter head and the tissue (avoiding an air gap).

Scanning electron microscopy (SEM)

SEM [18, 111] is a powerful non-optical tool that has been used for biomedical research into the structure of bacteria and viruses [112–114]. Electron microscopy has the capability to image details an order of magnitude smaller than those accessible via diffraction-limited methods [115]. A stream of electrons is focused into the surface layers of a conductive sample. Interactions take place, resulting in back-scattered electrons, secondary electrons and X-rays. These can all be detected to learn about the topography and composition of the sample surface. Biological samples (not normally conductive) generally require preparation before SEM imaging. Samples can be dehydrated, cleaned and fixed before sputter-coating in a thin layer of conductive material (gold and carbon mixture, for example) [116]. Use of electrons as a probing mechanism improves the resolution of SEM considerably compared to optical imaging methods, however biological samples cannot be imaged in their natural, unfixed, state. Propagation of electrons into such samples is limited by sample type and electron energy [16, 22].

2.4.2 Optical imaging examples

For mid-resolution data (on the subcellular scale), we can turn to optical imaging methods (see figure 2.1 for context). Some of these methods rely on fluorescence imaging (see sections 2.3.4 and 2.3.5, whereas others exploit scattering or transmission of the incident beam itself to extract information about features within a sample. Generally speaking, due to contrast and specificity, fluorescence-based imaging offers the highest resolution of the optical imaging subset.

Optical Coherence Tomography (OCT)

OCT is often described as ultrasound with light. Instead of measuring acoustic backscattering, OCT measures light which has backscattered from tissue microstructures [117]. OCT is a label-free method which employs interferometry to measure the time-of-flight and generate depth-sectioned images. The OCT signal is affected by scattering intensity and attenuation, which is based on the optical properties of the tissue. Each measurement is called an "A-scan" and inspects features directly below one surface coordinate. "B-scans" involve successive A-scans in a line to capture 2D information. "C-scans" are the 3D equivalent. OCT is therefore a "point-scanning" imaging technique (not wide-field). The resolution of OCT in medical imaging ranges from 0.5-2μm [118, 119] and the FoV is around 2-3mm in opaque samples [118, 120], although this distance is extended in optically transparent media (for example human eyes, which by nature transmit a broad range of wavelengths in our visible range [121]). In the context of medical microscopy, OCT is used for clinical gastroscopy and other medical microscopy applications which can be fibre-based [108]. Fibre-compatibility makes OCT an appropriate tool for areas of the body that can be reached by endoscopy. However, endoscopy procedures are invasive and often unpleasant. Many patients require sedation, which adds risk to any medical procedure.

Brightfield (slide-based) microscopy

This is the most common type of optical imaging currently used for medical histopathology, or the study of disease in tissue. A typical microscope for this application is illustrated in figure 2.11. Conventional brightfield microscopes evenly illuminate a sample with a diffuse white light source. Typically, the light is transmitted through a slide with a $4 - 6\mu m$ thick layer of tissue in standard diagnostic imaging [122–126]. White light passes through a glass imaging platform, microscope slide, the structures inside a thin, pre-stained tissue layer and a protective glass cover. Dyes are used to selectively stain sub-cellular structures. For example, a common stain combination is hematoxylin and eosin (H&E). Hematoxylin is a blue nuclear stain. Eosin is a fluorescent pigment used to target cytoplasm. Eosin appears pink under a brightfield microscope.

Tissue slices are observed from above with a simple magnification telescope, or digitally with a camera. Where there is no stain, the pathologist sees a white background. Where stain has attached to nuclei, cytoplasm or some other targeted feature, the stain will absorb everything apart from one particular colour which our eyes are sensitive to. Brightfield microscopy is a wide-field imaging method. Medical brightfield microscopy is only appropriate for excised tissues which are prepared prior to examination. Results may not be available for days or even weeks due to the timescale of tissue section preparation. Further details on this process are outlined in section 3.2.

Bright-field microscopy fundamentally relies on each tissue section being thin enough that only one stained feature is contained at any given location in the focal plane. If slices are too thick, layers of information are not distinguishable from one another and contrast is lost. Additionally, the brightfield source may not be able to penetrate through thick volumes of scattering medium to reach the eye. Scattering through thick tissue sections causes lowered contrast and blurry features. If features are not adequately pre-stained, images can suffer from low SNR and the contrast may not be sufficient to resolve features

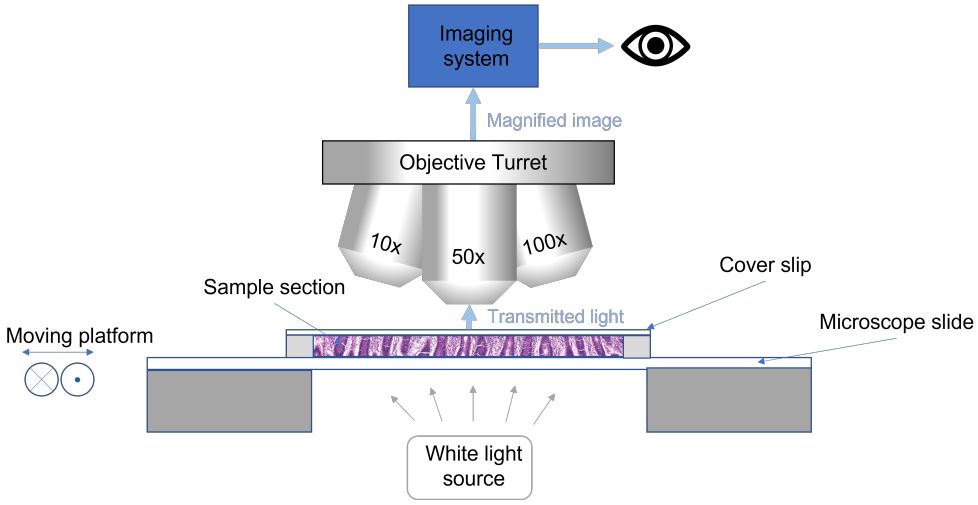

Figure 2.11 Schematic diagram of a bright-field microscope for imaging slide-based samples widely used in pathology. An objective turret houses several different objective lenses with different magnifications. This enables imaging across length scales (higher magnification means smaller FoV and higher lateral resolution). The platform or slide can be scanned through the microscope focus to allow high resolution imaging of specific areas of interest. A bright white light source illuminates the underside of the glass slide evenly. Light focused into the eye of the observer consists of rays from the focal plane which were not absorbed by the sample (i.e. in selectively stained structures). A thin glass cover slip preserves the thin tissue slice so that the slide can be imaged again in the future.

from the bright white background. It is not possible to perform volumetric imaging of a thick sample with brightfield microscopy. Instead, a thick sample can be sectioned into a sequence of thin slices such that each frame is physically disjointed from the next and is functionally two-dimensional (2D). The minimum lateral resolution ($d_{x,y}$) needs to be as little as $2\mu m$ for medical-grade histopathology imaging in order to resolve individual nuclei (normally stained with hematoxlyin). The axial resolution (d_z) is equal to the tissue section thickness (normally about $5\mu m$). Limitations of brightfield medical microscopy are that tissue processing is necessarily destructive and can result in artefacts, and that worflow constraints only allows a finite number of tissue sections to be prepared. This can mean that important information is missed.

Microscopy with Ultra-violet Surface Excitation (MUSE)

Microscopy with Ultraviolet Surface Excitation (MUSE) is a wide-field fluorescence microscopy technique that exploits the limited penetration depth of ultraviolet (UV) light into tissue to achieve optical sectioning at the sample surface [127–130] (see section 2.3.3). Photons between $275-285$nm propagate $6-10\mu$m in depth due to the rapid attenuation of these high energy photons in human tissue. This depth is slightly greater than the axial resolution in conventional H&E slide-based microscopy, where the tissue is physically sectioned into layers that are $4-6\mu$m thick (section 3.2). Unlike traditional slide-based imaging, MUSE is a non-destructive technique that is compatible with fresh tissue samples.

Many types of tissue exhibit auto-fluorescence under UV illumination, however, higher intensity dyes are also available to achieve greater contrast in this range [129–132]. Due to the long Stokes shift associated with many fluorescent transitions with OPE in the UV range (see section 2.3.4), standard optics and cameras may be used to detect fluorescence, which is emitted in the visible range[7] [8]. Simple UV LEDs can provide sufficient incident intensity to elicit a fluorescent response for MUSE imaging. For an open-top MUSE setup, one or more LEDs may be positioned beneath the sample at an oblique angle to the (vertical) detection optics to alleviate the need for expensive UV-transmitting optics[9]. A vertical objective lens collects the fluorescence in the visible range. Multispectral detection can be further achieved by separating light into multiple detectors using dichroic filters. It is also possible to use a colour camera for detection. Whilst this option comes with increased imaging speed and is cheaper to implement, it comes at the cost of a lowered resolution to field of view ratio[10].

[7] Small pixel-size, wide FoV cameras are a readily available, mature technology, already used for wide-field imaging. However, most cameras are designed for peak quantum efficiency in the visible wavelength region.

[8] UV light is strongly attenuated in standard crown glass. Instead, fused quartz is normally used for optics designed to transmit these wavelengths.

[9] These optics would be required for a collinear epifluorescence configuration.

[10] Most colour cameras rely on Bayer filters, which effectively double the pixel-limited resolution for the green channel and quadruple the resolution size for blue and red channels compared to monochromatic

In pathology, MUSE is a promising intra-operative assessment tool [10, 127, 129, 134]. As a non-destructive, wide-field, rapid optical imaging technique that is compatible with downstream slide-based microscopy, there is potential for this method to appear around the world in tomorrow's pathology labs. The resolution in depth is slightly worse than that of traditional slide-based methods (6-10μm rather than 4-6μm) but the (fresh tissue) images may be acquired within minutes rather than many hours or even days later for fixed slide-mounted samples. The lateral resolution of MUSE is dependent on the choice of detection optics and is easily matched to that of slide-based brightfield imaging. The detected wavelengths in both cases are visible, and therefore the diffraction-limited resolution of detected fluorescence will be limited by the same range of wavelengths.

Confocal Fluorescence Microscopy (CFM)

Confocal microscopy has been repeatedly demonstrated to be a useful tool in pathology research and healthcare [10, 53]. This method encompasses two distinct approaches - confocal reflectance microscopy (CRM) and confocal fluorescence microscopy (CFM). Both rely on the principle of rejecting out-of-focus light by using a pinhole in the detection optical pathway. Here, I will focus on CFM as it provides a fair comparison to MUSE, structured illumination microscopy (SIM), non-linear microscopy (NLM) and light-sheet fluorescence microscopy (LSFM) (alternative fluorescence imaging methods). Figure 2.12 shows a diagram of a confocal fluorescence microscope. The blue illumination beam is relayed through a telescope and comes to a tight focus inside the sample. Fluorophores contained there emit (green) fluorescence, which is relayed back through the system. Collected light undergoes spatial filtering with a pinhole, which rejects light that originates from outside of the focal spot. Fluorescence from the spot is then spectrally filtered and deflected from the illumination pathway with a dichroic mirror. Finally, it is focused onto a detector. This is not a wide-field imaging technique. Point-scanning is used to image continuous areas and volumes of

sCMOS pixel arrays [133].

samples.

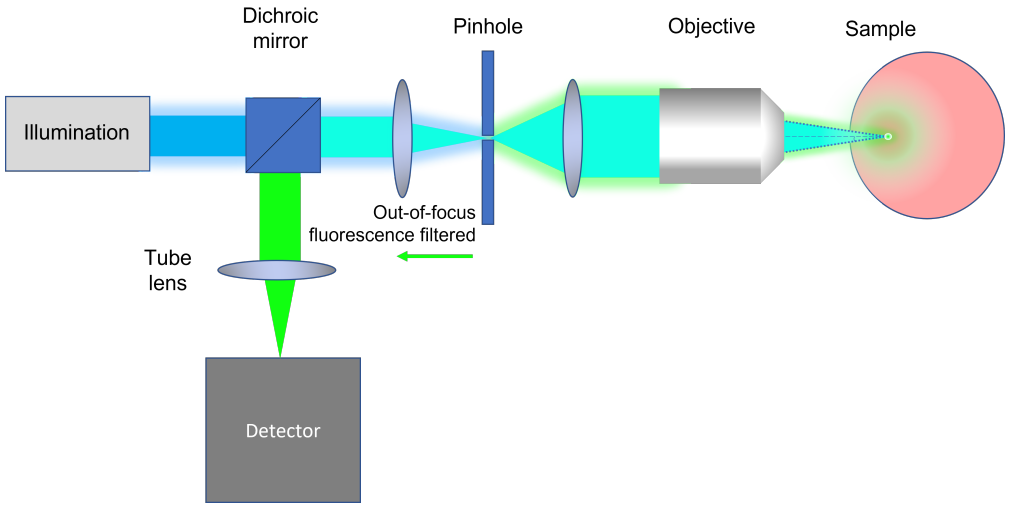

Figure 2.12 Typical confocal fluorescence microscopy (CFM) setup with epifluorescent geometry. Illumination (blue) is focused through a pinhole. Rays emerging from the pinhole are collimated into the back aperture of an objective lens. Fluorescence (green) is generated where the illumination is focused inside the sample. The fluorescence is collected and spatially filtered through the same pinhole. The signal is then spectrally filtered away from the blue light using a dichroic mirror and is relayed to the detector. CFM is a point-scanning imaging method, therefore less temporally efficient than wide-field imaging methods such as MUSE and LSFM.

The optical resolution of a CFM system is related to the size of the focused illumination spot inside the sample. A single spot is illuminated at any given time and images are acquired by raster scanning the spot or the sample sequentially in x, y and z. Due to this, it typically takes a long time to sweep a 2D area of a sample surface. CFM is not a super-resolution technique, however the enhanced sectioning ability generally gives more clarity in images than standard brightfield microscopy. Pinholes carry the disadvantage of total optical power reduction which is relevant to the SNR. Areas around the focal spot are also exposed to radiation. Figure 2.13 shows in more detail what is happening inside the sample in figure 2.12. In figure 2.13, the areas enclosed by the red lines are exposed to high intensity illumination but are not involved in the signal acquisition.

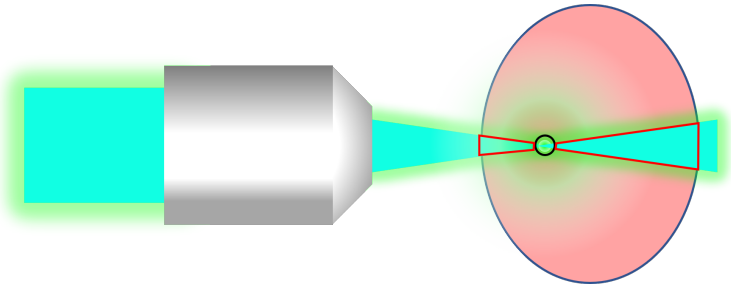

Figure 2.13 CFM - zoomed in on irradiation pattern within the sample. Blue, spatially filtered light illuminates a volume shaped like an egg timer. Fluorophores contained within this volume emit green light in response. The black circle indicates the FoV of the microscope in 2D (without point-scanning). The red lines mark a cross-section where the sample is irradiated but no information is captured due to the pinhole configuration used to section data in depth. The axial resolution is thus improved, however there is increased risk of photodamage due to inefficient dumping of optical power.

Confocal microscopy systems can be slide-based or deal with thicker samples. Slide-based CFM can have a lateral resolution of 250nm and an axial resolution of around 520nm with illumination at 488nm [135][11]. However, this style of CFM is optimised for thin, transparent samples sparsely embedded with fluorescent beads rather than for imaging deep in scattering tissue.

Although imaging depths of up to $250\mu m$ have been reported in uncleared human tissue [53], like other optical techniques the average imaging depth is much shallower (on the order of 10s of μm) and the achievable depth is highly dependent on the attenuation properties of each sample [136]. For tissue imaging at depth, a lateral resolution of 2μm and an axial resolution of 5μm may be expected for illumination at 488nm [53][12]. This is identical to the spatial resolution of brightfield slide-based microscopy which uses white-light absorption rather than fluorescence to construct images.

To summarise, CFM is a point-scanning imaging method which can be optimised for imaging at high resolution at the surface of a sample or lower resolution for volumetric

[11] both of these values can be reduced by around 20nm when normal spherical aberrations are minimised [135].

[12] Deconvolution is sometimes used to improve the axial resolution of CFM [137].

imaging. This method has the disadvantages of prolonged imaging times required for point-scanning and high risk of photobleaching or photodamage to the sample (due to the low photon efficiency).

Structured illumination microscopy (SIM)

SIM is a SR, wide-field, optical microscopy method [86, 138, 139]. High spatial frequencies become increasingly difficult to resolve as we approach the Abbe diffraction limit (equation 2.14). However, it is possible to engineer a situation where sub-diffraction "super" resolution information is encoded within low spatial frequency images that we *can* resolve with diffraction-limited detection optics. Although there are several super resolution optical resolution methods (e.g. STORM and PALM [140]), I discuss SIM only here as it can be readily used in conjunction with other wide-field imaging methods (for example light-sheet microscopy). Typically, standard SIM can achieve a lateral resolution of 88nm (or 0.5× the diffraction limit) [141] and an axial resolution of under 400nm [142, 143]. Figure 2.14 shows how SIM is implemented.

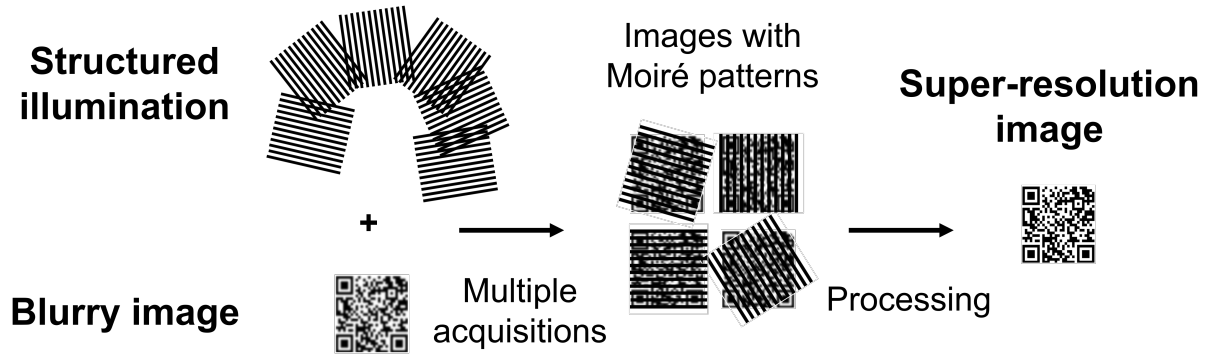

Figure 2.14 Diagram of the structured illumination method for microscopy. A series of known, orthogonal illumination patterns is sent into a sample causing fluorescence to occur in selective regions. Images are taken during illumination with each pattern. Each low spatial frequency image that is recorded is a convolution of the unique illumination pattern and the corresponding fluorescence pattern from the sample. By combining a series of low spatial frequency images, we can decode high spatial frequency information about the underlying sample.

When two high spatial frequency patterns are overlaid, "Moiré fringes" can appear. These are lower frequency patterns which contain information about the two images that created them. For SIM, one of these images is the sub-diffraction-limited sample information which we would like to resolve. The other is known structured illumination with particular known properties across the FoV [86]. These structured patterns contain varying spatial sine functions. With each permutation, a low-resolution fluorescence image is acquired. The interference patterns from each acquired frame are deconvolved in frequency space and the set of decovolved images are then combined to reveal a single SR image after post-processing. This image is considered to be SR (even if the resolution is not strictly below the diffraction limit given by the Abbe criterion) because the method can resolve features which are smaller than the optical resolution of the microscope that captured them. There are multiple instances of SIM being demonstrated as a successful tool in pathology [54, 85, 144, 145] and biomedical research [146, 147]. Spatially modulated illumination can be used in conjunction with other microscopy techniques (for example light-sheet fluorescence microscopy [148]). SIM can therefore be utilised to lend its SR capability to a broad range of optical imaging tools [149].

Non-linear microscopy (NLM)

In section 2.3.3, I explained the varying ability of light to penetrate through human tissue at different wavelengths due to "therapeutic windows" through common biological compounds. In section 2.3.5, I described the phenomenon of multi-photon fluorescence. These two concepts are combined for non-linear fluorescence microscopy (NLM) inside human tissues. Non-linear fluorescence can be exploited in conjunction with some of the optical imaging methods that we have discussed. I have used CFM with a visible source vs CFM with an NIR source as an example of how NLM can improve the quality of in-depth microscopic images of thick samples. The difference is shown in figure 2.15. Attenuation and redirection of light in the therapeutic window are reduced, which means more photons will travel further within a

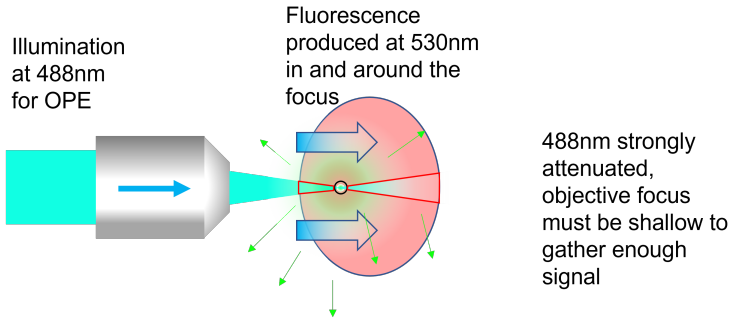

(a) One photon excitation (OPE) microscopy with excitation in the blue range. Areas outlined in red represent where fluorescence can occur due to incident photons. The black-edged area represents the region where fluorescence is collected. This illustrates that the CFM method has a relatively low photon efficiency.

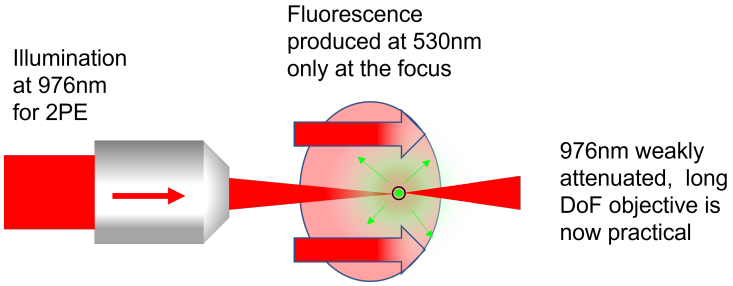

(b) Two photon excitation (2PE) microscopy has an extended possible depth of focus due to the lower attenuation of near infra-red (NIR) light in human tissue. While photons travel through the entire area shown in red, they are only absorbed to produce fluorescence at the focus (represented by the circle with black edge). A pinhole is therefore not required for high sectioning ability and photobleaching is prevented in areas outside of the focus.

Figure 2.15 A comparison between linear fluorescence microscopy and non-linear fluorescence microscopy using CFM as a base technique to achieve sectioning in depth. Near infra-red (NIR) illumination is less attenuated by human tissue, which is represented in this example. Therefore many more photons are able to reach a focal point deeper inside the sample. A longer working distance objective can be used, increasing the DoF of the optical setup. Additionally, fluorescence is only produced at the focus with NLM compared to linear microscopy where fluorescence is produced throughout the beam path through the sample.

human tissue sample before being scattered.

Figure 2.15a shows CFM using blue light for illumination. The compact detection objective has a short working distance (see figure 2.10 for more details) which matches the depth of focus to the maximum extent of sufficient fluorescent signal. Blue wavelength excitation can only travel a short distance through tissue before being scattered. Back-scattering is likely at short wavelengths in the Rayleigh scattering regime. In the NLM case shown in figure 2.15b, NIR illumination is used. NIR light increases the average number of scattering lengths and reduces back- scattering by shifting to the Mie scattering regime. This discourages the generation of out-of-focus fluorescence whilst ensuring that sufficient signal reaches a new, deeper, target depth. NLM offers enhanced sectioning ability and reduces photobleaching compared to fluorescence microscopy using OPE illumination in the visible range. NLM has been combined with SIM and single pixel detection to resolve individual HEK293T/17-GFP cells through 200μm of human colon tissue [150]. NLM has also been combined with LSFM in several ways [151–154].

2.4.3 Comparisons

Each of these optical and non-optical imaging methods are contextualised in figure 2.1, which shows which spatial resolutions and penetration depths are generally accessible. In the next section (2.5), LSFM is discussed separately.

2.5 Light-sheet fluorescence microscopy (LSFM)

The particular geometry of light-sheet fluorescence microscopy was first developed in 1902 [155], however it was some time before its importance to biomedical research was realised. Almost a century later, researchers began to use this configuration for imaging applications [156, 157]. More recently, LSFM has been gathering significant momentum in biomedical research applications [55–58, 127, 149, 158–177]. In this section I will explain how light-sheet

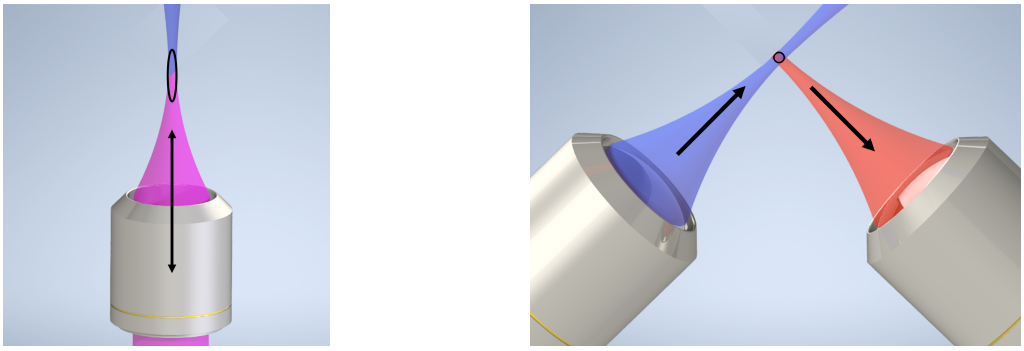

(a) Collinear geometry **(b)** Decoupled pathways

Figure 2.16 Figure 2.16a shows two overlapping paths, one red and one blue giving purple when combined. The black extended ellipse over the FoV represents the region over which both beams are in focus. Standard light-sheet geometry is shown in figure 2.16b. A low NA beam identical to the illumination in 2.16a is now delivered at 45° to the vertical axis. Collection is orthogonal, captured by a second objective lens. In this case, the two objectives need not be the same. It is more typical to use a low NA delivery objective for a large FoV light-sheet and a higher NA collection objective to gather high lateral resolution data from within the light-sheet plane.

microscopy works and compare it to other optical imaging methods.

Decoupled illumination and detection

CFM, OCT, brightfield and SIM share a collinear geometry[13]. The path of the incident and returning photons overlap. A representation of collinear geometry is shown in figure 2.16a, where there are two overlapping beam paths, one illumination (blue) and one detection (red) to give purple when overlayed. The combination of the two profiles give the system a spheroidal focal "point spread function" (PSF) at the focus, represented by the black ellipse in figure 2.16a.

LSFM uses an alternative geometry: pathways are decoupled and typically orthogonal. When we decouple the pathways in this way, we reduce the overlapping region between focal regions of the two pathways and therefore reduce the FoV in the axial dimension. The smaller

[13]This is sometimes the case for MUSE too, although the high opacity of glass at UV wavelengths means that it can be more practical to introduce illumination off-axis using an LED or other light source [128–130, 178, 179].

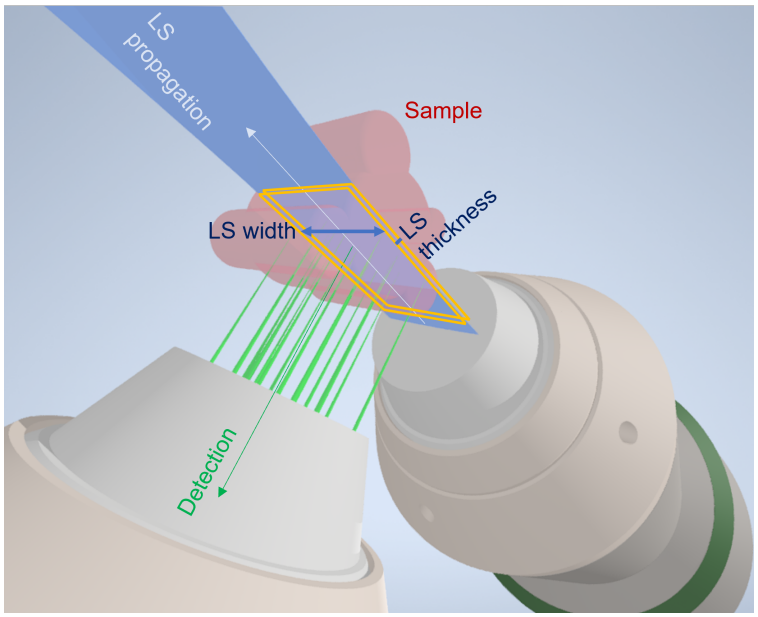

Figure 2.17 Standard LS geometry. A light-sheet propagates through a thin section of a sample. Fluorescence is generated within the plane of the light-sheet and is collected orthogonally by a second objective lens. The sample must fit in the space between the two objective lenses, which is constrained by each of their working distances.

black circle in figure 2.16b represents a cross-section through the reduced FoV enjoyed by LSFM.

Light-sheets

Sheets of light are created to optically section light over a 2D area. The illumination (the blue beam in figures 2.16b and 2.17) are collimated beams focused in one cross-sectional axis to produce a thin planar volume of light. Figure 2.9 represents what is happening in the focus of the decoupled collection objective. An artistic rendering of the orthogonal LSFM geometry is shown in figure 2.17. The light-sheet (LS) is transmitted through an arbitrary sample which contains fluorescent particles. Some particles in the focus of the LS are also in the focus of the collection objective, which gathers the response at a 90° angle to the LS.

Light-sheets are rotationally asymmetric about the axis of propagation. Light-sheet thickness refers to the size of the light-sheet in the focused direction and is directly related to

the axial resolution of the light-sheet microscope (see figures 2.16b and 2.17). Light-sheet width refers to the size of the beam along the unfocused axis. The LS width is related to the FoV of the fluorescence microscope[14] Both of these LS dimensions are labelled in figure 2.17. The FoV of the microscope is highlighted between the two yellow rectangles. If the FoV constraints set by the camera match the FoV of the light-sheet (figure 2.17), all of the area irradiated contributes the image. This maximises photon efficiency and helps to reduce photo-bleaching which can be a problem for other fluorescence imaging methods (CFM, for example).

The image of this plane of the sample section is magnified and relayed through a detection objective and then focused onto a camera detector array using a tube lens. Spectral filters are used to remove traces of the original illumination beam and any other background light, as these both reduce the contrast of the fluorescence image. When the camera captures photons (for a finite exposure time), a 2D acquisition has taken place. To capture volumetric data, the sample is scanned with respect to the light-sheet (or the other way around). After each step in the one-dimensional scan, another digital fluorescence image is recorded. Because of the unique geometry, this method is a highly efficient volumetric imaging tool. The detection optics can be tailored independently from the illumination optics to give a high lateral (in-plane) resolution.

A note on sample mounting

The unusual geometry of LSFM can place constraints on the sample dimensions, particularly if using short WD air objectives. If fluorescence from a sample passes through any irregular or angled RI boundaries prior to the objective lens, then images will contain noticeable aberrations. Oil and water objectives allow a sample to be fixed in space inside some index-matching medium, which should be matched to the average refractive index of the sample as far as possible.

[14]The magnification of detection optics and camera array size also play a part in this.

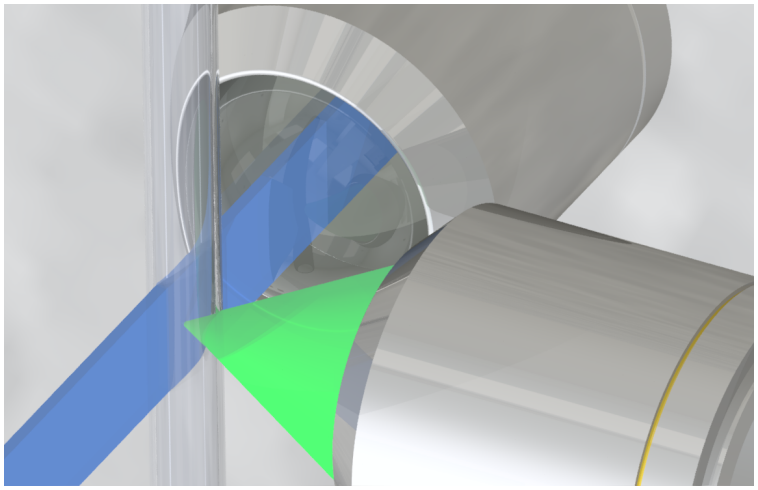

Figure 2.18 FEP tube-based sample mounting configuration for light-sheet microscopy. The LS is transmitted through the side of the tube and into the sample while a second higher NA detection objective collects fluorescence from an orthogonal direction. The tube can be suspended in an index-matched medium to avoid aberrations caused by rays travelling through curved or angled surfaces. The external medium, transparent tube and any fixative medium inside the tube should all be index-matched. Figure created using Autodesk Inventor. Not drawn to scale.

Figure 2.18 shows one way in which small samples can be mounted inside an orthogonal water-based objective lens configuration for LSFM. A transparent fluorinated ethylene propylene (FEP) plastic tube holds the sample in place. This plastic is index-matched to water (RI=1.33), and is therefore a popular choice for housing biological samples (dead or alive) in water-based fixative media. In this example, the FEP tube and objective tips would all be submerged in water to reduce optical aberrations occurring around the sample. It would be important to avoid air bubbles in or around the FEP tube, as these, too, would cause aberrations due to the refractive index mismatch between water and air.

LSFM is also possible in open-top geometries [56, 58, 174]. For LSFM, this means that the orthogonal illumination and detection optics are each positioned at 45° to the vertical axis and to the plane of the horizontal platform. This LSFM configuration is explored in chapters 3 and 4.

Standard (Gaussian) light-sheets

Ordinarily, light-sheets have a Gaussian distribution. The side of a light-sheet (the thickness, labelled in figure 2.17) is defined by a small Gaussian intensity profile where the beam is focused (beam radius given by equation 2.9). On either side of the in-focus region, the thickness of the light-sheet expands again and the intensity in the centre of the profile wanes as energy spreads out (according to equation 2.8). Along the orthogonal axis of the light-sheet (the width, shown figure 2.17), there is a broad uniform intensity distribution that does not change as the (unfocused) beam propagates. Uniform intensity light-sheets can be created by opting for "virutal" light-sheets which are ordinary symmetric beams focused in both dimensions that are scanned across the FoV of the detection optics. This can be done by placing a galvo-scanning mirror in the Fourier plane of the light-sheet in the illumination pathway.

2.6 Exotic beam shaping

We can make adjustments to Gaussian light-sheets in order to engineer particular desirable light-sheet properties using "beam shaping". In the context of this thesis, beam shaping is a term applied to spatial and phase manipulation of illumination. Airy and Bessel beams are useful for extending the field of view of a focused laser beam without loss of resolution. They can be compared to standard Gaussian beams, where the beam waist size is inversely proportional to the numerical aperture of the focusing optic and the FoV scales inversely with the square of the beam waist radius (equation 2.10). Airy and Bessel beams are known as "propagation-invariant" beams, so called because the PSF (see section 2.3.11) remains relatively unchanged over a long propagation distance (z axes in figures 2.19c, 2.19d, 2.23c and 2.23d). Airy and Bessel beams have another desirable property known as "self-healing", which essentially means that they are able to reform themselves after the beam encounters some obstacle in its path. In this section I will describe the profiles of Airy and Bessel-Gauss

beams and discuss ways in which they may be generated.

2.6.1 Airy beam

Airy beams are a type of propagation-invariant solution to the 1D paraxial wave equation [180, 181]. Figure 2.19 shows an Airy beam in comparison to a Gaussian beam with the same numerical aperture. Gaussian beams are not propagation-invariant. Equation 2.21 is the general form of the Airy beam solution, which assumes an infinite field and infinite energy [182].

$$\Phi(\xi,\, s) = \mathrm{Ai}(\, s - (\xi/2)^2) \exp(i(\, s\xi/2) - i(\xi^3/12)) \tag{2.21}$$

Equation 2.21 The Airy beam equation in 1D as defined here [180]. Φ is the wave function expressed in terms of ξ, which is equal to z/kx_0^2), and s, which is a normalised length equal to x/x_0. Ai is the Airy function [183]. x_0 is a dimensionless coordinate at the focus of the 1D Airy beam.

The cross-sectional profile of an Airy beam consists of a main lobe and several side-lobes which decrease in size and intensity moving away from the main lobe. This characteristic intensity profile is shown in figure 2.19f. Airy beams are distinctively curved, therefore the beam profile changes position across the FoV although the shape is maintained. Figure 2.19 illustrates this point. The Airy beam curves/accelerates through space and maintains a sharp central maximum at depth. Multiple side-lobes carry separate bundles of energy in this way. The side-lobes give Airy beams their "self-healing" property. The cross-sectional intensity distributions in e and f show a marked increase in the normalised maximum intensity in the Airy beam after 25μm in this propagation simulation compared to the simulated Gaussian beam with the same NA. Both beams have a maximum intensity of 1AU at their focus. This feature of Airy beams is exploited in the studies presented in chapter 3 of this Thesis.

Airy beams can be formed when a cubic phase profile is applied to a focused Gaussian beam in the Fourier plane of the focus. The amplitude of the cubic phase profile is defined by

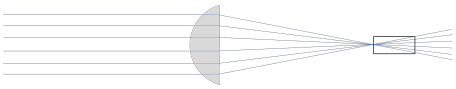

(a) A collimated Gaussian beam with planar wavefronts is focused to a point using a paraxial lens. The black box represents the area shown in 2.19e.

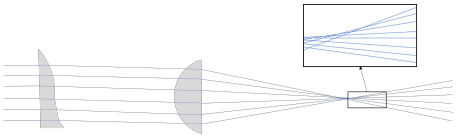

(b) The setup in 2.19a is modified by adding a 1D cubic phase across the planar wavefront, resulting in an Airy-Gauss beam at the focus.

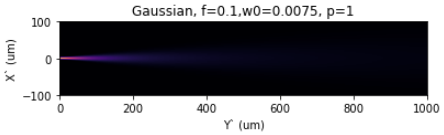

(c) Gaussian beam propagation. Latter half of the FoV viewed side-on. Sharp focus quickly dissipates away from the focus.

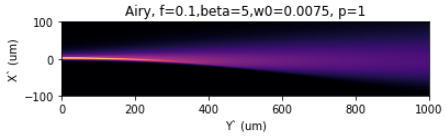

(d) Airy beam propagation. The right hand side of the total FoV is shown here for comparison to the Gaussian post-focus beam propagation.

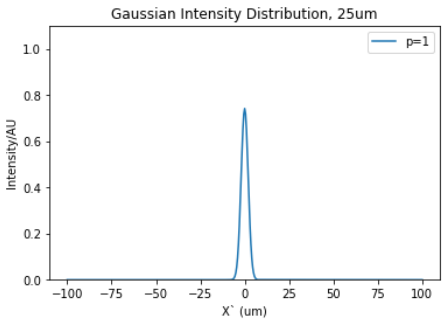

(e) Cross-sectional intensity distribution of a Gaussian beam propagating from the focus.

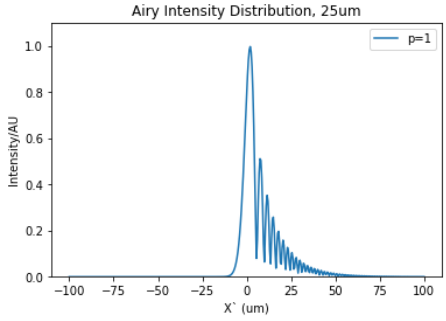

(f) Cross-sectional intensity profile of an Airy beam with an identical numerical aperture measured at the same location in space.

Figure 2.19 Simulations of Gaussian (a, c, e) and Airy (b, d, f) beams produced using similar optical setups. "p" denotes the order of fluorescence excitation used to calculate each PSF function, in this case we are inspecting the OPE case.

a unitless coefficient, α, which relates the additional phase to the position (u_x) via equation 2.22. Note that u_x is used to scale the size of the phase profile relative to the actual beam size in the focal plane, which is measured along x.

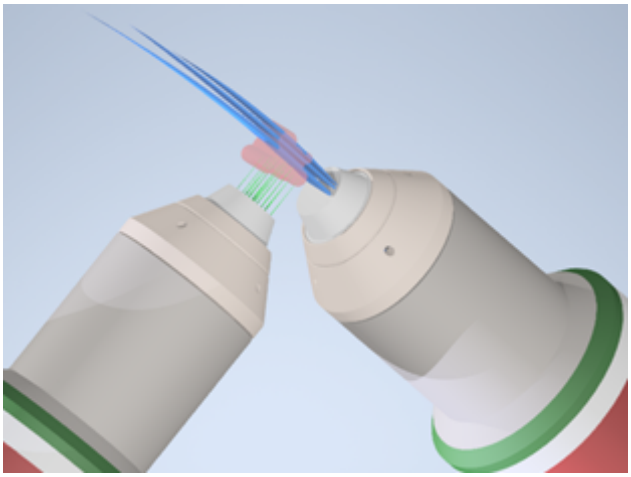

Figure 2.20 Airy LSFM. The LS has multiple side-lobes, the image of which is convolved with spatial information related to the sample when fluorescence microscopy is performed. This data set is deconvolved to reveal just the sample-dependent information. The detection pathway is orthogonal to the illumination pathway, as with Gaussian LSFM. The focal plane of the illumination is slightly curved in one dimension.

$$\Phi(u_x) = e^{i\alpha u_x^3} \tag{2.22}$$

Equation 2.22 Equation describing the cubic phase which can be added across one cross-section (u_x) of a propagating Gaussian beam to form an Airy beam when the rays are focused. When $\alpha = 0$, we have a Gaussian beam at the focus.

We can generate 1D Airy beams, where the extra phase profile is added along one axis, or 2D Airy beams where there is an Airy profile in both u_x and u_y dimensions. For light-sheet with Airy beam shaping, a 1D cubic phase mask can be used so that the curved shape exists only in the plane perpendicular to the detection pathway (in the plane of the illumination propagation). Figure 2.20 shows a schematic of an Airy beam LS setup.

As the PSF has multiple lobes, an Airy light-sheet image requires deconvolution in order to resolve the single localised source of each multiple-lobed feature in the convolved image [58, 166, 184]. See section 2.6.3 for more details.

2.6.2 Bessel beam

Bessel beams are another type of propagation-invariant exotic beam. The electric field of a Bessel beam with infinite energy is given by equation 2.23. Polar coordinates are used as Bessel beams have rotational symmetry about the optical axis. In this Thesis, I will only consider zero-order Bessel beams ($J_n = J_0$) [185].

$$E(r, z) = J_n(k_r, r)exp(ik_z z) \tag{2.23}$$

Equation 2.23 The electric field of a Bessel beam. J_n is the Bessel function [185]. k_r is the wave vector in radial space and k_z is the wave vector along the axis of propagation. k is the absolute wave number and is equal to $\sqrt{(}k_r^2 + k_z^2) = 2\pi n/\lambda$, where λ is the wavelength and n is the refractive index of the propagation medium.

Infinite energy beams are not practical outside of a theoretical setting. To model a realistic laboratory-generated Bessel beam, the radial profile is enveloped in a Gaussian function to produce a Bessel-Gauss beam. In this case, equation 2.23 is modified to form equation 2.24 when evaluated for a zeroth-order Bessel beam at the focus (z=0). Bessel and Bessel-Gauss beams do not curve through space like Airy beams. Zeroth-order Bessel-Gauss beams have a central maximum that is consistent along the optical axis (as shown in figure 2.23). Around this central maximum are concentric rings of minima and maxima caused by interference of planar wavefronts.

$$E(r) = J_0(k_r, r)exp(-r^2/w_0^2) \tag{2.24}$$

Equation 2.24 A Bessel beam profile enclosed within a Gaussian envelope to model realistic Bessel-Gauss beams passing through finite apertures in an arbitrary optical setup. w_0 is the radius of the Gaussian envelope at the Bessel-Gauss beam focus.

Using an axicon lens

Axicon lenses are widely used for Bessel beam shaping [186–189]. They are conical lenses that typically have one planar surface and one convex conical surface. A representation of

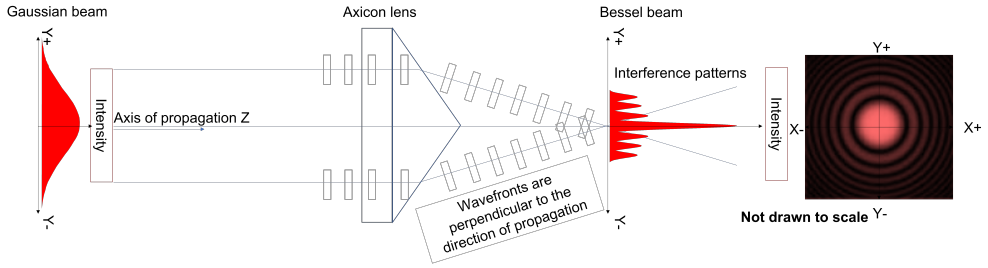

Figure 2.21 Plane waves strike the back aperture of the axicon lens. When the waves exit, wavelets are angled by refraction from the conical surface. Interference patterns are produced in the focus of the axicon lens. This Bessel-Gaussian beam has a high intensity central lobe. Concentric side-lobes around the focus can carry additional high spatial frequency information which is useful for high resolution fluorescence microscopy.

how one might be used to produce a Bessel-Gauss beam is shown in figure 2.21.

Using an annulus

Annuli are widely-used for Bessel-beam shaping and the beam profiles from such objects have been studied closely. There are some differences between Bessel beams generated with axicon lenses and Bessel beams generated using annuli. Each method of Bessel-Gauss beam shaping is prone to slightly different aberrations. In this chapter, I will use simulated beams from a hypothetical beam focused onto an annulus as a comparison for alternative Bessel-like beam shaping methods.

The normalised spatial profile of a Bessel beam using the annulus method is similar to that of an axicon-generated Bessel beam, provided that they are engineered to have a similar FoV and central lobe diameter. The wavelength of light affects the spatial dimensions of the shaped beam. Figure 2.23 compares the intensity maps of two simulated beams; one focused Gaussian beam and the second identical to the first but with the optical power redistributed so that it is only applied through the aperture of an annulus in the Fourier plane of the spherical focusing lens. In reality, adding an annuls would reduce the total optical power available. If optical power is at a premium for some imaging application, use of an axicon

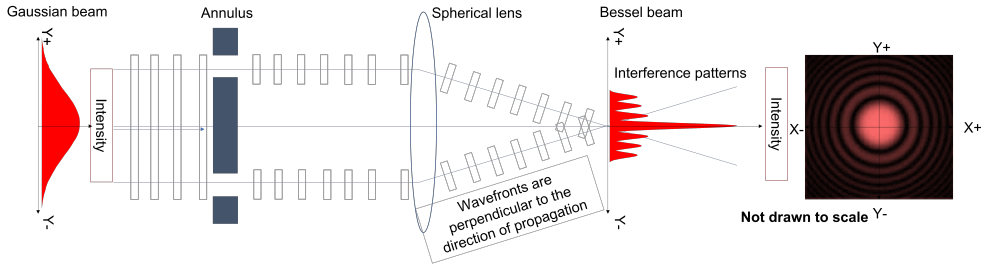

Figure 2.22 Plane waves strike the back aperture of the annulus, which is one focal length away from the spherical lens. Wavelets are diffracted when they pass through the small aperture around the edge. Interference patters are produced in the focus of the spherical lens, forming a propagation-invariant Bessel-Gauss beam.

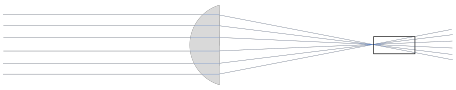

(a) Focused Gaussian beam

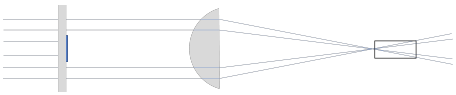

(b) Optical power redistributed to form a ring at the back aperture of the focusing lens

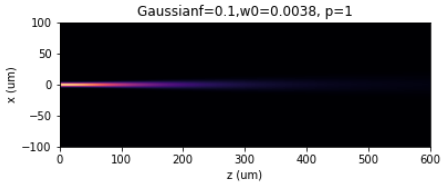

(c) Gaussian beam

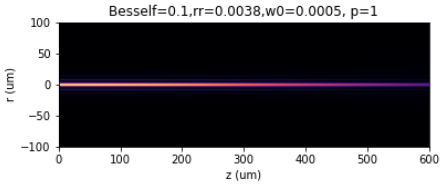

(d) Bessel-Gauss beam

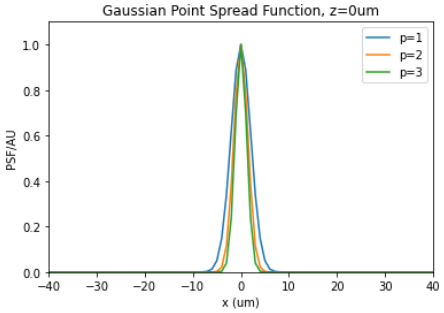

(e) PSF of a Gaussian beam at the focus

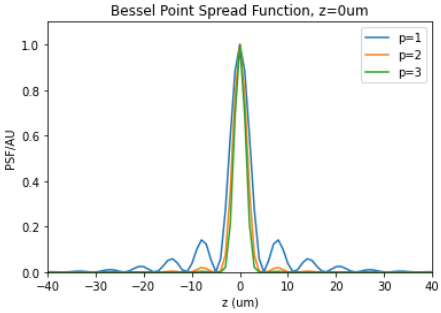

(f) PSF of comparable Bessel-Gauss beam with symmetric side-lobes

Figure 2.23 A simulated Bessel beam compared to a simulated Gaussian beam with the same numerical aperture. In the case of the Bessel-Gauss beam, optical power has been redistributed to form a ring on the back aperture of the focusing lens prior to running the propagation simulation.

lens to create the Bessel-Gauss profile may be preferrable.

The main benefits of Bessel and Airy beams over Gaussian beams are the extended FoV (due to propagation-invariance) and self-healing properties. The downside is that deconvolution must be applied to LSFM images and this step can take time. In chapter 5, I use simulations of non-infinite-energy Bessel-Gauss beams to make fair comparisons between (simulated) Bessel profiles that you could expect in a laboratory environment and Bessel-like profiles that were measured in practice using non-standard Bessel-beam generating devices.

2.6.3 Deconvolution

As propagation-invariant beams, Airy and Bessel-Gauss beams lend an extended depth of field compared to Gaussian illumination. Their multiple side-lobes are advantageous in that they provide alternative routes for energy propagation through the medium. This gives the beams self-healing properties. However, LSFM images produced using shaped illumination require post-processing to separate the sample information from the multi-lobed PSF contribution to the signal. This is done by deconvolving the data set. Knowledge of the specific PSF across the focal plane is essential to perform this step. The PSF of the optical system is mapped across the imaging plane using a combination of analysis of the illumination optics alongside a more iterative process of trial deconvolutions of sub-diffraction limited bead sample data. Deconvolving data takes time, particularly for large volumetric data sets.

2.7 Summary

This chapter has looked at key principles which underpin the research presented in the remainder of this Thesis. I have presented medical microscopy as a broad field which includes optical and non-optical imaging methods. Medical microscopy methods are essential tools for diagnostic information retrieval for healthcare purposes. Within these applications, sub-

cellular scale features must be resolved in human tissue samples. Typically, non-invasive, non-destructive methods are preferred for point-of-care diagnoses, whereas *ex vivo* imaging tools with high throughput capability can be more suitable for slower turnover pathological studies. Rapid, fresh tissue imaging tools could help to alleviate bottlenecks surrounding tissue processing in these cases. Light-sheet fluorescence microscopy is suggested as a tool with potential for routine pathology. This method is an efficient way to capture volumetric information from fresh, intact tissue samples. I have introduced propagation-invariant beam shaping (using Bessel and Airy beams) as well as non-linear fluorescence generation. These are the two primary routes which I will take to tackle the challenge ahead. Armed with this introduction, we will now look at how the FoV of light-sheet fluorescence microscopy could be extended (compared to standard CW Gaussian LSFM) for deeper tissue imaging for medical microscopy applications.

Chapter Three

Bench-top light-sheet microscopy for histopathology with Airy beam shaping

3.1 Overview

In chapter 2, I introduced LSFM as a promising technology for biomedical imaging applications. My first practical task was to develop a compact light-sheet fluorescence microscope capable of volumetric imaging of freshly excised tissue *ex vivo*. I designed an open-top light-sheet (OTLS) microscope which was specifically tailored to have desirable characteristics for diagnostic histopathology. This microscope uses CW illumination at 488nm to produce a linear response in fluorescent samples (fluorescence is generated at around 530nm). I incorporated (optional) Airy beam shaping into the design to test both beam shapes in tissue samples for a direct comparison. As discussed in chapter 2 section 2.6.1, Airy beams were expected to extend the FoV of the OTLS medical microscope compared to the same setup with Gaussian illumination due to their propagation-invariance and self-healing properties (potentially useful for imaging inhomogeneous samples). This chapter describes in-house testing of this microscope using a variety of human and other animal samples. Deep learning post-processing was later added to the methodology to enhance the resolution of widefield biological data at depth (the depth aspect was extended by Airy beam shaping). The full

method has been published in OSA Continuum [58].

3.2 Gold standard histopathology

Hospitals all around the world have busy pathology departments. In these departments, various tissue samples are processed and analysed by skilled pathologists. This process informs diagnoses and the next stages in treatment where applicable. In the next section I will describe modern gold standard histopathology to provide some context for OTLS microscopy and how this newer technology could fit into the well-established pathology imaging workflow.

3.2.1 Current practices

Histopathology is a mature field, with many of the techniques first appearing in the 19^{th} century [126, 190]. It encompasses all study of disease in tissue. To view microscopic changes for diagnostics, a biopsy is generally required. Excised tissue is prepared and imaged using rigorously standardised processes. Thin tissue slices or "sections" are viewed under a (brightfield) microscope by one or more highly trained pathologists (see section 2.4). This is a crucial step for diagnosis of many common illnesses, including most cancers. In cancer diagnosis, a number called a Gleason score is given to each evaluated tissue section [191]. The Gleason score is a measure of how likely the tissue sample is to contain cancer. A single sample may be analysed by several expert pathologists to reduce errors in diagnosis [192]. It is not uncommon for multiple pathologists to analyse the same sample and come up with different Gleason scores. In these cases, it could be helpful to view a tissue slice along a different axis within the excised volume. Switching imaging planes retrospectively is not possible using a slide-based brightfield imaging method, instead core needle biopsies are used [193]. A timeline for a typical patient undergoing surgery for cancer treatment is as follows [124, 194]:

1. Surgeon removes a volume of suspicious tissue from patient. Tissue begins to degrade as soon as it has been cut away

2. Sample is immediately taken to the pathology department, often in a different part of the building [123]

3. Pathology team formalin-fix (FF) the sample. It is now ready to be processed, stained and slide-mounted. Table 3.1)

4. Meanwhile, operation is concluded and patient is taken to Recovery

5. Pathologist studies the slides a day or two later and advises the team in surgery of their findings

6. If cancerous material is still found on the outer perimeter of the sample, it is likely that cancerous cells remain within the patient. If this occurs, a secondary operation may be required and the process begins again at part 1

Table 3.1 outlines each stage of the tissue preparation for brightfield imaging[190]. The whole process normally takes a couple of days to complete with extra time needed for perfusion through larger tissues, meaning that intra-operative assessment is not routinely taken. Methods such as frozen tissue sectioning or intraoperative X-ray may be used, however, these have their own disadvantages (discussed in sections 2.4 and 3.2.1). Artefacts in sectioned tissue images are likely, unless key parts of the process are undertaken by highly skilled workers. Further, there is a high cost in both time and lab consumables. With modern technology, digital storage of the information is now possible, however, it is still standard practice to physically reserve large volumes of processed tissue for future reference[123, 195–197]. This leads to storage issues for patient records in many hospitals.

	Process	**Duration**	**Potential issues**
1	Excision	t=0	Tissue compression, torn edges
2	Fixation	12-48 hours	Tissue stuck to container, large samples may degrade internally before fixation is complete
3	Trimming	Minutes	Incorrect positioning
4	Pre-embedding	9-12 hours	
5	Embedding	Minutes	Incorrect positioning
6	Sectioning	Minutes, plus overnight for drying	Technique crucial to image quality
7	Staining and mounting	Minutes	Technique crucial to image quality

Table 3.1 Standardised tissue preparation (adapted from [190]). The total time for process and sample analysis is generally a couple of days. H&E staining or an alternative (section 3.2.1) is implemented at step 7.

Common stains

This section elaborates on the introduction to brightfield microscopy that I presented in section 2.4. Exogeneous, selectively binding stains can be used to "tag" key features in the tissue. This increases the contrast in the images[198]. Higher contrast images allow pathologists to perform carefully practiced pattern recognition to identify regions of abnormal cell growth. Typically, two colours are used (a stain and a "counter-stain") to separately tag two layers of information in a single layer of slide-mounted cells. This information is crucial in allocating a Gleason score to the tissue sample. The two most common stains that are

used for this are hematoxylin and eosin (H&E) [199]. Hematoxylin is a blue stain which selectively binds to nucleic acid. Eosin is a pink stain which counterstains the cytoplasm. The staining protocols have been fine-tuned for various (fixed) tissue types and are well-established and standardised, although there may be some small preferential differences in processing between pathology labs [123]. Other stains and combinations are available to enhance alternative tissue features. Note that brightfield microscopy as described in section 2.4 does not rely on a fluorescent response from stains in the tissue, rather selective absorption of white light.

The aim of this chapter and of chapter 4 is to demonstrate how LSFM can be used for histopathology. Therefore, it was important that any fluorescent stains chosen to mimic H&E slide-based data have similar binding properties to create comparable resolution, contrast and precision in the resultant images. The colour of the fluorescent stains is not so crucial as false colouring is fast and easy with digital processing [200, 201]. Acridine orange (AO) is well established as an alternative nuclear stain for fresh tissue fluorescence imaging [53, 54, 56, 202, 203], so I began by using this stain to test the LSFM system.

Frozen section analysis (FSA)

FSA is an option for diagnostic imaging during an operation ("intra-operative assessment"). This is also a physical sectioning method for bright-field slide-based pathology. Briefly, frozen sections are produced by rapidly cooling volumes of tissue down to -20 to -30°C using a cryostat. Frozen water in and around the tissue gives the normally soft tissue a rigid structure that maintains the morphology of the tissue sample during sectioning. Once frozen, the frozen block can be physically sectioned. The whole process typically takes 5-10 minutes [204]. The flash-freezing acts as a fixative and thin slices can be cut away from the block without deforming the tissue and features within. This sectioning method is not as precise as sectioning from FFPE (formalin fixed and paraffin embedded) tissue blocks. The sections are thicker (on average (5-10μm [204]) to minimise tearing and shifting of features

during the slicing process. An analogy for frozen tissue sectioning is attempting to slice a thick, farmhouse loaf of bread into slices. If the blade is not sharp or not angled correctly, the sides of the bread will be torn rather than cut. The bread in the centre could be compressed as you press downwards. If we froze the loaf of bread, tearing would be less likely. The structures in the centre would hold their shape as we section the bread. However, we may have freezing artefacts (e.g. the gluten structures could become damaged and the bread may be soggy once we defrost it again). [1]

3.2.2 Histopathology as an application of LSFM

To summarise, there are disadvantages in the current model for pathological imaging for healthcare. A list of the main areas for improvement is given below.

1. Morphological artefacts due to pressure on tissue during physical sectioning
2. High overhead and processing costs [205]
3. Very long processing times
4. Limited "context" around each physical slice (images limited to distinct 2D slices rather than continuous data from a 3D volume)
5. Brightfield imaging is a destructive method
6. Limited resolution due to low contrast compared to fluorescence-based microscopy
7. Incompatible with fresh tissues - formalin fixation or flash freezing is required

The following list contains advantages of current gold standard histopathology. These are features which should (eventually) be matched or surpassed in a complementary imaging method if that method is to become relevant in healthcare beyond biomedical research and clinical trials.

[1] If you are now hungry, I suggest a snack break at this point as the following sections are less appetising.

1. Method is very well-established - machinery is readily available and costs have been reduced as the technology has matured [194]

2. Pathologists have received extensive training to interpret slide-based data. LSFM data will ideally replicate this data format to avoid the need to re-train the workforce [123]

3. Troubleshooting protocols exist to minimise processing errors [124]

4. The biochemistry of stain-selectivity and effect on images is very well understood [194]

LSFM provides optically sectioned volumetric data – therefore there is no need to cut thin sections from a 3D volume of tissue[2]. Without the requirement for thin tissue sections, you can remove lengthy FFPE processes from the workflow. LSFM can image fresh tissue within minutes of excision from a patient[3]. As a fluorescence microscopy technique, LSFM provides an opportunity to improve the resolution of tissue imaging with an enhanced SNR compared to brightfield imaging (in which unstained regions add to the captured signal in the form of bright white light). LSFM combines the benefits of fluorescence microscopy with the capacity to gather high resolution data at depth *as well* as near the surface (unlike SIM, MUSE and CFM, which are more suited to high resolution imaging at the surface). In the next section, I'll describe the OTLS microscope which I purpose-built for histopathology studies off-campus in research hospitals.

3.3 Building an open-top light-sheet (OTLS) microscope

I combined features from two previous OTLS systems to build a compact LS microscope for microscopy [56][4]. As explained in Chapter 2, LSFM has decoupled illumination and detection

[2]Provided that we only want to image regions on the edge of the sample within the FoV of the microscope.

[3]If the system is fairly close by - not always the case, hospital lab space is often far away from Surgery.

[4]See chapter acknowledgements for a full summary of work in this area before I started my project with the Optical Manipulation Group.

pathways. I was therefore able to optimise characteristics for each branch separately in the development of this system. In this chapter, I will separately describe light-sheet delivery, sample mounting in an open-top configuration and collection of fluorescence. I will then explain how and *why* Airy beam shaping was integrated into the delivery section. Figure 3.1 shows a diagram of the optics in this system. Note that this image does not show how the beam path was folded to reduce the footprint. The blue line represents the illumination beam path and the green line represents the path of collected fluorescence.

My goal was to build a functional LSFM system with a footprint of no more than 45x60cm. These dimensions were chosen to fit the system onto a small bench space in a hospital lab during downstream trials. I built upon similar previous optical designs (see section 6.4.2 and [56]). The system required two parallel imaging modes (Gaussian and Airy) in order to fairly compare the two beam shapes during trials. I constructed a proof-of-concept design which aimed to perform imaging of nuclei in fresh volumes of human tissue. The size, shape and distribution of nuclei in human tissue can often be an indicator of tissue health.

3.3.1 Illumination

Choosing and adapting the laser source

The target application was OPE in the visible range for imaging of nuclei in human tissue samples. Acridine orange (AO) was selected as a trial stain as it has been well-documented in many other instances of fluorescence microscopy for visualisation of nuclei [53, 54, 202]. The one photon absorption peak of AO is centred on 500nm with a broad tail covering the blue region [206]. Once bound to nuclei in human tissue, AO fluoresces with a peak at 530nm [207].

There are many continuous wave (CW) laser sources that are suitable and commercially available for OPE absorption in the blue region. I opted for a solid-state diode laser (STRADUS-488-150, Vortran) with peak emission at 486nm and a peak average output

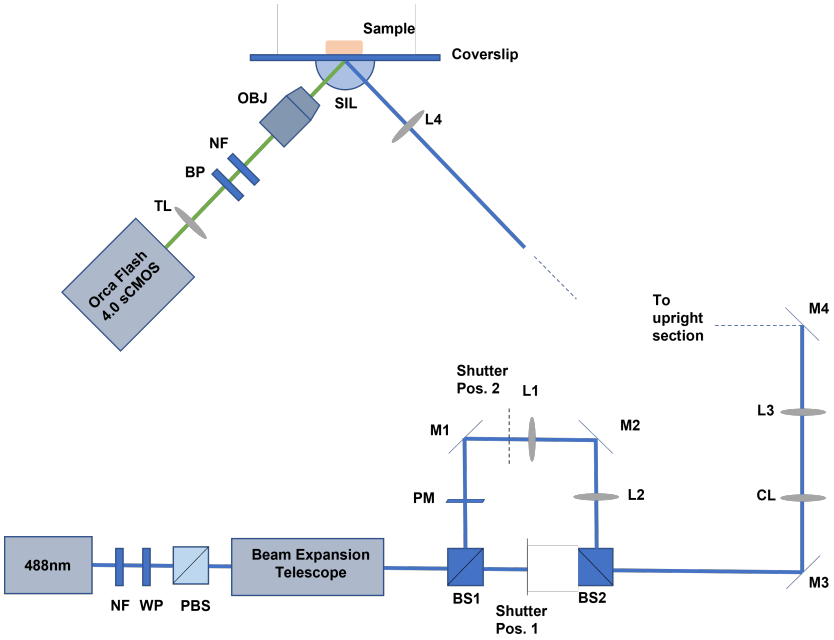

Figure 3.1 Compact OTLS microscope for off-campus studies - optical design. A compact solid state diode laser at 488nm is coupled into the setup. Beam is spectrally cleaned using a green notch filter (NF) and manual power control is achieved with a half wave plate (WP) on a rotation mount and a polarising beam splitter. The beam expansion telescope increases the diameter of the beam by 10×. Two beam splitters (BS1 and BS2) are used to couple light into the optional "Airy pathway". An adjustable shutter is moved between the undiverted "Gaussian pathway" and the Airy section. Passage through PBS, BS1 and BS2 each results in a 50% loss of beam power. A phase mask (PM) adds a 1D cubic phase profile across the Airy pathway in the Fourier plane of the light-sheet. M1, M2, M3 and M4 are planar silver steering mirrors. L1 and L2 are two spherical lenses which form a 1× telescope. This allows small adjustments to the position of the Airy beam focus relative to the Gaussian beam focus in the sample image plane. CL is a cylindrical lens which is used to focus the beam in one direction and therefore form a light-sheet in the focal plane. The CL is attached to a rotation mount allowing rotation of the LS within the sample. L3 and L4 are another identical spherical lens pair (f=100mm) used to relay the LS into the sample. The solid immersion lens (SIL) reduces aberrations resulting from the 45° angle of incidence of the beam on the glass below the sample. The infinity-corrected 4× objective (OBJ) is focused on the LS plane (when CL angled in relevant orientation. The second NF removes background blue light from the collected rays. BP is a bandpass filter used to further isolate the green fluorescent signal from sources of noise. The tube lens (TL, f=150mm) focuses spectrally filtered light onto a pixel array inside the camera.

power of 150mW. The laser head is small (100×45×45.11mm) and lightweight (210g), ideal for incorporation into a portable system. A diagram of the compact LSFM setup in shown

in figure 3.1. The laser is secured to a 45x60cm breadboard (B4560A, Thorlabs). The breadboard is reinforced with an aluminium hexagonal core structure to prevent small flexes in the base when the system was moved and acts to absorb some vibrations from its environment[5]. Four air pumped vibration isolation feet (PWA074, Thorlabs) were placed below this breadboard to further decouple the optical setup from external vibrations. Two coupling mirrors (PF01, Thorlabs) (not pictured in figure 3.1 were used to align the laser beam into a cage-based optics system from free space. The beam was passed through a half wave plate (WP) (WPH05M-488, Thorlabs) in a rotation mount (CRM1LT, Thorlabs) and then a polarising beam splitter (PBS) (CCM1-PBS251/M, Thorlabs) to allow manual average power adjustment of the beam. Remote control was also possible via micro-USB laser control and PC interface from Vortran. The laser output had an M^2 value of 1.16 in the x direction and 1.12 in the y direction. The collimated output was polarised in the vertical direction, however this did not impact the system as all optics used after the PBS were polarisation-invariant. I manipulated the output of the laser (which had an initial diameter of 0.78mm in x and 0.79mm in y to have a beam diameter of 7.5mm in both directions (this diameter was stipulated by the width of the phase mask - see section 3.3.4 for details). I achieved this using two cage-mounted Keplerian telescopes ((2×)LA4148-A-ML, LA4380-A-ML and LA4158-A-ML, Thorlabs) which required a total path length of 450mm for both telescopes. All four lenses were mounted on X-Y translation mounts (CXY1, Thorlabs) to ensure that the brightest part of the slightly asymmetric beam profile was centred with respect to the central cage axis. An adjustable iris was positioned after the telescopes to apodise the edges of the beam profile symmetrically around the centre. The collimation of the beam was also checked at this point using a portable wavefront sensor (WFS30-7AR/M, Thorlabs) and by directly measuring the beam profile at various distances from the telescope output. Spectral measurements revealed an unexpected leakage of the laser in the green region – this caused

[5]Important as the setup was to be implemented in hospital research labs not set up for low vibration optical measurements.

a significant amount of unfiltered background fluorescence in images so I later added a green notch filter before the WP (FF01-480/17, Semrock) to address this issue.

3.3.2 Creating the light-sheet

The light-sheet (LS) was generated by positioning a cylindrical lens (CL) (f=100mm, LJ4395RM-A, Thorlabs) to focus the collimated illumination across one dimension only. At this point, the beam becomes rotationally asymmetric. The width of the beam at the back aperture of the cylindrical lens dictates the width and thickness of the LS (the latter is related to the numerical aperture) (see figure 2.17). The maximum diameter was 7.5mm, but a manually adjustable slit was added before the cylindrical lens to alter the LS NA as required (the X' direction as shown in figure 3.2). No adjustable slit was added to control the diameter in Z (out of page, figure 3.2) as there was no benefit to clipping the width of the light-sheet. This would simply reduce the attainable FoV of the microscope (see section 3.3.5). The LS was focused between L3 (LA4380-A-ML, Thorlabs) and CL, 100m from CL as shown in figure 3.1. The LS Fourier plane (FP) is focused onto M4 (figure 3.1) (PF10-03-P01, Thorlabs) in an angled mount (KC45D, Thorlabs) to deflect the beam upwards at an angle of 45° from the breadboard. L4 (LA4380-A-ML, Thorlabs) refocuses the LS so that the focal point lies just above the coverslip (figures 3.1 and 3.3). L3 and L4 form a 4-f Keplerian telescope (so called because the total optical path length is equal to 4xf, where f=f1=f2.) This telescope has no magnification so the relative diameters of the beam (and numerical apertures) in X' and Z were not affected at the focal plane in the sample.

3.3.3 Open-top geometry

OTLS requires both delivery and collection of light to happen beneath a sample. Gravity is used to hold a tissue sample of arbitrary shape and dimensions atop a transparent platform. Illumination and detection pathways were positioned to approach the underside of

the platform at 45° to the bench normal (the X axis as shown in figure 3.2) and at 90° to one another. Figure 3.2 shows cartoon of concentric, curved wavefronts shifting with respect to their optical axes when crossing the air-glass boundary. Both the plane-like LS and the image of fluorescence from within the distorted LS plane are aberrated. OTLS microscopy requires other optical components to minimise such aberrations.

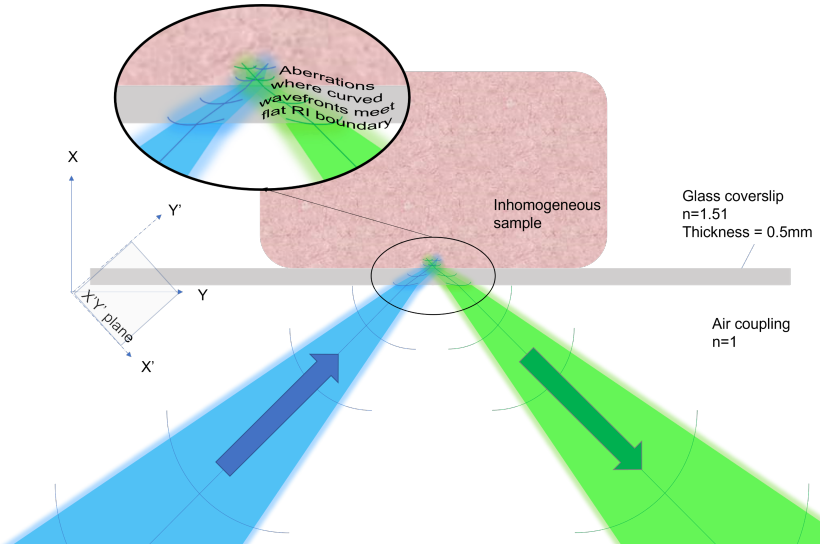

Figure 3.2 Aberrations in the beam shape occur where wavefronts cross a refractive index boundary at an angle. We require an optical component that either removes the RI mismatch from the beam path or closely mimics the curved form of the wavefronts. The latter method means that wavelets can freely pass into a new RI medium without undergoing a directional change in momentum.

Solid immersion lens (SIL)

Solid immersion lenses have previously been implemented to facilitate open-top LSFM [56]. I used a custom-made solid immersion lens (SIL) (BMV Optical, Ottawa, ON Canada) in the same manner to construct an open-top LSFM for studies discussed in this chapter. This SIL is a hemisphere of high quality fused silica glass, 15mm in diameter. The radius of curvature of the curved surface is designed to match the shape of wave-fronts meeting the boundary (see figures 3.2 and 3.3). The solid immersion lens adds a magnification factor equal to the inverse of the RI of the lens (n=1.46). This RI was selected to match the average RI of many

human tissue samples. The (de)magnification of the LS image results from the focusing effect of rays passing through the curved optic [208]. The NA of the illumination optics was also increased by a factor of 1.46 due to the RI of the lens [56]. This may be understood using equation 2.15; the angle of convergence has not changed but the "immersion medium" has an RI increased from 1 (in air) to 1.46 (in the fused silica glass SIL). Figure 3.3 shows a diagram of how the SIL is positioned with the flat top sealed against the glass cover slip layer using index-matching oil (MXA22192, Nikon). A custom-made aluminium stage was built to house the SIL (see figure 3.9). I added reinforcements to the original design (see section 6.4.2) to prevent flexing of the sample stage with respect to the scanning axis over time.

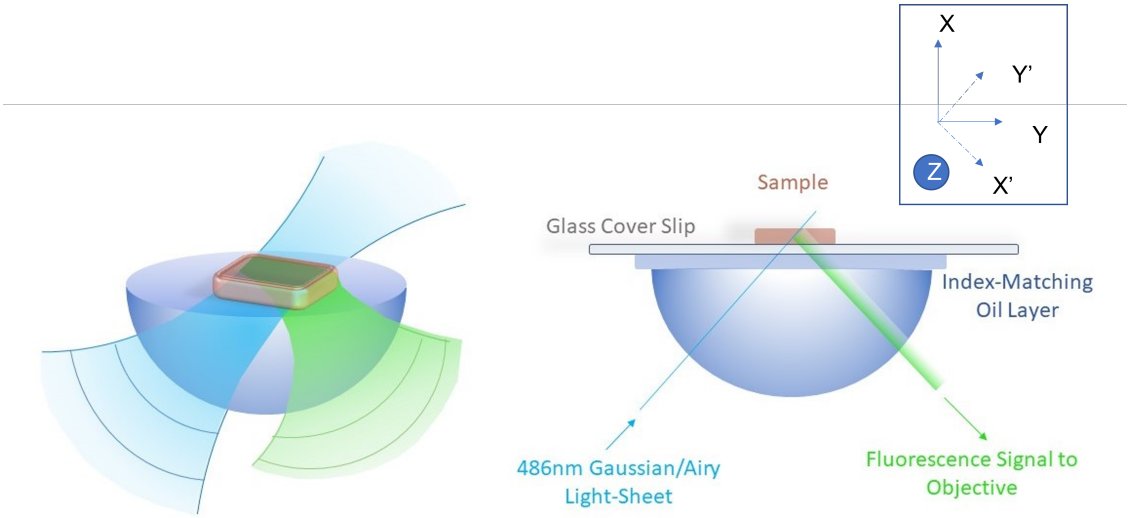

Figure 3.3 Solid immersion lens (SIL) approximates the wavefront curvature of an approaching Gaussian light-sheet at 488nm in the X'Y plane . Not drawn to scale. Note that in the Y'Z plane, the light-sheet is unfocused. The SIL will cause some unintended focusing and distortion to the planar wavefronts approaching the sample in this plane. The SIL is suspended in air using a precisely manufactured aluminium mount. An aperture in the stage just meets the edges of the lens. The planar lens surface is flush with the stage surface. Figure 3.9 shows two representations of the lens mount with a sample positioned on top.

3.3.4 Airy beam shaping

This section is provided to show how the theory of LSFM with Airy beam shaping (section 2.6) is practically implemented into the OTLS setup. From their introduction in section 2.6.1, we know that Airy beams are produced by placing a cubic phase mask in the Fourier plane of the sample. A custom made 1D cubic phase mask (PM) (LightForge, PowerPhotonic, UK) was used to add a cubic phase shift to the Gaussian light-sheet[6]. The PM was positioned in the FP of the Airy LS. Lenses L1 and L2 (a 1× relay telescope shown in figure 3.1) were used to adjust the focal position of the Airy LS relative to the Gaussian LS. By removing the shutter at Pos1/2 and rotating the LS with the CL, it was possible to view both light-sheets from the side simultaneously with the normal detection pathway. The PM was positioned as shown in figure 3.1. It was mounted using a rectangular optics mount (CYLCP/M, Thorlabs). The size of the PM necessitates an expansion to 60mm cage diameter in this section, whereas the cage is 30mm throughout the rest of the system. I used an α value of 5 for imaging (equation 2.22). This value was selected as a compromise between a thin (deconvolved) light-sheet and an extended field of view; α=5 is estimated to produce an Airy light-sheet thickness of $<5\mu$m throughout the FoV (see table 3.2), closely matching the axial resolution of slide-based brightfield images used for mainstream medical pathology. The α value was experimentally verified by comparing the theoretical PSF that α=5 would produce to the measured PSF across the FoV. Figure 3.4 shows the simulated beam propagation of the LS in the sample plane, side on, for α=0 (Gaussian mode) and α=5 (Airy beam mode). The cross-sectional intensity profiles are shown for each beam at two positions; at the focus (Y'=0 μm) and 1000 μm into the sample (Y'=1000 μm or at a vertical depth of 707 μm) (along the X axis).

The FoV of the Gaussian LS (with NA=0.15) is estimated to be 60μm. At a distance

[6]The previous design of the system by Dr Corsetti (see section 6.4.2) did not have an independent pathway for Airy beam-shaping, making it difficult to realign between measurements and to ensure that the Gaussian and Airy beams were focused at the same point in the sample plane relative to one another.

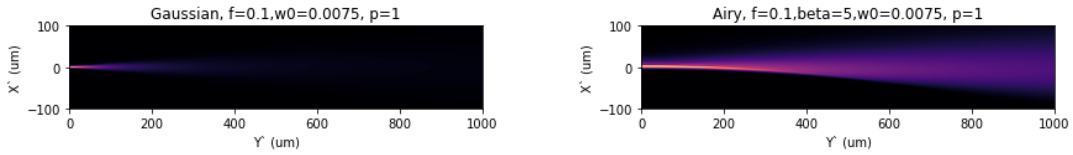

(a) α=0, Gaussian LS **(b)** α=5, Airy LS

Figure 3.4 OTLS with beam shaping for histopathology. Comparison of (simulated) Gaussian and Airy modes. The plots show the side-on intensity distributions for each mode. The "1p" denotes that these a one photon excitation intensity profiles. The beam diameter at the back aperture of the cylindrical lens is 7.5mm. The focal length of the cylindrical lens is 100mm. The intensity distributions shown here and in figures 3.5 and 3.6 assume that no sample is in place; refractive index is 1 and there are no local fluctuations in RI. Beam propagation inside tissue would require separate modelling for each tissue type, which vary in average refractive index.

of 25μm into the sample, the peak intensity drops to 74% of the maximum value (see figure 3.5). The region of highest focus is matched to the surface of the sample. This marries the highest achievable resolution of the beam with the most accessible area of the sample. Attenuation occurs exponentially at depth due to absorption and scattering, particularly for Gaussian beams (which are not self-healing). Non-uniform samples increase the likelihood that photons will scatter. Self-healing beams shapes (with multiple lobes) mitigate this by providing alternative paths through the tissue. The FoV of this setup in an Airy mode (PM with α=5) is estimated to be 250μm (see table 3.2). Note that the FoV is the distance that light travels inside the sample, whereas the depth of focus is equal to $\sqrt{\frac{FOV^2}{2}}$ due to the angled imaging geometry. Figure 3.5 shows how the peak intensity of the Gaussian LS drops quickly as the beam propagates through space, whereas the α=5 Airy LS maintains 72% peak intensity to a depth of 250μm (figure 3.6). When the side-lobes disperse (beyond the FoV), lobes merge into one another. This results in an increase in resolution size. Side-lobe merging occurs because the Airy LS is enveloped in a Gaussian function; only a beam with infinite energy could be infinitely propagation-invariant. The modulation transfer function (MTF) (see section 2.3.11) for each beam shape shows how the spatial frequencies contained in the beam profiles influence the contrast (and therefore spatial resolution) in the axial

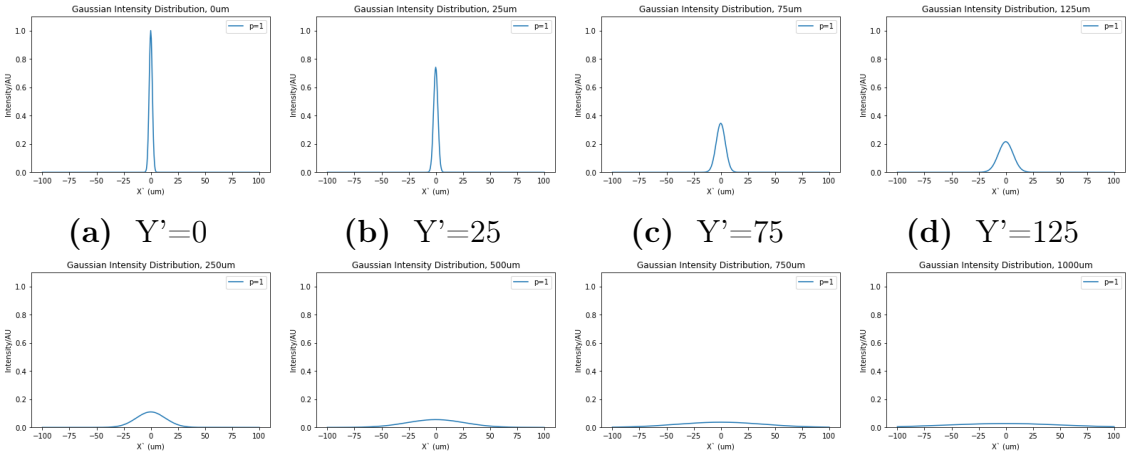

(a) Y'=0 **(b)** Y'=25 **(c)** Y'=75 **(d)** Y'=125

(e) Y'=250 **(f)** Y'=500 **(g)** Y'=750 **(h)** Y'=1000

Figure 3.5 Gaussian LS beam propagation simulated for the OTLS for histopathology setup at 3.6a) 0 μm, 3.6b) 25 μm, 3.6c) 75 μm, 3.6d) 125 μm, 3.6e) 250 μm, 3.6f) 500 μm, 3.6g) 750 μm and 3.6h) 1000 μm into the sample. The Y axis is the intensity and spans 0-1 AU. The X axis is the cross-sectional position (orthogonal to light-sheet width and propagation direction) and spans -100 to 100 μm. The peak intensity immediately begins to drop as the beam propagates through space. Photons disperse outwards leading to a broader beam profile at depth. This reduction in peak power worsens the SNR and the broadening of the beam (LS thickness) results in a poorer lateral resolution for the setup. Note that at all depths the Gaussian LS has one single lobe and that lobe is centred on the optical axis at all times.

direction for a LS microscope (equation 2.20). The resolution is defined using the spatial frequency at which two emitters become indistinguishable from one another. After data has been deconvolved as appropriate, this is based on the FWHM of the image of a point source. Figure 3.7 shows Gaussian and Airy MTFs with increasing propagation distance Y'. Table 3.2 shows the resolution achievable at each propagation distance Y' for Gaussian and Airy LS modes.

3.3.5 Detection

I will now describe the detection pathway of the OTLS. There is no difference in the detection optics for Gaussian vs Airy imaging modes. The lateral resolution is primarily dependent on the following. The SIL (see section 3.3.1) impacts the fluorescent light leaving the focal plane.

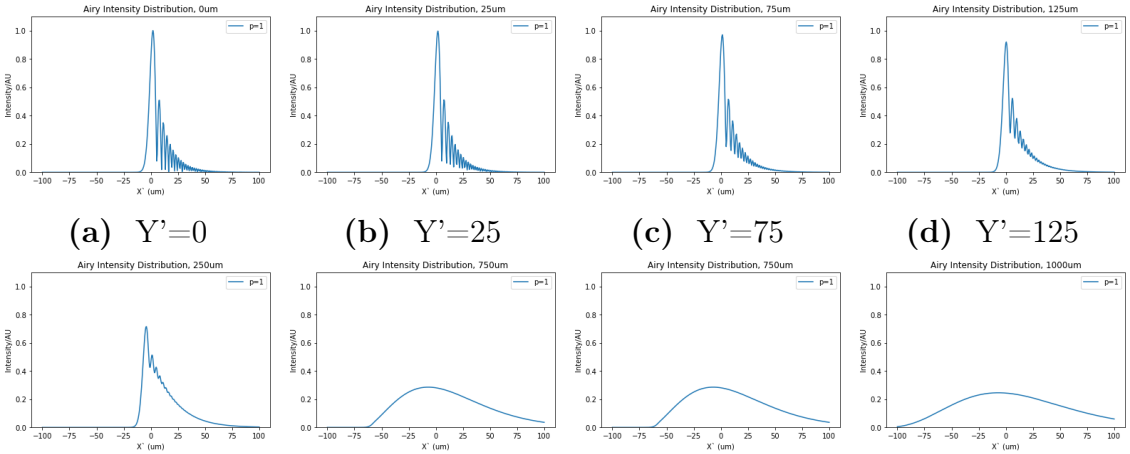

(a) Y'=0 **(b)** Y'=25 **(c)** Y'=75 **(d)** Y'=125

(e) Y'=250 **(f)** Y'=500 **(g)** Y'=750 **(h)** Y'=1000

Figure 3.6 Airy LS beam propagation simulated for the OTLS for histopathology setup at 3.6a) 0μm, 3.6b) 25μm, 3.6c) 75μm, 3.6d) 125μm, 3.6e) 250μm, 3.6f) 500μm, 3.6g) 750μm and 3.6h) 1000μm into the sample. The Y axis is the intensity and spans 0-1 AU. The X axis is the cross-sectional position (orthogonal to light-sheet width and propagation direction) and spans -100 to 100 μm. α=5. Peak intensity remains above 92% of the maximum value after 250μm propagation. The central peak shifts towards negative X as the beam propagates due to the curved nature of the Airy beam. The tail broadens as power spreads away from the main lobe, however the propagation-invariance of shaped Airy illumination means that this transition happens relatively slowly compared to Gaussian LS illumination. There is a noticeable change in the intensity profile at 375μm. The loss of differentiated side lobes translates to a sudden increase in axial resolution of the system (table 3.2) and a loss of contrast in data from this depth (figure 3.7n). Multiple side lobes are visible up to Y'=250μm from these images. The side lobes reduce in number and intensity at depth. Deconvolution is required as a post-processing technique to decouple sample features from the multi-lobed PSF of this imaging system (see sections 3.4.2 and 2.6.3).

The detection optics collected cones of light leaving the LS plane, each cone with a particular solid angle. The SIL, as with illumination, multiplies both the scale of the image and the NA of the collected rays by a factor equal to the refractive index of the lens (RI=1.46 for fused silica at 488nm). An air-based fluorescence detection objective (MRD00045 FL 50mm, 4× NA 0.2, CFI Plan Apochromat Lambda, Nikon) was cage-mounted at an angle of 90 degrees to the illumination pathway on the vertical breadboard section below the imaging platform (see figure 3.9). The *air based* WD of this objective is 20 *mm*. Accounting for

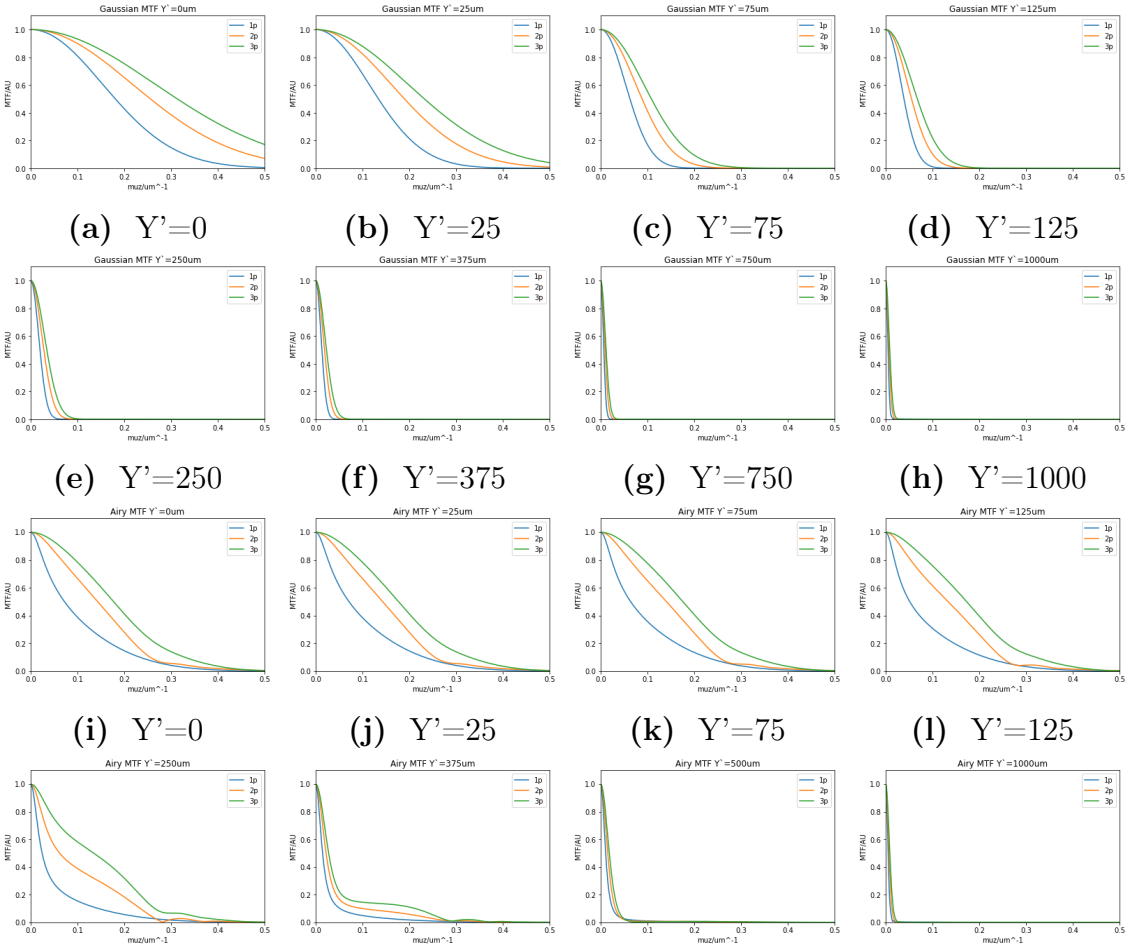

(a) Y'=0 **(b)** Y'=25 **(c)** Y'=75 **(d)** Y'=125

(e) Y'=250 **(f)** Y'=375 **(g)** Y'=750 **(h)** Y'=1000

(i) Y'=0 **(j)** Y'=25 **(k)** Y'=75 **(l)** Y'=125

(m) Y'=250 **(n)** Y'=375 **(o)** Y'=500 **(p)** Y'=1000

Figure 3.7 Modulation transfer function (MTF) for Gaussian mode and Airy mode as each beam propagates from 0μm to 1mm (or 0.7mm in depth). The Y axis is the MTF and spans 0-1 AU. The X axis is the spatial frequency (0 to 0.5 μm^{-1} in all subplots). These plots show the one photon (1p), two photon (2p) and three photon (3p) MTF at each depth. This information is included as the modest enhancement in resolution with Airy beam shaping for multi-photon excitation is relevant for chapter 5[7]. In this model, there is a clear advantage to using Airy beam shaping to improve the axial resolution of the OTLS below 375 μm in depth. Table 3.2 shows the axial resolution of the system measured from each of these MTFs.

5.857mm of fused silica (RI=1.46) and 1.625mm of glass and index-matching oil (RI=1.51) between the lens surface and the focal plane, the tip of the detection objective should be positioned 23.53 mm away from the LS plane. The objective is infinity-corrected, which provided some flexibility in the optical pathway for the detection. Collimated light leaving

Propagation distance/μm	**Gaussian mode (α=0) axial resolution/μm**	**Airy mode (α=5) axial resolution/μm**
0	2.66	3.48
25	3.59	3.49
75	7.68	3.56
125	12.37	3.71
250	23.95	4.75
375	35.61	10.26
500	47.07	28.64
750	71.84	61.12
1000	95.25	87.17

Table 3.2 Axial resolution calculated using the MTF (a function of spatial frequency). The values apply to simulated light-sheet propagating through air (RI=1). In the presence of a biological sample, it is expected that the practical minimum resolution of both beams would be impacted by attenuation of photons at depth (lack of contrast eventually leads to increased resolution size). In air, Airy beam shaping allows an axial resolution of under 5 μm to be maintained up to 250 μm propagation distance, whereas Gaussian LS resolution surpasses this benchmark before 75 μm in depth. Recall that for brightfield histopathological imaging the acceptable axial resolution is 4-6 μm. The Airy LS axial resolution remains within 7% of the minimum value for 125 μm and increases by 36% after 250 μm. The "propagation-invariant" distance is proportional to the α value [166] (α=5 gives a propagation depth of 170 μm in air for this Airy beam). In water, the FoV is theoretically extended to 229 μm due to the increased refractive index of the propagation medium (RI=1.33). This compares to a FoV of 12 μm for the Gaussian LS in air and 15 μm in water.

the detection objective was spectrally filtered to remove stray rays from the background or the illumination source. A 488 nm notch filter (NF is figure 3.9), and a 532/50 nm bandpass filter (BP) were used to filter out stray laser light and other background signals. A tube lens (f=150mm, AC254-A-ML, Thorlabs) focused the image of fluorescence from within the LS plane onto the sCMOS array of a camera (Orca Flash 4.0 v2, Hamamatsu). These components are also represented in figure 3.9. The total magnification of the detection arm

is 4.38× ($M = 4 \times \frac{150mm}{200mm} \times RI_{SIL}$). The numerical aperture of the detection optics is 0.29 ($NA = NA_{Obj} \times RI_{SIL}$). Using equations 2.17 and 2.18, the FoV captured by the camera array for the Orca Flash 4.0 v2 is 3×3 mm.

Pixel-limited vs optical resolution

Airy beams can be used to maintain a small axial resolution at depth for widefield LSFM, however the lateral resolution of the setup is still limited by the pixel size of the camera. With a FoV of 3 mm, each pixel sampled 1.6 μm of real space in the focal plane of the microscope. The Nyquist sampling theorem (2.16) states that the achievable lateral resolution with this pixel size is therefore 3.2 μm. The optical diffraction limit for this setup is given by equation 2.14 ($d_{x,y} = \frac{532nm}{2\times0.29} = 0.92\mu m$). To satisfy Nyquist sampling of the optical diffraction limit, we therefore require each pixel to sample 0.46 μm in the lateral direction. A zoom lens (MVL6X12Z, Thorlabs) was added to the detection arm to image across length scales (not shown in figure 3.9). With the adjustable zoom lens, the FoV was scaled between 4 mm [8] and 1 mm with a pixel size of 2 μm and 0.5 μm respectively. The field of view could not be increased beyond the maximum of 3 mm in either dimension, however the fixed number of pixels (1024 × 1024) could sample a smaller area (down to a minimum of 675×675 μm) with increased spatial frequency. This allowed us to attempt resolution enhancement post-processing of sub-sampled images and then check the result against a real fully-sampled image of the same area[9].

Sample scanning and data orientation

The sample stage was scanned in the Y direction using a motorised piezo actuator and a DC motor controller (M-230.10, C-863-11, Physik Instrumente). Figure 3.8 shows how the optically sectioned images are angled at 45° to the sample surface. The post-processing

[8] Cropped to 2 mm due to the diameter of zoom lens back aperture

[9] Fully sampled subsections were mosaicked to re-construct the full sub-sampled area for comparisons.

program automatically assumed that the data set is a cuboid rather than parallelopiped. A process called "shearing" is used to re-orient the slices in the data with appropriate padding to reflect the true geometry of the information, as shown in figure 3.8. Shearing is crucial to understand the actual positioning of features within the tissue with respect to the features captured in the dataset. Shearing is discussed in more detail in section 3.4.

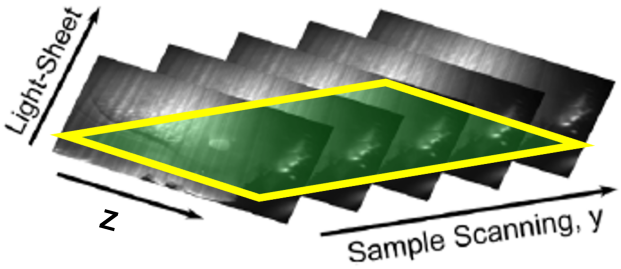

Figure 3.8 Geometry of OTLS data with respect to the light-sheet propagation direction. The yellow box contains a frame of data parallel to the surface of the sample. The sample is scanned along the Y direction and frames are captured at equally spaced intervals. The step-size was selected to match the pixel size in the lateral direction. Adapted from [58]. The FoV in the plane of the sample surface is limited by the scan range of the actuator and the FoV in Z.

3.3.6 Overview of OTLS

Figure 3.9 shows the realisation of the compact OTLS design for histopathology. Schematic designs (3.9a and 3.9c) and photographs (3.9b and 3.9d) are shown. For day-to-day use, the entire microscope was contained within an interlocked box and all suspended on top of 4 vibration isolation feet. The microscope was controlled externally using a HP laptop (Intel(R) Core(TM) i5-8250U CPU @ 1.60GHz 1.80 GHz). Once enclosed, the LSFM was classed as a Class 1 laser system and safe for use by medical personnel.

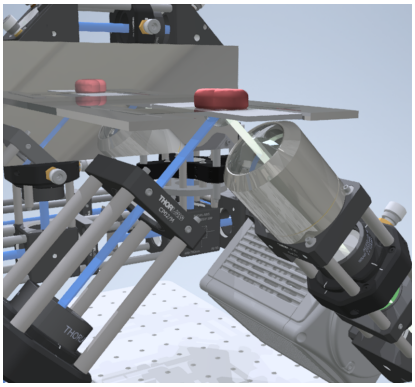

(a) Rendering of OTLS sample platform, created using Autodesk Inventor.

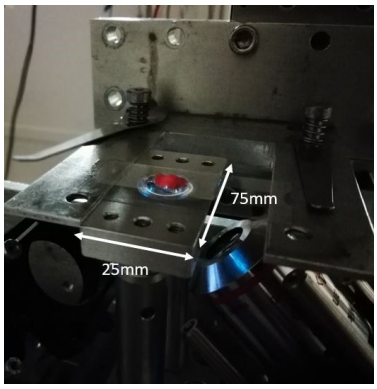

(b) Close up photograph of a sample on the custom-built sample mount.

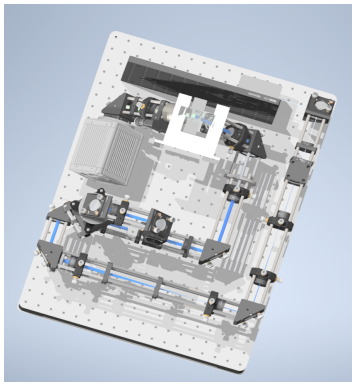

(c) Rendering of entire compact OTLS, created using Autodesk Inventor.

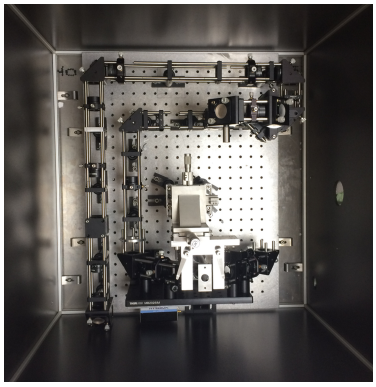

(d) Photograph of the compact OTLS during set-up at the Albert Einstein Institute, New York.

Figure 3.9 Theory of OTLS design and virtual modelling transformed into a working LSFM for histopathology. 3.9a) Illumination and detection optics are situated under a glass platform. The platform is scanned in one direction to efficiently deliver volumetric data. 3.9b) The sample is a fresh (flash frozen and defrosted) piece of colon tissue which has been stained with a nuclear dye (acridine orange). Spring-loaded clamps hold the glass cover slip in place during scanning. 3.9c) The entire system was designed to fit onto a 45×60 *cm* breadboard for off-campus collaborations. The system is pictured without its opaque laser safety enclosure to reveal the inner workings of the microscope. 3.9d) The system was enclosed by a custom-built opaque laser safety enclosure. In this image, the camera has not yet been attached. There is a hole on the right-hand-side for cables from the camera, motorised stage and laser head.

3.4 Methods

3.4.1 Sample preparation

Preparing bead samples for calibration measurements

First, create 1% low melting point (LMP) agarose gel[10]. Agarose gel is used to embed the beads and hold them still during imaging.

1. Mix distilled water with low melting point agarose powder with a weight ratio of 1:99. Use a large conical flask with plenty of space for expansion
2. Stir thoroughly with a clean spatula
3. Place in a 700W microwave and heat for 1 minute watching carefully for signs of bubbling. Boiling happens very quickly, turn microwave off if liquid level rises suddenly
4. When the liquid is ready the agarose powder should have dissolved and the liquid will be clear rather than cloudy. Take care and handle with heat resistant gloves as the flask may be very hot
5. Before the agarose solution has set into a gel, pipette carefully into individual pre-labelled eppendorfs. The agarose gel will set within 10-20 minutes
6. Store gel samples in the fridge

With the agarose gel prepared, you can then make slide-mounted fluorescent bead samples to calibrate the LSFM setup.

To prepare bead samples:

[10]The sample in figure 3.15 was prepared using 1.5% LMP agarose gel; quantities in the protocol were adjusted accordingly. Using a higher concentration of agarose powder makes the samples firmer, however it can make the gel cloudy and it does alter the RI slightly [209].

1. Gently heat agarose gel in dry heat bath at 80°C for half an hour. When the gel is ready it will turn from its chilled solid state to a clear, viscous liquid

2. Meanwhile, place beads (diluted to desired concentration in 5MΩ distilled water) in sealed eppendorfs inside a sonicator. Sonicate for around 20 minutes. This process will heat the liquid slightly and remove clumps from the bead solids

3. Before the agarose gel cools, mix the gel with bead solution to the required concentration. This can be done in an eppendorf, gently pumping the liquid up and down without pulling the pipette tip above the liquid level. It is important to avoid introducing air bubbles into the mix as these will distort images of the samples. The vortex shaker can be used to amalgamate the two liquids

4. Pipette a couple of droplets onto the centre of clean glass cover slips. Vinyl circular spacer stickers can be pre-applied to the coverslips used to support the edges of the droplet while the gel cools. Tall droplets (>3 mm) are needed to investigate the PSF of this particular LSFM design across the full FoV

5. Once the gel suspension has set, a couple of droplets of distilled water can be added over the top to mitigate evaporation of the sample before and during imaging

Staining fresh tissues

This protocol has been effectively used to stain fresh colon tissue samples for imaging of nuclei in flash-frozen "fresh" human colon samples [58].

1. Put fresh tissue sample (roughly $1cm^3$) in phosphate buffered saline solution for 5 minutes. This is to open up the cell membranes to allow dye to pass through the tissue more freely

2. Douse in 1mM acridine orange hydrochloride solution for 40 seconds

3. Rinse in fresh PBS solution for 10 seconds to remove excess stain from the sample surface

4. Blot dry

5. Place onto glass cover slip and image immediately. Press tissue down gently to remove air gaps between the glass coverslip and the sample. For samples with very irregular surfaces, a biologically compatible index-matching liquid (e.g. glycerol, RI=1.46) can be applied between the tissue and the glass[11]

3.4.2 Post-processing

There are several steps to process this data. Shearing is essential for all data sets (regardless of imaging mode) to ensure that the virtual representation of the sample is true to real spatial coordinates.

Shearing

The data is initially stored as a cuboid. The shearing angle is used to calculate how much additional space (how many blank voxels) should be padded around this cube to make space for shearing. Once the data set has been padded, layers of data are redistributed with respect to one another, based on linear interpolation. The end result is a parallelopiped of data encompassed within a cuboid of virtual space. Blank voxels remain at the corners. Figure 3.8 shows how this parallepiped of data relates to the light-sheet orientation, scanning direction and the lateral FoV of the microscope. The sheared data set can be viewed from any angle using clearvolume [163]. A single frame of data, in any orientation, can be accessed individually using FIJI tools. The data set can be further processed as a whole, or single frame processes can be applied if desired.

[11] RI=1.46 is the average RI of human adipose tissue [210]

I implemented a shearing method which could immediately be applied to recorded images through a modest laptop (Intel(R) Core(TM) i5-8250U CPU @ 1.60GHz 1.80 GHz, HP). ImageJ offers a free plugin (CLIJ2, affineTransform) which can shear 3D data sets at any desired angle. The correct shearing angle was deduced by analysing the orientation of tails in the PSF of bead phantom samples. The Gaussian LS has a larger axial resolution than lateral resolution, therefore each emitter in the volumetric data set has a small tail which points in the direction of propagation of the light-sheet (figures 2.17 and 3.3). This is not always at a perfect 45° tilt to the scanning direction and the bench, as some small scale misalignments will always be present. If the beads are smaller than the optical diffraction-limited resolution of the system, their images correspond to the PSF of the microscope at that position in the focal plane. Beads imaged using the Airy LS will have multiple side-lobes which resemble "comet tails".

Deconvolution

If the Airy mode was used, the sheared LS data set requires a deconvolution step. This is particularly true for OPE data; in chapter 5 we will see how deconvolution may not be necessary for multi-photon LSFM with shaped illumination. A Richardson-Lucy 2D deconvolution algorithm was applied to each XY frame along the Z axis[58]. The deconvolution process requires initial knowledge of the PSF of the microscope across the FoV inside the sample. The shape of the PSF at every point in the light-sheet is initially convolved with the fluorescence intensity data at the same location. Each PSF spans more than a single pixel and so some effort is required to separate overlapping signals from one another. The Richardson-Lucy algorithm trials different potential ground truth images with known PSFs across the field of view and looks for a converging solution.

The PSF was determined using theoretical Airy beam propagation with parameters particular to this open-top LSFM system. The theoretical PSF was verified and tuned with respect to the experimentally measured PSF over the same FoV. The deconvolution model

did not take into account that the Airy LS is in fact curved through the detection plane rather than uniformly flush with it (as with the Gaussian case). The model also did not take into account the slight vignetting of the light-sheet in the Z direction (figure 3.8). This may lead to a small deterioration in image quality, however it is not a dominant factor overall.

Deep learning post-processing with a generative adversarial network (GAN)

Without altering the number of pixels in the camera detector array, increasing the magnification of the system results in a loss of FoV. Similarly, expanding the FoV results in a loss of resolution. To get around this and achieve high resolution imaging across length scales, we can use deep learning to enhance the image resolution of sub-sampled data sets. The success of this technique was first demonstrated by Wang et al. [211]. In this section, I will briefly describe the architecture that we used and how we applied it to our images for our own publication [58]. This network performs a resolution improvement on a *single* widefield frame[12]. The model that we used was pre-trained using two sets of wide-field epifluorescence images. It was trained to transform features from low-resolution images (10x, 0.4NA) to high resolution (20x, 0.75NA) counterpart images of the same area. Our Gaussian and Airy data were captured with a maximum magnification of 4.3× and an NA of 0.29 (see section 3.3.5). The trained GAN model is available online [211]. We adapted the GAN and interfaced it using homemade MATLAB software, matching the pixel sizes of our data and the data used to train the model. Figure 3.10 depicts a flowchart showing the architecture of this deep learning network. Any or all frames from the data sets could be processed using the GAN as desired. Because shearing and deconvolution are not supported by the pre-trained network, this pre-processing was applied before the deep learning post-processing step. Each super resolution image took a few minutes to generate with our CPU. Further details on this method may be found in our paper [58] and the original publication on this method [211].

[12]Unlike SIM (see section 2.4) which uses multiple images of the same area to reveal finer details.

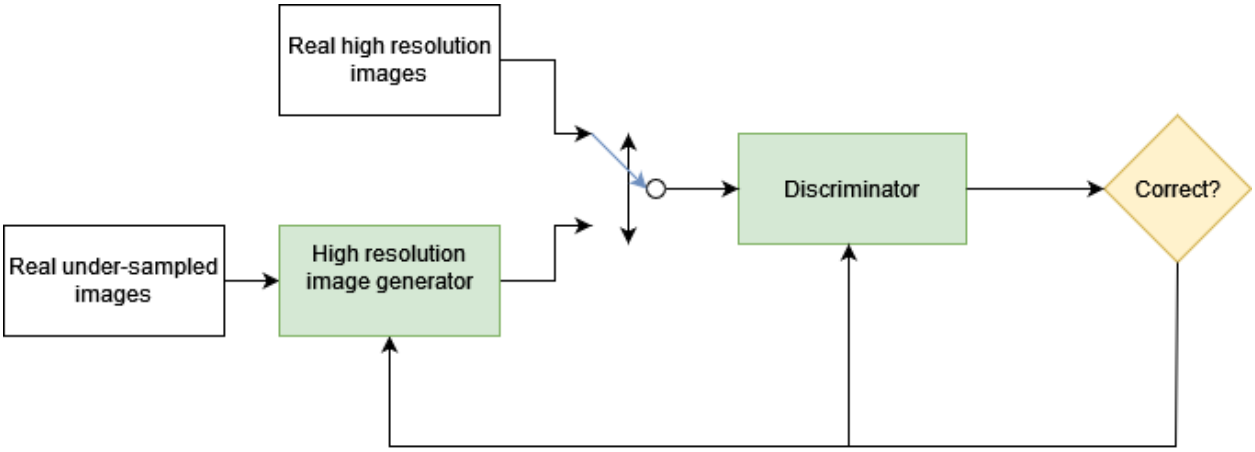

Figure 3.10 A flowchart showing how the generative adversarial network (GAN) enhances the resolution of under-sampled, widefield images until they are indistinguishable from real fully sampled widefield images of the same area. Thus, super resolution images are generated. This process can be applied to any biomedical widefield fluorescence images with minimal adjustments. Specific retraining for each microscope design is not required. This method was first demonstrated in 2019 [211]. Flowchart was created using app.diagrams.net.

Finishing touches

At this stage, FIJI (Fiji Is Just ImageJ) [212] was used to add a scale bar to the processed images. False colour maps were added to the images. These could be to mimic familiar colours from H&E mapping or simply changed to preference. ClearVolume [163] (a FIJI plugin) may be used to view the entire 3D data set at once pre or post data processing.

3.5 Biological test samples

Once calibration measurements had been performed using beads embedded in agarose, non-human samples were used to test of the system. Human tissue bank samples are precious and we only imaged these once we were confident that the microscope was performing properly. Initially, beef and porcine samples were stained using AO (section 3.4) and mounted onto the imaging platform.

Figure 3.11 shows OTLS piece of fresh porcine tissue. Nuclei have been selectively stained

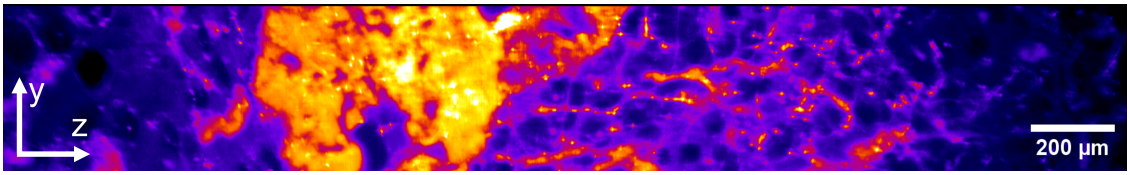

Figure 3.11 Porcine tissue stained with AO and imaged using OTLS (Gaussian mode). The axes are linked to the image geometry presented in figures 3.3 and 3.8. The FoV here is oriented in the plane of the sample surface, although the full data set sampled was volumetric rather than 2D. This image shows the surface layer of the tissue, where the LS has not yet been attenuated by interaction with complex biological features and the Gaussian LS is tightly focused in the axial direction. Many small bright dots (nuclei which have been targeted by AO) are clustered around the edge of the fat cells (dark circular features).

by AO and are fluorescing under blue illumination (λ=488nm) at the sample surface. Gaussian OTLS offers high resolution sampling of surface layers in this example. Individual nuclei have been resolved in this image with an average diameter of 5.0$\pm$1.3μm in the lateral plane. This tissue sample has an irregular surface texture. Left of centre, an orange patch shows where AO stain has pooled under the surface level. Fatty deposits in the tissue do not absorb AO, therefore they appear as dark spots in the image.

Figure 3.12 shows two images of muscle fibrils in beef tissue. In 3.12a, the fresh beef sample contains smooth continuous fibrils which indicate high-quality tissue [213] [13]. In figure 3.12b, the long, smooth fibril structures have been broken by frost damage. In this case, the sample was preserved by storing it in a -23°C freezer. For FSA of human samples for histopathology, a careful flash-freezing process is used to avoid this kind of damage (section 3.2.1). However, despite careful protocol, it is not uncommon to see some freezing artefacts in FSA samples [214].

As with the porcine sample shown in figure 3.11, fat cells in beef tissue do not readily uptake AO. Figure 3.13 shows a Gaussian OTLS image of fresh beef tissue. Nuclei have been selectively targeted by the stain and are visible as brightly coloured dots clustered around the edge of darker, circular regions (fat cells). Stain permeates around each fat cell giving the

[13] This microscope could have applications in the food testing industry.

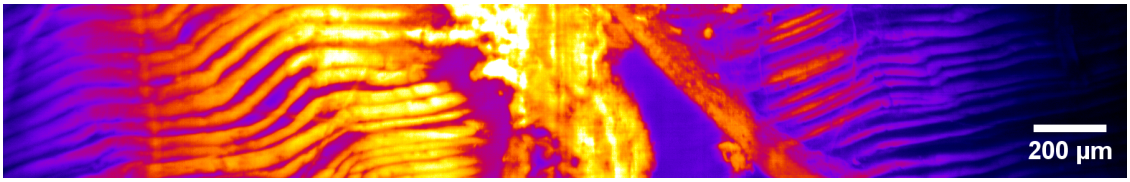

(a) Fresh beef muscle tissue stained with AO. Long parallel fibril structures are indicative of healthy muscle growth [213].

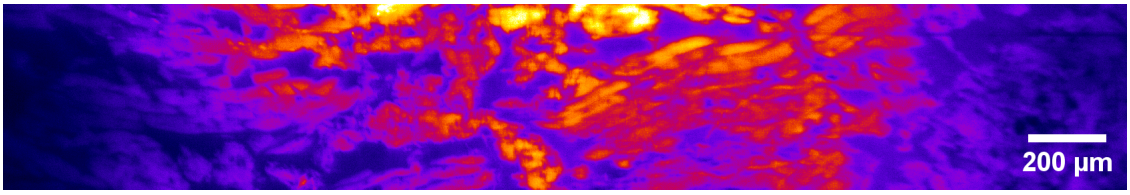

(b) Beef muscle tissue frozen at -23°C, thawed, and then stained using AO with the method described in section 3.4. The tissue has been structurally damaged by gradual freezing.

Figure 3.12 Muscular beef tissue. Both images were captured using the OTLS for histopathology in Gaussian mode. They are presented in the same orientation as the data in figure 3.11 and figure 3.13. This figure shows the effect of gradual freezing on muscle fibres. In both images, the stain has stuck to the outside of the fibril structures, however no nuclei are visible in this sample.

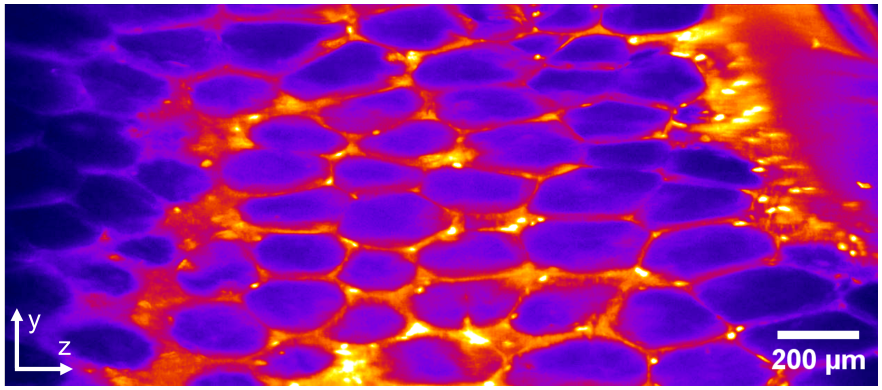

Figure 3.13 Fresh beef adipose tissue stained with AO (method described in section 3.4). The axes are linked to the image geometry presented in figure3.8. The dark rounded regions are cross sections through adipocytes. Bright dots scattered around the fatty deposits are nuclei, which AO selectively binds to. This sample has responded well to the staining protocol. When selective nuclear binding does not occur, nuclei in the image lack contrast and are often not visible.

ovals a bright boundary. Each of these samples shown in this section (figures 3.11, 3.12, 3.13 and 3.14) had irregular surfaces. In mounting the coverslip through the light-sheet plain, the samples were deliberately situated so that the outermost edge (in contact with the glass)

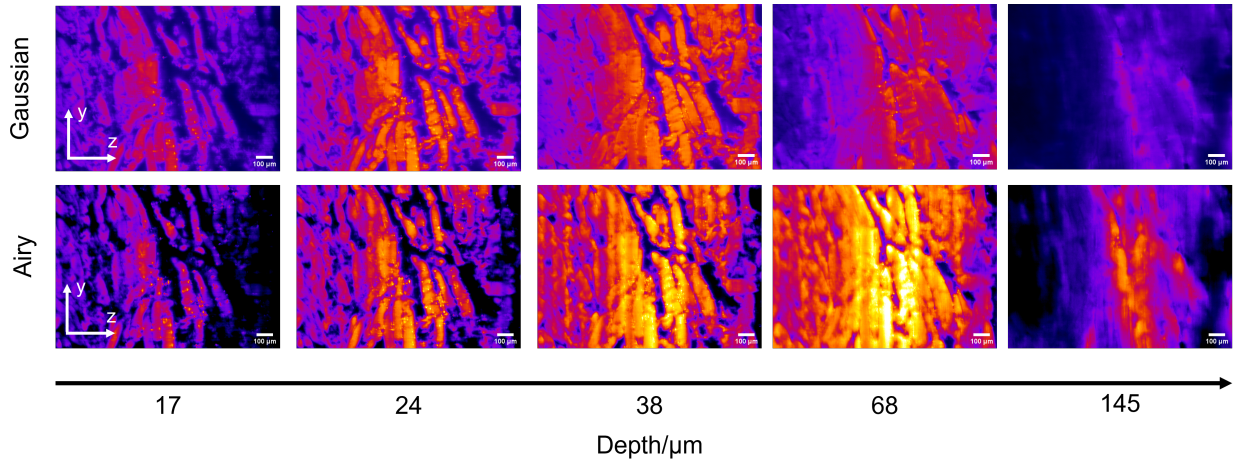

Figure 3.14 Beef tissue imaged with Gaussian mode and Airy mode at increasing propagation depth. The axes are linked to the image geometry presented in figure 3.8. Each image is in the plane of the sample surface. The depth axis corresponds to the distance in LS propagation (figure 3.8). Airy mode enhances the SNR with respect to Gaussian mode, and individual nuclei are visible at a depth of 145 μm compared to 65 μm using Gaussian mode. Scale bars are 100 μm.

coincided with the light-sheet. Indented sections of the sample surface are automatically lifted out of the most focused region of the LS. It was expected that Airy mode would make the LS more resilient to irregular sample surfaces due to the extended focal region compared to the LS in Gaussian mode.

Figure 3.14 shows preliminary data testing the OTLS in Airy mode. Again, AO was used to stain fresh beef tissue using the protocol described in section 3.4. In both modes, selectively stained nuclei are visible close to the surface of the tissue (at 17μm from the outermost edge of the sample). In Airy mode, individual nuclei are still visible after the LS has propagated 145μm in depth, whereas in Gaussian mode the distinct nuclei have disappeared after 145μm LS propagation. The Gaussian images of the beef sample were captured before the Airy images. The sample was not moved in between the data sets.

3.6 Results

3.6.1 Gaussian vs Airy OTLS

Measurements revealed that, as predicted, deconvolved Airy LS data improves the resolution of the OTLS over an extended FoV compared to Gaussian mode. Figure 3.15 shows full width half maximum (FWHM) measurements made of bead intensity profiles at increasing depth. As in figure 3.14, the depth here refers to the propagation distance of the LS rather than μm below the sample surface, which is scaled by $\frac{1}{\sqrt{2}}$ due to the sample geometry. Using beads smaller than the optical resolution of the setup (0.92μm laterally, minimum of 2.66μm axially[14].) allows us to inspect the PSF of the beads in three dimensions. The axial resolution of the system is governed by the thickness of the LS. The LMP agarose suspension has a RI of 1.33 [209]. We therefore have a theoretical FoV of 15μm in Gaussian mode and 229μm for the Airy LS. These values assume that the axial resolution becomes limited by contrast when the MTF for each beam shape reaches an arbitrary cut-off of 5% of the maximum value. In this orientation, the images show the LS side-on with the sample surface at the top (oriented out of the page). The acceptable axial resolution for current gold standard imaging for histopathology is 4-6μm, set by the thickness of tissue sections that can be imaged using brightfield microscopy (sections 2.4 and 3.2).

The information in this figure was procured using the compact OTLS for histopathology (figure 3.1). The data, published in OSA continuum [58], was collected onsite in St Andrews before the system was sent for a scoping exercise in a real pathology lab (see chapter 4 for details). We present a clear axial resolution improvement using Airy mode OTLS compared to equivalent Gaussian LS (both beams have the same numerical aperture in the illumination pathway). 200nm diameter beads are smaller than the diffraction-limited resolution of the setup, therefore looking at their profiles in this plane is equivalent to measuring the PSF of the setup in that location. The FWHM of sub-diffraction limited beads is consistent within ±5%

[14]Valid in air (RI=1). See table 3.2

using the propagation-invariant Airy LS. The Gaussian FWHM increases by 79% over the same 400μm propagation distance. However, the Airy data must be deconvolved in order to convert the high spatial frequencies carried in the MTF (section 3.3.4) into a high resolution image of the sample. The lateral resolution of the setup is experimentally measured to be 4.7$\pm$0.6μm for Gaussian mode and 4.2$\pm$0.6μm for Airy mode. These results are consistent with previous findings [215].

3.6.2 Airy mode OTLS with deep learning for human tissue analysis

We used the OTLS microscope with both Gaussian and Airy modes to distinguish between cancerous and healthy fresh human tissue samples[15]. Whilst Airy mode provided a clear resolution enhancement at depth in transparent agarose-embedded bead samples (figure 3.15), the improvement became more marginal in complex biological samples[16]. To enhance the benefits of Airy OTLS, deep network post-processing was applied to the Airy LS images. We imaged cancerous and benign human colon tissues provided by the Tayside Tissue Bank (request nos. TR000289 and TR000499, ethical approval application no. PA14500). Cancerous and benign breast tissues were obtained through Charing Cross Hospital in London with the Imperial College tissue bank licence under project R12047. The breast tissue samples were similarly imaged using the OTLS in both Gaussian and Airy modes. All patients consented to their tissue samples being used under these conditions. Please refer to our publication in OSA Continuum for more detailed information about how these samples were prepared prior to imaging [58].

Identifying colorectal cancer using OTLS

The Airy light field with its self-healing properties allowed the attenuated LS beam (at 488nm) to refocus and produce high resolution images from deeper inside colon and breast

[15]Fresh here means flash frozen, stored at -80C and defrosted before processing and imaging.

[16]This point is demonstrated later in figure 3.18.

tissue samples compared to conventional Gaussian LS imaging (figures 3.16 and 3.17). Wide-field imaging (without the optional zoom lens) provided a 3×3mm FoV with a pixel size of 1.6μm. This gives a minimal resolution of 3.2μm with the Nyquist sampling condition. In order to image with high resolution across length scales, a zoom lens was inserted into the detection arm (see section 3.3.5 for details). This allowed Nyquist sampling at the optical resolution (0.5μm per pixel) to be achieved for sub-sections of the unmagnified FoV. The Nyquist sampled data was used to verify the success of GAN deep-learning post-processing applied to the Airy OTLS data. Refer to section 3.4.2 and [58, 211] for details on the GAN architecture and to [58] for further information about how it was applied here to recover super resolution data from wide-field OTLS images.

Figure 3.16 shows images of two colorectal tissue samples from the same surgery. These samples were pre-labelled as "normal" and "adenocarcinoma" by experienced pathologists. The samples were flash frozen after excision at -80°C. They were thawed whilst submerged in PBS and stained with AO using the method described in section 3.4. In the normal tissue case (subfigures a-h), images contain rings of nuclei which surround colonic "crypts". The presence of these crypts is indicative that cancerous cell growth has not disrupted the normal morphology of the tissue. The crypts appear to be circular in this orientation. In 3D, crypts are sausage-shaped clefts in the surface of the mucosa. Airy OTLS with deep learning post-processing (e-h) allows individual nuclei to be resolved up to a depth of 83μm below the sample surface. With simple Gaussian OTLS and no neural network processing, nuclei are no longer distinct at 83μm. In normal tissue, colonic crypts are typically around 340μm and crypts in tubular adenoma samples can be twice as long [216]. In this example (subfigures i-n), adenocarcinoma presents itself as densely clustered bands of nuclei. This is characteristic of colorectal adenocarcinoma [217]. The case for 3D imaging over conventional 2D brightfield of these samples would be strengthened if it were possible to image over a comparable depth range. Unfortunately, even self-healing Airy patterned light-sheets are strongly attenuated at 488nm. This attenuation severely limits the ability of the OTLS

to resolve sub-cellular information (nuclear shape, density, distribution) at depth[17]. The increased propagation-invariance of the Airy LS is not fully exploited when imaging turbid, non-cleared colorectal tissue.

Using Airy mode OTLS to resolve features within an irregular sample surface - breast tissue samples

Whereas colon tissue is soft and "floppy", breast samples generally contain more adipose tissue and are therefore more rigid. Breast tissue samples tend to have irregular edges, particularly cancerous breast tissue [218]. Macroscopic changes like this are useful to surgeons during surgery. They can help to inform decisions about where to cut away tumours and how much tissue around the edges can be considered a safe margin of error [219]. Figure 3.17 shows a comparison of two breast tissue samples from the same patient, one benign and one cancerous. Acriflavine was used to stain the breast tissue samples. Like acridine orange, acriflavine is a nuclear stain which may be excited under 488nm illumination to produce green fluorescence. It has been previously used for several studies on fluorescence microscopy for pathology applications [220–222].

Both tissues were imaged using Gaussian mode and Airy mode plus GAN post-processing. For these breast samples, Airy LSFM has improved the image quality across the surface layers. This is likely due to the long DoF of Airy LS microscopy. The beam is focused over a relatively large distance at the sample surface, meaning that sections rising above the imaging platform can still be resolved. Additionally, heterogenerous sample surfaces make air bubbles between the tissue and the cover slip more likely. Self-healing Airy beams are better equipped to deal with small-scale refractive index mismatches caused by the presence of air than Gaussian beams.

As with the example shown in figure 3.16, deep learning has achieved super-resolution

[17]Staining protocol would need to be updated in order to permeate up to 340μm. Using the method described, AO nuclear binding is expected up to 90μm.

images from sub-sampled data across the entire FoV. The cancerous breast tissue sample shows characteristic chaotic clusters of nuclei where uncontrolled growth has occurred due to disease. In the healthy breast tissue, we can see more sparsely distributed nuclei through the sample. It is predicted adding a counter-stain and multiplexing this kind of data to produce two-colour images (i.e. showing nuclei and cytoplasm in seperate layers) will improve the interpretability of these images for diagnostic purposes [123].

3.6.3 Airy OTLS with deep learning for imaging cleared samples

We found that OTLS was able to distinguish between cancerous and benign fresh tissue with minimal sample preparation. However, the true extended FOV that Airy beam imaging provides is not accessible unless we demonstrate the technique using an optically transparent sample. In this example, we imaged a pre-clinical model of Alzheimer's disease in a chemically cleared mouse brain hemisphere. Amyloid protein deposits are a normal occurrence in the brain, however excessive build up into plaques can block the normal functioning of neural cells. This is characteristic of Alzheimer's disease in humans. The hemisphere was stained with thioflavin S and cleared using the same methods as described in [223, 224]. Thioflavin S is a selective dye which binds to amyloid protein and glows green under 488nm excitation. The amyloid plaques are 3D structures which extend throughout the hemisphere. Using the Airy beam LSFM method with GAN post-processing, we can resolve the amyloid plaques up to 1300μm in depth. Since the plaques are roughly 10μm in diameter, they are resolved without reaching the optical limit of the instrument. The resolution improvement at depth brought about through Airy beam shaping presents itself instead by a 2$\times$ improved SNR compared to Gaussian images of the same region. Tracking the plaque structures in 3D better informs our understands disease progression. The success of LSFM for imaging cleared biological samples has been widely demonstrated [56, 158, 173, 225–229]. Cleared samples are a common tool for biomedical research, particularly in neuroscience [57].

3.7 Summary

We demonstrated that the advantages of Airy beam shaping in light-sheet microscope can be married with post-processing to enhance the resolution across length scales. Deep learning post-processing with (α=5) Airy LS beam shaping gives a factor of 2× resolution improvement over the entire FoV compared to Gaussian LSM with the same numerical aperture. A propagation-invariant, self-healing Airy light-sheet is able to penetrate up to 30% deeper into non-cleared tissue than a Gaussian LS with the same numerical aperture. When Airy LSFM is used to image cleared samples, the full FoV of the LS is visualised within the tissue. This has been demonstrated using cleared mouse brain samples containing Amyloid plaques (which indicate the progression of Alzheimer's disease through the tissue). The Airy beam parameters that we used for this demonstration can be adapted to suit different sample types. For example, highly attenuating samples may not benefit from long FoV illumination, instead a shorter FoV can be used to image surface layers with higher resolution. Airy beam shaping improves the overall quality of surface images with irregular surface textures. If cleared samples are used, it may be preferable to choose a long FoV Airy LS with a larger axial resolution. The GAN post-processing can be used for long or short FoV LSFM images to improve the resolution retrospectively. Note that the volumetric data can be post-processed using frames from any plane. The GAN acts to enhance the lateral or axial resolution of the data depending on the orientation of the frame that it is applied to. This kind of post-processing does not require pre-training on each new widefield microscope design.

There is scope for LSFM with beam shaping and deep learning post-processing to be useful within biomedical research. However, there are important practical considerations that must be made before LSFM can be considered as an asset for histological imaging in everyday healthcare. Airy beam shaping requires deconvolution, and the full FoV offered by Airy modality is only accessible once volumetric biological samples have been chemically cleared.

Both deconvolution of Airy images and sample clearing are time-consuming processes. This effectively rules out using these OTLS techniques for rapid diagnostic assessment (i.e. during surgery). Practically speaking, without physical sectioning of volumetric tissue samples, we cannot extract sub-cellular resolution images from more than around 90μm inside fresh colon and breast tissue. The OTLS setup favours imaging of "floppy" samples with a smooth surface texture. In this case, Airy beam shaping is an improvement on the Gaussian fresh tissue imaging OTLS design that came before it [56], although processing the images can take 20-60 minutes (dependent upon the size of the dataset). In the future, a deep learning network that does deconvolution and super-resolving in one step could be developed and implemented for this application. We expect that implementation of such a network using a graphics processing unit could cut down the processing time to $<$1s per frame.

In the next chapter, I test the OTLS outside of this optimised laboratory environment. Characterisation of the system and testing (covered in section 3.6) revealed promise for this system with fresh tissue diagnostics. I will reveal how the microscope performed in a real clinical setting. I consider end-users (pathologists) as part of this scoping exercise. Their feedback and data have allowed us to evaluate how the technology can be better adapted for use in a pathology lab.

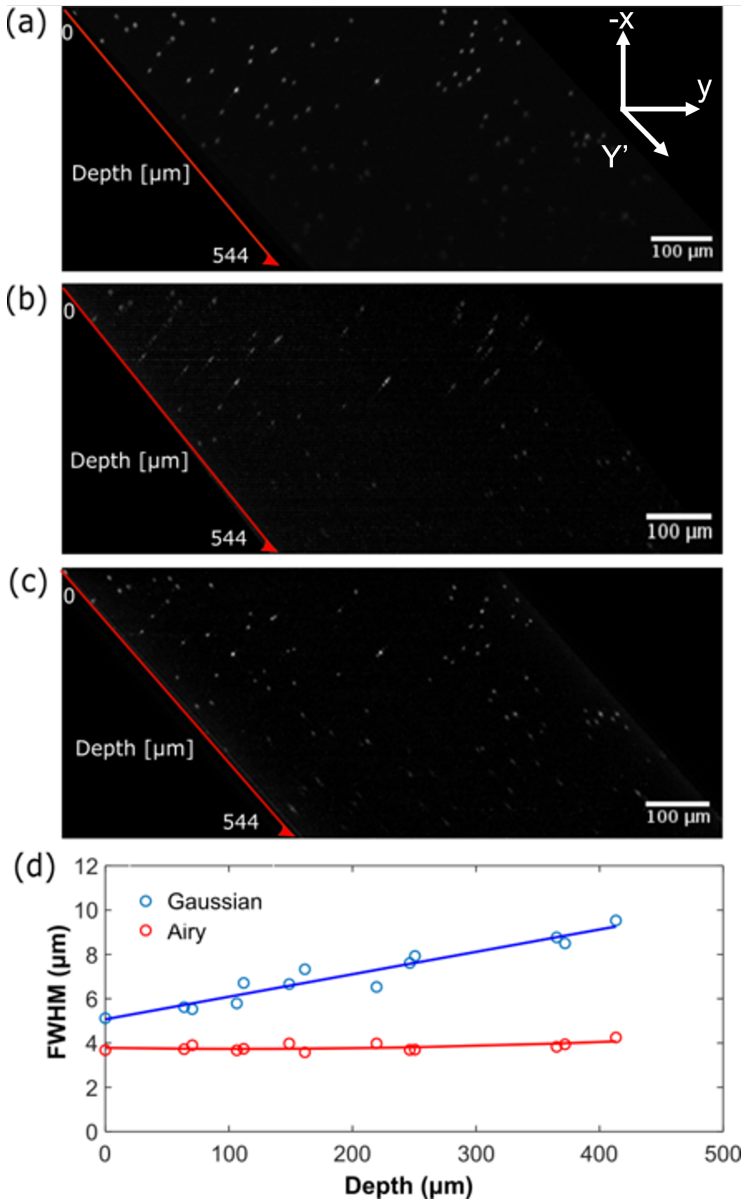

Figure 3.15 200nm fluorescent green beads embedded in 1.5% agarose gel, viewed here with the scanning direction along the x axis in figures a-c. This figure is published here [58]. The red y' axes spans 0 μm and the surface to 544 μm diagonally in depth below the surface. The beads are imaged using the OTLS in a) Gaussian (α=0) mode and b) Airy mode (α=5). The Airy data is deconvolved in c) to reveal the improved axial resolution afforded by the use of this propagation-invariant shaped beam. The beads are smaller than the diffraction limit, meaning that the profiles in a) and b) represent the PSF of the system at that position in the FoV. The same sample was imaged twice (taking care not to saturate the beads) to ensure that results were directly comparable. In d), bead profiles from a) and c) are analysed to show the axial resolution of the setup with increasing LS propagation distance.

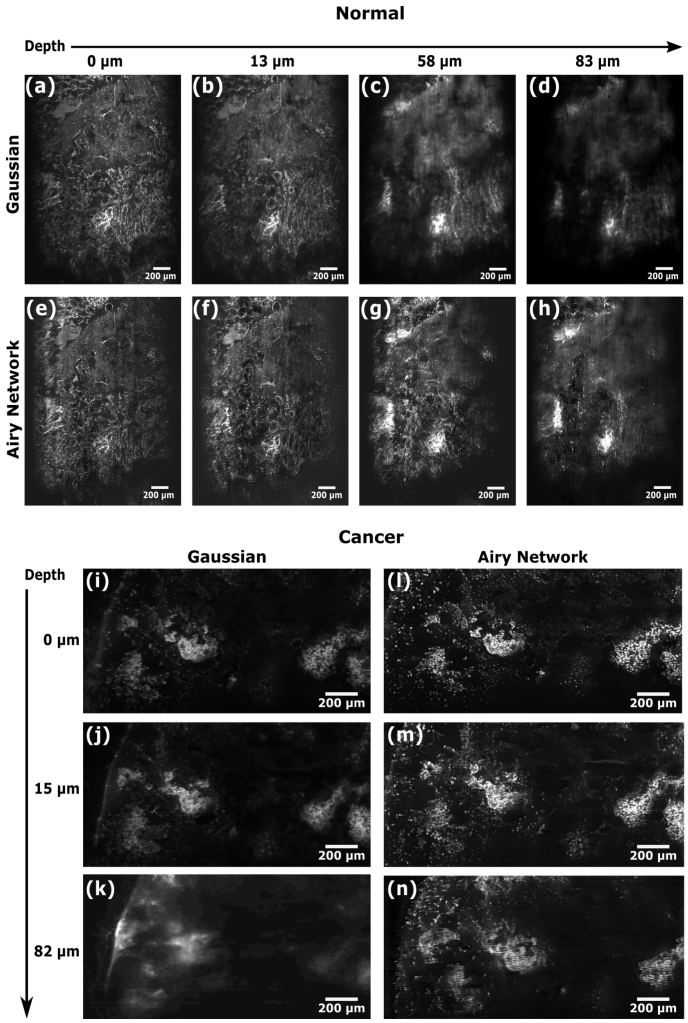

Figure 3.16 Published in OSA Continuum [58]. Benign and cancerous colorectal tissues have been selectively stained with nuclear dye acridine orange and imaged with the compact OTLS for histopathology. Airy mode with deep learning post-processing affords an increased resolving power across length scales. The tissue is highly attenuating to the illumination (at 488nm) in both Gaussian and Airy mode, however Airy beam shaping mitigates this to some extent due to its self-healing properties. In subfigures a-h normal colorectal tissue is imaged using Gaussian (a-d) and Airy (e-h) modalities. Figures c, f and j show Airy data with the deep learning post-processing algorithm applied to enhance the resolution. Small, circular distributions of nuclei indicate healthy, normal growth of colonic crypts and the absence of cancer. In subfigures i-n, we present OTLS images of colorectal tissue which was previously known to contain cancerous cells. Adenocarcinoma is signalled here by regions that are densely packed with nuclei in unstructured masses. In both normal and cancerous colon tissue, Airy beam shaping combined with deep learning post-processing allows the nuclei to be resolved up to 82μm in depth. This is 30% deeper than Gaussian imaging alone, where nuclei are resolved up to 58 μm in depth.

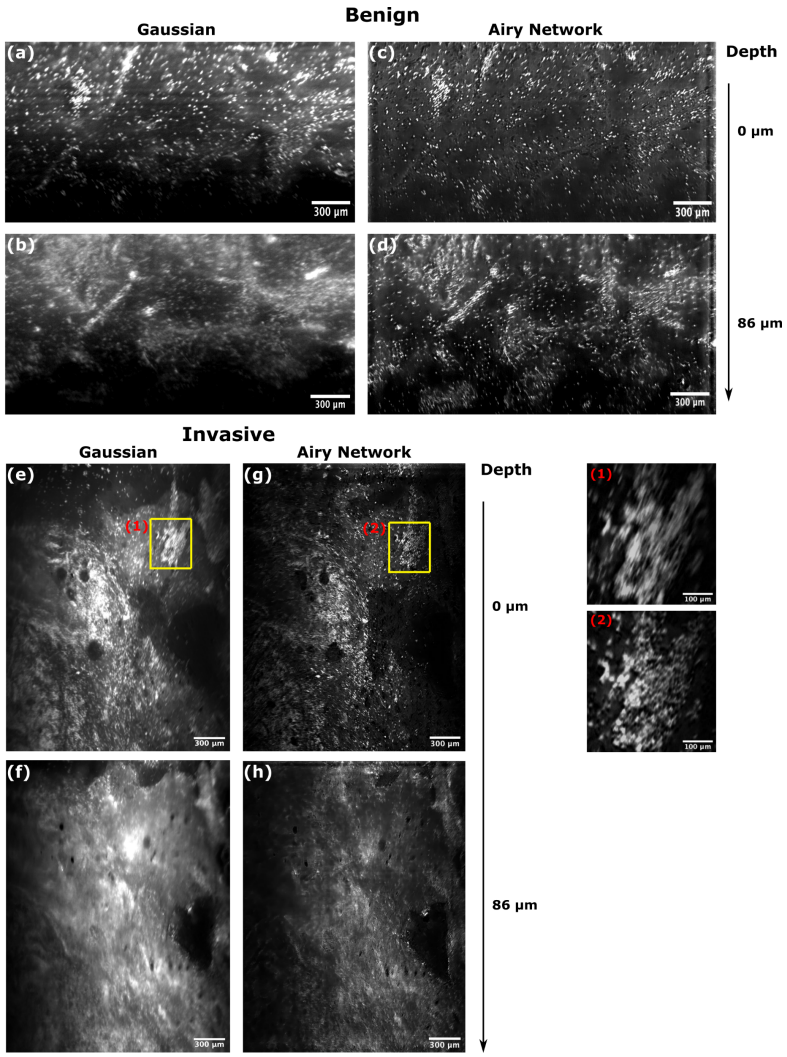

Figure 3.17 Figure from [58]. OTLS images of healthy and cancerous breast tissue. Both samples were stained using acriflavine and imaged using Gaussian and Airy light-sheets at 488nm, producing fluroescence in the green region. This figure has been pre-published [58]. Gaussian mode allows resolution of nuclei at the sample surface (a-b, e-f). The yellow boxed region in subfigure e) is blown up in the first inset. It shows that the Gaussian data is blurred even at the sample surface for the cancerous breast tissue images. Using Airy mode with neural network post-processing (c-d, g-h), nuclei are resolvable up to 86μm below the sample surface. Image quality using the Airy beam at the surface level (inset 2) is compared to the equivalent region imaged using Gaussian mode. The Airy LS has an extended depth of focus which makes it more "forgiving" of highly textured sample surfaces. Gaussian beams are focused over a small range only, so if the sample surface lies above that short focal region then even the surface data will be sub-optimal. Cancerous tissue is typically more irregular in texture [123].

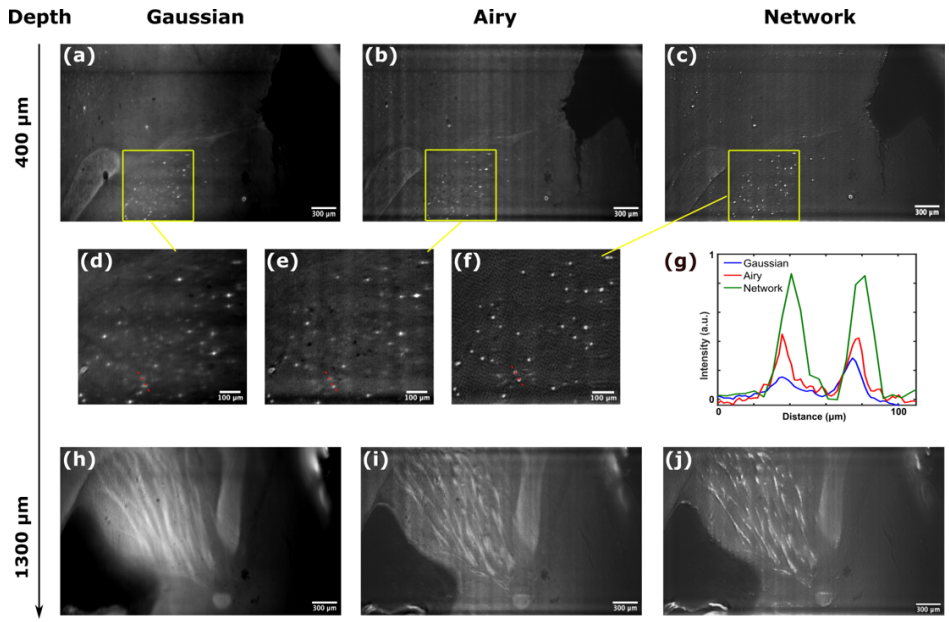

Figure 3.18 Figure from [58]. Amyloid plaques in mouse brain stained with thioflavin S are imaged using a wide-field open-top light-sheet microscope. The plaques are consistent with others from this model of Alzheimer's disease in 5xFAD mice of the same age group. The sample was imaged twice, once with a Gaussian beam (a, d and h) and again with Airy beam shaping (b, e and i). Our generative adversarial neural network was applied to the Airy images giving a further reduction to the achievable resolution over this field of view (g). The improvement in resolution with Airy beam shaping and deep learning compared to Gaussian imaging is demonstrated to a depth of $1300\mu m$.

Chapter Four

Towards clinical use: optimising tissue analysis with OTLS

4.1 Introduction

The OTLS was deliberately designed to be a portable, benchtop device ($< 1\ m^3$) in order to facilitate the scoping exercise described in this chapter. I packed up the OTLS microscope and travelled with it to the Albert Einstein Institute in New York. I stayed there for a period of two weeks whilst I set up the system in their pathology lab and trained local staff to operate it. We imaged several tissue samples together during the training period. The collaboration continued remotely for a period of 6 months until March 2020 using Microsoft Teams, regular email correspondence and Anydesk remote laptop access. Some of the data from this collaboration is presented here. The goal of this collaboration was to establish how the microscope performed in the real-world context of a busy medical laboratory and consider how the technology could be improved for use in pathology in the future.

4.2 Setup

The setup described in chapter 3 (figure 3.1) was not altered before it was taken to New York. Note that the zoom lens was not used; the (fixed) FoV of the microscope was 3×3mm with a pixel-limited resolution of 1.6μm during these trials. We often did not capture the full FoV, particularly if a sample only adhered to the imaging platform over a small area. Data was stored securely on external hard drives as a massive storage capacity is required for LSFM imaging. The Airy mode for the microscope was tested, however after some issues with tissue processing and mounting, I limited my analysis to images taken using Gaussian mode. Please refer back to section ref 3.6 for analysis of how Airy beam shaping can improve the quality of the OTLS data when sample preparation methods have been well-tested.

4.3 Methods

The sample preparation methods used within this chapter are similar to those described in section 3.4, although the AO staining protocol had not been treated on many of these tissue types or on formalin-fixed tissue. The human tissue samples varied a great deal in shape. Acridine orange can permeate to a limited penetration depth in turbid tissue. Improper sample preparation can cause the surface layers to become over-stained. Fresh tissue samples are sensitive to immersion in water-based media. It is common for the peripheries of unfixed samples to degrade after a few minutes of immersion in PBS; timing tissue acquisition with preparation and imaging is critical.

Data storage and processing

Gaussian LS data requires very little post-processing; I created a Macro tool using FIJI to scale, shear and reference pixel size in each data set with one click. This step could be performed using the system control laptop. Select portions of data were uploaded to a shared

Dropbox folder to give both teams access. The total volume of data at the end of 6 months of collaboration exceeded 1TB. We used several external storage devices containing carefully labelled data sets to chronicle our collaborative efforts with the LSFM system.

Long-range practical assistance

Remote assistance was provided in two main forms during the collaboration. Firstly, I created a purpose-written "user-guide" aimed at non-physicists. This user guide (attached as an appendix B) contains standard operating procedures, an explanation of each optical component, common aberrations and how to recognise and mitigate them, and some notes on image processing and data interpretation. The second method was being available online for regular video calls to discuss progress with the project and to tackle obstacles as they arose.

Workflow summary

Figure 4.1 shows the general structure of how optimisation was run during the scoping exercise.

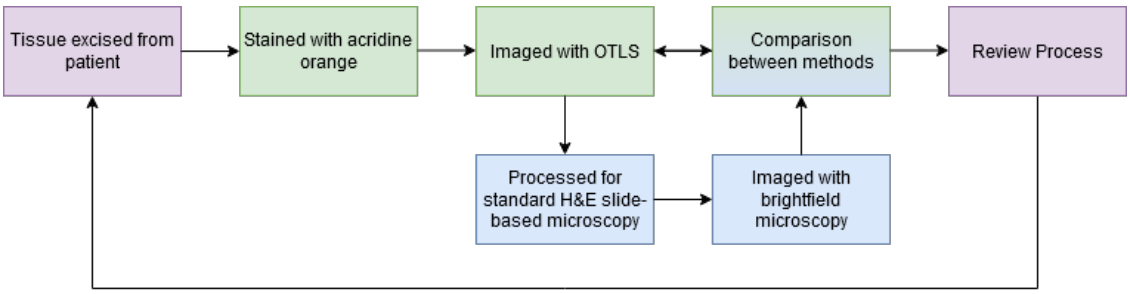

Figure 4.1 Work flow for optimising tissue analysis with the OTLS setup.

4.4 On-site testing

Re-characterisation after transit

On arrival, the OTLS was set up and realigned using methods described in chapter 3 and appendix B. Once aligned, I prepared some agarose bead suspension gel droplets on cover slips using the method described in section 3.4. Droplets of liquid fluorescein solution on the imaging platform were also used to verify successful system realignment. The light-sheet, produced using the cylindrical lens (CL in figure 3.1), could be rotated inside the sample using the rotation mount on the CL. Viewing the LS from the side, I made adjustments so that the focused part of the sheet lay just above the uppermost surface of the mounted coverslip. This process was to verify that the beam profiles in Gaussian and Airy mode were comparable to those that had been measured when the system was previously set up in St Andrews (i.e. 3.2μm lateral resolution and 5μm axial resolution at the Gaussian LS focus). Local staff were involved in the alignment and re-characterisation process for training purposes.

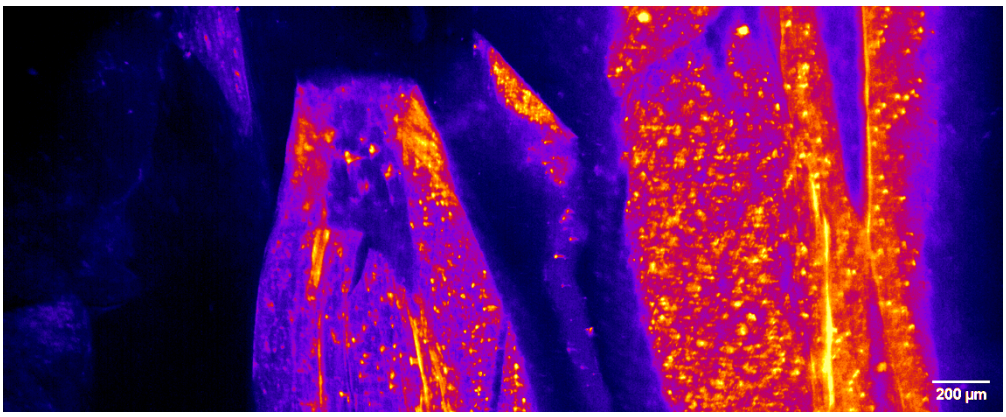

Figure 4.2 Test sample imaged using the OTLS in Gaussian mode. Naturally transparent blood orange flesh contains autofluorescent anthocyanin which fluoresces under blue laser light. This sample was imaged to check system set up properly for imaging at depth. The scale bar reads 200μm.

As a quick demonstration, I imaged a small piece of blood orange. Blood oranges naturally contain anthocyanin [230, 231] which is known to fluoresce under blue excitation [232].

This test sample also offered the opportunity to assess the beam quality in depth as the fruit tissue was more transparent to visible light than the animal test samples (beef, porcine) which we could obtain locally. Figure 4.2 shows the results of this test.

Autofluorescent samples

Autofluorescent samples are helpful for limiting the number of controllable variables. There is no-need to optimise a staining protocol for a specific sample/microscope combination prior to imaging. Autofluorescence is typically a weaker signal than light produced by fluorescent stains [233]. It should also be noted that all fluorescence imaging in this configuration is highly sample-dependent. Therefore, we can assess the general performance of the system using a sample such as this, however it is not advisable to make direct comparisons between dissimilar samples with exogenous staining. Armed with this knowledge, we were ready to begin trials with human tissue samples.

4.5 Results: human tissue imaging

4.5.1 Overview

This was a scoping exercise rather than a clinical trial for a specific application of histopathology. We imaged a variety of tissue types with the aim of better understanding the potential versatility of OTLS for histopathological fresh tissue imaging. Each tissue type has a different firmness, smoothness, stainability, water content and drying rate. Therefore, it was a practical challenge to rapidly image multiple sample types particularly when it was not known in advance which tissues may be available. During the two weeks of in-person collaboration at the start, most tissue available was pre-fixed and left over from recent operations. We had never tested our acridine orange staining protocol with fixed tissue samples before and it was not known in advance how the stain would interact with these tissues. Over the

next few pages, I will discuss particular data sets on a case-by-case basis. Many of these samples were imaged by pathologists after I left New York. It is not possible to make direct comparisons between all of these data sets as the data in each figure is separated by tissue type and system condition. Misalignments occurred naturally with long-term use of the setup. Images captured closer to the beginning of the 6 month collaboration were captured with a better calibrated microscope. At some point, it became difficult to tell if deficiencies in the data were due to optical aberrations, sub-optimal sample preparation or both.

There was varied imaging suitability for each tissue sample using the open-top method. The camera, housed inside the class 1 laser microscope box, released warm air into the box during imaging. This air had nowhere to escape to. Repeated heating and cooling is known to cause mechanical movements, particularly for metallic components. Additionally, the warm air was observed to dry out the samples. Sometimes, this caused the outer (upper) layer, not protected by the cover slip, to shrink around the centre of the sample. This caused morphological changes in the imaging planes and we were forced to reduce the FoV of image capture in many cases. For some samples, the warm air instead cause the entire sample to peel away from the cover slip surface and curl upwards. The original fear was that the laser beam itself was depositing enough energy into the sample to create this effect. However, "curling" of fresh and fixed kidney samples were noted even when the sample was mounted inside the closed microscope with the laser turned off. The kidney sample shown in figures 4.13a and 4.13b was physically sectioned using traditional slide-mounting methods with a tissue slice (10s of μms thick) to mitigate this effect.

Heart

We imaged both muscly left heart ventricle and fat-rich epicard tissue (both unfixed) using Gaussian OTLS. Acridine orange was used to stain all of heart samples shown here using the method described in section 3.4. Heart epicard fat had noticeable similarities to the beef adipose tissue Gaussian LS data (figure 3.13). AO did not attach to the interior of the

adipocytes, which appear as dark circular regions grouped closely together. The stain did however group around the edges of the adipocytes which resulted strong contributions to the signal (bright yellow-white regions in figure 4.3).

Figure 4.3 shows a side-view of the data set obtained from this sample. The region at the top of the image is dark because photons are strongly attenuated by the fatty tissue. The lower edge of the image is where the Gaussian LS is most in focus and the signal is strongest. The Gaussian beam was able to penetrate 3-4 layers of these epicardial cells although the nuclei were not individually resolvable below about 45μm under the sample surface (nuclei within this sample are shown in figure 4.4). This corresponds to the expected FoV (60μm) using the Gaussian light-sheet (see section 3.3.4).

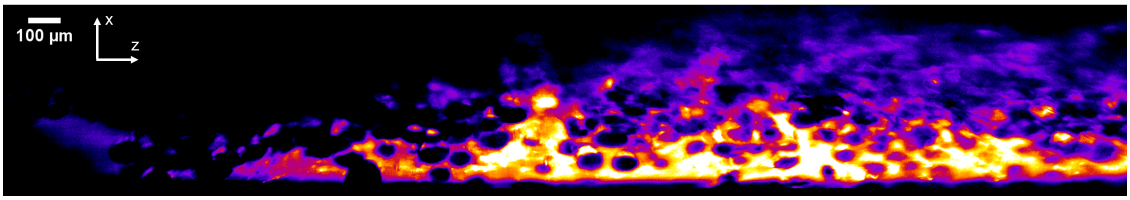

Figure 4.3 This is a side view of fresh heart epicard fat tissue which has been stained with AO and imaged with Gaussian OTLS microscopy. In this cross-section reveals several layers of fat cells. In this orientation, the Gaussian LS is propagating in the plane 45° to the plane of the page and 45° to the page normal. The predicted FoV of the Gaussian LS is 60μm in propagation distance and 42.4μm in depth below the tissue surface. This image is not well-resolved in the upper regions. The lack of contrast is likely due to a combination of low illumination intensity and inadequate staining. The scale bar is 100μm.

Figure 4.4 shows the same data set, this time visualised from planes parallel to the sample surface (along the plane of the imaging platform). Each (sheared) plane is horizontally displaced from the deeper and shallower planes due to the shape of the data set (see figure 3.8).

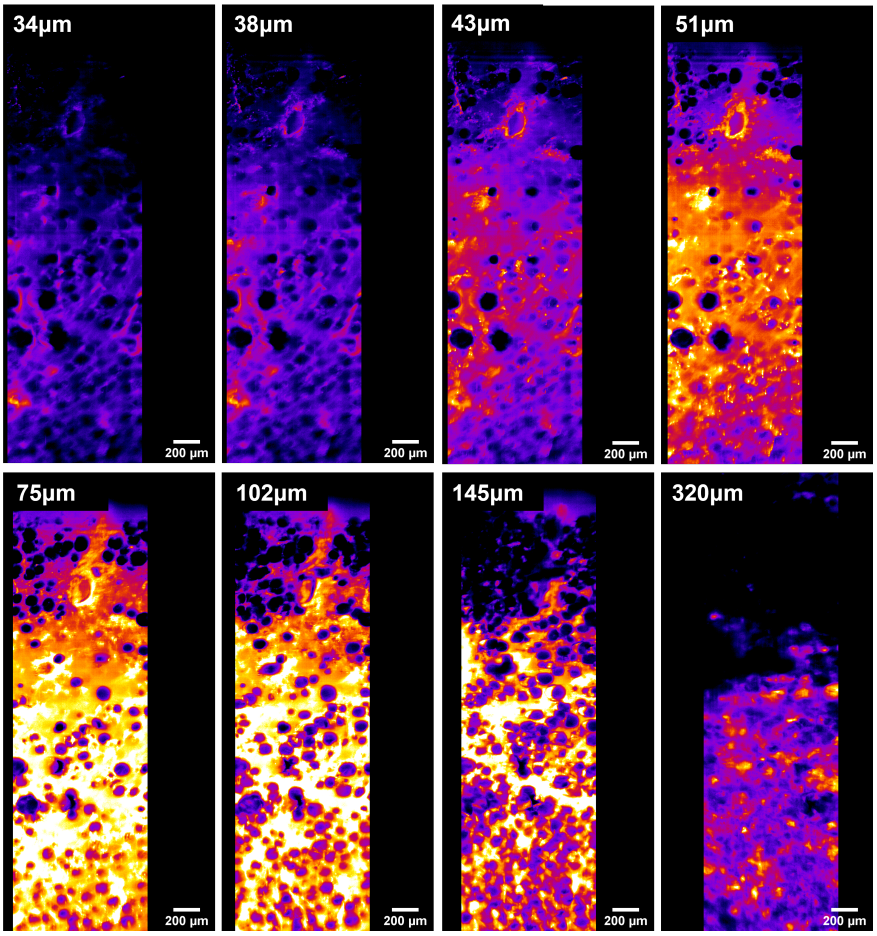

Figure 4.4 Heart epicard fat tissue stained with AO and imaged with a Gaussian beam. Data set is viewed in planes parallel to the sample surface. The tissue is shown at penetration depths between 34-320μm. Scale bars are 200μm. The PSF of the Gaussian LS beam is significantly broader by 320μm below the sample surface. Both contrast and resolution are reduced as an effect. The stain does not collect within the fat cells (darker circles). Individual nuclei are resolved near the surface. Figure 4.5 shows some nuclei from this sample in more detail.

Figure 4.5 shows a zoomed in section of this data at a depth of 37μm below the sample surface. Individual nuclei are clearly visible with Gaussian OTLS imaging. The nuclei are spheriodal so the cross-sections of their volumes shown here are roughly circular or elliptical. Clearly resolved nuclei is important as it adds diagnostic relevance. This data set shows us that OTLS in Gaussian mode has been successfully implemented for surface-level imaging of fresh heart epicard fat using acridine orange as a biological marker. However, resolution is insufficient and the complexity of the data is limited by monochromatic detection. Nuclei are

measured at 10.7±1.5μm across and we would expect them to have a radius of 6.5±1.8μm for this tissue type [234, 235]. A counter-stain tagging cytoplasmic structures through the same volume would be required for making confident deductions about the health of the tissue [123].

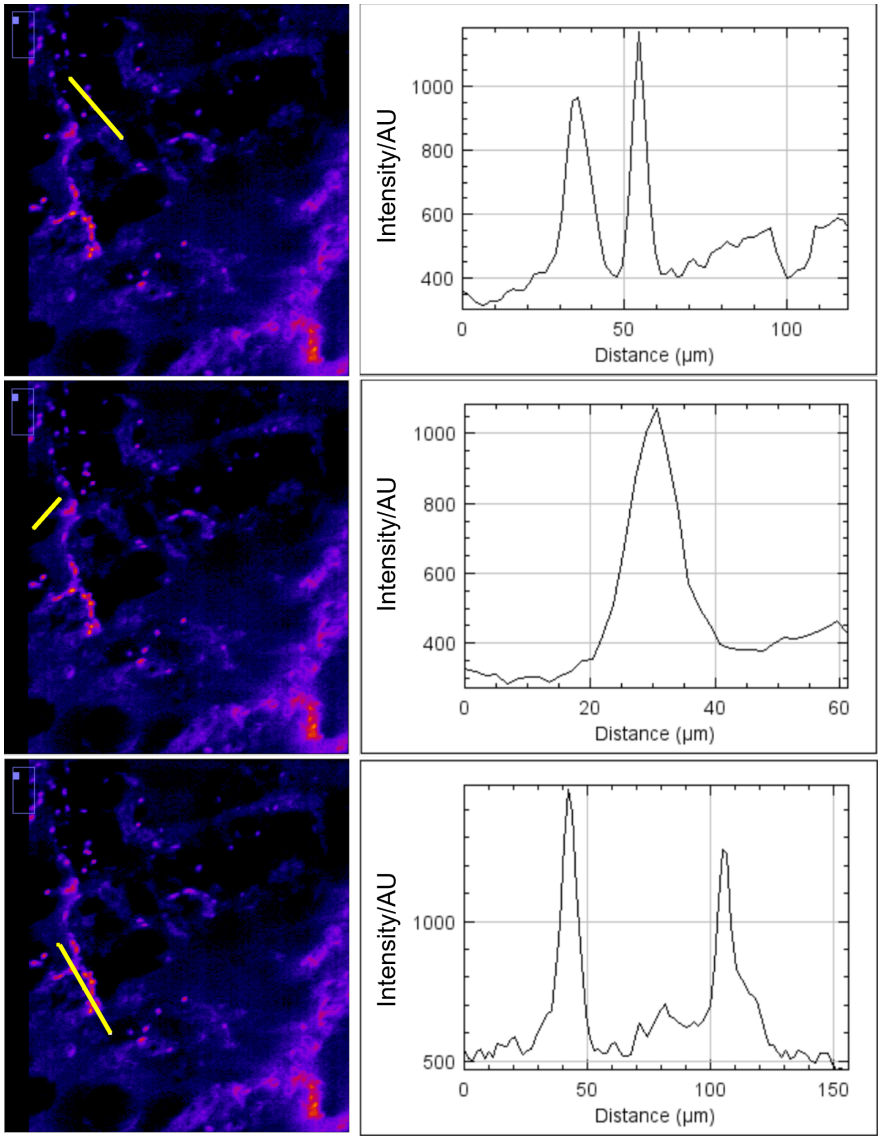

Figure 4.5 Individual nuclei stained with AO are imaged 37μm propagation distance into heart epicard fat tissue (close up of some frames in figure 4.4). The nuclei in this image are 10.7±1.5μm in diameter. This is larger than the average human heart cell nucleus size of 6.5±1.8μm [234, 235]. Discrepancy in the measured FWHM nucleus diameter could also come from sub-optimal staining, or perhaps from optical aberrations due to refractive index changes in the material between the cover slip (RI=1.51), possible air pockets (RI=1) and the sample itself (human adipose tissue estimated to have RI=1.47). The radius measurements here suggest that there is an issue with the sample preparation or the microscope setup or both.

The more muscular areas of the heart, for example tissue from the left ventricle, have structural similarities to the beef test tissues from section 3.5 (figures 3.12 and 3.14). Figure

4.6 shows a left heart ventricle sample, stained with AO and imaged with Gaussian OTLS. The muscle fibrils have absorbed a lot of the dye, however nuclei are not visible in this data set. The ventricle tissue was unfixed prior to imaging. Although fresh, some sample degradation may have occurred between Surgery and fresh tissue imaging in the Pathology department. Larger, whole, tissue samples take longer to undergo formalin fixation. As mentioned in table 3.1, slow fixation can cause the centre of such samples to degrade before tissue sections can be taken and imaged. The muscle fibres appear to be highly attenuating of the illumination. It may be that AO stain was not able to permeate through the thick tissue layers. 3D analysis of the data set reveals that the signal drops by 70.5% after after 60μm below the tissue surface across the whole FoV.

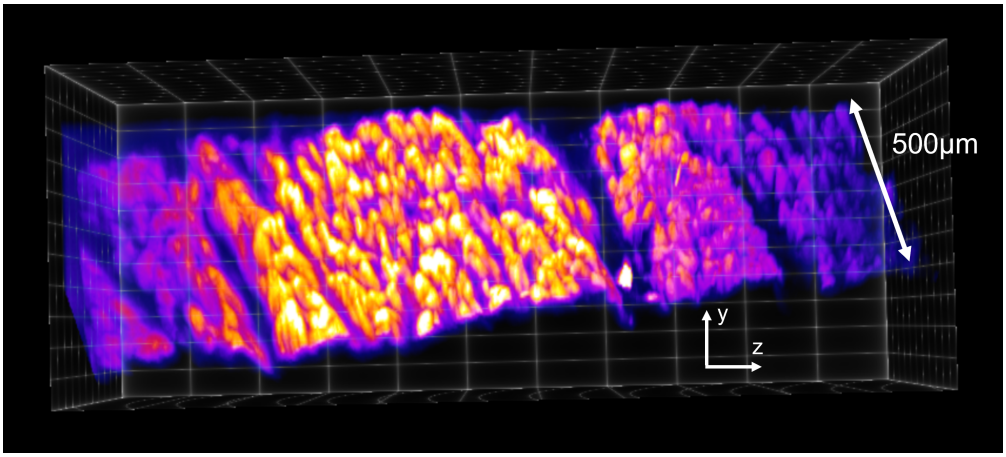

Figure 4.6 Unfixed (fresh) Heart left ventricle/human myocardium tissue. Frames are parallel to the sample surface (y z plane). Tissue is stained with AO and imaged on the OTLS (Gaussian mode). ClearVolume [163] was used to visualise the data set in three dimensions. The uppermost surface is the (bottom) surface of the tissue as it was mounted on the cover slip. The brightest area is also at the surface, where the beam is most focused and stain has penetrated the muscle fibrils. The surface topology is irregular, however across the entire FoV the signal drops by 70.5% after passing through 60μm of tissue.

Endometrium

Fixed endometrium tissue is rigid in structure. Our pre-established fresh colon staining protocol did not reveal nuclei in this tissue type. A test sample (figure 4.7) had a very

irregular surface with multiple pockets. These pockets filled with air during the mounting process, even when index-matching medium was used to fill the gap between the sample and the coverslip. The pockets also made it difficult to thoroughly rinse excess stain away from the surface. Figure 4.8 shows a diagram of such an air pocket which has not been properly rinsed. Acridine orange mixes with the index matching medium (more immersion oil in this case) and creates a fluorescent layer between the sample and the imaging device. Figure 4.7 shows a bright layer over the surface of the tissue with stain accumulated in small grooves across the top of the fixed endometrium tissue. Below the surface, signal quickly drops off. We noted that fixed samples seemed more resistant to uptake of the AO stain. They were also less flexible than fresh tissue samples in general, and this made uniform adhesion between the surface of the tissue and the glass cover slip much more challenging.

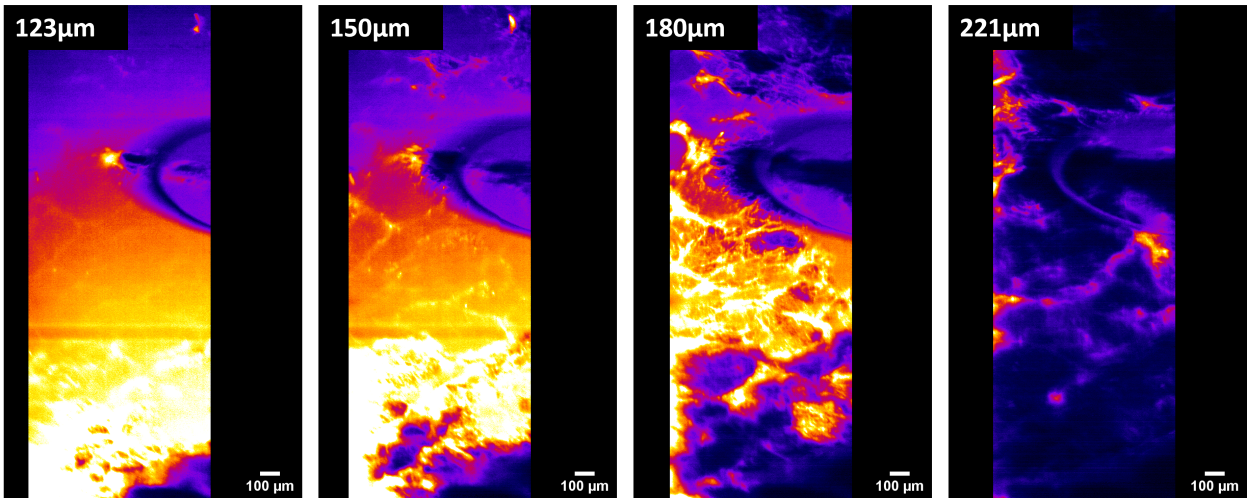

Figure 4.7 Endometrium tissue; fixed, stained with AO and captured in 3D using Gaussian mode OTLS. In this case, the depths at the top left indicate the distance between the cover slip and the plane of the image, which is parallel to the cover slip. A large air bubble at the top right can be tracked from the surface of the sample down to 221μm. No tissue structures are observed below the bubble. Features in this sample were not immediately recognisable to attending pathologists. Scale bars are 100μm.

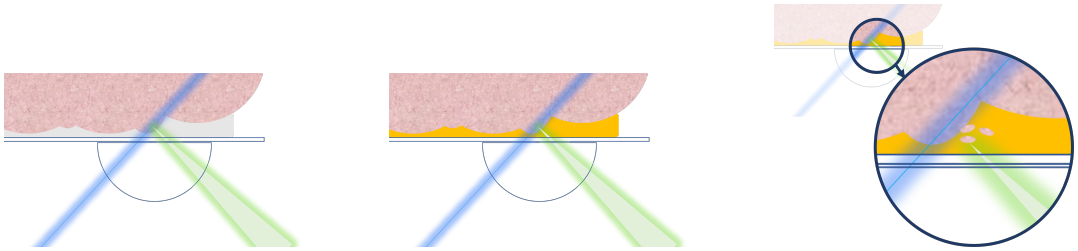

Figure 4.8 Index-matching liquid is used to fill the gap between an irregular sample surface and the planar cover slip. The blue line represents the light sheet (side-on) at 488nm. The green region represents fluroescence that is detected in the orthogonal imaging pathway. In the first image, clean index-matching medium fills the gap between the pink tissue sample and the planar glass cover slip. In the central image, pockets in the sample surface have not been rinsed properly; AO collected at the surface mixes with oil layer creating a fluorescent orange boundary. The image on the right shows how air bubbles or loose tissue can move around in the fluorescent liquid layer, further distorting the OTLS images.

Breast

Breast tissue presented more challenges to sample mounting. The tissue here was unfixed, although like the fixed endometrium sample discussed previously the surface texture was irregular and the breast tissue lacked flexibility. Adipose tissue has been noted to repel AO (A8097-10ML, Sigma Aldrich), a water-based stain. Figure 4.9 shows a series of planes inside an unfixed breast tissue sample. Each image is at a different depth below the surface of the sample (depth indicated in black boxes top left hand corner of each image). Nuclei are visible (indicating some selective staining has taken place), however the resolution is poor as was the case in the heart and endometrium examples. There were practical difficulties in mounting the breast samples onto the imaging platform due to irregular edges and large air gaps.

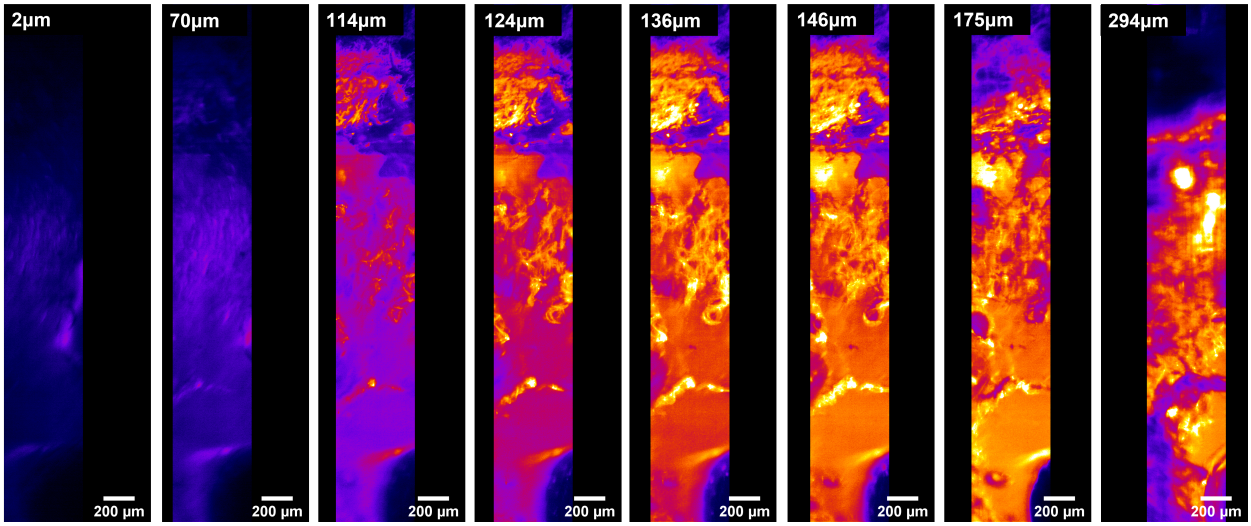

Figure 4.9 Fatty unfixed breast tissue, stained with acridine orange to reveal irregular surface structures using Gaussian OTLS. Each frame is in the Y-Z plane (see setup geometry shown in figure 3.8). Only a couple of nuclei are visible, and they are inadequately resolved. Scale bars read 200μm.

The quality (resolution, contrast) of the images in figures 4.9 and 4.10 is only sufficient to indicate that the sample preparation protocol and the OTLS alignment were sub-optimal during this data capture. The data is included here to contextualise improvements suggested in section 4.6.

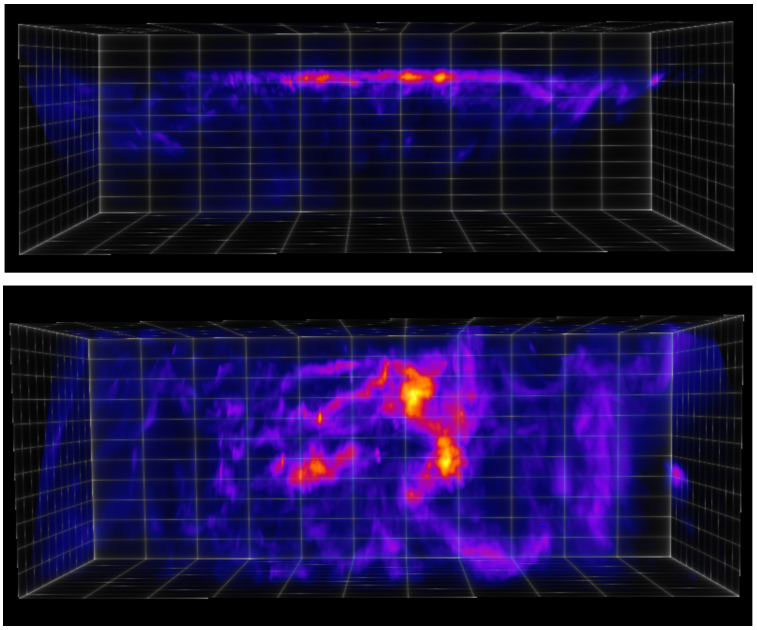

Figure 4.10 Fatty unfixed breast tissue stained with AO and imaged using Gaussian OTLS. The top image is in the X-Z plane and the bottom image is in the Y-Z plane (see figure 3.3). The data set is visualised using ClearVolume (an open-source FIJI plugin). Using this view, it is clear that only a small region at the top of the sample has produced a strong fluorescent signal. The tissue is naturally resistant to penetration by visible range photons entering the tissue. Similarly, any green photons produced by stimulated emission are likely to be blocked on their way to the detection pathway by absorption or scattering within the adipose tissue. It is also possible that the stain itself has not reached the interior of the volumetric tissue sample; this too would result in no fluorescent signal at depth. The top image is approximately 540μm across and 155μm between the bright plane (sample surface) and the base of the volume. The bottom image presents the same volume rotated to show the sample surface in the same plane as the page.

Stomach

Some fresh stomach tissue became available for imaging immediately after the OTLS had been aligned in the hospital lab, i.e. within 48 hours. Fresh healthy tissue is removed from patients undergoing sleeve gastrectomy for weight loss [236]. Healthy gastric mucosa is rich in nuclei, which are often clustered in rings when viewed as a 2D cross-section. Figure 4.11 shows four cross-sections of an unfixed stomach mucosa sample which has been stained with AO. The images show individually resolved nuclei in the surface layers were the tissue surface

is lying close to the cover slip. In the lower half of each frame shown in figure 4.11, all layers are displaced away from the focal range of the Gaussian LS due to a slight indent in the sample surface. The staining protocol (section 3.4) was initially developed for fresh colon samples. Gastric mucosa from the stomach is similar in composition [237]. The fresh mucosa tissue imaged here responded well to the stain, which selectively targeted nuclei and provided acceptable contrast in the OTLS images. The nuclei in the focus of the Gaussian LS are 8.4±1.1μm across. This is comparable to a diameter of 7.66±2.3μm quoted in literature [238].

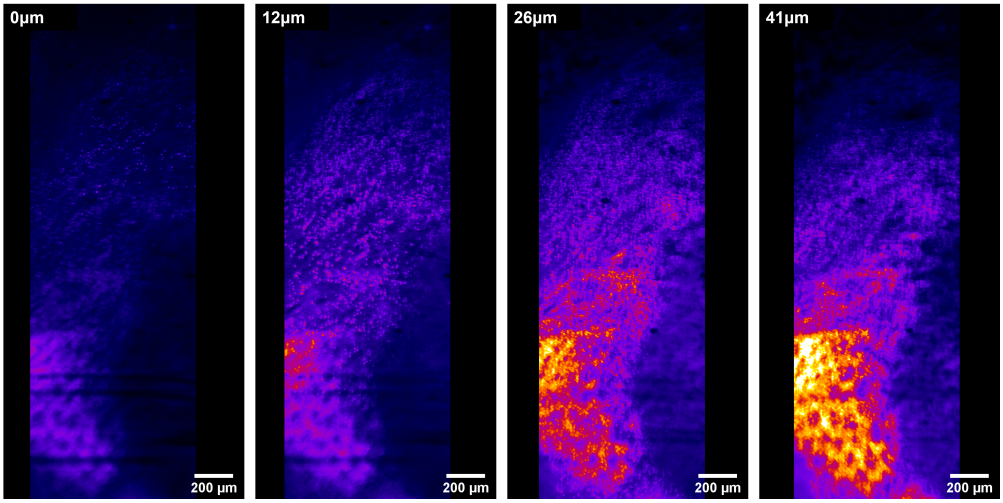

Figure 4.11 Unfixed stomach mucosa stained with nuclear dye acridine orange using a protocol developed for fresh colon tissue sections (described in section 3.4). Frames are all in the Y-Z plane. Nuclei at the sample surface lie in the focus of the (Gaussian) LS used to illuminate the sample. The nuclei have a cross-sectional diameter of 8.4±1.1μm in this plane. The resolution worsens at depth due to the expanding PSF of the propagating Gaussian LS. Uncleared stomach tissue is strongly attenuating to visible light. Nuclei are only resolved in the surface layers using Gaussian mode. Scale bars are 200μm.

Kidney

Kidney tissue is naturally firm when fresh and we noted that it did not adhere properly to the cover slip, as demonstrated in figure 4.12). These frames show the sample surface curving up and away from the cover slip throughout the FoV, with the lower half of the tissue sitting

higher above the cover slip than the upper half of the tissue in this orientation. As with the fixed endometrium, fresh heart muscle and fresh breast tissue shown here, the sample and or sample preparation were not well-suited to OTLS imaging. In addition, kidney tissue was particularly prone to dehydration. Sample morphology changed dramatically after only 10 minutes in the imaging enclosure, even with the laser turned off. Further studies are required in each case to fine-tune the staining protocol and to engineer ways to attach each tissue type more uniformly to the glass cover slip.

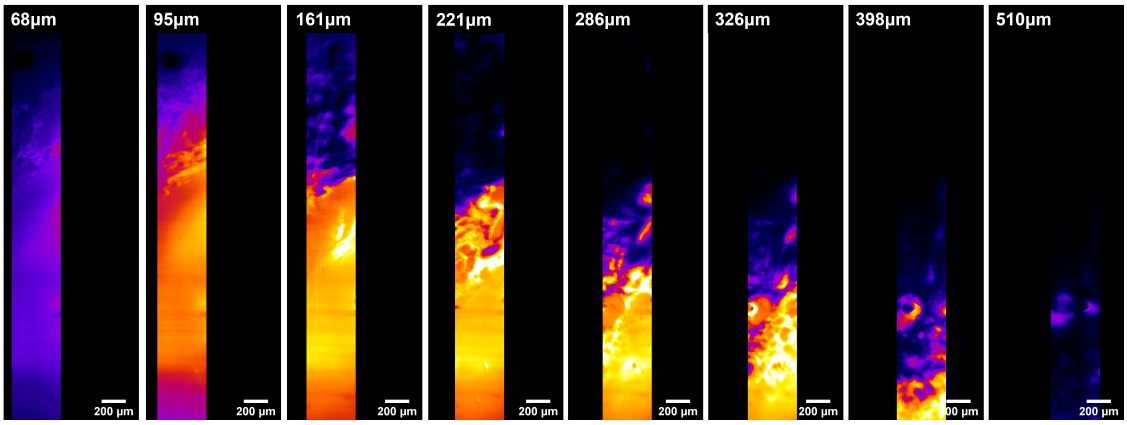

Figure 4.12 Kidney tissue (unfixed). Each frame is in the Y-Z frame. Kidney tissue is naturally firm and therefore unlikely to adhere to the OTLS imaging platform over a wide FoV. In this example there is a notable curvature across the sample surface, with the lower half of the tissue in each frame sitting higher above the cover slip than the upper half, resulting in a poorly resolved tissue surface in some areas. This data set was captured using Gaussian mode. Airy mode OTLS may help to mitigate this issue. Scale bars are 200μm.

During the collaboration, local pathologists experimented with their own, more familiar, tissue processing methods. The aim was to isolate staining imperfections from signal reduction and other aberrations caused by system misalignment. Traditional sample preparation allowed a wider field of view to be imaged compared to unsectioned volumetric kidney samples which naturally peeled away from the cover slip surface. A thicker section of kidney was cut away from a fresh volume and stained with hematoxylin and eosin. The tissue was trapped between the sample platform and a second glass slide, which acted to weigh down the tissue uniformly. Eosin can be excited by one photon excitation under blue illumination

[239], however hematoxylin was not expected to fluoresce at this wavelength. We therefore expect the resultant images to contain a 3D map of the cytoplasm in the tissue rather than the nuclei in this case. Figure 4.13 shows a fixed section of kidney tissue stained with H&E and imaged using Gaussian OTLS. It was noted at the time of these experiments that an additional piece of glass over thin samples appeared to cause some reflection of the LS. This was evident as bright streaks through the data set and increased blurring of fine features.

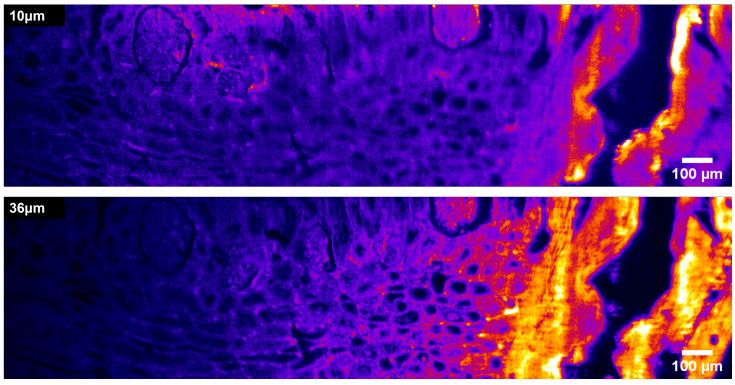

(a) Fixed kidney tissue section, H&E stained

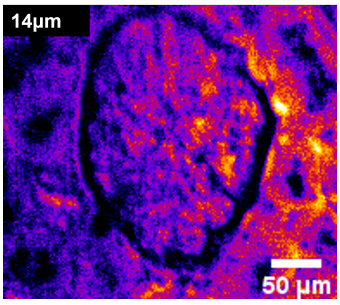

(b) A glomerulus

Figure 4.13 Kidney tissue; formalin fixed stained with hematoxylin and eosin using industry standard methods. Eosin Y (which selectively stains cytoplasm) fluoresces in the green region under blue Gaussian LS illumination. The tissue section was cut thickly to allow some shallow 3D analysis of OTLS imaging in Gaussian mode for this sample. Two glomeruli are visible. In subfigure 4.13b we see an expanded image of the glomerulus on the left of the image. The 3D structures can be followed through consecutive layers of this data set. This image was taken by Dr Joseph Albanese, who also prepared the sample. All frames are in the Y-Z plane.

4.5.2 Tissue Imaging Summary

This trial demonstrated that there is no "one-size-fits-all" approach for fresh tissue OTLS imaging. Each new sample type comes with its own textural and structural properties. It is necessary to spend time with each tissue type separately to develop an appropriate staining protocol. Fixed tissues reacted differently to acridine orange compared to fresh or fresh flash-frozen samples of the same type.

The way that tissues lie on the imaging platform is key. Curved or irregular samples

dramatically reduce the usable FoV in the plane of the sample surface. Due to our previous staining experience, we primarily used acridine orange as a nuclear stain for this study and in most cases we did not use a counter-stain to selectively view cytoplasm or other cytological features. The exception to this is the sample shown in figure 4.13 which was stained with hematoxlyin and eosin. In many samples, AO, which was intended to target nuclei, revealed no resolvable nuclei in Gaussian OTLS images. Further studies are required to understand exactly which elements were the cause of this in each case.

Some tissues were fresh (flash-frozen and defrosted or direct from surgery and not preserved in any way). Others were formalin-fixed prior to staining. This was due to tissue availability at the time of the study. Fixed tissues tended to be more stiff and as a result did not adhere well to the cover slip. This lead to reduced imaging area and surface images that were only partially in focus (see figures 4.7 and 4.12). Fixed tissues were generally less compatible with our existing AO staining protocol. In theses cases, AO was less selective and did not penetrate as deeply into the tissue in general. Kidney tissue tended to be more firm even before fixation and could not be attached properly to the cover slip (figure 4.12), except when physically sectioned with traditional methods and clamped to the platform using a glass slip on top (figure 4.13b).

The long-distance nature of this collaboration presented challenges. Without the means to re-align the setup at regular intervals, image quality degraded over a period of several weeks to the point where it was not possible to tell if image defects were from misaligned optics or from sub-optimal tissue processing. It is expected that future studies with well-established tissue processing procedures will benefit from the resolution enhancement and FoV increase afforded by Airy beam shaping and DL post-processing, as demonstrated in chapter 3.

4.6 OTLS redevelopment based on end-user feedback

The collaboration with the Albert Einstein Institute provided valuable insights into what the pathology community would like to see from this kind of technology. Their feedback clustered around four main points[1]:

- Spatial resolution
- Single vs two-colour imaging
- Sample preservation for longer term fresh tissue measurements
- User-friendliness

4.6.1 Spatial resolution

In practice, the spatial resolution of the images captured during this collaboration was worsened by improperly stained tissues causing a reduction in contrast and optical misalignment after continued use of the setup. Therefore the data can not be considered to represent optimal system performance. However, we now have an improved understanding of what the medical community requires from diagnostic images. We also gained understanding of how an optical system such as this one may fit into the workflow practically speaking. The work presented in chapter 3 and the stomach tissue sample in figure 4.11 demonstrated that when the system is well-aligned and the staining protocol is optimised, both Gaussian and Airy OTLS can achieve sub-cellular resolution in the axial direction. Nuclei are resolved in 3D within the surface layers of uncleared, fresh tissue. An axial resolution of around 2μm is required to resolve the shapes of individual nuclei in human tissue. This scoping exercise demonstrated the importance of staining and optical engineering working harmoniously to

[1]The subject of using artificial intelligence to interpret digital pathology images was raised. Whilst this is outside the remit of this thesis, it is thought that machine learning could be a helpful, accessible tool to aid pathologists world-wide.

achieve sufficient contrast and resolution in the images. Without correct staining, the OTLS cannot be used to resolve nuclei in these tissue types. The *optimised* performance of the OTLS in a working pathology lab has not yet been demonstrated. Future studies of this kind may benefit from having experts in both pathology and light-sheet *in situ* with the setup during trials.

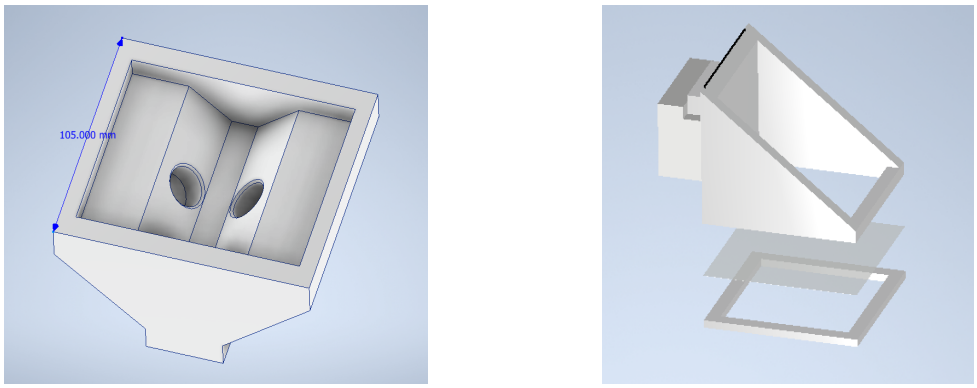

(a) Immersion chamber **(b)** Sample mount

Figure 4.14 4.14a Immersion chamber, measurement reads 105mm. The chamber is made from aluminium and can be filled with various immersion media [174]. The openings are precisely matched to identical immersion objectives, which are angled towards the sample surface plane as with the previous OTLS design (see figure 3.1). Once they are mounted, here is enough clearance above the top of the immersion objectives for the sample platform (4.14b) to be suspended and scanned laterally without impact. The design places the focal point of the objectives just above the clear fluorinated ethylene propylene (FEP) plastic sample mount. The FEP layer is trapped in place by magnets around the edge. FEP is selected for its biological compatibility and refractive index matching with water as an immersion medium (RI=1.33). The entire sample mount lifts out of the magnetic mounting system shown in parts in figure 4.14b. In an updated version, there is an opaque flap that goes over the angled section over the sample to protect the sample from the external environment during imaging.

This compact system design suffers from astigmatism aberrations due to small refractive index changes through the angled beam pathways below the imaging platform. This could be mitigated with the addition of a second cylindrical lens in the detection path as done so here [56]. In the next design iteration of the Airy OTLS for histopathology I have opted for dual multi-immersion objectives (54-10-12 FL 13.8mm, 4× NA 0.367, Special Optics,

Navitar) housed in a custom-built aluminium immersion bath. This is similar to the designs described here [174, 240]. Table 4.1 describes how the change in illumination and detection optics would alter the system parameters. My designs for a dual immersion objective chamber with sample scanning platform are shown in figure 4.14.

4.6.2 Two-colour imaging

Current gold-standard histopathological diagnosis is essentially pattern recognition. In section 3.2 I described how hematoxylin and eosin are typically used to selectively stain features in tissue sections (nuclei and cytoplasm respectively). From these two overlaid layers of information imaged simultaneously using brightfield microscopy, pathologists are able to pick out sub-cellular features which indicate healthy or diseased tissue with some margin of error. Our prototype light-sheet microscope is capable of revealing the first "layer", or monochromatic nucleic information[2] using AO as a selective fluorescent stain. To approach images which are interchangeable with the H&E bright-field variety, a counter-stain must be added. To engineer images with equivalent biological meaning, the stains used for LSFM must closely approximate the selectivity expected from hematoxylin and eosin.

In version 3, I propose the addition of a second laser (central wavelength 532nm) and fibre coupling for both lasers into the system. The new system is designed to sequentially image nuclei (stained with AO, excited by 488nm laser) and then cytoplasm (stained with eosin Y, excited with 532nm laser). Figure 4.15 shows the excitation and emission spectra of AO and eosin Y. These stains were selected because of prior success using them for selective tissue staining with fluorescence microscopy [53, 54, 134, 202, 241][3].

[2] Along with some other features which were not the intended target.

[3] Despite some successful studies, eosin stain has been noted to "leak" in unfixed and hydrated tissue [130], meaning that feature selectivity is not always optimal.

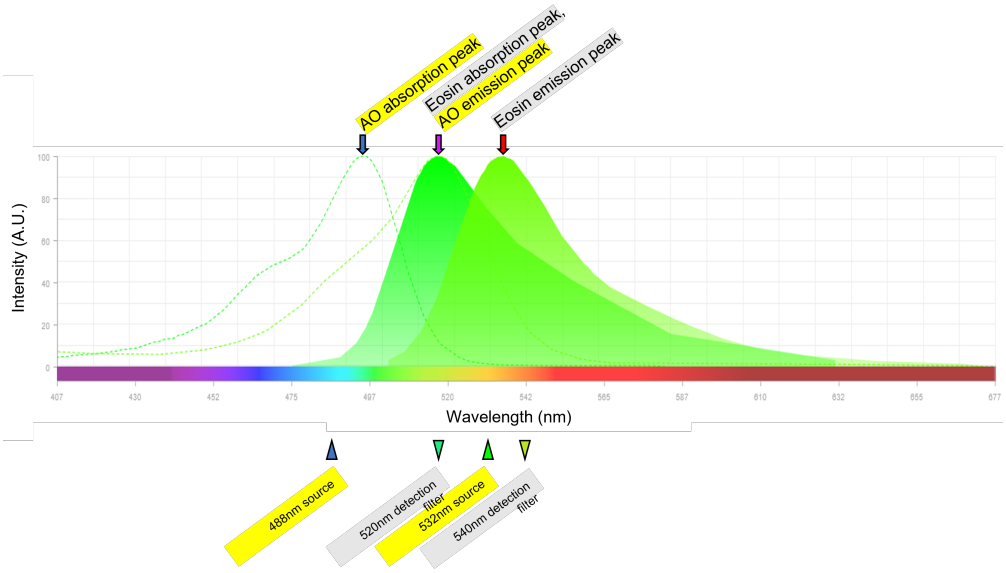

Figure 4.15 Absorption and emission spectra of acridine orange (a nuclear stain) and eosin Y (a cytoplasmic stain). There is overlap between the 532nm source and the emission spectrum of acridine orange. For this reason, the two layers of data should be imaged separately so that the detected AO fluorescent signal is not masked. A false colour map may be applied to each layer of data to make them more distinguishable to the human eye. Sequential imaging means that the same camera can be used each time. The detection filters should be switched in between imaging nuclei (488nm notch filter, 520±20nm band-pass filter) and cytoplasm (532nm notch filter, 550±10nm). This figure was adapted from from ThermoFisher's SpectraViewer [242].

More colour imaging options

Alternative staining combinations were also considered. If there is no overlap between laser source spectra and fluorescence emission spectra, it may be appropriate to use multi-coloured detection. There are three ways that this could have been implemented into the OTLS without the need to sequentially image each colour channel.

1. Use a colour camera

2. Use two monochromatic cameras and split detection pathway with a dichroic mirror

3. Split detection pathway using a dichroic mirror and allocate half of the pixel array inside the same camera to each colour channel

Colour cameras are readily available and relatively cheap [243, 244]. This option is the most light-weight of the three and it is the most economical on system footprint as the filtration is in-built into the detector array. However, the colour cameras that we investigated were all reliant on Bayer filter to segment red, green and blue colour channels. Bayer-filtered camera pixels carry an automatic increase in axial resolution as the nearest pixel correlating to information from the same wavelength is two pixels up or sideways for red and blue or one pixel position diagonally for the green channel. Thus, these colour cameras do not provide the necessary spatial resolution to resolve 2μm nuclei without reducing the FoV by 2-3$\times$ compared to the equivalent monochromatic sensor option[4].

It is possible to place a dichroic mirror in the detection pathway and channel separate colours towards separate detector arrays. This is the most expensive option, as two high quality monochromatic sCMOS cameras would be required for our OTLS for histopathology setup [243, 244]. This option offers the best spatial and spectral resolution with the widest FoV. However, the footprint of the setup would be increased by around 14$\times$45cm plus the additional camera [243, 244].

Lastly, we explored single camera dual-channel colour imaging options from Teledyne Photometrics and Hamamatsu (Optosplit II and W-View Gemini respectively). These products split the image in two by wavelength. Each filtered image of the same FoV is relayed to occupy half of the camera pixel-array. This option has some increase in weight and footprint, but less so than option 2. The FoV is reduced for a particular pixel array size, as with option 1. The Optosplit II has the option to adapt the signal levels from each half of the array independently so that the signal levels from each colour can be matched. Options 2 and 3

[4]A higher magnification objective would be required to make the pixel-limited resolution comparable. A higher magnification objective would have a higher NA, meaning that the optical resolution of the detection arm would also change.

become incrementally more complicated, expensive and bulky for each colour channel that is required. The beam-splitters mentioned here are for two-colour imaging.

Note that figure 4.13a does not count as a two colour image despite the presence of a counter stain. We did not expect to see any emission from the hematoxylin stain as the absorption peak was not matched to our illumination wavelength. Other research projects have used AI to retrospectively apply a contrasting colour to some features for single-sweep two colour imaging [245, 246].

Options 1, 2 and 3 all address the issues that come with sequential colour channel imaging. Imaging the same area twice can lead to the sample quality being reduced during the second colour acquisition, particularly for fresh tissue imaging. Samples can dehydrate over time. This can cause morphological changes, which would lead to the two colour maps being spatially mismatched in the final overlayed image. Fresh sample preservation could be prolonged by cooling and reducing air currents inside the OTLS enclosure.

4.6.3 Sample and system preservation

The interlocked laser safety enclosure built for off-campus collaborations is an essential safety feature of the OTLS. However, the downside of a fully-enclosed microscope is that warm elements (the camera, for example) heat the air around the sample and the optical instruments. Changes in temperature can misalign optics, which in turn means that full system re-alignments are required more often. This made the prototype OTLS impractical for long-term collaborations across continents as it was practically impossible to do routine maintenance on the optics without a highly trained optics engineer on-site.

Warm air also has the unfortunate effect of dehydrating delicate tissue samples. Both fresh and fixed tissues of all varieties dried out in the warm environment of the microscope enclosure. In some cases, the outer sample layer (not touching the glass surface) became hard and the entire sample would begin to curl upwards in the heat. We attempted to mitigate

this effect using damp pieces of gauze to cover the samples on the platform during scanning. This appeared to help.

To address both of these issues, the new design has the detection camera and laser heads mounted outside of the box. Figure 4.16 shows a schematic diagram how the optical components are separated. Water cooling can be added to the Hamamatsu camera. By positioning the camera outside of the laser safety enclosure, air can circulate around it freely without travelling past other optical components or the sample platform. The new design has two fibre-coupled lasers. It is expected that commercially available fibre collimators will improve the long-term resilience of the setup. Vortran Stradus offer fibre coupling elements for their blue and green solid state lasers. The collimators can be adapted to produce a particular output beam diameter, removing the need for 2 Keplerian expansion telescopes from the illumination pathway design. The fibre-couplers are designed to be very stable over time. By reducing the number of free-space optics, we reduce the number of opportunities for mechanical changes in the optics to interfere with the image quality.

4.6.4 User-friendliness

The prototype system can be adapted to be more "turn-key" for end users. Switching the SIL for a multi-immersion chamber eliminates the need to clean the sample platform and lens in between each sample (figure 4.14). Switching between Gaussian and Airy mode is made easier with a binary sliding shutter (see figure 4.16). The entire system has been engineered to have more stability with integrated beam expansion and reduction systems and fibre-coupled illumination sources.

The image processing software, like the microscope, was still in its embryonic stages when the pathologists got to grips with it. A more turn-key image-processing system is recommended for future iterations, along with a higher capacity machine which can process and store larger quantities of information. Such a machine is described in [174] along with

their processing procedures. This could be adapted to include an Airy deconvolution step and GAN post-processing as described in chapter 3 [58] for improved resolution at depth even when the image resolution is limited by pixel-size.

Discussions with the pathologists at Albert Einstein and with our partners in industry, M^2 Life, lead to my proposed new design for the OTLS for histopathology. This section gives an overview of the suggested new setup.

4.6.5 Proposed OTLS for future studies (version 3)

I combined all of this feedback to amend our previous OTLS design. The design laid out here has never been built and tested - it is included should it be useful for future studies. Given the improvement demonstrated with Airy beam imaging (see chapter 3), it may be more sensible to forgo the the possible Gaussian pathway and simply opt for constant Airy mode. This would require all images from the system to undergo deconvolution. Figure 4.16 shows an annotated schematic diagram of the proposed setup for future work. Table 4.1 describes key system parameters at key locations (labelled via letters in figure 4.16). For the Gaussian beam with the adjustable iris at c at its widest; we have a light-sheet thickness of 2.7μm (blue) and 3.0μm (green) with Gaussian LS FoV of 47μm and 53μm respectively using equations 2.14 and 2.10. The Airy beam is not shuttered at c, therefore the full phase pattern is included to give α=5 across the incident beam cross-section. The minimum Airy FoV using α=5 is estimated to be 112μm (blue) and 114μm (green) using beam propagation simulations.

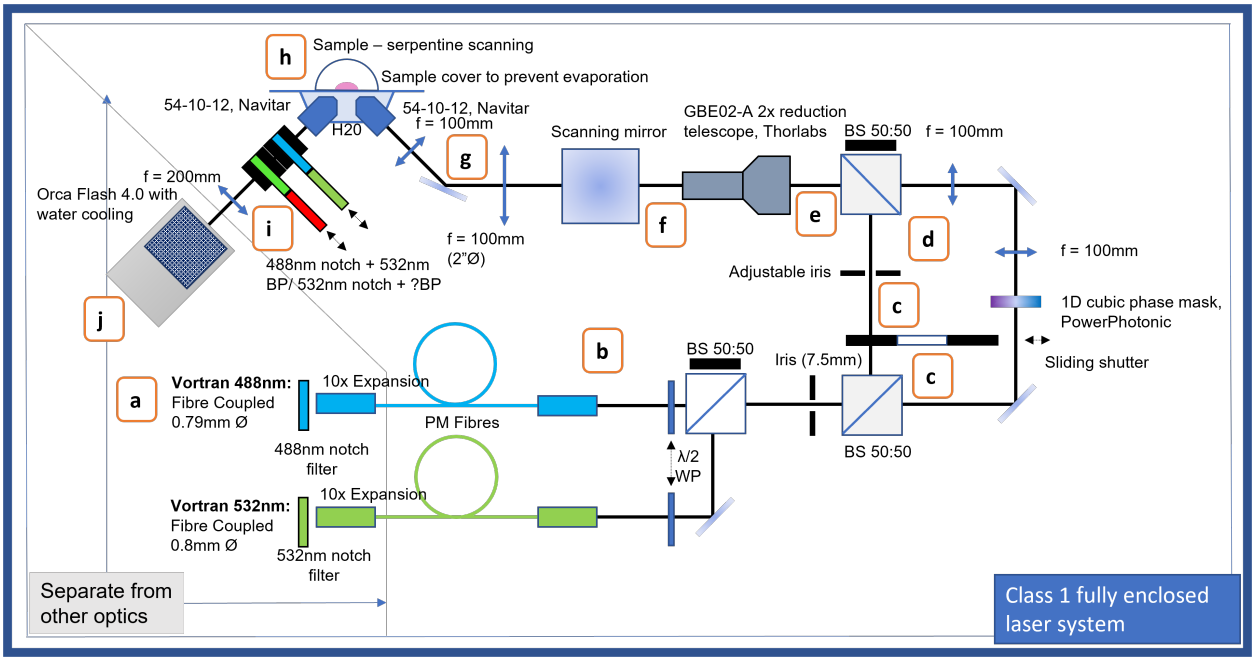

Figure 4.16 Proposed new OTLS for histopathology studies schematic diagram. Adjustments based on end-user feedback gathered during collaboration with the Albert Einstein Institute. System parameters at key locations (labelled with letters) are linked to descriptions in table 4.1.

Location	**Useful information**
a	Two alternative fibre-coupled Vortran Stradus lasers are fibre-coupled into the OTLS (488nm and 532nm). Initial beam diameter is 0.8mm in both cases. Notch filters are used to clean up and narrow each laser line to within ±10nm
b	10x magnification from fibre collimator. Beam diameter is now 8mm for each beam path. PM fibre used. $\frac{\lambda}{2}$ waveplates in rotation mounts
c	75% of average power from both beams now lost due to beam splitters (not including any losses from fibre coupling). The beam diameter is clipped to 7.5mm
d	For Airy beam, there is now a 1D cubic phase shift imparted onto cross section. 1× relay telescope to adjust focal point in sample to match focus of Gaussian beam. Meanwhile, in Gaussian pathway there is an adjustable iris to change the NA and resolution as required. At maximal width, we have a diameter of 7.5mm
e	Gaussian and Airy beams recombined in space, but separated in time by automated sliding shutter (at c) which only allows one pathway at a time. A further 50% loss of power due to third beam splitter
f	Beam diameter reduced 2× by backwards beam expander to 3.75mm. This falls within 5mm maximum set by Thorlabs scanning mirror diameter
g	Fourier plane of light sheet halfway through final 1× relay telescope before illumination objective. FP lies on mirror for handy alignment in the imaging plane
h	NA = 0.09 (underfilled back aperture of NA=0.367 objective, assuming RI=1.33 inside sample). This corresponds to the shortest Gaussian Rayleigh range, and the smallest focus possible. Light-sheet width set with scanning mirror
i	Detection arm magnification: $4\times\frac{200mm}{200mm}$=4×. Filter options for each detection band. May add zoom lens here in future – leave some space in box
j	Pixel projection = 1.6μm in sample (no zoom lens). FOV in camera: 3.3×3.3mm. Pixel-limited lateral resolution: 3.2μm. Optical resolution: $\frac{520}{2\times0.367}$ or $\frac{545}{2\times0.367}$=708nm or 742nm depending on fluorescence detection band (from equation 2.14)

Table 4.1 Proposed redevelopment of OTLS for histopathology - parameters and information from key positions in optical path (shown in figure 4.16).

4.7 Discussion

The scoping exercise revealed several practical difficulties. Fresh and fixed tissues could be imaged for diagnostic applications, however the development of such a system should be carried out alongside careful optimisation of the sample preparation protocol for each tissue type. In the future, LSFM may provide relevant data quickly enough to enable intraoperative assessment. A key advantage of one photon LSFM (especially with Airy beam shaping) is that it is a highly efficient *volumetric* imaging technique. We must consider that most human tissues are highly attenuating to visible wavelengths. In many cases, volumetric fresh tissue imaging may only be applied to the first 90μm of tissue closest to each surface (as detailed in chapter 3). This may not provide any more diagnostically relevant information than can already be provided by so-called 2D surface imaging techniques (for example MUSE). LSFM systems are expensive to build and the design trialled in this chapter was prone to misalignment. After several weeks without a complete alignment overhaul, data quality began to suffer. This is an important consideration.

4.8 Conclusion

Our collaborators at the Albert Einstein Institute gathered a wide variety of images from fresh and fixed human heart, lung, endometrium, kidney, stomach and breast tissue. Out of these, the fresh stomach tissue was most similar to the flash-frozen defrosted fresh colon samples that had been pre-trialled with the OTLS in St Andrews. The established staining protocol revealed characteristic distributions of nuclei clustered in rings, which was expected in this healthy stomach tissue removed from a patient during a sleeve gastrectomy procedure for weight loss. Epicard fat cells and individual nuclei were resolved in images of a fresh sample of human heart epicard fat, also stained in Acridine Orange dye using the same staining protocol.

We established that the firmer tissue samples (with worse adhesion to the cover slip on the OTLS sample stage) did not image well using this method. However, it is expected that a fine-tuned sample mounting procedure with an index-matching liquid layer combined with beam shaping could increase the imageability of firm tissue samples too.

I have presented a revised version of the OTLS to improve the usability, stability and versatility (by incorporating optional two-colour imaging) of the compact open-top light-sheet fluorescence microscope used during this pre-clinical use scoping exercise.

For LSFM systems to be truly helpful in a healthcare environment, they must be "turn-key" and highly stable over time so that attending pathologists can rely on their output. The data that they provide should be directly comparable to H&E slide-based data sets which are the basis of most professional pathology training. The newly designed OTLS microscope may assist this effort. It may be that biomedical research rather than healthcare is the most relevant field for LSFM technology as continues to mature. In chapter 5, I will investigate if this outlook changes when we consider alternative LSFM methods. Specifically, I look at how we might use illumination in NIR region for MPE coupled with alternative beam shaping and fibre-optic based design.

Chapter Five

Multi-photon light-sheet microscopy with Bessel beam shaping

5.1 Introduction

Thus far, I have discussed how Airy beams may be used to extend the FoV of LSFM using one photon excitation (see section 3.6). In this chapter, I will explain why Airy beams do not work well for LSFM with multi-photon excitation (MPE). I'll demonstrate that Bessel beams are a suitable alternative shape for MPE sources and consider how Bessel-like beam shapes could be implemented into the illumination pathway of a MPE LSFM setup.

5.1.1 Why would we want to use multi-photon excitation for biological samples?

Here is a summary:

1. There is increased penetration depth of NIR illumination photons into human tissue compared to visible wavelengths (see section 2.3.3) [247, 248]. NIR illumination can also be used for non-linear microscopy (NLM) of autofluorescent features in tissue for a variety of biomedical imaging applications [249–254]. Label-free imaging (enabled by

MPE of auto-fluorescent samples) is appealing for *in vivo* applications.

2. There is increased optical sectioning ability using MPE due to smaller fluorescent cross sections (σ_{MPE}) of fluorophores compared to OPE (σ_{OPE}) [255, 256] (see sections 2.3.4 and 2.3.5). Fluorescence is only generated where illumination is sufficiently focused. Figure 5.1 compares the 2PE case to the OPE case, where fluorescence is generated inside a greater volume around the beam focus [1]. This reduces the risk of photobleaching in out-of-focus areas when MPE is used compared to OPE.

3. Fluorescent photons generated by NIR MPE are emitted in the visible range ∴ diffraction limited optical resolution of fluorescence detection is comparable to the diffraction-limited resolution obtained using visible CW illumination for OPE (see equation 2.14).

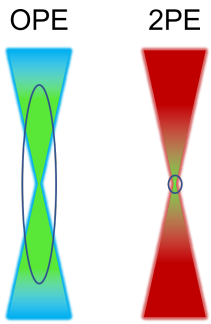

Figure 5.1 In the first example, one photon excitation generates green fluorescence throughout the blue Gaussian illumination beam shape. There is limited optical sectioning ability in the axial direction. If we instead use NIR illumination with roughly twice the wavelength of the OPE case, we again generate green fluorescence but this time only within a small spheroid at the beam focus where the intensity of illumination photons is the highest. This is two photon excitation (2PE). The 2PE sectioning is more confined in all three dimensions. More details can be found in section 2.3.5. If we inspected the equivalent 3PE case, we would find an even smaller spheroid of fluorescence at the focus. Adapted from [256].

[1] There is a small catch. Whilst the fluorescence generated by MPE is more confined in 3D, we must remember that the shape of the illumination beam is altered by using longer wavelengths. For the same NA, a NIR illumination beam will have a wider focus than for a visible beam (see section 2.3.7). This is due to diffraction (see equation 2.14)

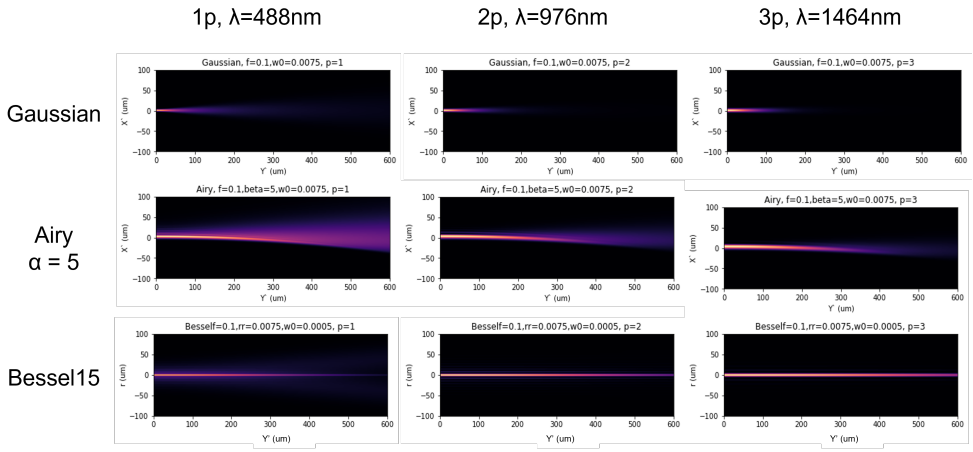

Figure 5.2 Intensity profiles for a Gaussian, Airy (α=5) and Bessel15 beam. The "15" here describes the ratio between the annulus aperture width and the annulus diameter for a Bessel beam produced using an annulus and focusing lens system (described in section 2.6.2). Each simulation assumes a uniform propagation medium of RI=1, an incident beam 7.5mm in diameter and a focusing optic with f=100mm (all three beams have the same numerical aperture). The Y' axis in each subplot is the propagation distance in μm with divisions of 100μm where the beam focus is at 0μm. The X' axes are in units of μm with 50μm divisions. The use of propagation-invariant beam shapes can dramatically extend the usable FoV of an illumination beam for fluorescence microscopy. The first column considers OPE. The middle column contains simulated intensity profiles for 2PE and the third column on the right hand side contains simulated 3PE intensity profiles. The optical sectioning is improved when we use higher order fluorescence intensity profiles (for the reasons described in section 5.1). However, the beam shape is also changed with longer wavelength illumination due to the diffraction limit. For example, the FWHM (dependent on illumination wavelength and the order of fluorescence response) of the Gaussian beam cross section measured at Y'=0 is 2.94μm for OPE, 3.30μm for 2PE and 3.82μm for 3PE.

5.2 Why Bessel beams for multi-photon LSFM?

In chapter 2, I introduced both Airy and Bessel beams as alternatives to the more traditional Gaussian beam that is normally used in LSFM. Chapter 3 explored the use of the Airy beam for one photon LSFM, and we found that it provided enhanced resolution over an extended field of view due to its propagation-invariance and self-healing properties. Simulations (see figures 5.2 and 5.3) corroborate the claim that propagation-invariant Airy beams have a more consistent PSF at depth compared to a Gaussian beam (with an identical numerical

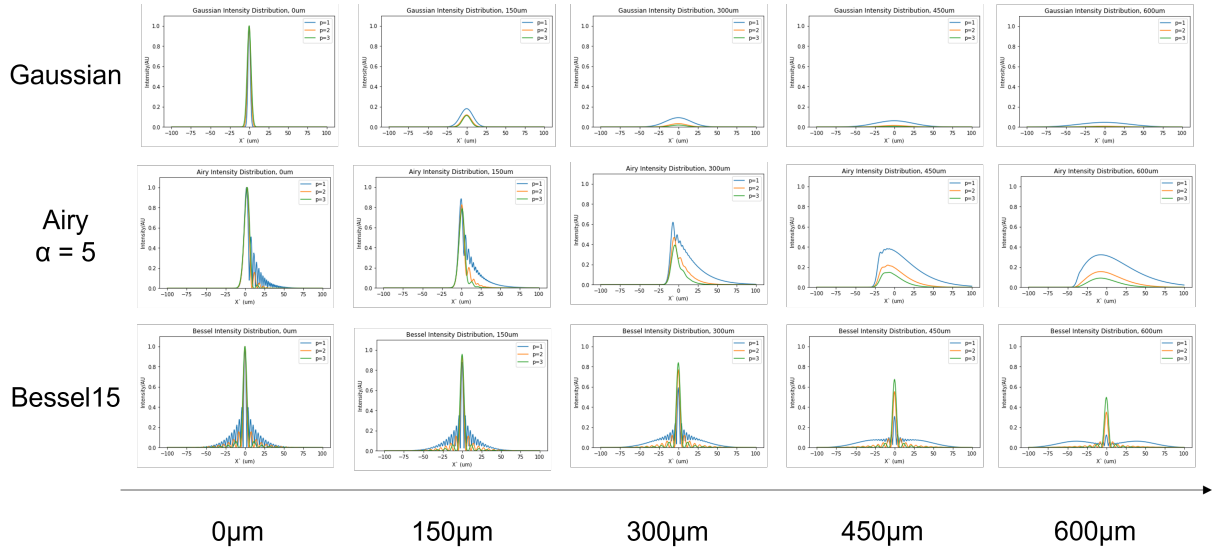

Figure 5.3 Intensity profiles taken from Y' slices of the data shown in figure 5.2. In each plot, the y axis is the normalised intensity in arbitrary units (AU). The x axis in each plot is position through the LS thickness (along X' in figure 3.3) from -100 μm to 100 μm. The orders of fluorescence are represented with blue (OPE), orange (2PE) and green (3PE). As predicted, the Airy beam maintains a large peak intensity at depth compared to the Gaussian case (7× greater maximum intensity for OPE at Y'=600μm). The encoded spatial information from fluorescence images can be revealed by using point spread functions deduced from these intensity profiles for deconvolution post-processing. This was verified in the results section of chapter 5.1. The Bessel beam has a peak PSF value which is 2.7× greater than the Gaussian equivalent for OPE at 600μm depth, and a 4.4× improvement for the 2PE case.

aperture). However, while the advantages are clear for one photon fluorescence microscopy, Airy beams do not perform well in the multi-photon case as contrast is reduced at depth. This is only revealed when we study the modulation transfer functions (MTFs) for these beam shapes. Figure 5.4 shows the MTFs related to each PSF plot in figure 5.3. The x axes in figure 5.4 are the normalised spatial frequency. Gaussian, Airy (α=5), and Bessel15 beams with the same NA are all able to transmit low spatial frequency information at 600μm propagation distance for OPE, 2PE and 3PE beams with comparable contrast. High spatial frequencies encode high resolution information. In practice, a low MTF FWHM (units are μm^{-1}) at propagation depth Y'(μm) means that fluorescence images taken at Y' μm will have low contrast. The Airy beam has increased performance for OPE at depth (blue lines

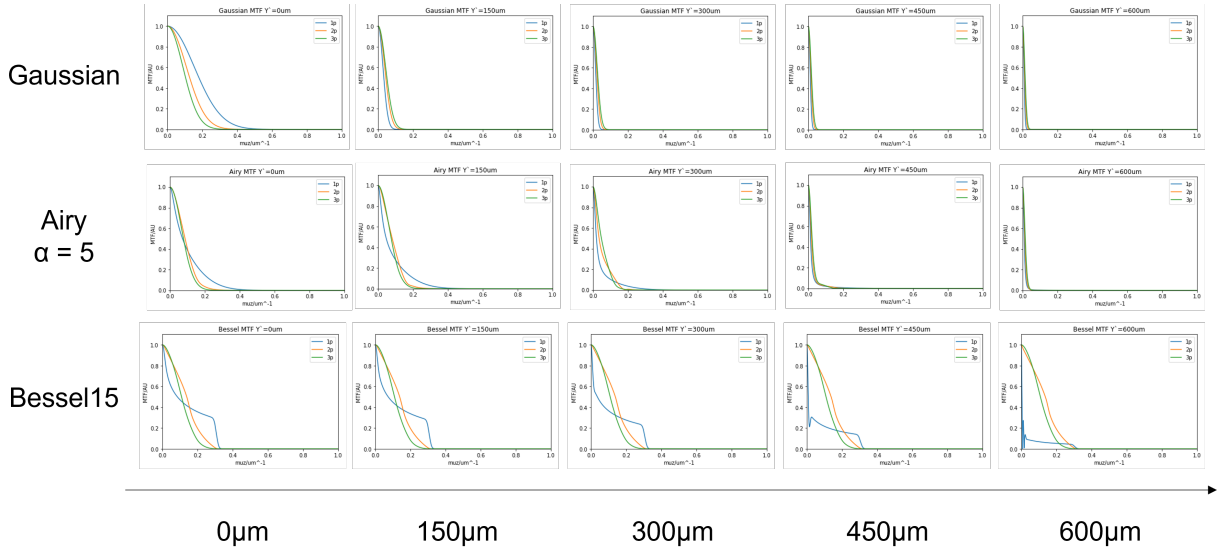

Figure 5.4 Modulation transfer functions (MTFs) calculated using the intensity profiles shown in figure 5.3. The x axis is the normalised spatial frequency found using the Fourier transforms of PSFs from each beam. The Y axis in each plot is the MTF (0 to 1, AU). The Airy beam maintains a high MTF for larger spatial frequencies for the OPE case, however high spatial frequencies are not well conserved for multi-photon excitation.

in figure 5.4) compared to the Gaussian beam. However, the MTF drops quickly for 2PE (orange) and 3PE (green) at high spatial frequencies meaning that Airy beams are not well suited for multi-photon fluorescence imaging at depth. Instead, figure 5.4 shows that Bessel beams are a suitable choice for propagation-invariant beam shaping with a multi-photon source. The simulation reveals an increased MTF at higher spatial frequencies for both 2PE and 3PE Bessel15 cases at 600μm depth. These results are consistent with a previous similar study [166], which considered Bessel5 and Bessel10 simulated beams in comparison to Gaussian and Airy beams. In all simulations presented in figures 5.2, 5.3 and 5.4 I have assumed that $\lambda_{OPE} = \frac{1}{2}\lambda_{2PE} = \frac{1}{3}\lambda_{3PE} = 488nm$ and that the propagation medium has a uniform RI of 1. Details of how the PSF and MTF are calculated can be found in chapter 2 in sections 2.3.7 and 2.6. In the context of LSFM where shaped illumination is viewed side-on, the profiles shown in figure 5.3 represent the pattern of the LS intensity profile if the light-sheet is viewed side-on and orthogonally to the beam propagation direction. Figures

5.5 and 5.6 summarise key values from these preliminary simulations. Figure 5.6 compares the axial resolution that we could expect from a light-sheet fluorescent microscope (constant illumination and detection NA) with illumination that is Gaussian, Airy or Bessel for OPE, 2PE or 3PE fluorescence detection.

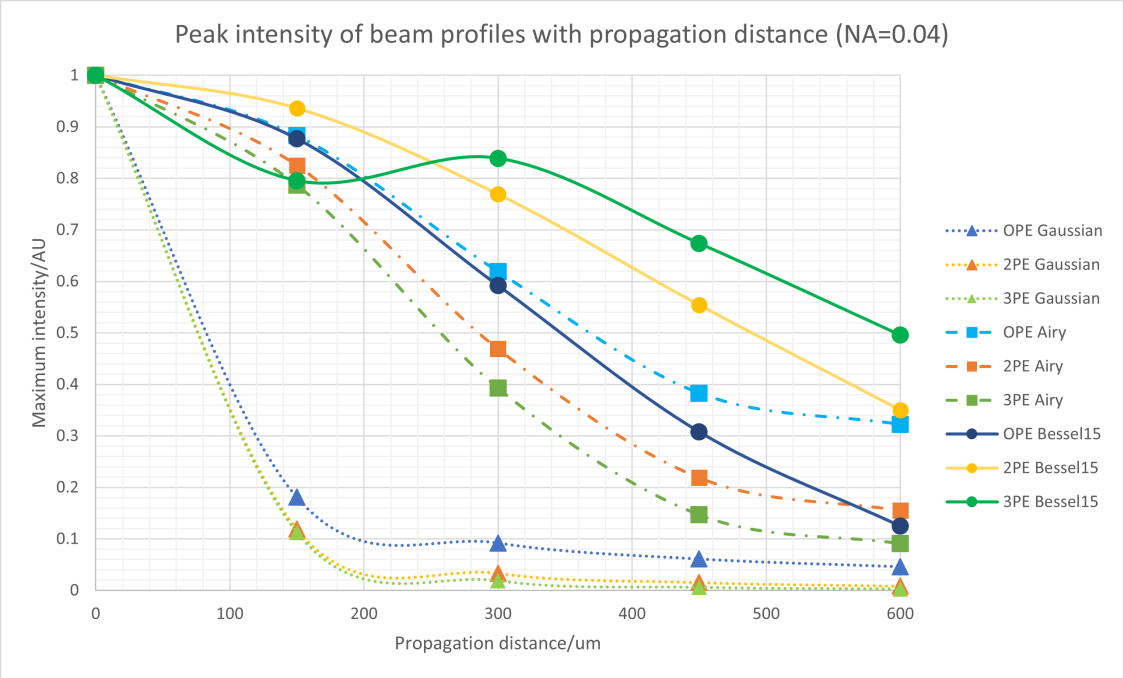

Figure 5.5 These curves correspond to the data shown in figure 5.3. Peak intensity is reduced as each of the three beam types propagate, however the rate of decay is slower for propagation-invariant Airy and Bessel15 beams. OPE λ=488nm, 2PE λ=976nm, 3PE λ=1464nm. Intensity values are all normalised so that the maximum of 1AU is positioned at the focus of each beam (Y'=0μm).

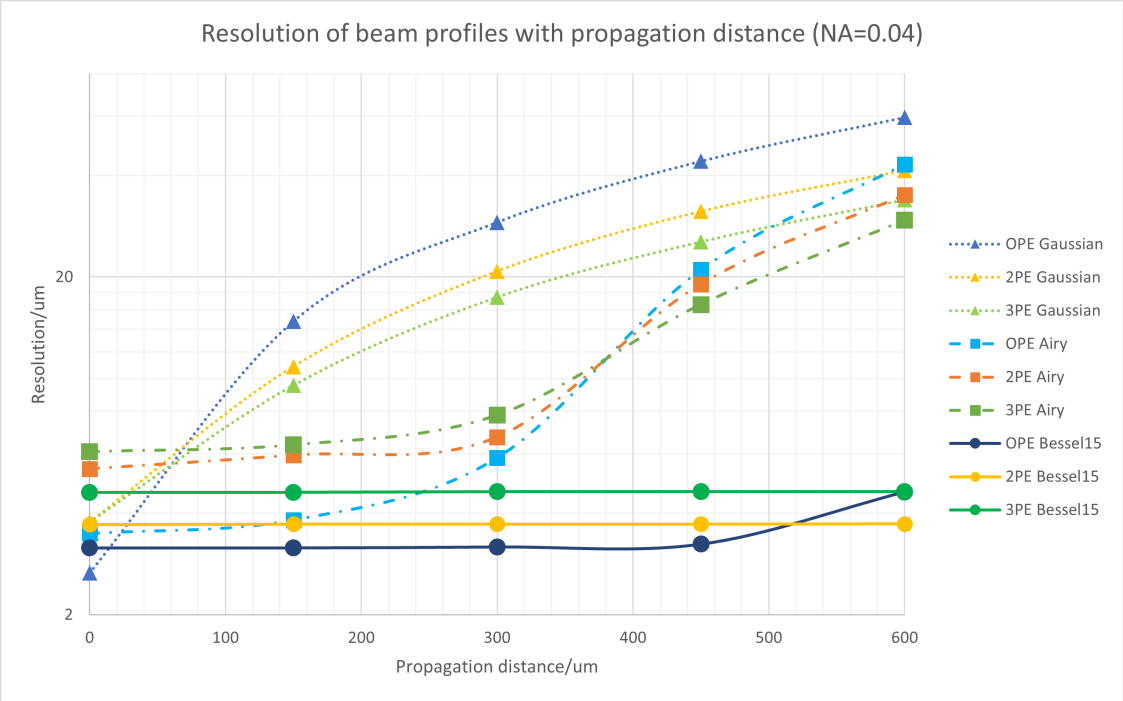

Figure 5.6 These curves correspond to the data shown in figure 5.4. The resolution is calculated by finding the distance at which the MTF drops to half of the maximum value at each propagation depth. The resolution is related to the inverse of the transferred range of spatial frequencies. Bessel15 beams maintain a lower resolution throughout this propagation range compared to Gaussian and Airy beams with the same NA, for 1^{st}, 2^{nd} and 3^{rd} order fluorescence excitation. Using MPE, the minimum resolution is 3.71±0.02μm for Bessel15 2PE and 4.62±0.02μm for Bessel15 3PE with an NA of 0.04. The 3^{rd} order Bessel15 profile has an increased resolution compared to the 2^{nd} order Bessel15 profile because the λ=1464nm beam is initially less confined due to diffraction (see equation 2.14).

Having established that we should choose Bessel beams for MPE, I will now look at how to implement Bessel-Gauss beam shaping in a MPE LSFM design.

5.3 Possible alternative methods for Bessel-like beam shaping in a prototype LSFM setup

In chapter 2 section 2.6, I described how Bessel beams can be produced using axicon lenses (figure 2.21) and by placing an annulus in the Fourier plane to the sample/imaging plane

(figure 2.22). Whilst axicons, annululi and spatial light modulators (SLMs) can all be used to create high fidelity Bessel outputs, I was interested in using alternative optics for Bessel-like beam shaping with multi-photon illumination. Specifically, I investigated two separate optical element types: (1) Bessel beam generating (BBG) meta-surfaces for their potential low loss and low dispersion properties and (2) BBG optical fibres due to fibre-based technology being inherently compatible with many healthcare applications [257–259].

5.3.1 Aims and experimental design

The aim of the following experiments was to investigate the suitability of two BBG optical components for MPE, biologically compatible LSFM. I measured the spatial profiles of the components (in 3D) to assess the propagation-invariance and scale of the output beams. I also investigated the interaction between the devices and non-linear sources. Specifically, I measured the pulse durations, spectra and average power before and after each device under a range of conditions. All of the BBG components were supplied by external collaborators (see section 6.4.4 for details). My experimental results were used by collaborators to adapt designs of the components over a number of research and development cycles. Once the components had been optimised, we aimed to demonstrate a proof of concept multi-photon light sheet fluorescence microscope with novel Bessel-like illumination. The hope was that this demonstration would prove useful in the biomedical sector moving forwards.

In order to make fair comparisons of these "Bessel-like" beam shaping methods with standard Bessel-Gauss beam shapes, I use a theoretical beam propagation simulation of Bessel beams produced using an annulus. A diagram of the optical setup that these models are based on is shown in figure 2.22. The incident beam diameter (outer annulus diameter), focal length of the spherical lens and inner annulus diameter were altered to simulate Bessel-Gauss beams with similar central lobe diameters to those that I observed in experiments using the BBG meta-surfaces and BBG fibres. This allowed me to make fair comparisons of

the relative propagation-invariance between experimental and theoretical beams of the same wavelength for similar central lobe diameters. The simulated beams propagated through uniform virtual space (RI=1 to match air) with the wavelength matching sources used in experiments.

Both novel optic types produced Bessel-like beams rather than traditional Bessel-Gauss beams found in literature, so to conduct fair comparisons I used the following criteria to compare the beam shapes:

- Central lobe diameter over propagation range (indicative of the axial resolution and FoV that a LSFM using this optic type could provide)
- Ratio of the central lobe maximum to the first outer lobe maximum (gives an indication of how necessary deconvolution will be in fluorescence images). Diminished side-lobes can remove the requirement for deconvolution as a post-processing step [260]
- Maximum central lobe intensity over FoV – would the SNR be preserved over the full range or would deeper signals lack contrast?

I explored the beam shapes produced by each of the two component types. Summaries of Bessel-like beam profiles from each optic type are given in sections 5.4 and 5.5.4. I will discuss how these components affected pulsed light. Using this combined data, I'll consider the suitability of each case for use in multi-photon light-sheet fluorescence microscopy. Finally, I will describe a proof-of-concept experiment showing a BBG fibre optic light-sheet fluorescence microscope used to induce 2PE and detect the signal in a fluorescent bead phantom sample.

The next section covers the BBG meta-surface devices and summarises my findings. Section 5.5 contains a similar report of the BBG fibre optic devices. Section 5.6 describes a novel light-sheet microscope design with fibre-integrated Bessel-like illumination and demonstrates proof-of-concept experimental results.

5.4 Meta-surfaces for Bessel-like beam generation

5.4.1 Optical design of BBG meta-surfaces

"Meta-atoms" are sub-wavelength scale etched features which alter the phase of light passing through a meta-surface [261–266]. Cylindrical silicon meta-atoms were fabricated on the surface of a quartz substrate to create a Bessel-like beam profile in light passing through. Figure 5.7 shows a model of the silicon-covered quartz substrate surface etched with cylindrical meta-atoms. The height (h), spacing (d) and radius (r) of the cylinders is carefully designed to alter the incoming beam phase profile between 0-2π as desired across incident planar wavefronts [267]. Increasing r and h increases the effective refractive index over that area of the meta-surface. This increases the relative phase change of any light passing through. d is chosen to balance the phase changes across the beam by ensuring that the phase changes do not average out in space whilst still maintaining an acceptable resolution (of the meta-surface structures with respect to the light field). The choices of d, r and h are limited by manufacturing constraints. A representation is shown in figure 5.7a. A macroscopic photograph of one such meta-surface is shown in figure 5.7b. There is a small 2mm circle just visible in the centre of the quartz square. This circle is where the 280nm silicon surface layer has been etched using laser beam lithography to produce cylindrical structures. The radius of the cylinders varies between 130 and 209.5nm in 8 discrete steps. These meta-surfaces were designed to work with 1064nm incident illumination. The minimum wavelength of such a design is limited by the resolution of the electron beam lithography system used for fabrication.

The meta-surfaces are designed it impart a phase profile onto a Gaussian beam as if it has been focused using an axicon lens. This phase profile is given by equation 5.1, where $\Theta(x, y)$ is the phase at any given position on the surface, which is assumed to be 2D. n is the refractive index of the modelled axicon lens, λ is the illumination wavelength and ϵ is the angle of the conical axicon lens being approximated.

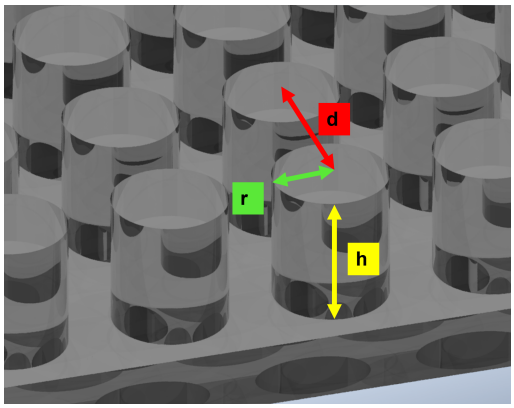

(a) Meta-surface close-up. Diagram was created using Autodesk inventor. The cylinders are silicon and the base layer is made of a quartz substrate. The height of each cylinder is alterable in 8 steps to cover a potential phase shift range between 0 and 2π.

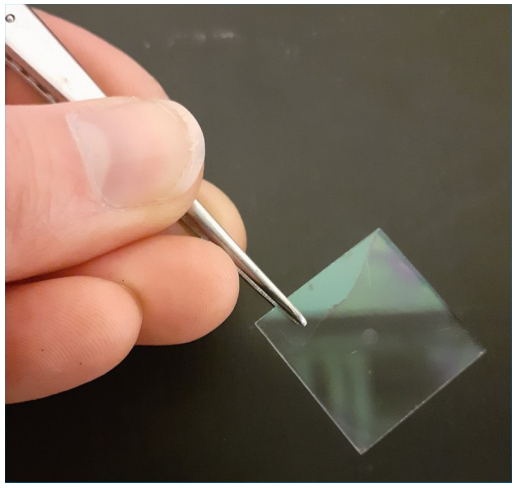

(b) Photograph of etched quartz dielectric meta-surface for Bessel-like beam generation. Cylindrical meta-atoms cover a 2mm diameter area in the centre of the sample.

Figure 5.7 Meta-surface developed at IIT Madras for Bessel-like beam generation at 1064nm.

$$\Theta(x,y) = \frac{2\pi n}{\lambda} * (R - \sqrt{x^2 + y^2}) \tan(\epsilon) \tag{5.1}$$

Equation 5.1 Two-dimensional phase profile added by an axicon lens with refractive index n, incident wavelength λ, cone angle ϵ and incident beam radius R [261].

5.4.2 Experimental setup (part I)

To use the meta-surfaces in a microscope setup, illumination of 1064nm was collimated to form a circular beam profile with a diameter of 2mm. This was incident directly on the etched features on the wafer surface (1998μm across). Figure 5.8 shows the experimental setup that I built and used to image the beam profiles outputted from the meta-surfaces. The profile was measured after transmission using a simple microscope. Images of cross-sections through the beam were recorded digitally and fed to a laptop using μ-Manager. The meta-surfaces are polarisation-invariant and were not expected to create different spatial profiles depending on whether the source was CW or pulsed. This was experimentally verified by

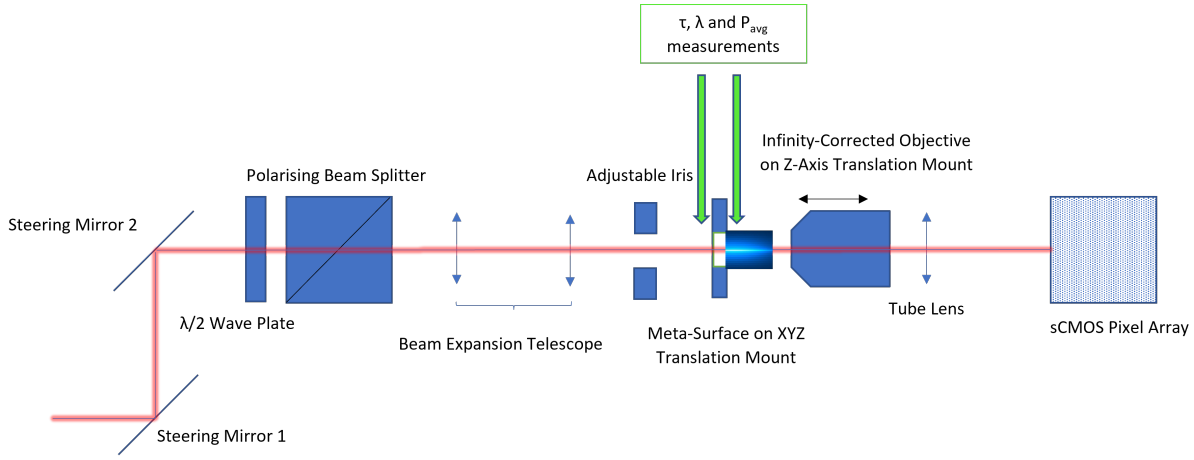

Figure 5.8 Diagram of experimental setup for meta-surface characterisation. The etched side of the meta-surface faces the incident beam. Figure 5.7 shows the quartz and silicon meta-surface in more detail. The entire setup was mounted onto a portable breadboard to allow trials with various laser sources across different locations. I used YLM-10-1070-LP, IPG (10W maximum average power, 1070nm, CW) and Chameleon Ultra II, Coherent (<0.5W maximum average power at 1064nm, pulsed, 80MHz repetition rate) to measure the interaction of the meta-surfaces with CW and pulsed illumination. When pulsed illumination was used, a Carpe microscopy autocorrelator (2P), A.P.E. was used to measure τ at at the laser output and at different locations through the optical pathway. Fibre-coupled spectral measurements were obtained using AQ6374 Wide Range Optical Spectrum Analyzer, Yokogawa and free space spectra were measured using CCS100 Compact Spectrometer, Thorlabs with CCSB1 cosine corrector attachment.

rotating the sample with respect to the linearly polarised sources and by comparing profiles from similar CW and pulsed sources with the same average power.

The setup shown in figure 5.8 was mounted onto a portable breadboard to allow for testing in two separate labs (one containing a 1070nm CW laser; YLM-10-1070-LP, IPG and the other a tunable pulsed laser; Chameleon Ultra II, Coherent). Broadband dielectric steering mirrors (E03, Thorlabs) were used to guide the NIR light into the centre of a cage-based optical pathway for light delivery. Power reduction optics were essential as the full average and peak powers of all trial lasers were far higher than required for simple shaped beam propagation measurements. In the first instance, this was achieved using two pairs of a $\frac{\lambda}{2}$ wave-plate (WP) (WPH05M-1064, Thorlabs) and a polarising beam splitter (PBS) (CCM1-

PBS253, Thorlabs) along with several neutral density (ND) filters (NDUVxxA, Thorlabs). However, later modifications swapped CCM1-PBS253, Thorlabs for narrow band polarising plate beamsplitter (PBSW-1064R, Thorlabs) in order to reduce the volume of glass that beams had to travel through prior to reaching the meta-surface. This reduced pulse dispersion (see section 2.3.6) in the illumination patwhay. The incident beam was collimated using a simple Keplerian telescope (combinations of AC254-xxx-C-ML, Thorlabs to produce a beam diameter of just over 2mm) and then the edges were spatially cleaned with an adjustable iris (SM1D12C, Thorlabs). The iris diameter was set to 2mm using vernier calipers to match the diameter of the manufactured profile on the meta-surface. The meta-surface position was adjustable in X,Y and Z using a manually adjusted translation stage (M-562-XYZ , Newport). Tilts of the surface relative to the wavefront plane of the light had an effect on the beam shape at the output. This effect was minimised by manual adjustments to the wafer mount and through trial-and-error by observing asymmetries in the beam profile at the other side of the wafer. The manufactured phase profile and beam shape produced by it are rotationally symmetric about the optical axis. Therefore, asymmetries in the shape at the output can generally be attributed to asymmetry in the incident beam or to angular misalignment in the beam path. A photograph of a meta-surface wafer mounted in the optical pathway is shown in figure 5.9.

An infinity-corrected objective (M-10X, Newport, 10×, 0.25NA, 16.5mm focal length), was used to relay cross-sectional profiles of the wafer output through a tube lens (AC254-100-C-ML, Thorlabs), ND filter (NDUVxxA, Thorlabs) and onto a camera array (Orca Flash 4.0 v2, Hamamatsu)[23]. Motorised translation of the detection objective was achieved in the z axis (direction of beam propagation) using a separate translation stage with motorised

[2]Average and peak power measurements potentially damaging to sCMOS array. Care should be taken to keep both quantities below the damage threshold of each optic.

[3]Note that the quantum effiency for this camera is very low at 1064nm, however the spatial profiles were still visible using long exposure times (>100ms).

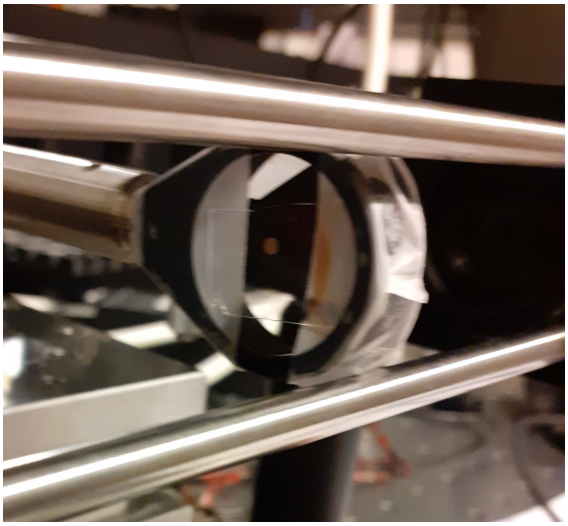

Figure 5.9 The quartz substrates have irregular edges. Beam profiles generated using these optics were susceptible to tilts of the surface normal relative to the optical axis. Rotations of the meta-surface about the optical axis had no effect. The optic was mounted onto a translation stage that was decoupled from the caged system to allow adjustments of the circular profile in the plane of the wafer and along the propagation axis.

piezo actuator (M-230, Physik Instrumente). μ-Manager was used to synchronise z-steps with image capture. Average power measurements were made using two alternative portable power metres (S132C, Thorlabs and 13PEM001 Broadband Power/Energy Meter, Melles Griot for high power measurements).

5.4.3 Methods (part I)

Assessing the spatial properties of the Bessel-like beams

Incident power on the meta-surface was kept below (2mW) (with a peak power of no more than 180W when using pulsed illumination). The manufacturer predicted FoV of the BBG meta-surface to be 7.1cm, a distance greater than the maximum travel of the objective lens mount. Therefore, the volumetric intensity profile from meta-surface samples was measured in 6 separate batches with the objective stage moved axially between each. FIJI was used to stitch and inspect the complete volume of data. Individual cross sections (like the one

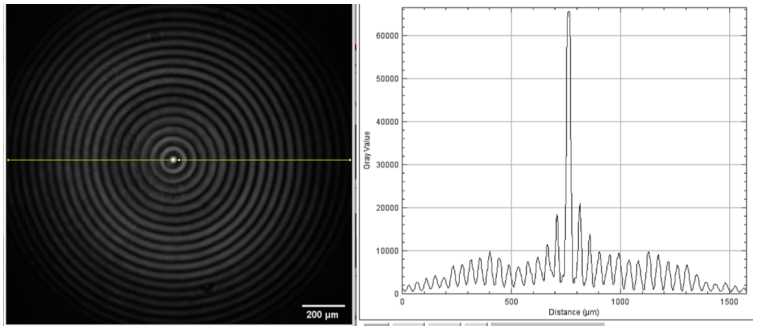

Figure 5.10 A example intensity profile measurement from Bessel-beam generating meta-surface wafers. This one was captured at a distance of 30mm from the wafer back aperture (etched surface of wafer facing incoming beam). A line is drawn through the centre of the concentric ring pattern horizontally and then vertically (not shown). Each line is used to create an intensity plot like the one shown on the right-hand side. The Y axis is intensity (AU) and the X axis is position (μm). The data is later shifted so that X=0μm is in the centre.

shown in figure 5.10) were sampled. The intensity was measured in each plane by drawing a line vertically through the centre of the concentric ring pattern and horizontally through the same point. The intensity profiles were co-registered using the central peak and then averaged to produce a measure of the radial intensity profile through the Bessel-like beam. The peak intensity was measured from the central lobe in each plane. The second innermost lobe was measured from left and right peaks and then averaged. The FWHM of each central lobe was measured. Successive frames were analysed in this way to produce a summary of the propagating Bessel-like beam shape.

Looking for evidence of non-linear interactions

To investigate potential dispersion due to the meta-surfaces, I measured the pulse duration and spectra directly before and after each meta-surface in the optical pathway. Average power was also measured to check for other losses or changes to the beam due to interaction with the meta-surface wafer.

The need for beam downsizing

Due to the design of these meta-surfaces, the FWHM was expected to be on the order of 20μm. This is too large to produce the precision of optical sectioning required for most biomedical applications. If we were to incorporate this Bessel-like beam into a light-sheet fluorescence microscope, the axial sectioning (based on the light-sheet thickness) would be limited by this 20μm central lobe FWHM even after deconvolution. We require an axial resolution of 4-5μm to match the axial resolution of gold standard histopathological imaging (see section 3.2 for more details).

However, it is possible to scale a three dimensional beam shape using simple telescopic optics. The setup and methods described in sections 5.4.2 and 5.4.3 were adapted to accommodate down-scaling of the meta-surface beam profiles using the approach described in section 5.4.4.

5.4.4 Experimental setup (part II)

Scaling beam profiles in 3D

A 3D profile like the ones produced by these BBG meta-surfaces can be scaled in all three dimensions using a Keplerian telescope. The optical arrangement is shown in figure 5.11. If spherical lenses are used a perfect system will produce a magnification of $\frac{f_1}{f_2}$ in the image plane in both X and Y. The profile in Z will be scaled according to equation 5.4. These two magnification factors should be considered in parallel. We wish to minimise the profile dimensions in the XY plane to produce a thin light-sheet offering high axial resolution for LSFM. However, doing with a telescope so will also reduce the FoV of the illumination beam.

$$FOV_1 = f_1 - Z_1 \tag{5.2}$$

Equation 5.2 The FoV of the original Bessel beam represented in figure 5.11.

$$FOV_2 = Z_2 - f_2 \tag{5.3}$$

Equation 5.3 The FoV of a re-imaged 3D beam profile after passing through a Keplerian telescope (shown in figure 5.11.)

$$Z_2 = -(\frac{f_2}{f_1})^2 Z_1 + f_2(1 + \frac{f_2}{f_1}) \tag{5.4}$$

Equation 5.4 Z_2 is the length of the Bessel-like beam measured from the focus to the edge of the FoV). A Keplerian telescope constructed from two lenses ($f_1 > f_2$) will reduce the dimensions of the profile in each XY plane by a factor equal to $\frac{f1}{f2}$. The axial dimension, Z_1, will be scaled according to this equation, where the FoV of the object and image beams are given by equations 5.2 and 5.3 respectively [81].

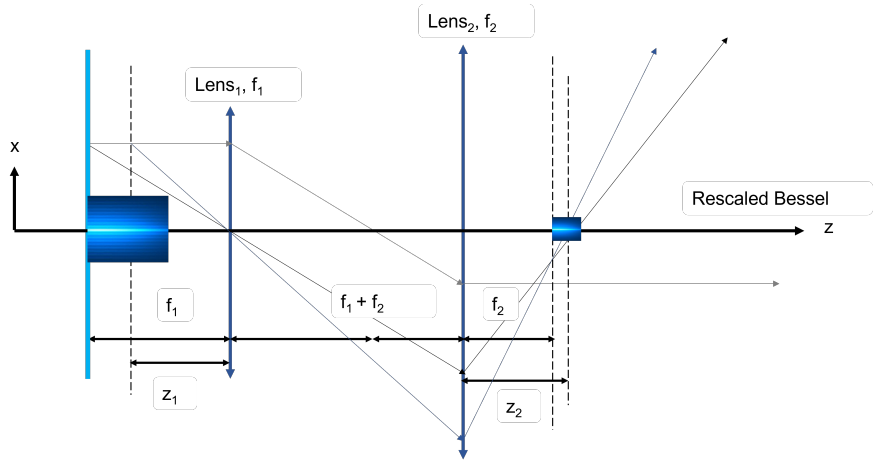

Figure 5.11 Adapted from [81]. Bessel-like beam scaling using a Keplerian telescope. The light blue line represents the surface of the BBG wafer (see figure 5.12).

To accommodate 3D profile re-scaling, the setup shown in figure 5.8 was modified to produce the setup shown in figure 5.12. Reduction telescopes of 2× and 3× were used to experimentally verify equation 5.4. It was expected that the addition of two more spherical lenses would impact the total pulse dispersion through the optical pathway.

5.4.5 Methods (part II)

The experimental method was as described in section 5.4.3, however there was no need to image the beam profile in subsections as before since the scaled down Bessel-like beam could

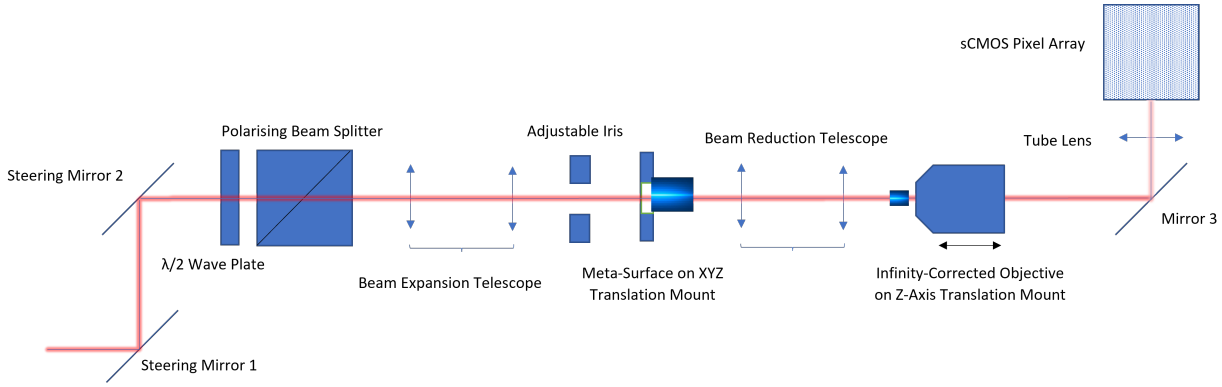

Figure 5.12 Setup with down-scaling telescope included. The setup was otherwise identical to the one shown in figure 5.8. Beam reduction telescope was adapted to produce different FoVs and central lobe diameters in the image of the beam profile.

be sampled using one travel length of the objective translation stage in this case.

5.4.6 Experimental results

Unscaled intensity profile

A summary of the cross-sectional intensity profile measured from the Bessel-like beam generating meta-surfaces at 1064nm is shown in figure 5.13. Without any optical scaling, the average central lobe diameter for these surfaces was 23.6μm over a propagation distance of 17.2mm from the surface of the element. The central lobe diameter increased sharply to 35μm at 17.5mm propagation distance due to the second lobe merging with the first. The central lobe diameter had a standard deviation of 9μm over this range before the lobes merge. The disruption in beam profile at 17.2mm propagation resulted in a shortened propagation-invariant distance for this Bessel-like beam compared to the estimated 71mm range. However, the anomaly was self-corrected at 17.8mm and the following measurements did not contain a second central minimum until 42mm from the wafer back surface.

The BBG meta-surfaces produced cross-sectional intensity profiles with high rotational symmetry. Prior to averaging horizontal and vertical intensity profiles to produce the summary in figure 5.10, the intensity ratio between equivalent points from the vertical and

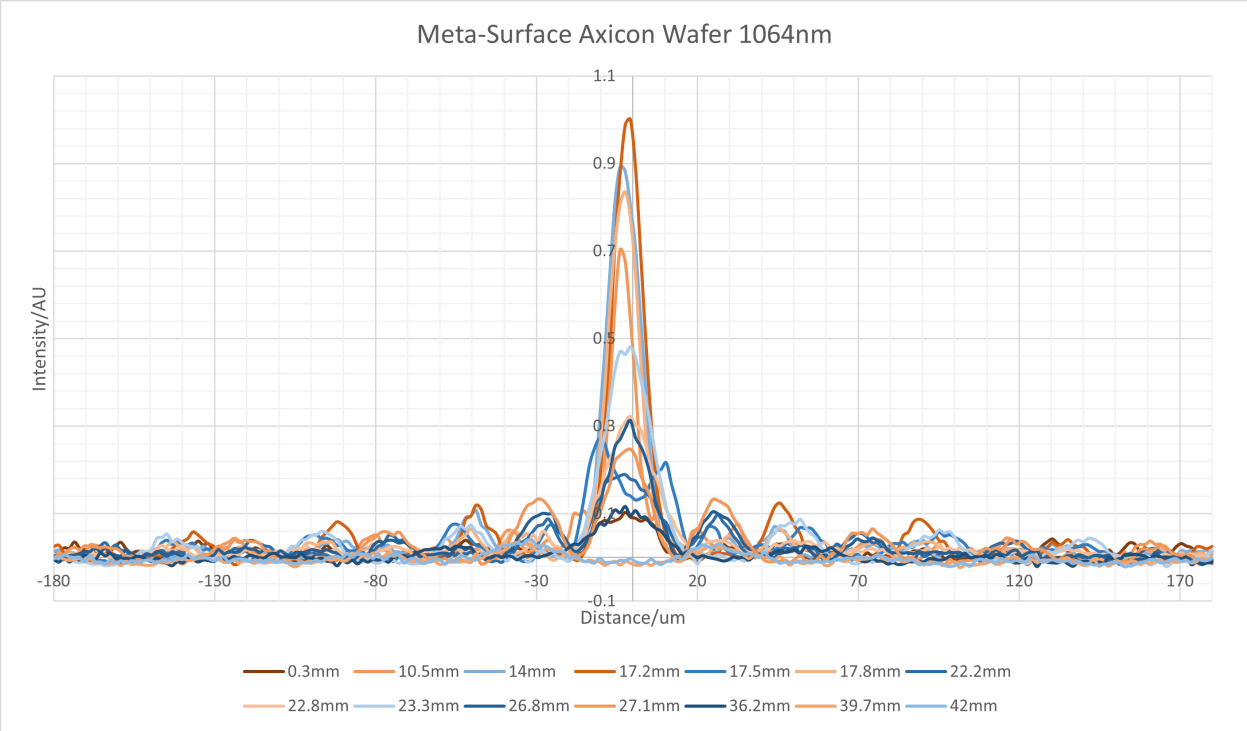

Figure 5.13 Spatial profiles show that the meta-surface has not produced a propagation-invariant beam. At 17.5mm, The central lobe becomes a ring with a central minima. This effect was not predicted by the manufacturer's simulations. At most propagation distances sampled here, there is a maximum peak at the centre of the profile and several concentric side-lobes with lower peak values.

horizontal profiles was 1:0.996 on average with a standard deviation of 10.5%. There was high variation in the central peak maximum intensity across the FoV with an average of 0.32±0.25AU.

Optically scaled 0.5× intensity profile

Figure 5.14 shows the experimental result of scaling the meta-surface profile by 0.5× using the arrangement shown in figure 5.11. The average central lobe FWHM of this data is 6.8±1.4μm sampled in 1mm steps between the wafer surface and a distance 10mm away along the propagation axis. This compares to a theoretical average FWHM of 4.3μm using equations 5.2, 5.3 and 5.4 and the average FWHM of 23.6μm measured before down-scaling of the profile. The central peak intensity over this range varies greatly; 0.57±0.23AU.

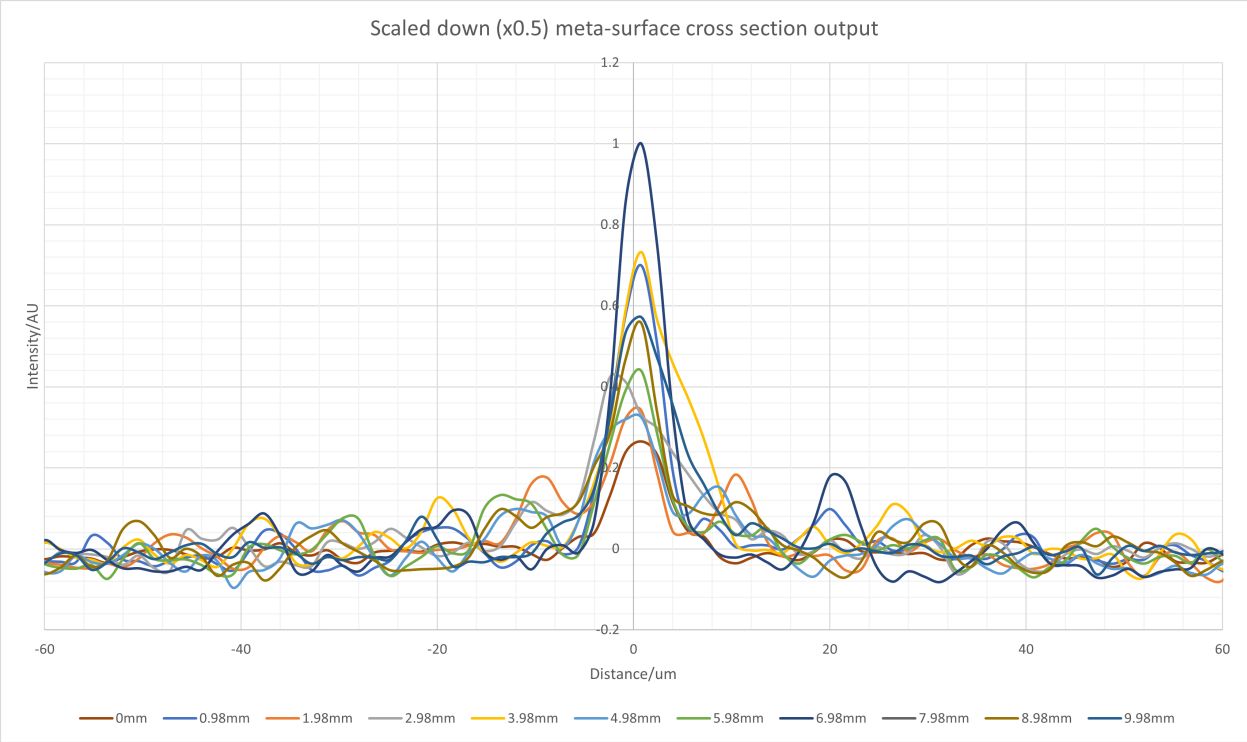

Figure 5.14 Cross-sectional intensity data measured at different propagation depths through the 0.5× scaled BBG output. As with the unscaled Bessel-like profile, there was great variety in the central lobe peak power (40%) over 10mm propagation length. The FWHM of the central lobe increased by 50% between z=1.98mm (FWHM = 6.4μm) and z=2.98mm (FWHM = 9.6μm). At 3.98mm, the FWHM is 8μm. The absolute error in each case is ±0.5mm.

Quantifying spectral and temporal changes due to the meta-surfaces

Small changes to the pulse duration were detected throughout the optical pathway when the Chameleon 80MHz rep rate laser was used with central wavelength at 1064nm. The pulse duration was measured to be 188.3±0.3fs at the source output, 193.5±0.3fs just before the meta-surface wafer in the optical path (see figure 5.12), 202.2±0.2fs just before the detection objective with no wafer present and 204.8±0.2fs at the same location with a BBG meta-surface inserted before the beam reduction telescope. There was no discernible change to the beam spectrum when measured before and after the meta-surface wafer in the setups shown in figure 5.8 and 5.12.

5.4.7 Discussion

With or without the reduction telescope, there is high standard deviation of the central lobe peak intensity and diameter over the field of view for this meta-surface design. This means that any Bessel light-sheet microscope using these meta-surfaces would have a high variance in resolution over the field of view, unless the meta-surface design is altered, or if some correction was added into the illumination pathway. This would require accurate knowledge of the profile shape across the FoV.

The major cause of peak intensity and central lobe diameter variation was linked to merges of side lobes with the central lobe. Some of these merging artefacts could be removed by realignment of the meta-surfaces with respect to the incident beam (the surfaces are particularly sensitive to angular misalignment with respect to the incident beam) however other spatial anomalies were repeatable across all data sets. After discussion with our collaborators, it was established that these lobe merges are likely due to defects in the manufacturing process which could be ironed out in the coming months and years. It is also possible to construct similar devices using lithography systems with a shorter operating wavelength [268]. This would allow the structures to be engineered with finer detail and it may then not be necessary to spatially scale down the beams after the meta-surface output.

Spectral measurements revealed that there was no discernible change in spectra measured before and after the meta-surface. The wafer element added 2.6±0.2fs on to 202.2fs pulses (80MHz @ 1064nm) propagating through the substrate and etched design. These temporal and spectral observations suggest suitability of the dielectic BBG meta-surfaces for MPE applications, where it is normally important to minimise dispersion and other non-linear effects. These observations are relevant for future work with these surfaces. Future iterations of the BBG meta-surface design will aim to improve propagation-invariance of the Bessel-like profiles.

We have established that smaller, more uniform Bessel-like profiles will be required for

MPE fluorescence imaging for medical microscopy applications. With that in mind, I will now discuss a second method for generating Bessel-like beams.

5.5 Bessel-beam generating fibre optics

5.5.1 Optical design

In 2010, Lee et al. published a paper describing a novel fibre optic design which produced a propagation-invariant, Bessel-like beam output at a fibre tip [269]. This paper contains an analysis of the generated beam profile and demonstrates how such fibres can be used for optical trapping of 10μm polystyrene beads. A diagram of one such fibre with a Bessel-like beam generator (BBG) fibre tip is shown in figure 5.15. A single mode fibre (SMF) of arbitrary length is used to transport a stable single mode from a laser source to close to a sample. Whilst the beam is coupled into the fibre core, the wave-fronts are guided by total internal reflection. The SMF has carefully selected properties (core material, core diameter, cladding diameter) which are designed for low losses for a particular band of illumination wavelengths. The SMF is spliced with a coreless silica fibre (CSF) tip. The CSF is an example of a multimode fibre (MMF). The CSF supports multiple spatial modes. Additional modes are produced when light from the SMF section propagates through the silica. The number and nature of additional spatial modes depends on the radius, r, and length, l, of the CSF section. A micro-lens is in-built into the tip of the CSF to focus exiting modes externally. The electric field inside the Bessel-like beam generator is given by equation 5.5. r and l are optimised to produce the desired Bessel-like spatial profile at the micro-lens focus.

$$E_{out}(r, \Phi, l) = \sum_{m=1} C_m e_m(r, \Phi) \exp -i\beta_m l \tag{5.5}$$

Equation 5.5 Electric field distribution inside a coreless silica fibre (CSF) Bessel-like beam generator (design schematic in figure 5.15) using a cylindrical coordinate system [269, 270]. The field is rotationally symmetric about the optical axis, assuming that the input beam is rotationally symmetrical. r is the radius, l is the length of CSF, C_m is the relative amplitude of each spatial mode, $e_m(r, \Phi)$ is the mode electric field in cylindrical coordinates and β_m is a mode-specific propagation constant which describes the accrued phase.

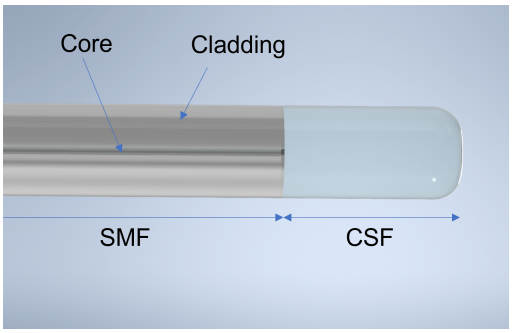

(a) Labelled side-view of Bessel-like beam generating (BBG) fibre optic.

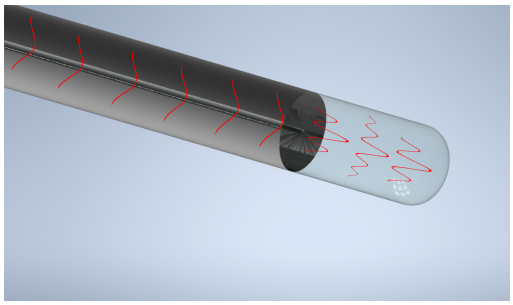

(b) Coreless silica fibre (CSF) is spliced to a length of single mode fibre to engineer a pattern of multiple overlapping modes.

Figure 5.15 BBG fibre-optic device. This basic structure (introduced by Lee et al. [269]) was modified to support pulsed illumination at 920nm for fibre-integrated Bessel-like illumination for LSFM with two photon fluorescence excitation. Images generated using Autodesk Inventor. Not drawn to scale.

5.5.2 Experimental setup

Each fibre measured was designed and produced by our collaborators at Yonsei University (see section 6.4 for further details). All of the BBG fibres tested in this section are composed of a SMF fibre section and a MMF tip (which is where the Bessel-like beam is generated). To test the BBG fibres as a whole, the SMF and MMF sections were analysed as separate components to better understand the BBG fibres as a whole. This data accompanied measurements made from the composite BBG fibre outputs.

To measure the BBG fibre beam profiles, an optical setup (represented in figure 5.17)

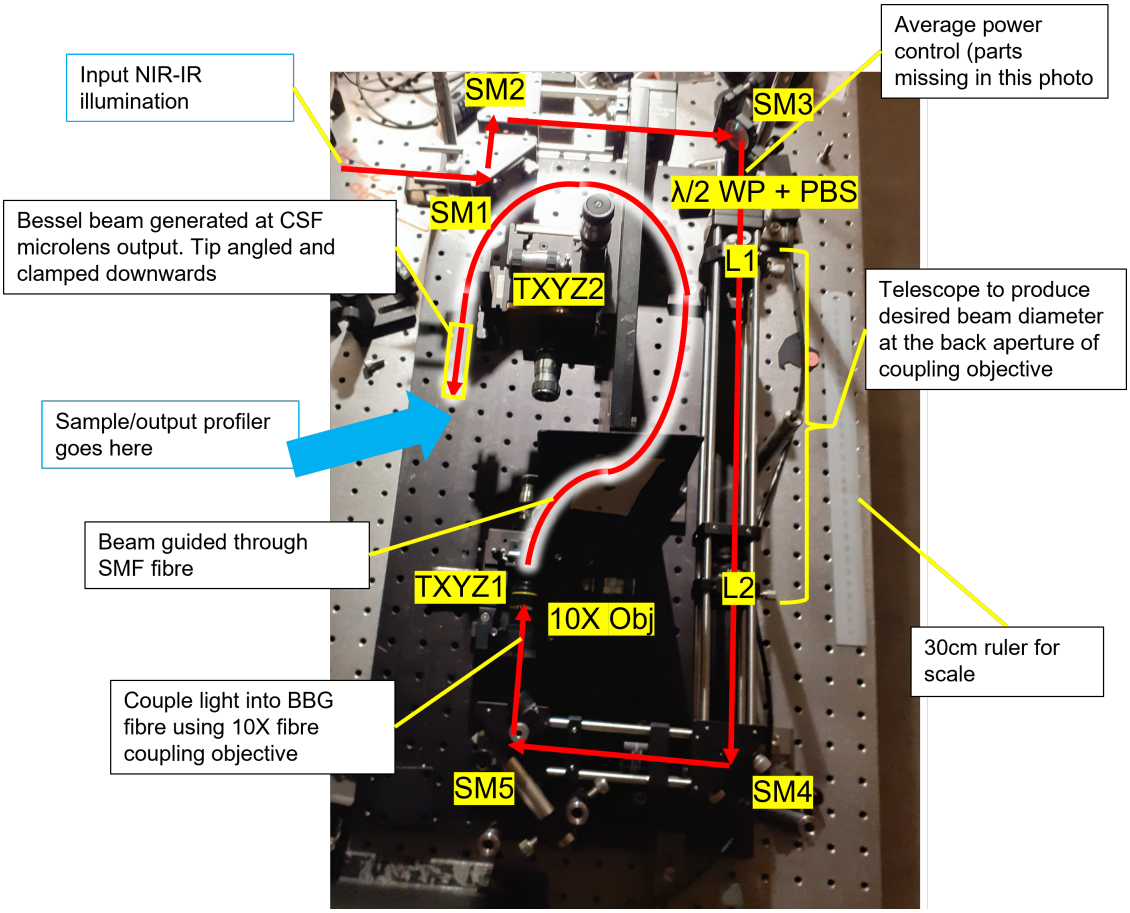

Figure 5.16 Experimental setup used to test the BBG fibre optics pictured here without the decoupled detection pathway. A 30cm ruler is beside the setup for scale. SMx: steering mirrors, $\lambda/2WP$: half wave waveplate, PBS: polarising beam splitter, Lx: lenses used for input beam scaling, 10× Obj: fibre coupling objective, TXYZx: 3D translation stage (manually controlled, used to align proximal and distal ends of the fibre optics with the rest of the optical setup) Table 5.1 contains information about the laser sources that were coupled into this optical setup.

was constructed. Steering mirrors (SM) (E03/E04, Thorlabs) were used to guide the source beam around the cage-mounted setup. A half-wavelength waveplate ($\frac{\lambda}{2}$WP) (WPH10M-830/WPH10M-980/WPH10M-1310, Thorlabs) in a rotation mount and polarising beam-splitter (PBS) (CCM1-PBS253/M, PBSW-808R, Thorlabs) were used for manual adjustments to average optical power. Lenses 1 and 2 (L1, L2) (AC254-250-B-ML, AC254-050-B-ML/ AC254-250-C-ML, AC254-050-C-ML) were used to fill the back aperture of the coupling objective. The beam was spatially filtered twice before L1 and SM4 using adjustable irises.

A 10× objective (M-10×, NA 0.25, WD 5.5mm, Newport) was used to to couple illumination into the fibres. Two XYZ translation stages (MDE122, Elliot Scientific) were used to align each end of the optical fibres independently. A separate detection pathway (not pictured here) was horizontally mounted at 90° to the fibre output, which was vertically mounted (output pointing downwards). The detection arm was fully mounted onto a separate XYZ translation stage (M-562-XYZ, Newport). A version of the detection pathway is shown in figure 5.34. In the separate detection pathway, two alternative infinity-corrected objectives were used (20× Plan Apo, Mitutoyo/ 4× CFI Plan Apo Lambda, Nikon) to capture light at the fibre tip. The detected light was filtered and steered through a tube lens (AC254-200-B-ML/AC254-200-C-ML, Thorlabs) and onto an sCMOS camera array (Orca Flash 4.0 v2, Hamamatsu).

Table 5.1 contains information about each laser source that was used to test the fibre optic devices. These sources were coupled into the setup shown in figure 5.16 in turn. For 820-980nm, alternative steering mirrors (E03, Thorlabs) were used and spherical lenses were swapped for NIR-coated versions (B-coated rather than C-coated Thorlabs lenses). The focal lengths and positions of lens 1 (L1) and lens 2 (L2) were varied to account for differences in beam diameter between laser sources. This ensured equivalent filling of the back aperture of the fibre coupling objective and therefore the same spot size and NA for coupling into SMFs. Figure 5.17 shows the optical setup used to detect fibre output profiles.

5.5.3 Methods

Alignment at fibre input

1. Ensure clean fibre input tip with a flat proximal surface (see methods for cleaving and cleaning later in methods section 5.5.3).

2. Ensure average power in system below 1mW and peak power below 5kW where applicable.

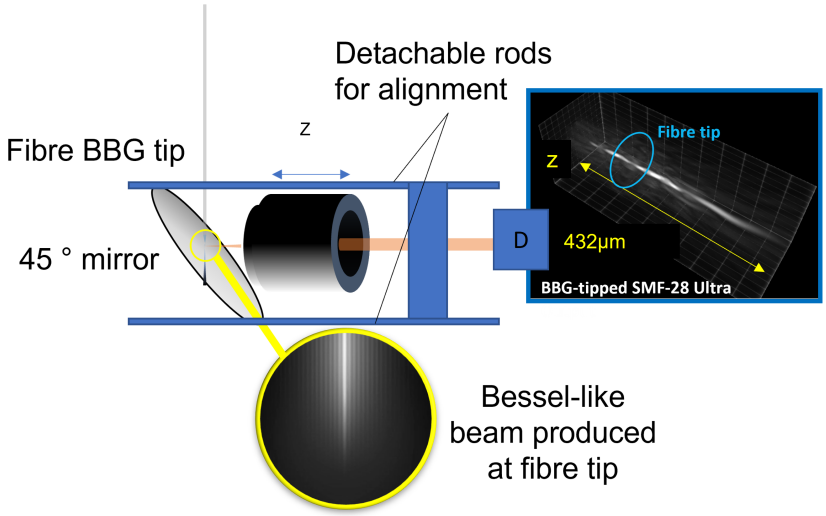

Figure 5.17 Spatial profiling of BBG fibre output beams. The setup shown in figure 5.16 was designed with a downwards facing fibre output mount due to constraints on sample geometry introduced by LSFM (see section 5.6) and for safety reasons. This necessitated a 45° angle in the detection pathway for on-axis measurements as the camera and objective would not fit below the fibre output. Alignment of the mirror was challenging; a lower magnification (4×) objective was used for initial setup and a higher magnification objective (20×) was used to sample the beam profile with a pixel-limited resolution of 0.4μm. The detection arm was mounted on a separate translation stage to decouple its movement from the fibre tip and the angled mirror. The z-step was programmed to match the pixel-limited resolution in x and y. The detector (D) captured images at each z step. The FoV at the fibre output begins at the tip and continues for around 500μm along the optical axis. Long WD objectives were selected and the fibre tip was lowered as close as possible to the mirror surface to allow imaging of the entire BBG fibre FoV.

3. Without the fibre in place, ensure beam travels through centre of cage-mounted system with the output of the fibre coupling objective blocked to ensure that the beam is contained.

4. Move fibre input stage (see figure 5.16) until the fibre mount is further away than the working distance of the fibre coupling objective (z direction).

5. Find objective focus using a viewing card and roughly align the translation stage along the x and y axes.

6. Block laser, place fibre input in the translation mount. Place an average power meter

Name	λ_C/nm	$P_{avg,Max}$/W	τ_{min}/fs	$\delta\lambda$/nm	$f_{rep,Max}$/MHz	Chirp
Chameleon Ultra II	820	3.8	140	8	80	+
Chameleon Ultra II	917	>2	140	<13	80	+
Opera-F/Monaco	920	<0.9	70	37	1	-
Chameleon Ultra II	980	2	140	13	80	+
FPL1053P	1310	0.08	N/A	5	N/A	N/A
Opera-F/Monaco	1320	<0.9	89	38	1	-

Table 5.1 Table of laser options used for BBG fibre trials. A CW laser was included for beam shaping comparisons at 1310nm. τ is measured using autocorrelator detector positioned at the output of each laser (>4m away for Chameleon and Opera-F lasers). $\delta\lambda$ is the FWHM of maximum intensity peak from spectra measured just before entry to optical setup (setup shown in figure 5.16). The Opera-F/Monaco at 1320nm was used to test fibres for non-linear behaviour in the 3PE regime. The Opera-F/Monaco tunable laser was used in negative-chirp mode, whereas the Chameleon Ultra tunable laser produced pulses with a positive chirp (see section 2.3.6 for more information). f_{rep} was tunable between 10kHz and 1MHz using the Opera-F laser and fixed at 80MHz using the Chameleon.

at the beam output (below fibre output translation stage, see figure 5.34).

7. Un-shutter laser and gently move fibre input along x and y until some power is registered at the output. Ensure the output end of the fibre is completely blocked from ambient light and any stray light from the input; signal will be very weak during early stages of alignment.

8. When peak is found in x and y, gently move stage in the z direction towards the objective focus to increase the power at the output.

9. Repeat the last two steps incrementally until it is not possible to increase the power at the output any more. For composite fibres and pulsed illumination, this normally occurred at around 50% coupling efficiency.

10. If necessary, slight adjustments to lenses 4 and 5 (see figure 5.16) can be altered to

achieve an equivalent relative translation between the objective focus and the fibre tip during the coupling process.

For measuring pulse duration and spectra at the fibre output

1. Maximise coupling efficiency
2. Position Carpe 2p pulse duration sensor (or spectrometer detector head) on an XYZ translation stage below fibre output for pulse duration measurements.
3. Gently lower fibre output to just above the detector.
4. Gently increase the fibre input average power to get a small signal using the Carpe Autocorrelator software and then adjust the Carpe detector head position and parameters in Carpe software until pulses become visible. Note that it will not be possible to measure a pulse duration if pulses have been significantly distorted through the test fibre, or if the intensity at the output is too low.
5. For spectral measurements, average power at output was kept below 2mW. Spectrometer position was adjusted using Thorlabs computer interface to optimise the reading.

Fibre cleaving

This step is necessary for fibre inputs that have been burned, contaminated (not cleanable) or chipped. Poor quality cleaving dramatically reduces the maximum coupling efficiency.

1. Shave the coating from the end few centimetres of fibre using a blade held at around 20° to the fibre.
2. Continue until all coating removed as any remainder could impact cleaving.
3. Use portable cleaving device and clamp fibre in place. Bring cleaving blade down firmly to remove the end of the fibre and refresh the tip surface.

Fibre cleaning

1. **Method 1** The fibre (input) tips can be bathed in acetone, however the plastic coating should be removed by cleaving (see previous method) first as acetone will dissolve this and the glass tip could become contaminated with residue.

2. **Method 2** Place a piece of sticky tape with the sticky side up on a clean bench. Gently hold down the tape with one hand and use the other to delicately tap the dirty fibre tip against an unused section of tape. This method is best for BBG fibre outputs which cannot be cleaved without destroying the Bessel beam generating section.

Alignment at fibre output for spatial profiling measurements

Note that the coupling efficiency of each fibre into the setup should be maximised before the light at the output can be analysed. Care was taken to avoid unnecessary movement when setting up measurement devices at the distal end of the fibre.

For on-axis beam profiling

1. With the laser shuttered:

2. Create setup shown in figure 5.17 below fibre tip. Carefully clamp the 45° mirror in position below the beam on a separate stationary mount, however use cage rod holes on the mirror mount to align with detection arm cage during setup (remove rods when complete).

3. Ensure appropriate filters are slid into place in the detection arm (block some high source power and minimise interference from ambient light sources).

4. With laser still off, use ambient light to adjust the detection arm alignment. When aligned, the fibre output tip should visible and in-focus in the camera feed using back-lighting from a mobile phone torch. Fibre may need to be lowered towards the mirror

to bring tip within range of the detection objective WD. Adjustments to the detection arm are preferable to adjustments of the fibre output or angled mirror position.

5. Now, shield the system using safety box enclosure and turn the laser on with a low power. Detection arm z position is controlled externally using μ-Manager. Translating the detection optics along the optical axis at the output should not result in the image moving across the detector array inside the camera. If necessary, turn off laser and adjust mirror angle to correct any angular misalignment.

Comparative measurements

I wanted to investigate the dependence of 1) spectrum at fibre output, 2) pulse duration at fibre output and 3) average power at fibre output on a) average power at input and b) length and composition of BBG fibre optics (e.g. fibre types, lengths of each section, join types). To investigate the effect of (a) and (b) on (1), (2) and (3), I tested sections of non-composite fibre types that made up the composite BBG fibres individually before analysing composite fibres. This data is presented in section 5.5.4. In tandem, I aimed to verify that the spatial profiles emitted from the composite BBG fibres matched the manufacturer's predictions based on CW illumination at the same wavelength.

Choice of SMF and MMF fibres

Table 5.2 is provided for reference. It shows a complete list of each fibre type that was used for initial studies. Initial studies considered the use of IR pulsed illumination as well as NIR pulsed illumination for 3PE and 2PE studies respectively, therefore SMFs for NIR and IR sources were both considered to begin with.

Name	λ_0/Operating range/nm	Type	MFD/μm	d_{Core}/μm	NA
SMF-28 Ultra	1304$\leq \lambda_0 \leq$1324	SMF	9.2 @ 1310nm	8.2	0.14
780-HP	780-970	SMF	5 @ 850nm	4.4	0.13
FG050LGA	400-2400	MMF		50	0.22
FG105LCA	400-2400	MMF		105	0.22
FG025LJA	400-550, 700-1400	MMF		25	0.1

Table 5.2 Table of fibres used in trials. The trials aimed to find the contributions of each type to non-linear effects occuring in composite BBG fibre optics. λ_0 is the "zero-dispersion" wavelength. SMF: single mode fibre, MMF: multi-mode fibre, MFD: mode field diameter, NA: numberical aperture. These choices covered three target wavelengths for fibre-based Bessel beam generation: 820nm, 980nm and 1310nm. A combination of SMF leading to MMF (of a specific length and diameter) are required to combine multiple modes at the fibre output in such a way that a Bessel-like beam is generated at the output.

5.5.4 Experimental results

Figures 5.18 and 5.19 are calibration plots showing the coupling efficiency of the Newport 10× fibre coupling objective for 920nm and for 1320nm. In both cases, losses through the objective were linear over the maximum average power range. This information was used for fibre coupling measurements - rather than measure the power at the objective output (obstructed by proximity to the fibre), it was sufficient to measure the average power at the objective input as this inferred the average power available at the fibre entrance during measurements.

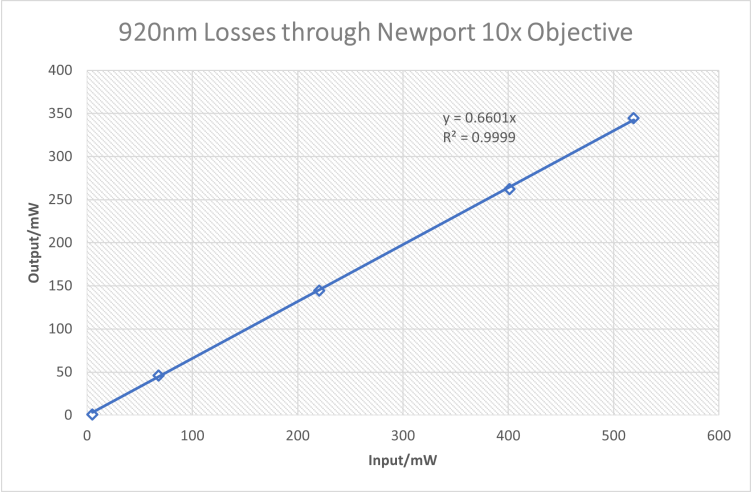

Figure 5.18 Losses were measured through the Newport 10× fibre coupling objective using the 80MHz Chameleon source at 920nm. The central wavelength was verified using a spectrometer. The losses are linear at 66% between 0 and 520mW.

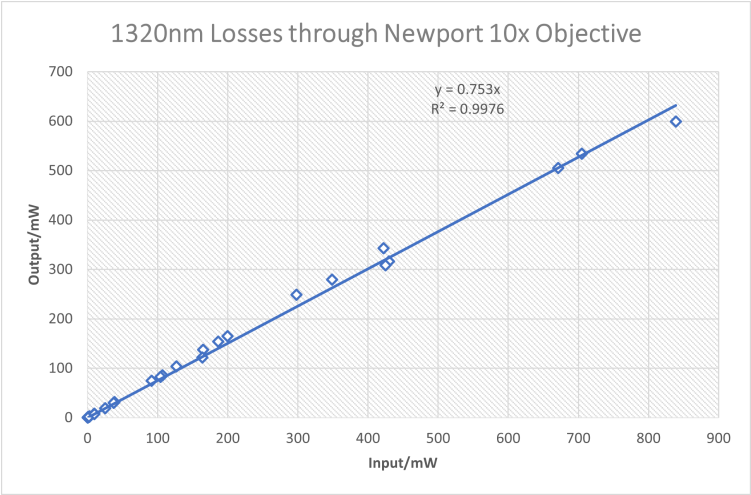

Figure 5.19 Losses were measured through the Newport 10× fibre coupling objective using the 1MHz Opera-F/Monaco source at 1320nm. The central wavelength was verified using a spectrometer. The losses are linear at 75% between 0 and 840mW.

Coupling Efficiency through non-composite SMFs and MMFs

Coupling efficiency (C.E.) can be an indicator of non-linear interactions occurring inside a fibre optic as well as the quality of the optical coupling at a fibre input. Non-linear effects can vary with average power, peak power, mode field diameter (MFD), fibre length, source

wavelength and time, whereas the quality of the coupling should remain relatively consistent with changes to these parameters assuming no damage or misalignment has occurred. The C.E. for each pair was first optimised with an average input power of below 1mW. The C.E. was measured after a) the laser source had warmed up properly (after an hour for Chameleon and Opera-F sources) and b) after at least 15 minutes with the optimised test fibre coupling left active at the low power level. This allowed time for transient effects to subside and the C.E. to stabilise.

It was expected that some non-linear behaviour would occur in the fibres, particularly for SMFs at high peak powers (short pulse durations), high average powers, long fibre lengths and small MFDs [271–276]. For 780-HP SMF (C.E. data shown in figures 5.20 and 5.21), the length of the SMF had an effect on the coupling efficiency. The Chameleon laser at 917nm (figure 5.20) produced pulses with τ = 140fs at the fibre input with f_{rep}=80MHz. The maximum peak power inside the fibre was 21kW. Longer sections of 780-HP had a reduced coupling efficiency above 200mW compared to the 1m section, presumably due to increased opportunity for non-linear interaction through a longer SMF at higher average power. This echoes a previous report where a fs source at 785nm (P_{avg}>200mW) produced evidence of non-linear behaviour which increased with SMF length [79].

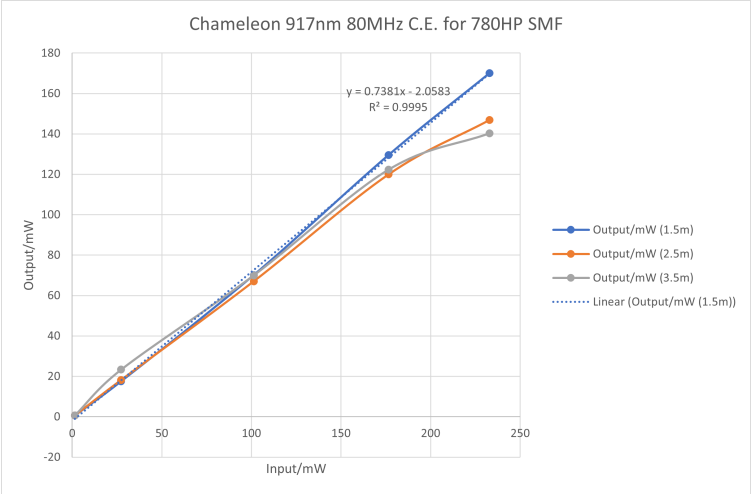

Figure 5.20 The effect of fibre length on coupling efficiency through a single mode fibre. The C.E. is similar for 1m, 2m and 3m. 2m and 3m sections of fibre showed a drop in C.E. above 200mW average input power, whereas the 1m section of 780-HP maintained a linear increase in output average power.

The Opera-F/Monaco laser at 920nm (figure 5.21) produced pulses with $\tau = 100$fs at the fibre input with f_{rep} between 330kHz. The average power at the input was varied by rotating the $\lambda/2$ wave plate in the fibre-coupling setup. The pulses from the Opera-F source had a negative chirp. The estimated maximum peak power inside the fibre was 2400$\times$ greater compared to the Chameleon laser at 817nm case with a peak power of 50MW (estimated using maximum pulse energy of 2μJ and a minimum pulse duration of 40fs). The maximum coupling efficiency was much lower in this case; 48% with 1.5m of 780-HP and 24% with 3.5m of 780-HP.

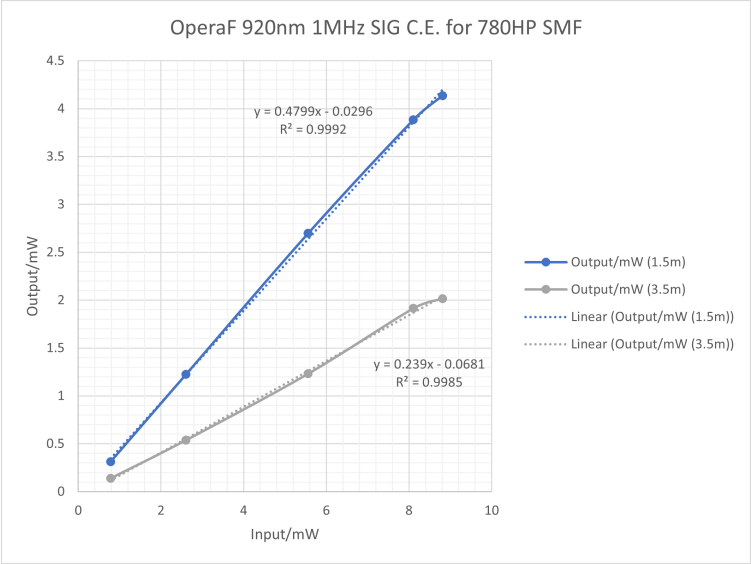

Figure 5.21 The effect of fibre length on coupling efficiency through a single mode fibre. Coupling efficiency was reduced with higher maximum peak power with 48% with 1.5m of 780-HP and 24% with 3.5m of 780-HP.

MMFs, by nature, have a larger core diameter compared to SMFs. It was more straightforward to couple light into the MMFs for C.E. measurements. We anticipated that the MMFs, required for BBG in the composite fibre design, would not cause excessive broadening of the pulse spectra as non-linear effects would be reduced due to reduced confinement of the pulses in the fibre cores [273–276]. These differences were reflected in the coupling efficiencies measured for FG105LCA and FG050LGS with pulsed illumination in the NIR range, as shown in figures 5.22 and 5.23. Coupling efficiencies of >70% were typical, although some tailing-off in the C.E. was still observed at high average input powers for pulses on the order of 100fs. In these examples, test wavelength was selected to match the original design wavelength for the composite fibres (FG105LCA MMF tip for 820nm and FG050LGA MMF tip for 920nm). However, each fibre had similar coupling efficiency at 820nm and 920nm using the Chameleon Ultra II laser. Table 5.3 demonstrates the successful use of FG105LCA at 920nm.

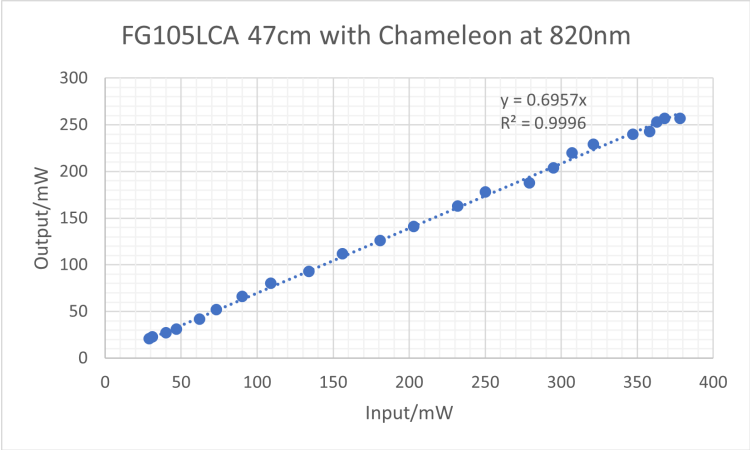

Figure 5.22 Coupling efficiency of 47cm of FG105LCA at 820nm with 140fs pulsed illumination. The coupling efficiency is 71% until 250mW average input power, at which point the C.E. drops to 69% on average between 250mW and 378mW.

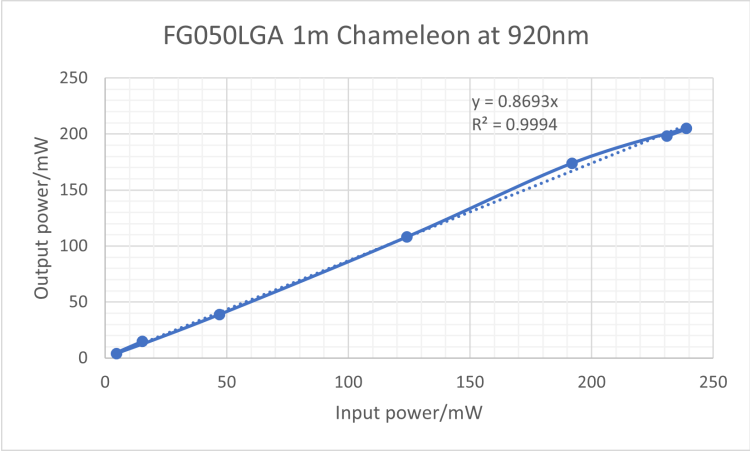

Figure 5.23 Coupling efficiency of 1m of FG050LGA at 920nm with 100fs pulsed illumination. The coupling efficiency is 88% on average with input power ranging between 4.7 and 239mW. At around 200mW there is a dip in C.E., suggesting that non-linear behaviour inside the fibre may be limiting the power available at the output.

MMF sections on the order of 1-3mm are required for generation of multiple spatial modes for the BBG fibre designs. Since the coupling efficiencies observed here were >70% for average input powers below 250mW through >45cm of MMF, it was anticipated that losses to average power at the composite fibre output would be primarily due to losses through the longer SMF sections and to non-linear effects generated throughout the composite fibres. We

expected that there would be a marked increase in optical power losses in composite fibres due to power loss and or non-linear behaviour where the SMF is spliced to the MMF. This was reflected in early data (shown in figure 5.24), where the coupling efficiency was measured through a composite fibre designed to produce a Bessel-like beam at 1320nm. SMF-28 fibre with no MMF spliced to the tip could be coupled with a maximum of 50% efficiency using the same arrangement. Inclusion of the BBG tip reduced the maximum achievable coupling efficiency to just 22% when using pulsed illumination at 1320nm.

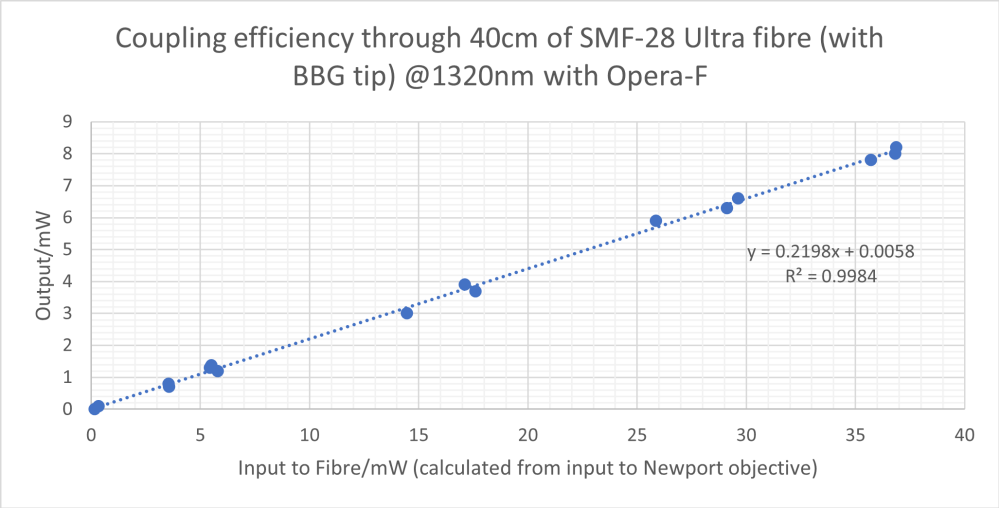

Figure 5.24 Coupling efficiency of 40cm of SMF-28 with BBG tip at 1320nm with 100fs pulsed illumination. The maximum coupling efficiency achieved using this arrangement was just 22%, compared to 50% using 40cm of SMF-28 with no BBG tip.

Pulse duration

Table 5.3 contains a summary of the pulse durations measured before and after sections of fibre. It was not possible to measure a value for the pulse duration (τ) in all cases. Pulses from the negatively-chirped Opera-F source underwent a reduction in τ. Positively-chirped pulses from the Chameleon laser increased in duration after passing through lengths of fibre. Lorentzian functions were fit to the temporal profiles of pulses to estimate τ. In terms of random error, τ was more unstable at the output when pulses were measured using the

Chameleon laser at 820 and 920nm. The pulse shapes were significantly changed in time using the Opera-F source. The random errors listed in table 5.3 do not account for repeatable results fitting to a non-Lorentzian function. Figure 5.25 shows how the pulse shape in time changes between the entrance to the fibre coupling objective (where τ=101±2fs) and the output of 1m of 780-HP SMF (where τ=54±2fs, Opera-F @ 920nm).

Fibre	Length/cm	λ/nm	Source	τ_1/fs	τ_2/fs
SMF-28	40	1320	Opera-F	70±1	54±2
SMF-28 + CSF BBG tip	40 (+2171μm)	1320	Opera-F	70±1	43±3
780-HP	100	920	Opera-F	70±1	NaN
780-HP	100	920	Chameleon	206±3	1500±100
FG025LJA	100	820	Chameleon	206±3	500±50
FG050LGA	100	920	Chameleon	206±3	NaN
FG105LCA	100	920	Chameleon	206±3	500±50
780-HP + FG105LCA BBG tip	40 (+1261μm)	920	Chameleon	206±3	600±50

Table 5.3 Pulse duration, τ, measured before and after lengths of SFM and MMF using illumination at 820, 920 and 1320nm. The uncertainties listed here are random uncertainties. Each measurement was made at least 3×. NaN represents measurements where no stable readings could be made at the fibre output.

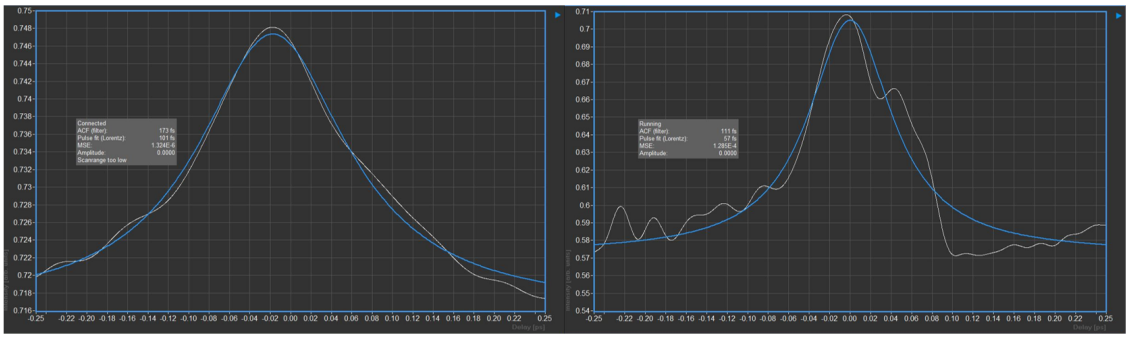

Figure 5.25 Change in shape of pulse in time before fibre-coupling objective and after 1 m of 780-HP fibre. These plots show that τ reduced from 101±2 fs 57±2 fs. to The Lorentzian fit (blue) over the auto-correlation function (white) gave repeatable measurements with a random error of 4%, however the Lorentzian fit itself is poor.

Spectral changes

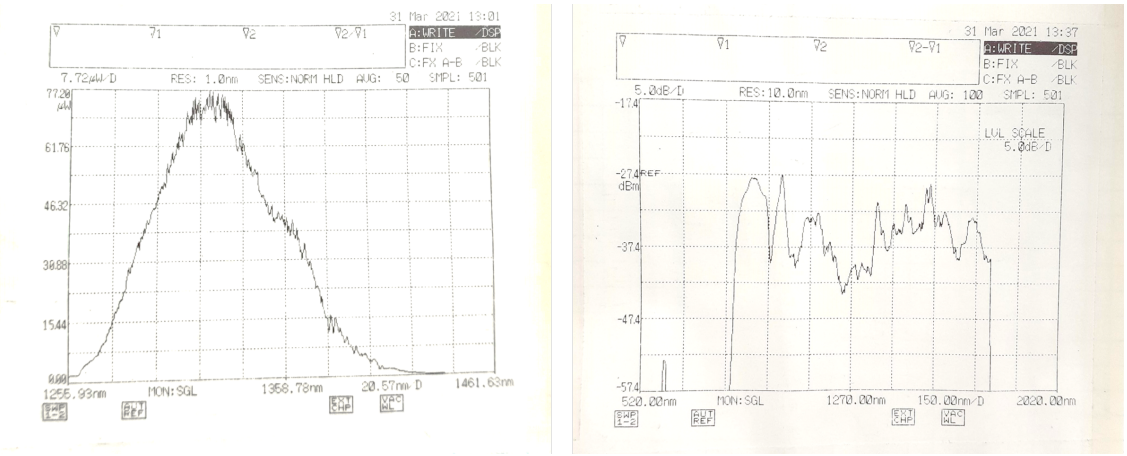

Figure 5.26 Spectrum from Opera-F source (centred on 1320nm) measured before and after 40cm of SMF-28. The bandwidth has been broadened dramatically (80nm to around 900nm). Signs of "cat-ears" were visible on either side of the broadened spectrum. These, plus the spectral broadening indicates the presence of self-phase modulation within the fibre. An additional peak appeared at 600nm, suggesting 2HG or 2PE has occurred within the fibre too.

Initial results from pulse duration measurements suggested that excitation at 1320nm using a negatively-chirped source would be a suitable choice for achieving a low pulse duration at the output of a BBG fibre optic suitable for 3PE fluorescence imaging. However, during these measurements it was noted that orange light appeared at the output of SMF-28 using this source, particularly at average input powers >200mW. Additionally, where the fibre was curved at the input end, signs of supercontinuum generation in the visible range were apparent. Figure 5.26 shows spectra from before and after 40cm SMF-28 using Opera-F pulsed illumination at 1320nm with 330kHz repetition rate. These measurements were taken using a wide range optical spectrum analyser (AQ6374, Yokogawa), which was itself coupled to the measurement site using a MMF. Using these measurements alone, it is not possible to tell exactly how much pulse broadening is due to behaviour in the SMF-28 fibre in the IR region. The visible-NIR range was also measured using a free space coupled spectrum analyser (CCS100 + CCSB1, Thorlabs). This data is shown in figure 5.27. It is clear

from this data that significant generation of NIR and visible light occurs due to non-linear interactions between SMF-28 fibre and pulsed illumination at 1320nm from this femtosecond laser source.

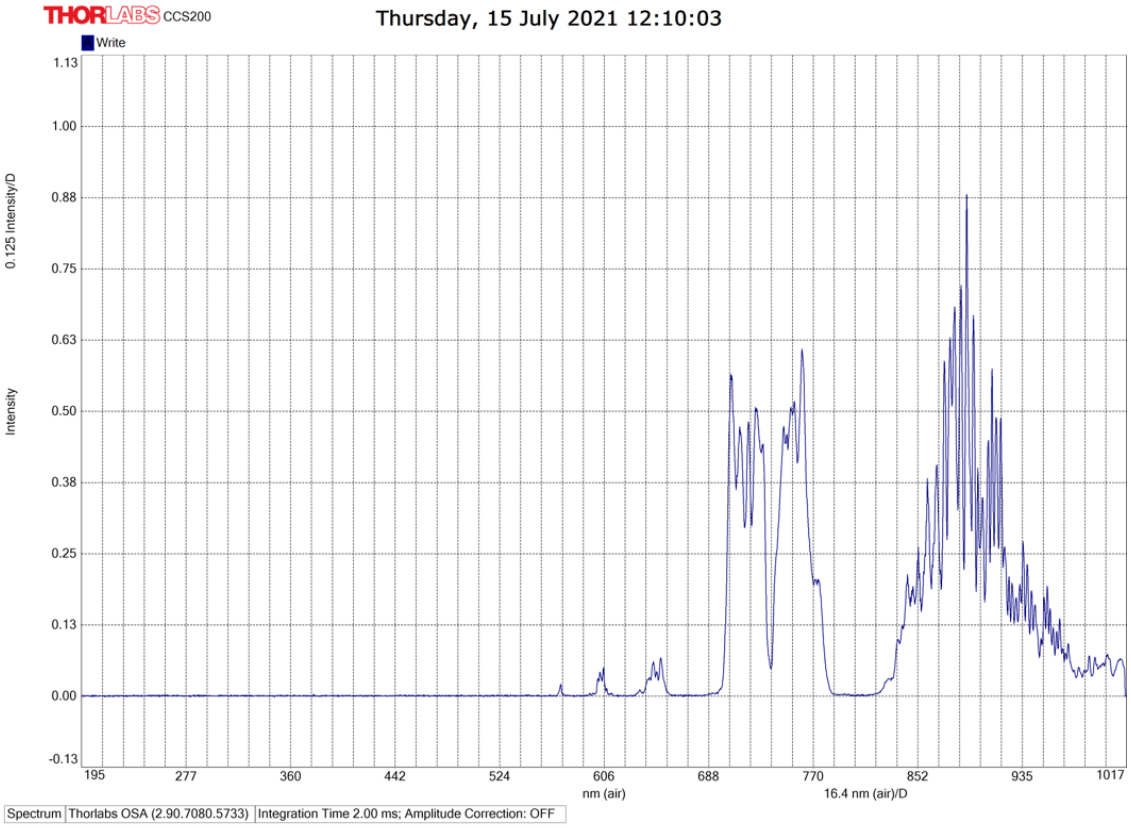

Figure 5.27 Spectrum from Opera-F source (centred on 1320nm) measured before and after 40cm of SMF-28 using visible-NIR Thorlabs spectrometer. Signficant emission in the visible and NIR region (well away from initial peak at 1320nm) is suggestive of significant non-linear interaction between the high energy pulses and the SMF-28 fibre.

Photon production in the visible range is an issue for MPE fluorescence imaging applications. Filtering illumination from the fluorescent signal is difficult when there is overlap between light from the fibre output and signal from a sample. Future work using these fibres with illumination at 1320nm should aim to reduce non-linear behaviour in the fibre itself and/or aim to spectrally filter the SMF output prior to Bessel-beam generation. A thin filter could be added after the microlens at the fibre tip, however any dimension added here is

equivalent to a loss in FoV of the illumination. We put 1320nm illumination to one side and instead pursue use of the BBG fibres with 980nm for 2PE fluorescence imaging.

There were significant changes to the shape of the spectral distribution when Opera-F illumination at 920nm was coupled into 1.5m of 780-HP fibre. The original distribution (shown in grey in figure 5.28 splits in three after the pulses have travelled through the SMF. Increasing average input power increased the separation between the three new peaks and added to the total increase in spectral range FWHM from 35nm to 78nm at 8.8mW average input power.

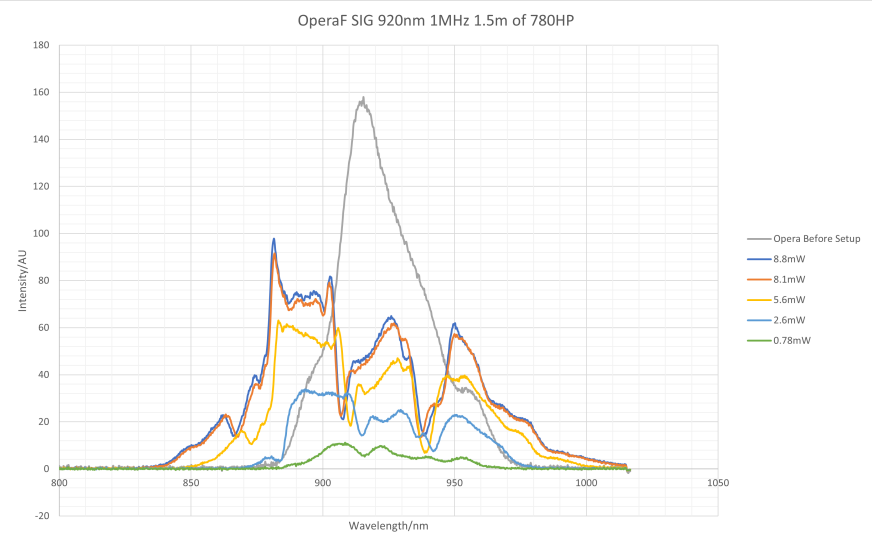

Figure 5.28 Spectrum from Opera-F source (centred on 920nm) measured before and after 40cm of SMF-28 using visible-NIR Thorlabs spectrometer. The FWHM increases from 35nm at the fibre input to 78nm at the output when 920nm illumination at P_{avg}=8.8mW was used.

Pulses from the Chameleon laser at 920nm underwent spectral broadening in 780-HP fibres. Figures 5.29 and 5.30 show the effect of changing fibre length and average power on the spectrum respectively. "Cat ears" appeared in the output spectrum. The separation of the "cat ears" increased with SMF length. The cat ears are attributed to self phase modulation [70, 277]. Spectral broadening is also likely to be caused by this non-linear phenomenon. The FWHM of the spectrum increased from 10nm before the fibre to 56nm

after 1.5mm, 59nm after 2.5m and 64nm after 3.5m.

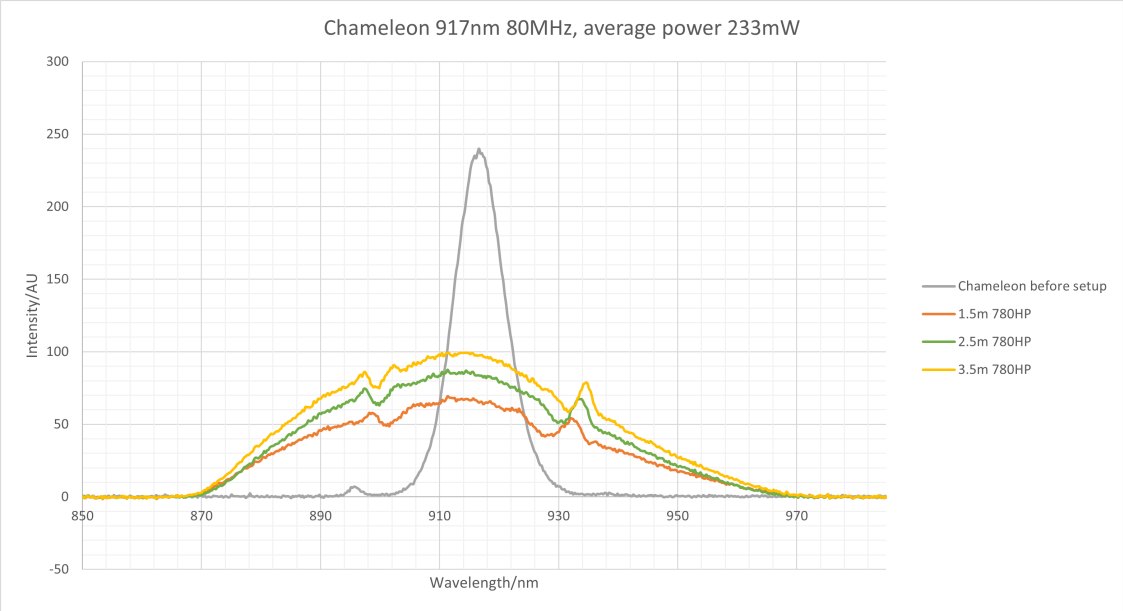

Figure 5.29 Plot showing spectra before and after 1.5m, 2.5m and 3.5m of 780-HP SMF using pulsed illumination at 920nm. Spectral broadening and cat ears are indicative of self phase modulation, a non-linear effect widely observed in SMF [70, 71, 277]

Increasing average input power also increased the FWHM of the spectrum at the output when pulses at 920nm were coupled into 3.5m of 780-HP fibre, as shown in figure 5.30. The spectrum FWHM was 10nm before the fibre, 41nm with 101mW input power and 57nm with 233mW average input power. Cat ears were also visible in this case, however increasing the average input power did not affect their peak wavelength in a repeatable manner.

The peak became slightly blue-shifted with increasing optical power. This shift has been observed previously in the literature [79] and is possibly due to another non-linear interaction called self-steepening [76, 77, 278]. Self-steepening has been associated with 100fs pulses and occurs when changes in the optical intensity at a particular position cause the dispersive properties of the medium (as seen by the propagating pulse) to change in time.

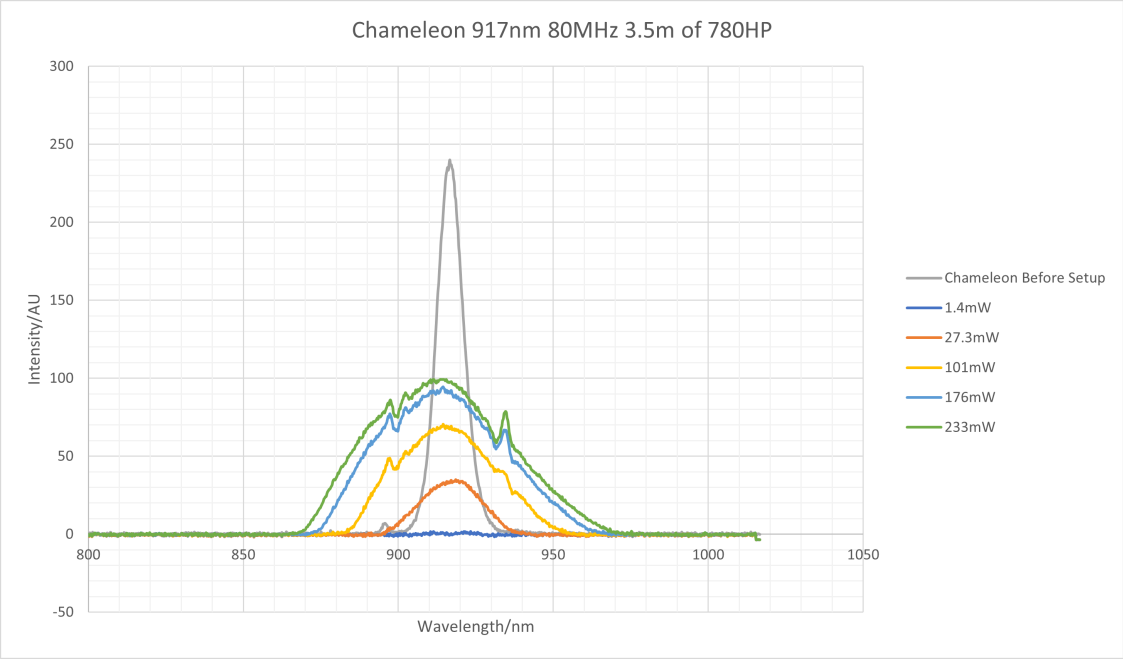

Figure 5.30 Graph showing the effect of changing SMF length with respect to the spectrum at the output. Spectra are blue-shifted and broadened with respect to the input spectrum.

Using the Chameleon Ultra II laser at 920nm, no significant changes to the shape of the spectrum were observed at the output of 1m of FG105LCA, which was selected as the CSF of choice for Bessel-like beam generation at 920nm. The pulse duration increased over the same length of fibre from 206±3 fs to 500±50 fs (see table 5.3).

Three-dimensional spatial profiles

This section summarises the spatial output of the BBG fibre design used to provide Bessel-like illumination with a central wavelength at 920nm. A 40cm length of 780-HP was spliced with 1.261mm of FG105LCA to produce a Bessel-like profile with a FoV of 650μm, over which distance the central lobe FWHM was 7.4μm with a standard deviation of 10.8%. Between 250μm and 650μm from the BBG tip (giving a FoV of 400μm), the central lobe diameter was 7.9μm with a standard deviation of 5%. This compares to a constant central lobe diameter of 7.6μm for a simulated Bessel-Gauss beam over the same range (see figure 5.33), and

7.5μm maintained over 500μm for a similar BBG fibre designed to produce the same profile at 1080nm with CW illumination [269]. The variation in peak intensity over the 400μm measured FoV was 19%, compared to 5% over the same range for the simulated Bessel-Gauss beam. These experimental measurements were made from cross-sectional intensity images taken at the fibre output which were analysed as described in section 5.4.3.

Figure 5.31 shows the average lateral intensity profiles (average of central lines in x and y) from the BBG fibre measured through the central peak at different propagation lengths (z). An example of a 2D intensity image, taken near the surface of a BBG fibre output, is shown in figure 5.32.

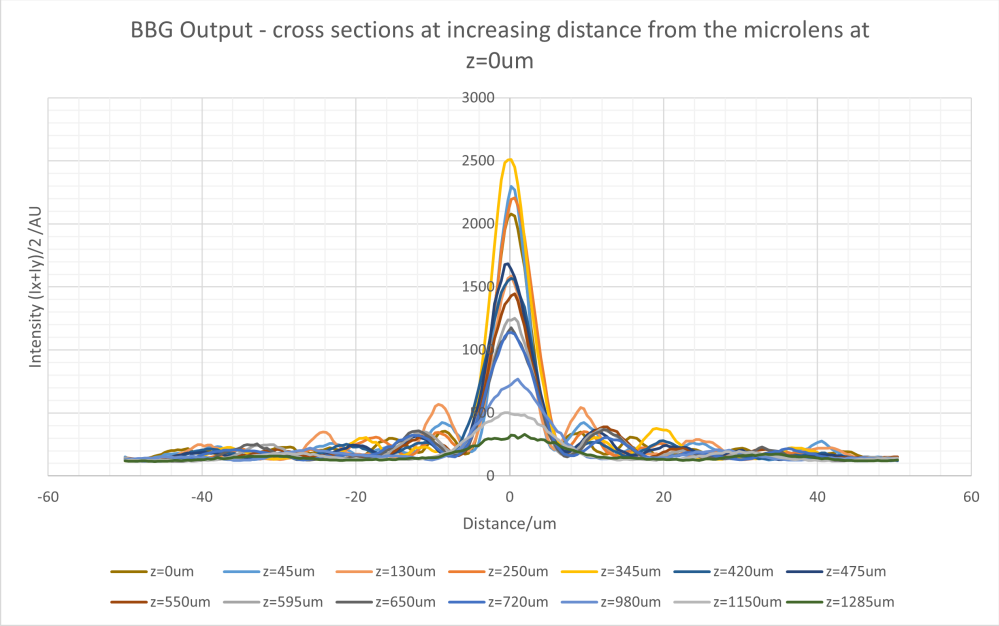

Figure 5.31 Cross-sectional intensity profiles measured through the BBG fibre output at different propagation distances. Horizontal and vertical lines were drawn through the central lobe in each image and these intensity profiles were averaged to produce the data in this plot. Each profile was measured independently to find the FWHM of the central lobe and the peak intensity. An example of an image that was analysed to provide this information is shown in the next figure (figure 5.32).

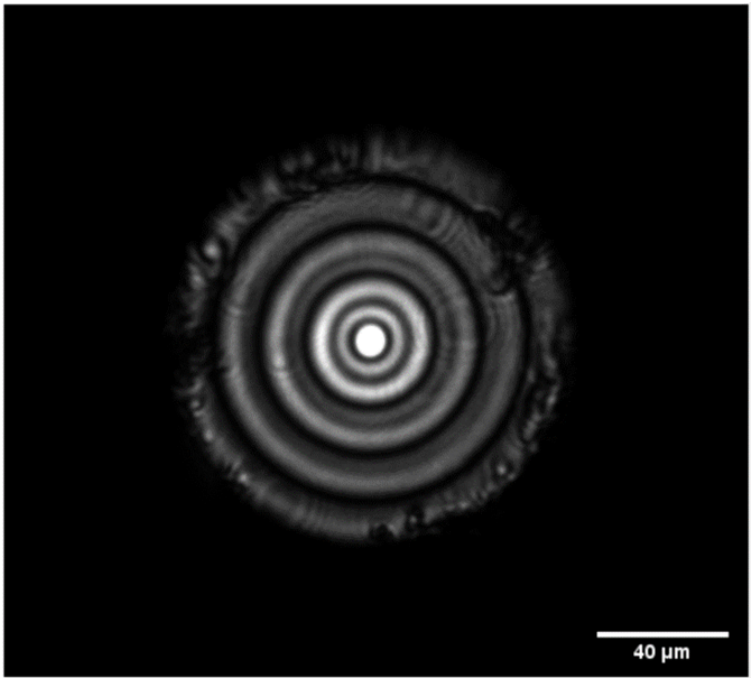

Figure 5.32 An example of a cross-sectional intensity profile at some distance from the BBG fibre output. Some specs of dust on the micro-lens reduce the rotational symmetry of the beam by causing dark spots and diffraction patterns through the outer lobes.

Figure 5.33 compares central mode diameter of the BBG fibres to the central mode diameter of a simulated Bessel-Gauss beam over the same propagation distance.

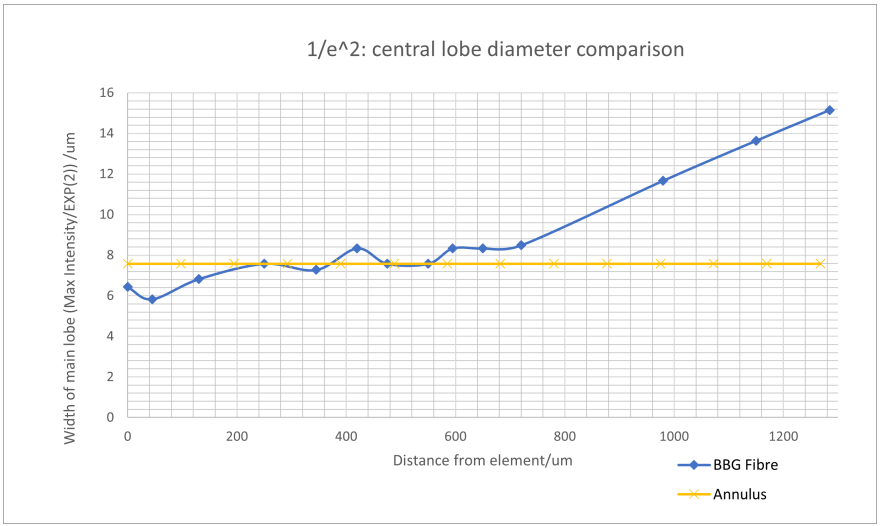

Figure 5.33 Comparison between the central lobe diameter with propagation distance for simulated Bessel beams and BBG fibre outputs. The simulated Bessel-Gauss beam has greater uniformity in central lobe diameter over a greater distance, however there is reasonable similarity 250μm to 700μm from the BBG fibre output at z=0μm.

5.5.5 Discussion

The BBG fibres produced Bessel-like beams at the focus. These beams had an extended FoV with a central lobe FWHM of 7.9±0.4μm over a FoV of 400μm beginning 250mm from the fibre tip. Pulsed light was affected considerably by non-linear effects through the BBG fibres, particularly in the SMF sections. Pulse duration and spectral measurements lead us to select a target wavelength of 920nm and keep the maximum pulse peak power below 21kW. Section 5.6 gives a summary of how 40cm 780-HP fibres with FG105LCA multi-mode tips were used to deliver pulses short enough to generate 2PE in a fluorescent sample despite spectral and temporal broadening through the BBG fibre design.

5.6 Two-photon LSFM with BBG fibre optics

This section will describe a proof-of-concept experiment showing evidence of two-photon excitation of fluorescent beads using Bessel-like illumination from a fibre optic and light-

sheet detection.

5.6.1 Setup

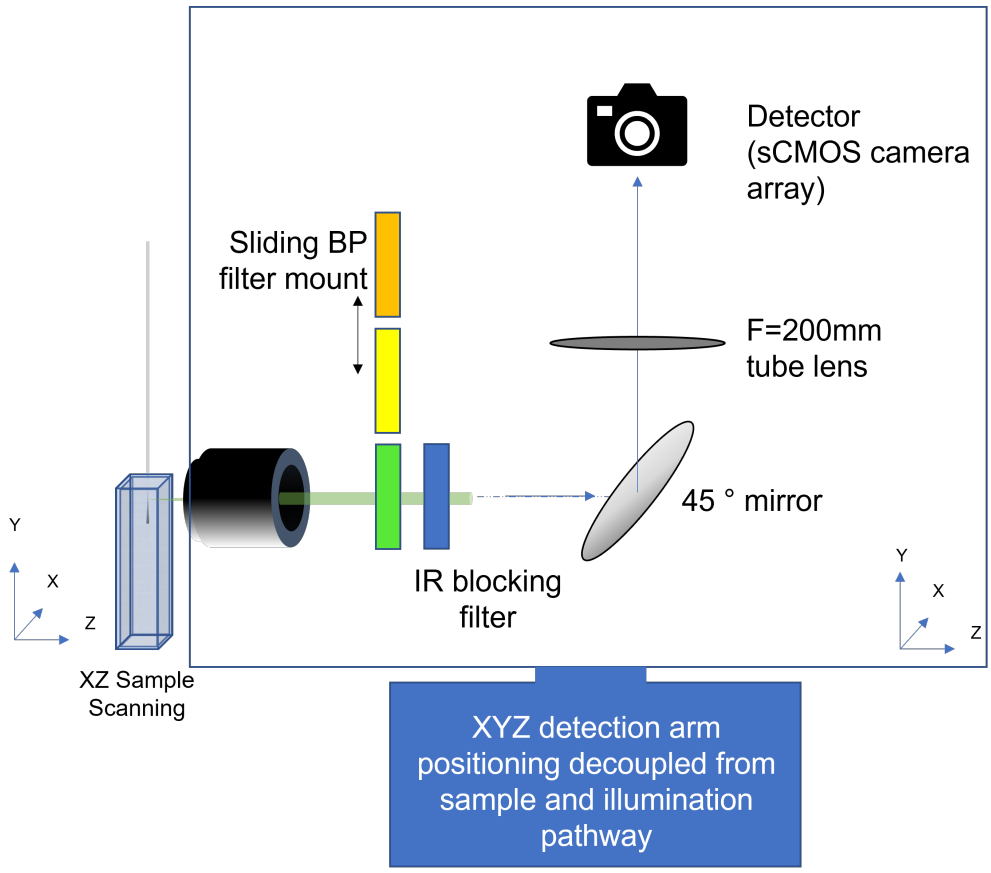

Figure 5.34 Setup for two-photon fibre-based light-sheet fluorescence microscopy with Bessel beam shaping integrated into the illumination. Images of the XY plane were acquired for a particular depth in Z, dictated by the position of the sample and the fibre output.

Figure 5.34 shows a schematic diagram of the optical setup that I used to demonstrate 2PE Bessel fibre-based LSFM. The BBG fibre was coupled to the laser source (Chameleon Ultra II @ 920nm) using the arrangement shown in figure 5.16. The fibre optic consisted of 40cm length of SMF (780HP, Thorlabs) fusion spliced with 1.261mm length of MMF (FG105LCA, Thorlabs). The laser produced positively chirped pulses of 140fs at a repetition rate of 80MHz. For these fibres, optimal coupling efficiency (CE) (taking into account power

loss due to non-linear effects) was maximised at around 50%. The sample was mounted inside a quartz cuvette (shown in figure 5.34). The sample consisted of fluorescent green beads of various sizes from Spherotech, Duke and Thermofisher. Each type of bead was measured separately. Beads were fixed in 1.5% agarose gel made with D_20. Before the agarose gel had set, cuvettes were carefully covered using a 12μm layer of FEP, making sure that no air bubbles remained between the sample and the FEP. The FEP layer was included to prevent damage to or contamination of the BBG fibre tip. Cuvettes were held in place using a custom 3D printed mount (shown in figure 5.35.

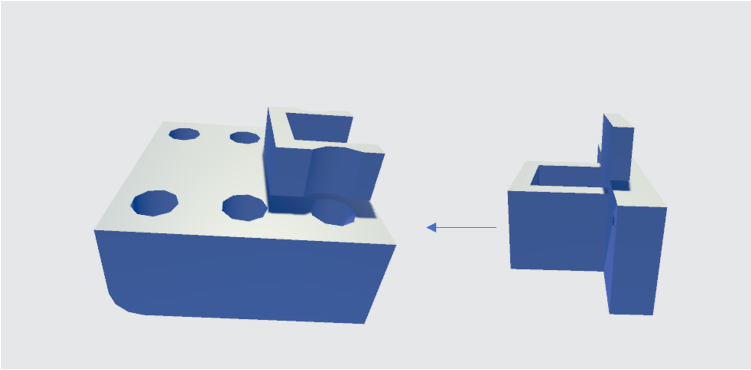

Figure 5.35 Custom-made cuvette mount. The parts were made using a 3D printer. Cuvettes are fitted by slotting vertically into the part on the right hand side before mounting into the system. This part then slides into place on the XYZ mount laterally to fit beneath a pre-aligned BBG fibre optic output. The mounted cuvette is aligned separately using an XYZ translation stage. Lateral scanning in the direction orthogonal to detection and the illumination is used to create a virtual light-sheet within the cuvette-mounted sample.

For detection, I used the same objective arrangement described in section 5.5.1. Cuvette-mounted samples were inserted in place of the 45° mirror shown in figure 5.34.

5.6.2 Methods

To test the non-linearity of the fluorescent response of the beads, background light was minimised as far as possible. The duration of the pulses sent into the fibre was kept constant at 140fs. The average power at the fibre input was tuned between 0 and 500mW using

ND filters and by rotating the $\lambda/2$ waveplate in the illumination path (see figure 5.16). Pulse duration, coupling efficiency and spectra out of the fibre were checked prior to sample imaging using the methods described in section 5.5.

A virtual light-sheet was generated inside the bead sample by scanning the cuvette, mounted on an XYZ translation stage (M-562-XYZ, Newport) laterally using a piezo actuator (M-239, Physik Instrumente). The scanning direction was orthogonal to the LS propagation direction and the detection axis. At each discrete interval along this axis, a snapshot of the fluorescence in the sample was captured with the centre of the vertical Bessel-like beam in focus. A NIR filter (TF1, Thorlabs) and a green bandpass filter (FF01-575/59-25, Semrock) were used to limit illumination light and background radiation from entering the camera. μ-Manager was used to synchronise scanning and image acquisition. The entire process was run from a laptop.

Light-sheet images were reconstructed from the data using a home-made deconvolution program. I trialled two approaches for deconvolution, both of which are described below.

1. Take a wide-field snapshot at each interval. Sum up all the pixels in each frame horizontally to form a column of data for each frame. Stitch the column together to form a 2D image and normalise.

2. Image a single column of pixels down the central lobe of the beam. Stitch columns together directly to form 2D image. 3D imaging could be achieved by repeating this over multiple layers in depth, however it should be noted that with the setup that I used this would involve refocusing the objective between each depth layer.

I found method 2) to work best for my experimental data. No deconvolution or deep learning post-processing was performed prior to the image stitching. The scan step size was matched to the pixel dimensions in the XY plane (orientation shown in figure 5.34). Method 1 includes more the background signal and contributions from any fluorescence generated within sidelobes of the Bessel-like profile. Method 2 does not sample from the sidelobes in

the lateral direction (although there may still be small contributions from side-lobes in front and behind the image plane). This difference results in an increased SNR for method 2 compared to method 1. The apparent resolution of beads in the sample plane may therefore appear to be improved when images are produced using method 2.

It is important to note that the pixel array inside the camera had to be aligned with the Bessel-like beam propagating into the sample (when viewed from the side). If it was not, then another step would be required to rotate the data in the XY plane before a vertical column of pixels is selected for image processing.

5.6.3 Results

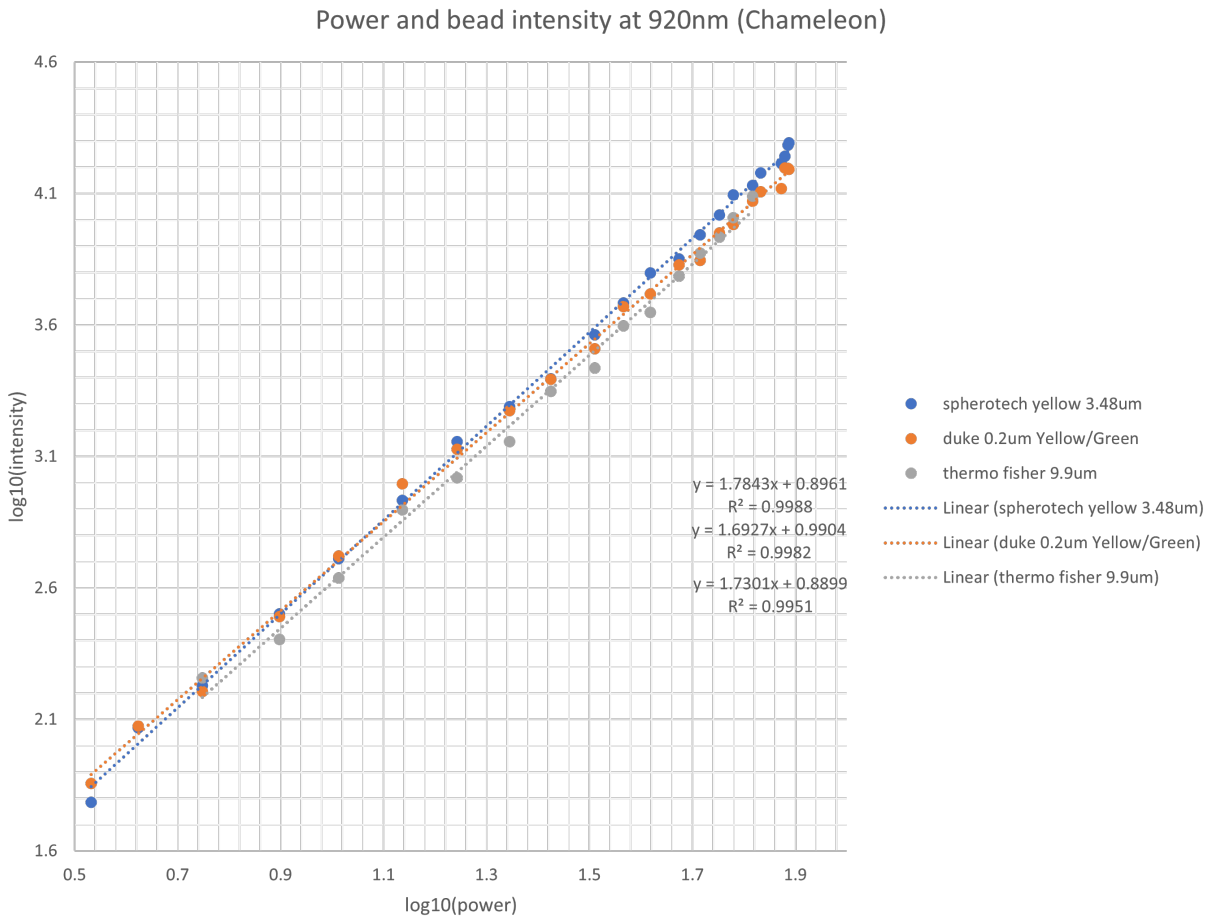

Figure 5.36 Evidence of two photon excitation of fluorescent beads using a BBG fibre to deliver illumination. Several types of beads were measured independently to gather the data shown in this plot. There was strong correlation between the response of beads from Spherotech, Duke and Thermo Fisher of varying average diameters under the same illumination.

Figure 5.36 shows the non-linear relationship observed between the average power at the BBG fibre output and the fluorescent response (measured in maximum intensity over the same field of view in the camera). The log-log plot shows that the bead samples did not have a linear response to the illumination, as this would result in a gradient of 1. 2PE fluorescence is expected to give a gradient of 2 when the data is presented in this way. The data from the three bead samples has an average gradient of 1.74±0.03. We would not

expect a perfect value of two (this would ignore normal experimental uncertainty). This value suggests that 2PE is occurring, however secondary processes could be contributing to the signal as well. Spectral broadening due to self phase modulation in the 780-HP section was consistently observed. This broadening increased with average power. As more optical power is shifted away from the peak absorbance of the sample, it is expected that the total fluorescent response will reduce due to a lowered absorption cross section at those wavelengths. Additionally, the pulse shape measured at the output became increasingly unstable with high average input power. Sub-optimal pulse shapes are expected to reduce the peak power available at the output and thus reduce the likelihood of threshold intensity for 2PE being reached.

Nonetheless, sufficient absorption occurred to image 20μm beads (Yellow High Intensity, Spherotech) using pulsed illumination at 920nm. Images from the centre of the fibre optic Bessel-like output, and then stitching was performed to produce the deconvolved data shown in figure 5.37. The measured bead FWHM was 22.5±1.1μm in y (the LS propagation direction) and 26.6±1.5μm in x (the sample scanning direction). The average dimension measured in x falls within the bead manufacture quoted range of 18.0-24.9μm, however the spread of values in y suggests that the deconvolution process is not yet functioning to completely remove optical modulation from the LS system.

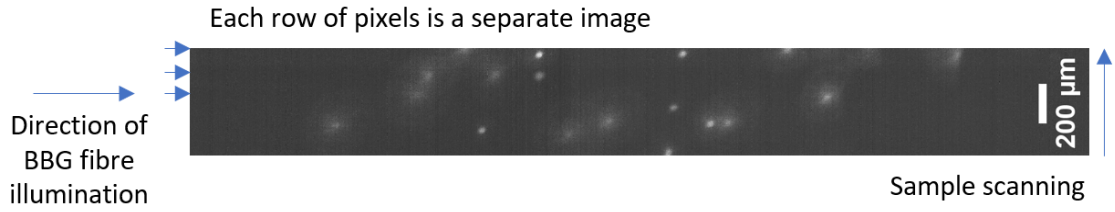

Figure 5.37 Proof-of-concept of fibre-based Bessel-like illumination used to generate two photon excitation for light-sheet detection. The measured bead profiles have an average FWHM of 22.5±1.1μm in the LS propagation direction and 26.6±1.5μm in the sample scanning direction (x axis as shown in figure 5.34). The light propagates from the left had side of the image (y axis in figure 5.34).

5.7 Chapter Summary

I demonstrated that Bessel beams are preferrable to Gaussian and Airy beams for increased depth of penetration with MPE. I have explored two optical elements for generating Bessel-like beams for LSFM with MPE. From beam profile measurements, I found that the meta-surfaces did not produce the propagation-invariant patterns that we were hoping for. However, the BBG meta-surfaces did handle pulsed illumination well with no significant changes to pulse duration or spectra on passing through the thin wafers. There is scope for using these meta-surface elements for future MPE LSFM designs. On the other hand, BBG fibre optics are not intrinsically well-suited to MPE delivery. Significant dispersion of pulses was noted through the BBG fibres, as well as pulse broadening and blue-shifting of the spectra. However, the spatial characteristics of the beam profiles closely mimicked the properties of a "perfect" simulated Bessel-Gauss beam with a 4% difference in average FWHM of the central lobe over a 400μm FoV between 250μm and 650μm from the micro-lens at the BBG fibre output. I successfully used a BBG fibre to generate a Bessel-like virtual light-sheet at 920nm and used this LS to excite 20um fluorescent green beads to produce a non-linear response with 2PE. A light-sheet image was taken using this arrangement to demonstrate proof-of-concept.

Chapter Six

Conclusions

This chapter recaps the goals and findings of the projects described in chapters 3, 4 and 5. Section 6.4 outlines contributions made by others towards these goals.

6.1 Chapter 3

In this chapter, I described the design of a new open-top light-sheet microscope for fresh tissue pathology imaging applications. This microscope improved on previous similar work [56] via the introduction of Airy beam shaping. The design was compact to facilitate off-campus testing in a research hospital environment (see chapter 4). Airy beam shaping was incorporated into the illumination pathway of the OTLS design. The compact OTLS was engineered to allow comparisons to be drawn between Gaussian and Airy imaging in the same sample. The goal of this project was to demonstrate an increase in penetration depth into human tissue using Airy beam shaping with this system compared to Gaussian illumination.

Airy beam shapes were analysed using simulated beam propagation to confirm that we should indeed expect an increased FoV compared to Gaussian beams propagating from the same numerical aperture. The MTF of the two beam shapes were studied across multiple propagation distances to confirm that Airy beam shaping could improve the contrast at depth when used for OPE fluorescence imaging. Bead phantom samples were studied

experimentally using Gaussian and Airy beam shapes. Beads smaller than the resolution limit of the OTLS were chosen to allow experimental measurements of the PSF to be made across the FoV of the microscope for Gaussian and Airy modes. Airy bead data, once deconvolved, demonstrated that Airy mode gave a minimum resolution of $4.2\pm0.6\mu$m. The resolution remained within $\pm5\%$ of this value throughout the FoV in depth. This compared to a minimum lateral resolution of $4.7\pm0.6\mu$m and $\pm79\%$ variation across the 420μm FoV measured for Gaussian mode.

When Airy beam shaping was combined with deep learning post-processing, a resolution improvement of $2\times$ was recorded across the FoV when the OTLS was used to study biological specimens. If biological structures within the sample were larger than the pixel-limited resolution, the resolution enhancement presented itself as an increased signal to noise ratio. Airy mode allowed the OTLS to resolve individual nuclei up to 30% deeper within fresh colorectal samples compared to Gaussian mode imaging of the same area. The extension of the FoV in depth with Airy beam shaping is attributed to the propagation-invariance and to the self-healing properties of this beam type. However, even with Airy beam shaping the penetration depth was limited to around 90μm in the fresh tissue samples that we tested.

Airy OTLS was observed to improve the image quality across the surface of rough-surfaced breast tissue samples compared to Gaussian imaging over the same area. Thick sections of breast tissue, which was much more firm than the colon tissue (also trialled), did not naturally slump to give good attachment across the planar surface of the imaging platform. Airy beam shaping increases the DoF of the OTLS. This makes the setup more forgiving to samples which are raised away from the focal plane at the imaging platform surface.

Fresh cancerous and healthy human colon and breast tissue samples were imaged using the OTLS. The system was able to resolve nuclei shape and distribution, which identified samples as being healthy or diseased. This is indicative of the setup being useful in a modern pathology lab, where every week tissue samples must be processed, imaged and analysed as

quickly as possible and current brightfield imaging requires hours/days per sample. Furthermore, Airy beam shaping increased the depth at which nuclei could be resolved without requiring the samples to be cut. However, in all fresh (non-cleared) tissue the maximum depth of penetration was limited by the strong scattering of blue light. 90μm maximal penetration depth may not be deep enough to allow cellular growths inside thick tissue samples to be fully understood in 3D as in this case we would ideally be able to track changes through more than 2-3 layers of cell growth [123].

A cleared tissue sample was also studied. This sample was a section of mouse brain containing amyloid plaques stained with fluorescent thioflavin S. The images demonstrated that Airy beam OTLS could be of value for biomedical research applications. Amyloid plaques build up during the progression of Alzheimer's disease in humans. Accurate, high resolution, 3D reconstruction of these features growing in mouse brains allow us to develop improved models of the disease in humans.

6.2 Chapter 4

The work presented in this chapter covers a scoping exercise undertaken in collaboration with the Albert Einstein Institute in New York. We wanted to understand how the microscope would perform as an everyday medical microscopy tool. The goal was to identify if and when the OTLS could provide diagnostic information in a shorter timeframe than brightfield microscopy could.

However, first we required local staff to learn how to use the light-sheet system. We also required a framework that allowed structures revealed in OTLS data to be matched up to features visible using traditional brightfield imaging, as changes to the staining protocol and optical imaging technique meant that we could not assume equivalence.

Chapter 4 describes the workflow that we employed to address these points. We used Gaussian OTLS only for this initial study. The scoping exercise revealed that whislt there

is potential for LSFM to be applied to diagnostic pathological imaging, the trailed design cannot be treated as a one-size-fits-all fresh tissue imaging device. The firmness and surface texture of the samples that we tested (including heart, breast, endometrium, stomach and kidney) required tailored approaches to sample mounting. Whilst the LSFM was designed for fresh tissue imaging, the reality is that human tissue begins to decompose as soon as it is excised from a patient. Usually, fresh tissue imaging must take place within one hour of excision. This is not always practical. Preservation techniques such as flash freezing or fixing in formaldehyde are necessary for delayed imaging. We imaged an array of fixed tissue samples, which behaved quite differently to fresh samples of the same type. Fixed tissues were generally more rigid.

In a hospital environment, it is difficult to predict ahead of time which samples will need to be imaged and when. For practical reasons we were not able to develop staining and mounting protocols for each tissue type prior to the installation of the microscope at the hospital. We found that our fresh tissue staining protocol with acridine orange, originally developed for flash-frozen then thawed colorectal tissues, was only partially suited to other kinds of fresh tissue staining and even less suited to formalin-fixed samples. Future work on this project should account for the time that will be needed to develop sample-specific staining protocols for this kind of fluorescence imaging.

Pathologists who operated the LSFM provided valuable feedback alongside their microscopy data. This feedback included suggestions on how the design could be improved to make future work run more smoothly. Towards the end of chapter 4 I describe an adapted version of the compact OTLS setup. The new version facilitates two-colour imaging to image the stain and counter-stain H&E brightfield images that all modern pathologists are familiar with. The design is more resilient to misalignment over time, which is also important if an instrument is to run for several months without a service. Airy beam shaping mode is included in the design. Airy beam shaping mode is recommended for imaging samples were the staining protocol has been optimised and deeper information is required. This mode may

also help to image samples with irregular surfaces or firm samples that do not adhere well to the imaging platform. This design is available for anyone wishing to continue working in this vein.

6.3 Chapter 5

In this chapter, I abandoned visible light in favour of NIR illumination for LSFM which can exploit a therapeutic window into human tissue (see section 2.3.3). The aim was to produce an alternative light-sheet microscope design that incorporated beam shaping with an NIR pulsed laser source.

First, I demonstrated that Airy beams are not an ideal candidate for extending the FoV of illumination for non-linear fluorescence microscopy. Beam propagation modelling showed that the MTF of the Airy beam was reduced for MPE compared to OPE throughout the FoV. Bessel beam shaping, also propagation-invariant and self-healing, is a more suitable alternative for MPE. Indeed, Bessel beam shaping has already been successfully combined with LSFM on many occasions [55, 279–282]. I explored two separate avenues for Bessel beam shaping with LSFM.

The first method was Bessel beam generation using custom meta-surfaces provided by collaborators at IIT Madras. The meta-surfaces had a negligible effect on the average power (<1%), bandwidth (none measured) and pulse duration (<3fs) of high peak energy beams at 1064nm (P_{peak}<21kW). They produced concentric ring patterns with an average central lobe diameter of 23.6±9μm up to 17.5mm from the wafer substrate. With cross-sectional down-scaling, the FoV was reduced to around 10mm but with substantial changes in the central peak FWHM (21%) across the FoV and the beam had a central lobe peak intensity variation of 78%. These numbers indicate that use of this meta-surface design for LSFM illumination would not result in a uniform LS across the FoV.

Meta-surfaces are thin, lightweight and readily tailored to produce specific beam param-

eters for a particular incident wavelength. Future work could include the development of a BBG meta-surface designed to have a central lobe diameter of $<5\mu$m for 980nm incident light. The FoV would likely be shorter for this central lobe diameter due to diffraction effects, however the Bessel-like profile would then contain spatial frequencies high enough to resolve sub-cellular features in the axial direction should the illumination be used in an LSFM setup. Small variations ($<10\%$) in the central lobe peak intensity and FWHM could be tolerated if there was some way to predict the location of the changes so that the altered PSF could be deconvolved from fluorescence images later during post-processing.

Chapter 5 also considered the use of BBG fibre optics to produce patterned illumination for LSFM. The beam profiles produced by these fibres were more uniform than those produced by the meta-surfaces, with a central lobe diameter comparable to that of a similar simulated annulus generated Bessel-beam 250-700μm from the fibre tip (as shown in figure 5.33). The average FWHM was measured at 7.4$\pm$0.8μm. However, we wished to use pulsed illumination to combine the benefits of propagation-invariant beam shaping with the improved sectioning ability of non-linear fluorescence and illumination in the NIR to exploit the therapeutic window into human tissue. This BBG fibre design relies on a single mode section of fibre to set up the initial conditions necessary for Bessel-beam generation at the tip. It is well known that non-linear effects can be striking when pulsed illumination is transmitted through single mode fibres [70, 71, 79, 272–277, 283, 284]. In this chapter, I summarised the new design of a BBG fibre for 920nm pulsed illumination; a collaborative effort with Yonsei University. We attempted to reduce the non-linear effects by increasing the core diameter of single mode fibre sections, experimenting with multi-mode delivery and shortened single mode sections, and a variety of source parameters. This was with the aim of maintaining a short pulse duration between the source and the fibre output, reducing additional wavelength generation and maximising fibre coupling efficiency.

The result of these studies was a demonstration of 2PE LSFM with Bessel-like beam illumination delivery with a fibre optic. The BBG fibre composition was 40cm of 780-

HP spliced with 1261μm of FG105LCA MMF. This design increased the pulse duration by around 3$\times$ compared to the pulse duration at the fibre input (from 206fs to 600fs). The SMF section increased the spectral bandwidth from 10nm to $\leq$56nm and blue-shifted the peak from 917nm to 912nm when an average input power of 233nm was applied. These effects are attributed to self-phase modulation and to self-steepening respectively. The fluorescent response of beads from Spherotech imaged during this demonstration varied with $I_{ex} \propto I_{em}^{1.78}$. This suggests that 2PE was a dominant contribution to the measured signal, however light-leakage from non-linear effects inside the fibre were also contributing to the overall response. A "pure" demonstration of 2PE would have $I_{ex} \propto I_{em}^{2}$. The bead sample was scanned through the Bessel-like beam to produce a virtual light sheet. Images taken at each interval of the scan were deconvolved to produce a single LSFM image showing 20μm fluorescent green beads undergoing 2PE.

Future work should aim to further reduce the non-linear effects produced in the fibre optics, perhaps with pre-compensation for pulse dispersion. The output of the BBG fibre could include an integrated spectral filter to remove visible or NIR light (distinct from the sample absorption spectrum or overlapping with the sample emission spectrum) generated inside the fibre from NIR illumination. The detection optics of the LSFM could also be fibre-based, using a GRIN lens for fibre detection. This would allow the development of a compact probe head for *in vivo* medical microscopy applications. The deconvolution process should be bettered to further remove artefacts from the imaging system from the data in the sample scanning direction. The setup could be further adapted to allow volumetric light-sheet imaging. In the air-based sample mount that I used here, any changes in distance between the sample surface and the detection objective required manual refocusing of the detection optics. This issue could be resolved by a) automating the refocusing for 3D acquisitions or b) developing a fluid-based sample mount where the fluid and sample are RI-matched.

6.4 Acknowledgments

6.4.1 Chapter 2

The beam propagation code used for simulations shown here and in chapter 5 was adapted from a program developed by Dr Philip Wijesinghe.

6.4.2 Chapter 3

Prior to my engagement with this project, Dr Stella Corsetti had developed a similar OTLS microscope with Airy beam shaping for this application. This system was inspired by a publication by Adam K Glaser *et al.* [56]. Dr Corsetti and I spent two weeks working together on it before her maternity leave began. I then took over the project with remote assistance from her for off-campus studies. I redesigned the optical path lay out and built a new (more compact) OTLS based on her initial work. The new system had a second beam path for Airy mode to make Gaussian and Airy LS comparisons easier to conduct. The Airy pathway contained a second telescope to allow the focus of the two beams to be matched inside samples. I also added a laser safety enclosure, vibration isolation feet and switched from desktop to laptop control to improve portability. I folded the beam path in such a way that mirrors would be positioned in the focal planes of telescopes where possible to allow for easier alignment of the LS. Dr Jonathan Nylk and Dr Federico Gasparoli assisted me with practical aspects of the system redevelopment. The deep learning algorithm was developed for our OTLS microscope by Dr Philip Wijesinghe. He applied this algorithm to data supplied to him by Dr Stella Corsetti and myself. Dr Shuzo Sakata provided and processed the mouse brain samples. Prof Simon C Herrington assisted in our application to the Tayside Tissue bank for human tissue samples. Dr Khushi Vyas provided the breast tissue sample, facilitated an early trial of my redesigned OTLS at Charing Cross Hospital, London and provided valuable insight into the implementation of such systems in a hospital

research laboratory.

6.4.3 Chapter 4

I am grateful to the team at the Albert Einstein Institute. In particular, Dr James Pullman invested a huge amount of time and energy into this work. Prof Michael Prystowsky oversaw the project on the NY side. Dr Ijeoma Green, Dr James Pullman and Dr Joseph Albanese ran the setup on a day-to-day basis and assisted me with interesting discussions on how this technology could fit into the pre-existing workflow of their pathology department. Dr Joseph Albanese and Dr James Pullman prepared the human tissue samples and imaged the samples on the setup, with assistance from me to begin with. Dr Jonathan Nylk accompanied me to New York. In the first instance this was to conduct his own separate collaboration, however mutual practical assistance enabled setup and alignment of our separate systems, particularly when some parts needed to be re-attached to our setups post-transit. I processed the data shown and generated all figures in this chapter. Dr Stella Corsetti and Dr Philip Wijesinghe joined discussions on the redevelopment of the OTLS for histopathology.

6.4.4 Chapter 5

The meta-surfaces were made by Yerragadda Guruvaiah at IIT Madras. I am grateful to Dr Shanti Bhattacharya for her discussion on fabrication of meta-surfaces. Dr Hyeonwoo Lee fabricated all of the BBG fibres used in this chapter and shared a lot of his time discussing new designs with me. Professor Kyungwhan Oh and Professor Kishan Dholakia assisted with design considerations. Dr Philip Wijesinghe, Dr Saba Khan, Dr George Dwapanynin and Dr Mingzhou Chen assisted me by offering their knowledge on aspects of the physics of non-linear fluorescence and fibre optics. Dr George Dwapanyin offered practical assistance with the LSFM setup and fibre optic testing in the lab.

APPENDICES

Appendix A

First Appendix

Mainly colon actually.

Appendix B

User guide for compact OTLS

Compact Light-Sheet Microscope for Histopathology User Guide

Persephone Poulton

August 2019

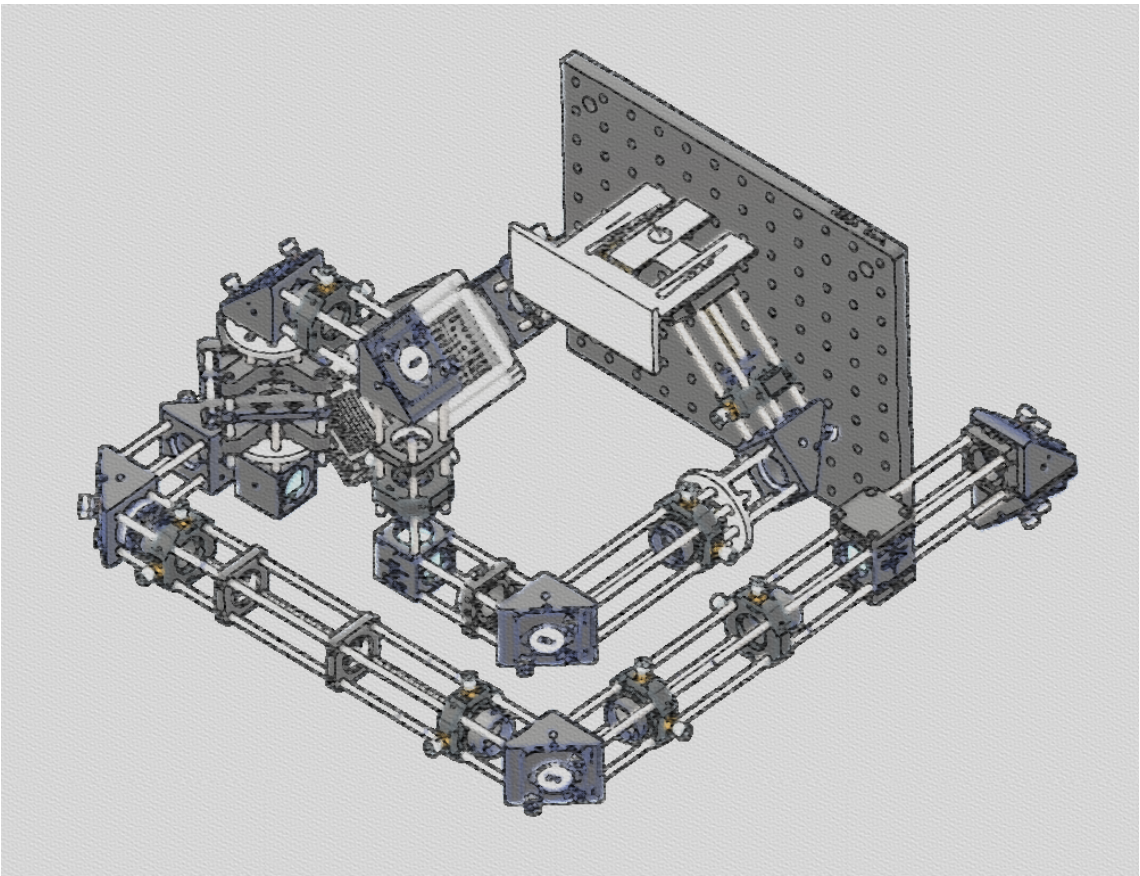

University of St Andrews | FOUNDED 1413

List of Abbreviations

CLSM	Compact Light-Sheet Microscope
FOV	Field of View
FWHM	Full Width Half Maximum
LS	Light-Sheet
LSFM	Light-Sheet Fluorescence Microscopy
LSM	Light-Sheet Microscopy
NA	Numerical Aperture
PBS	Phosphate-Buffered Saline
PSF	Point Spread Function
sCMOS	Scientific Complementary Metal-Oxide Semiconductor
SIL	Solid Immersion Lens

Contents

1 Safety **1**
- 1.1 Laser Safety . . . 1
- 1.2 Chemical Safety . . . 1
- 1.3 Sharps . . . 2
- 1.4 Bio-hazardous Waste . . . 2

2 Kit List for Alignment and Testing **2**
- 2.1 General . . . 2
- 2.2 Sample Preparation . . . 3

3 Introduction **3**

4 System Overview **4**
- 4.1 Components . . . 6
  - 4.1.1 Vortran Stradus 488 Diode Laser . . . 6
  - 4.1.2 Filters . . . 7
  - 4.1.3 Phase Mask . . . 8
  - 4.1.4 Mirrors . . . 10
  - 4.1.5 Cylindrical Lens . . . 10
  - 4.1.6 Spherical Lenses . . . 10
  - 4.1.7 Hamamatsu Orca Flash 4.0 sCMOS Camera . . . 11
  - 4.1.8 Nikon 4× Objective Lens . . . 11
  - 4.1.9 Solid Immersion Lens . . . 13
  - 4.1.10 Aperture . . . 14
  - 4.1.11 Wave-plate . . . 14
  - 4.1.12 Polarising Beam Splitter . . . 14
  - 4.1.13 Motorised Sample Stage . . . 15
  - 4.1.14 Zoom Lens . . . 15

5 Alignment **15**
- 5.1 Alignment Protocol (Rough Guide) . . . 15
- 5.2 Ideal "Unaberrated" Beads . . . 17
- 5.3 Test Samples . . . 18

6 Potential Imperfections **21**
- 6.1 Spherical Aberration . . . 21
- 6.2 Astigmatism . . . 22
- 6.3 Coma . . . 23
- 6.4 Incorrect Oil Layer Thickness . . . 23
- 6.5 Scanning Errors . . . 24
- 6.6 Dirty Lens . . . 24
- 6.7 Illumination Beam Not Focussed at the Surface . . . 24
- 6.8 Twisted Camera . . . 25
- 6.9 Hanging Camera . . . 25
- 6.10 Objective Not Focussed . . . 25

7 Software **25**
- 7.1 Vortran Stradus . . . 26
- 7.2 PI MikroMove . . . 26
- 7.3 HC Image Live . . . 26
- 7.4 μ-Manager . . . 27
  - 7.4.1 Connecting External Hardware . . . 27
  - 7.4.2 Live . . . 28
  - 7.4.3 Stage Control . . . 28
  - 7.4.4 Crop . . . 28
  - 7.4.5 Multi-D Acquisition . . . 28
  - 7.4.6 Creating a New ".cfg" File . . . 29

7.5 FIJI (Is Just ImageJ) . . . 31
7.5.1 Brightness Contrast . . . 31
7.5.2 Re-slicing . . . 32
7.5.3 Set Scale . . . 32
7.5.4 Scale Bar . . . 33
7.5.5 Z Project . . . 33
7.5.6 Crop . . . 34
7.5.7 Transform . . . 34
7.5.8 Scale... . . . 35
7.5.9 Lookup Tables . . . 35
7.5.10 Plot Profile . . . 36
7.5.11 Measure . . . 37
7.5.12 Synchronize Windows . . . 37
7.5.13 Shear . . . 37
7.5.14 ClearVolume . . . 39

8 Sample Preparation **39**
8.1 1% Agarose Gel . . . 39
8.2 Fluorescent Beads . . . 39
8.2.1 0.2μm . . . 39
8.2.2 4.8μm . . . 39
8.2.3 9.9μm . . . 39
8.3 Fluorescein . . . 40
8.4 Tissue Samples . . . 40
8.5 Other Samples (e.g. cleared) . . . 40

9 SIL Cleaning Protocol **40**

10 Taking Measurements **40**
10.1 Fine-tuning the Focus . . . 41
10.2 Example Human Tissue . . . 42

11 Calibration **42**
11.1 Pixel Size (Lateral Resolution) . . . 42
11.2 Point Spread Function (PSF) in the Plane of the Light-Sheet (Axial resolution) . . . 43
11.3 Field of View and Width of the Light-Sheet . . . 44
11.4 Depth of Penetration in Various Samples . . . 44
11.5 Airy Profile (for Deconvolution) . . . 45

12 Image Processing **45**
12.1 Shearing . . . 45
12.2 Deconvolution (For Airy Data Only) . . . 45

13 Saving Data **45**

14 Everyday Use **45**

15 References **46**

1 Safety

When the microscope is used off-campus at collaborating institutions (not within the University of St Andrews), the host researchers are responsible for ensuring that appropriate safety measures are put in place. With that in mind, THIS SECTION CONTAINS SUGGESTIONS ONLY FOR OFF-CAMPUS USERS.

A complete risk assessment should be done for every activity that will be carried out. This assessment should consider potential danger to anyone who may come into contact with it, not just registered users.

1.1 Laser Safety

These notes have been written as a rough guide for Compact Light-Sheet (LS) Microscope users within the University of St Andrews campus. Formal laser safety training is provided by the School. This is compulsory training for anyone using lasers. When the microscope is used off-campus, the host institution laser safety rules apply instead.

- The lab is fitted with an interlock system. This should always be connected to any potentially harmful laser that will be used. The laser will cut out if anybody opens the door without entering the password (entering the lab) or pressing override (leaving the lab). Lab 250 is relatively busy with many different experiments – it is a good idea to knock in case somebody is using a laser that requires eye protection.
- Do not wear jewellery or other reflective things when using the experiment.
- Safety goggles are a last line of defence. Always check that the goggles provide the right protection for the particular wavelength and power that you are using.
- Never put your eyes to bench level or look somewhere where stray beams are possible.
- This laser has a very short warm up time. It should be turned off when not in use.
- Shutter the beam when taking optics in or out of the system.
- Always fix down tamper-proof laser safety box for normal use (this feature is not possible during maintenance and alignment). This box is fitted with its own interlocking system so that when the lid is removed, the beam is automatically shuttered.
- When working outside of normal lab (in a non-designated laser zone), warning signs should be put on the lab door and the temporary laser area protocol should be observed (see adjoining document).
- All persons using the compact light-sheet microscope (Compact LSM) must be laser safety trained by the host institution before doing so.
- Appropriate laser safety goggles must be worn when open beam work is unavoidable.
- The laser power supply box security key must not be left unattended with the system. A trained responsible person must keep the key somewhere secure.
- When the system is being aligned (no safety box), a temporary beam block should be fastened to the sample stage to avoid stray beam leaving the system at an upwards angle of 45°.
- The interlock cable **must not** be removed from the laser power supply box at any time when mains electricity is flowing. This error will render the interlocking system useless. The cable must be fixed to the box securely and a label will be added to the power supply to warn users of the risk.

1.2 Chemical Safety

Check the safety data sheet for each chemical before you use it, and include the recommended actions in your risk assessment. The following substances are used on a daily basis for cleaning, imaging and preparation of samples. The following notes are **only a rough guide**: please go through and read the official safety documentation yourself and familiarise yourself with it (e.g. SDS).

- **Immersion Oil:** Use in a well ventilated space. Wear protective gloves and wash skin well with soap and water if exposed. Wash work clothes seprately. We use type NF Nikon immersion oil (n=1.51) to provide a refractive index-matching layer between the solid immersion lens and the cover slip. Several immersion oils have been tested with the system; we have found that Nikon type NF is the most suitable (discontinued - type F2 is a superior replacement). Immersion oil is cleaned with ethanol and isopropanol.
- **Absolute Ethanol:** A small bath of this is used to remove the worst of the immersion oil from solid immersion lens (SIL).
- **Isopropanol:** Used to remove the ethanol and remaining oil residue from the SIL.
- **Phosphate Buffered Saline (PBS) Solution:** Used to improve the uptake of acridine orange dye into the tissue cells. https://www.sigmaaldrich.com/catalog/product/sigma/806544?lang=en&region=GB
- **Acridine Orange (Acridine Orange hydrochloride solution 10 mg/mL in H2O):** Used to stain nuclei in tissue samples for histopathology. Wear protective gloves and a lab coat in a well ventilated area. Wash work clothes separately. https://www.sigmaaldrich.com/catalog/product/sial/a8097?lang=en&region=GB.
- **1% Agarose Gel:** Prepared from agarose powder and pure water. Used to fix fluorescent beads. https://www.thermofisher.com/order/catalog/product/16520050
- **0.2μm Fluorescent Green Polymer Beads:** Used to measure the point spread function (PSF) of the microscope for calibration. https://www.thermofisher.com/order/catalog/product/G200
- **4.8μm Fluorescent Green Polymer Beads:** Used to check alignment of the microscope. Can also be used to confirm deconvolution parameters. https://www.thermofisher.com/order/catalog/product/G0500
- **Fluorescein:** Used to check alignment of system and measure the intensity profile of the beam. https://www.thermofisher.com/order/catalog/product/F1300
- **Pure Water** Used to make contaminant-free dilutions of bead samples and agarose gel.

1.3 Sharps

All cover slips, scalpels and other sharp items should be placed in a sharps bin after use (this includes sharps that are contaminated with biological waste). Collaborating institutions may have alternative waste management strategies.

1.4 Bio-hazardous Waste

Appropriate local guidelines regarding bio-hazardous materials should be adhered to. In particular, there should be a waste disposal scheme in place and appropriate personal protective gear should be worn (lab coats, protective gloves, eye shields may be appropriate). Extra precautions may also be required.

2 Kit List for Alignment and Testing

2.1 General

Aside from the aforementioned chemicals, the following lab tools and consumables are required.

- At least 3 t-shirts
- Assorted allen keys
- Assorted screwdrivers
- Optics cleaning tissues
- Soap

- Laser safety goggles (488nm)
- Gloves
- Spectrometer (not essential for normal use)
- Lab interlock/laser safety box (included with system)

2.2 Sample Preparation

- Cover slips
- Dry heat bath
- Pipettes and pipette heads
- Pasteur pipettes
- Mircowave
- Eppendorfs
- Vortex
- Sonicator
- Disposable blades/scalpel
- Small spatula
- Lab coat

3 Introduction

This is a compact light-sheet microscope system (CLSM) designed for rapid 3D imaging of histopathological samples (pictured in Figure 1). The open-top architecture allows samples of arbitrary shape and size to be mapped from underneath (cover slip and stage design may need to be adapted slightly for large sample). The sample is scanned through the stationary light-sheet (LS) beam for the 3D perspective of tissue. Stained tissue may be measured quickly with high lateral resolution (1.7μm - pixel-limited) over a large area or volume. The lateral resolution may be further reduced to 1.1μm (the optical resolution) using the zoom lens add-on. The axial resolution of the system is 2μm, and this is given by the thickness of the light-sheet. Depending on whether the sample tissue has been optically cleared or not, data will be collected from low depth (constrained to near the surface) or it will include planes deeper into the sample. "Airy beam mode" may also be used to increase the depth of collectable information. This user guide has been written to aid understanding of how each part works and to provide a practical explanation of how to align the components, capture data and analyse the images.

4 System Overview

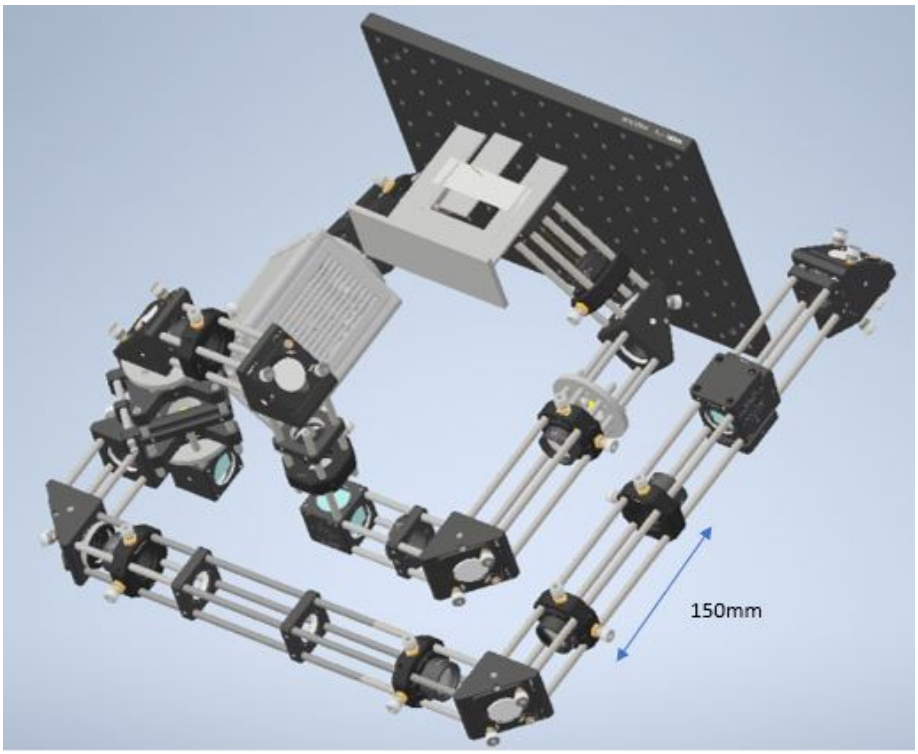

Figure 1: Compact light-sheet microscope system without supports and breadboard. Add in laser direction. The dimensions of the whole system including the laser safety box but excluding peripherals are $63x65x46cm$. All components are controlled remotely via a portable laptop (not shown).

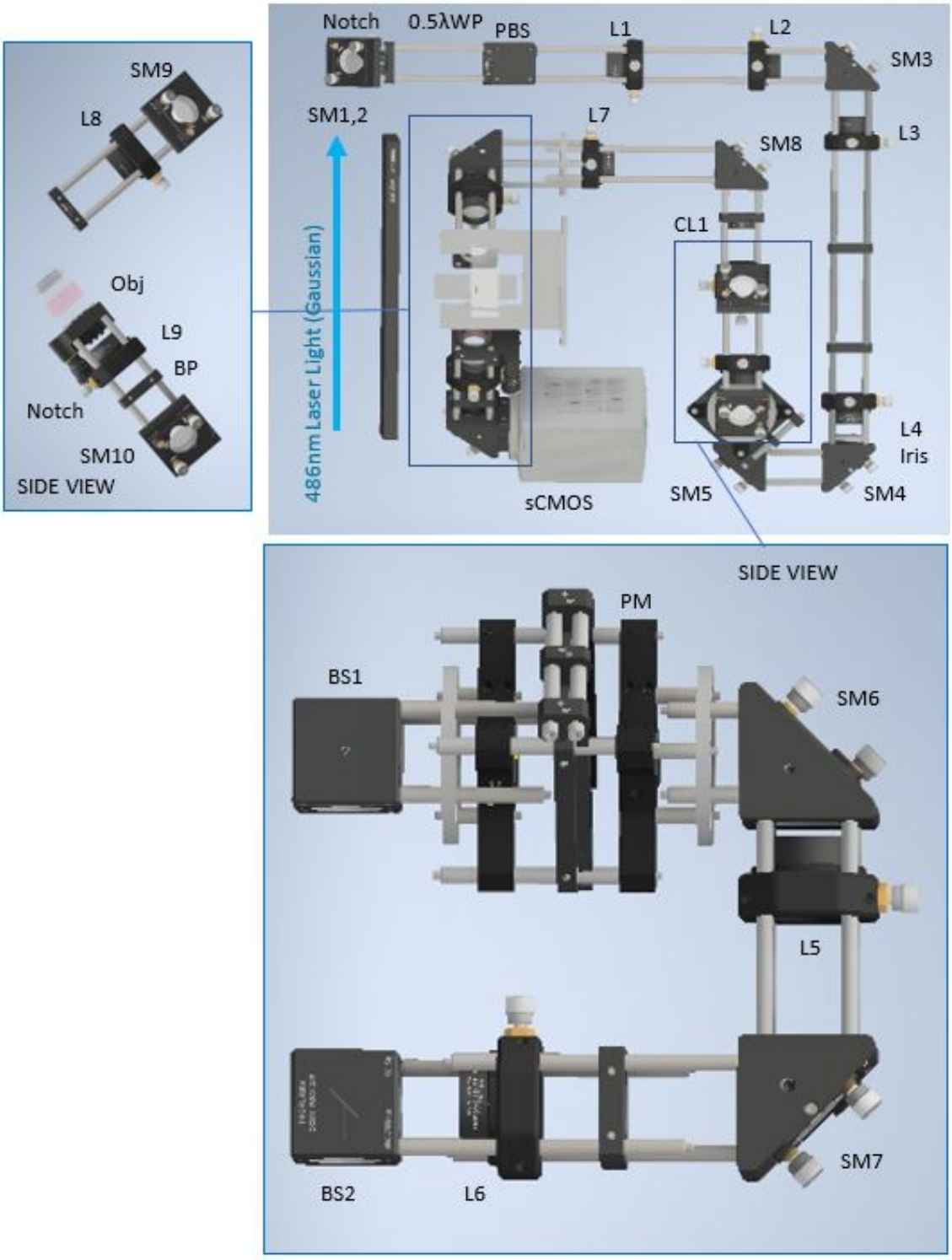

Figure 2: Overhead view of the CLSM system with side-panels showing vertical sections. Label side panels. L: spherical lens; SM: steering mirror; BS: beam splitter; PBS: polarising beam splitter; 0.5λWP: half wave-plate; PM: phase mask; sCMOS: Orca Flash 4.0 camera, Notch: notch filter; BP: band-pass filter; Obj: Nikon $4x$ Plan Apo objective; CL: cylindrical lens

Footprint (excl. safety box and peripherals)	$450x600mm$
Footprint (incl. safety box, excl. peripherals)	$630x650mm$
Height	$460mm$ incl. laser safety box
Weight	???
Laser wavelength (illumination)	$486nm$
Fluorescence range (detection)	$525nm$
Ideal temperature	$21°$ (sensitive to changes $+-1°$)
Sensitivity to vibration	Mitigated with floated optics bench or gas-filled vibration isolation feet underneath breadboard
Lateral resolution	$1.7\mu m$
Axial resolution	(Beam waist - TBC)
Maximum depth of signal in turbid tissue	$200\mu m$ (normally $80\mu m$). Affected by dye penetration,light attenuation and Rayleigh range
Width of light-sheet	3.2mm
Scanning range	10mm
Staining options	Acridine Orange, Fluorescein (not exhaustive)
"Airy mode "	Potential improvements to depth and resolution. $\alpha = 5$. Deconvolution essential
Data geometry	Parallelopiped
Time to stain	5 minutes
Time to scan	Roughly 15 minutes per $10x3.2mm$ surface area of sample (although data is volumetric)
Cover slip dimensions Zoom lens and SRRF	$25x75mm$ subject to change... thickness? characteristics TBC
Tissue clearing	Index match to $n = 1.46$. Tested with iDISCO and CLARITY methods

Table 1

4.1 Components

4.1.1 Vortran Stradus 488 Diode Laser

We use a Vortran Stradus diode laser designed to operate in the blue (486nm). The design is compact and easily transported as part of the portable microscope system. The maximum power output is 150mW. The peak-to-peak noise is 1.12%. In November 2018 it was noted that the laser was unexpectedly leaking wavelengths out with the normal bandwidth. There was some overlap with the wavelengths produced by the sample. This made the fluorescence almost invisible because of the relatively high laser power. A new filter was added at the start of the light path (Semrock FF01-480/17) to clean up the laser line removing green light (Figure 3). The beam propagation properties given by the manufacturer are stated in Table 2. The beam profile from the laser is visibly quite irregular. A spatial filter (circular) is used after the beam expansion telescopes to remove messy edges, however the beam is still not a perfect Gaussian shape and so it is important to align the brightest part of the beam within the iris (this will be further explained in the alignment section).

	X	Y	Units	
M^2	1.16	1.12		
Beam Diameter	0.78	0.79	mm	
Rayleigh Range	0.84	0.91	M	
Divergence	0.92	0.87	mrad	
Astigmatism				-4.41%
Beam Asymmetry				1.026
Divergence Asymmetry				0.943

Table 2: Beam properties for the Vortran Stradus 488 diode laser.

4.1.2 Filters

- Laser clean up filter: Semrock FF01-480/17. Positioned after SM1,2 in Figure **??** ("Notch")
- Notch filter: 488nm Stopline. Positioned behind Nikon detection objective in the detection arm ("Notch")
- Band-pass filter: 532/50nm. Positioned behind "Notch" filter in detection arm ("BP")

As well as the Semrock laser clean up filter, there are two other filters. These are situated in the detection arm at the back of the objective. One is a notch filter ($488nm$ Stopline) to block stray blue light from the laser. It is vital that this filter is in position before the light reaches the camera, as the laser light is still powerful enough to damage the pixels at this point. The other detection filter is a band-pass filter (532/50nm) which removes all light that does not lie within the green region of interest. This helps to reduce background signal. This region has been selected to reveal nucleic matter that has been stained with acridine orange. The notch filter should be placed in front of the band-pass filter relative to the incoming light.

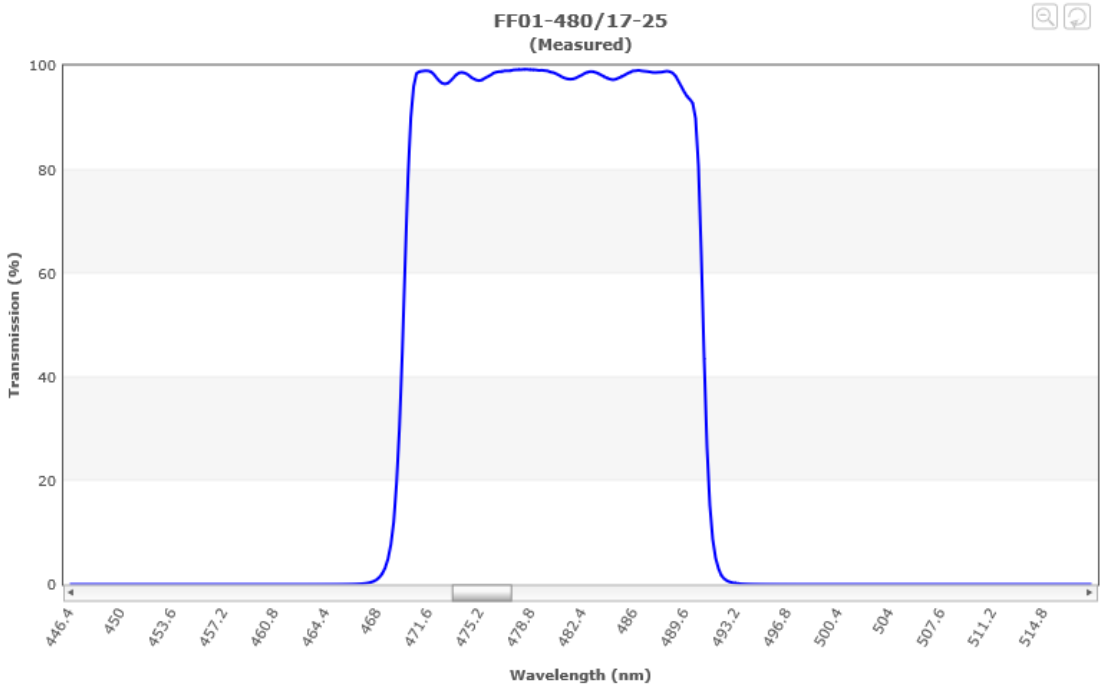

Figure 3: Semrock FF01-480/17 spectral information around 486nm laser peak (leakage from the green part of the spectrum is blocked).

4.1.3 Phase Mask

This custom-made component from PowerPhotonic creates the Airy profile across the light-sheet at its focus. The phase mask adds a one-dimensional cubic phase shift though the cross section of the beam. In the Fourier plane of the phase mask, we have the Airy profile. The beam diameter should be magnified to around 6-7mm before reaching the phase mask so that the laser beam fills the entire window and gain the full phase-shifted profile. The α-value of the phase mask describes the extremity of the Airy properties – high α-value means a greater bend in the beam and more side lobes. There are 4 windows in the glass, each with a different α value. We use α =21 (see Figure 4). The front of the mask (writing right way around) should face the incoming laser beam. The cubic phase shift should be placed in such a way that the Airy profile is through the cross-section of the light-sheet (ADD IMAGE). Airy beams carry power in the side-lobes making them resistant to obstacles that would normally distort a beam (they are self-healing or propagation-invariant).

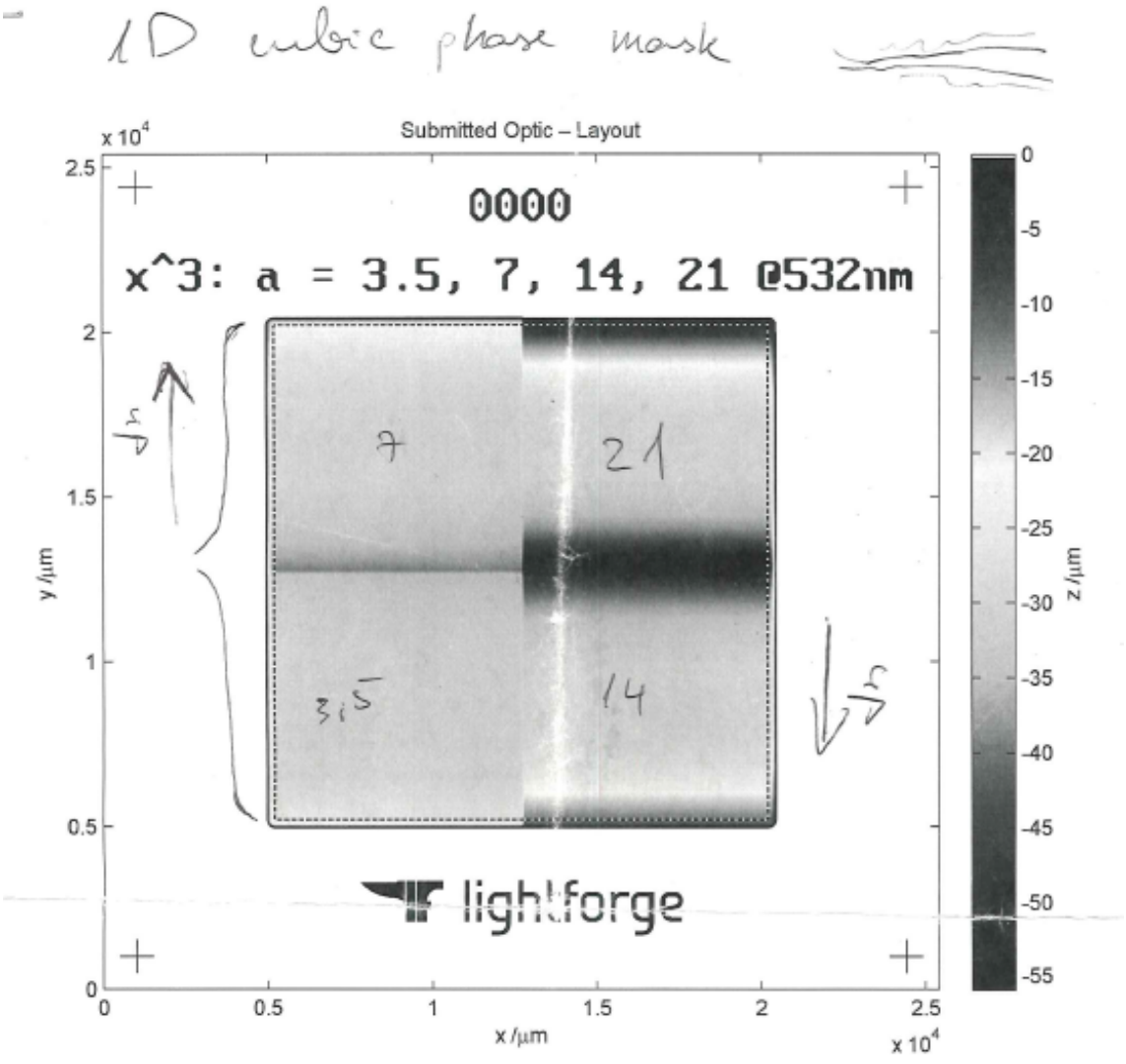

Figure 4

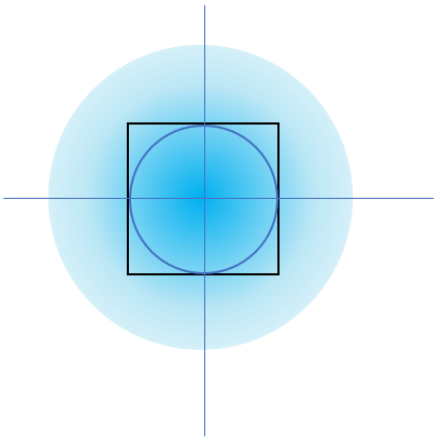

Figure 5: Aligning the phase mask (see fluorescent pinhole placed just before cylindrical lens "CL" in Figure 2). After the bright spot has been aligned in the centre of the iris and the cage and the phase mask window has been centred around that, close the iris until nothing outside of the square window is visible.

...This is checked by opening the iris and then closing it again until the circular profile just brushes the four edges of the square window (watch the shadows using a pinhole plate just in front of the cylindrical lens and remember to shutter the Gaussian pathway, expectation shown in Figure 5). If, once the beam is perfectly aligned in both arms, the square of the window looks offset to the circular beam, adjust the position of the phase mask until it sits at the centre. When the iris is adjusted, the point spread function (PSF) should be measured again as the beam diameter is related to the numerical aperture and therefore the resolution of the system. L2 (Figure 2) is particularly crucial for aligning the bright part of the beam through the iris correctly.

4.1.4 Mirrors

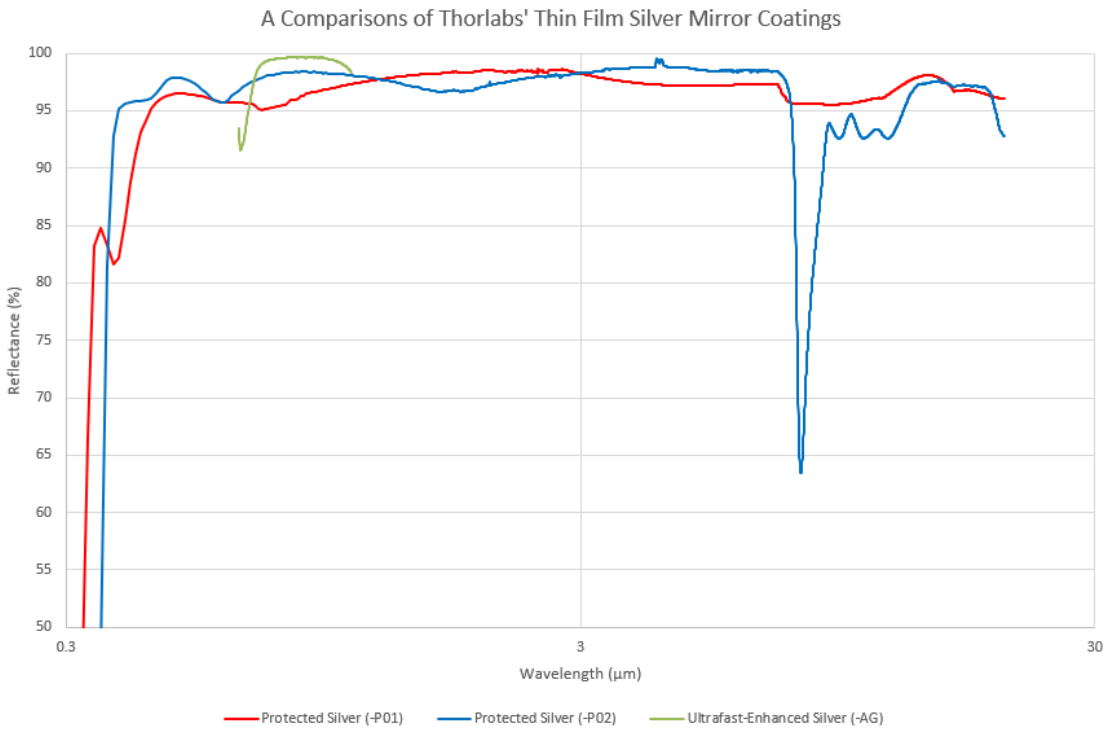

Figure 6

All of the mirrors in this microscope system are planar mirrors designed to reflect light between $450nm$ and $20\mu m$ (PF10-03-P01, Thorlabs). The relfectance is given over a range of wavelengths in Figure 6. A set of two ("steering") mirrors are used to guide light from the laser so that it enters the cage system exactly centred. From this point, only a single mirror is required to centre the beam in each subsequent cage section. If a single mirror is not sufficient to align in the new section, it means that an alignment in a previous section was not perfect. This takes for granted that all parts of the cage are perfectly leveled and at 90° to each other. Note that some mirrors may have been replaced with a different kind, however all mirrors are suitable for $488nm$ laser light. Be wary of stray beams. Never remove a mirror from this system without an appropriate beam block in place.

4.1.5 Cylindrical Lens

The cylindrical lens (f=100mm, LJ1567RM-A, Thorlabs) is anti-reflection coated for light between 350nm and 700nm. Collimated light from Gaussian pathway and the Airy pathway recombine at this point, so it is important to always keep one beam shuttered. The collimated light is focused into a line through the cylindrical lens at a distance of 100mm away. This is the Fourier plane of the phase mask (for Airy mode).

4.1.6 Spherical Lenses

There are 9 spherical lenses in this system. Unlike the cylindrical lens, these focus light in two dimensions. The first 8 of these lenses are 4 sets of telescopic pairs. The first 2 telescopes are for beam expansion (sequentially: AC254-050-A-ML, AC254-100-A-ML (2×) and AC254-050-A-ML, AC254-250-A-ML (5×) Thorlabs). These two pairs result in 10 magnification of the original beam diameter (Figure **??**). The 3rd telescope pair is for fine-tuning the focal point of the Airy beam to match the Gaussian focal point in the sample and does not magnify the beam (AC254-100-A-ML (2 identical), Thorlabs). The final telescope is also a 1× magnification telescope (AC254-125-A-ML (2 identical), Thorlabs) and this relays the focused light-sheet into the sample (through the Solid Immersion Lens (SIL)). The 9^{th} spherical lens is a tube lens (AC254-150-A-ML, Thorlabs) which focuses light from the objective into the camera. This tube

lens has a focal length of 150mm rather than 200mm which is the standard length used with this Nikon objective. This means that the total magnification of the image is $\frac{150}{200} = \frac{3}{4}$ of what it would otherwise be.

4.1.7 Hamamatsu Orca Flash 4.0 sCMOS Camera

This is a high quantum efficiency camera and $6.5 \times 6.5 \mu m$ pixels. The compact LSM system utilises the USB 3.0 connection. Ambient air cooling is sufficient. The camera is heavy; although it is cage mounted, additional support is advised to avoid gravitational misalignment.

Figure 7: Hamamatsu Orca Flash 4.0 sCMOS Camera

Note: The camera is fragile and packaged separately from the rest of the system during transport.

4.1.8 Nikon 4× Objective Lens

We use a CFI Plan Apochromat Lambda 4X objective. It has a numerical aperture of 0.2 and a working distance of 20mm. The 2cm working distance allows enough room for this objective to be tilted at an angle of 45° from the normal below the sample stage (Figure 8). The highest transmittance for this objective is in the green region (Figure 9). For full $4x$ magnification, this objective should be paired with a tube lens with $f = 200mm$ at some arbitrary distance away. We use a tube lens with $f = 150mm$, and so the magnified image is $3x$ larger than the object.

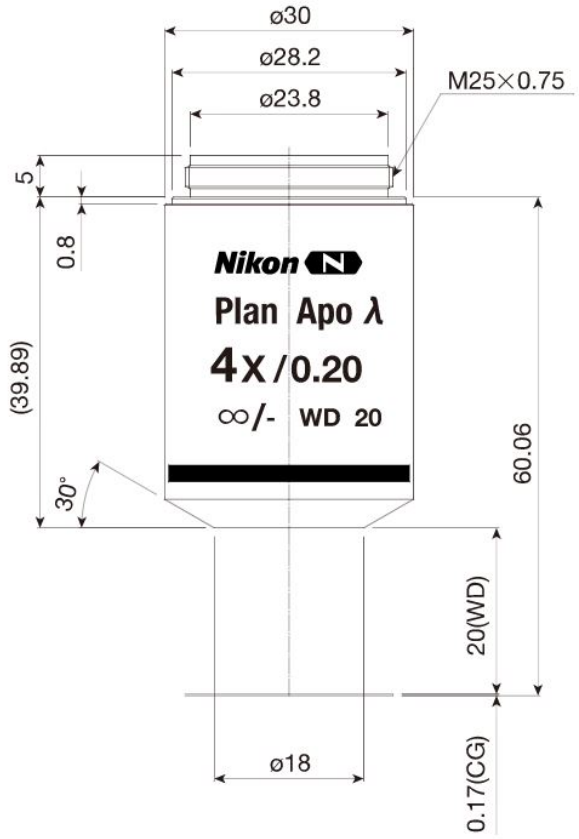

Figure 8: Schematic diagram of CFI Plan Apochromat Lambda 4X objective which is suitable for fluorescence imaging in the visible range.

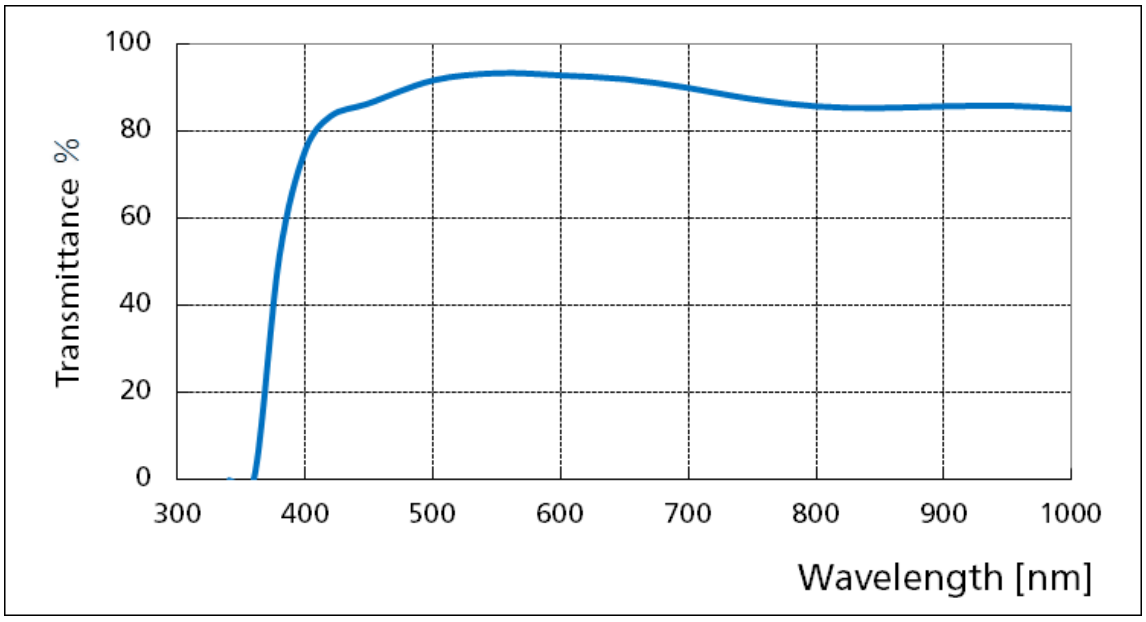

Figure 9: This graph shows the transmittance of the CFI Plan Apochromat Lambda 4X objective around the visible range.

4.1.9 Solid Immersion Lens

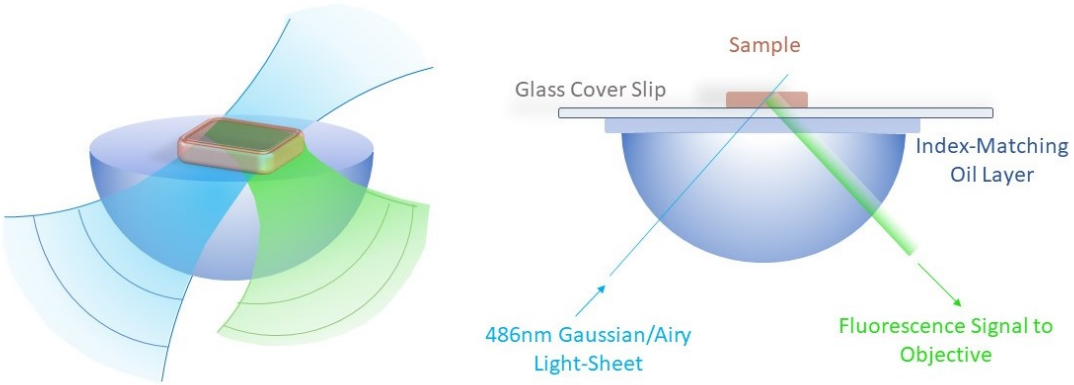

Figure 10

The solid immersion lens (SIL) was custom-built by BMV Optical. It is designed so that the radius of curvature of incoming wave-fronts match the radius of curvature of the lens. This means that although the refractive index changes as the waves pass from air to glass, the light does not bend very much. This helps to reduce aberrations in the light-sheet at the focus. The wave-front curvature matching is illustrated in Figure 10. The dimensions are given in Figure 11. The height of the lens is specifically chosen so that the natural focus of the beam in the centre will be one wavelength ($486nm$) above the top surface of the cover slip, in other words just inside the surface of a sample which is touching the cover slip.

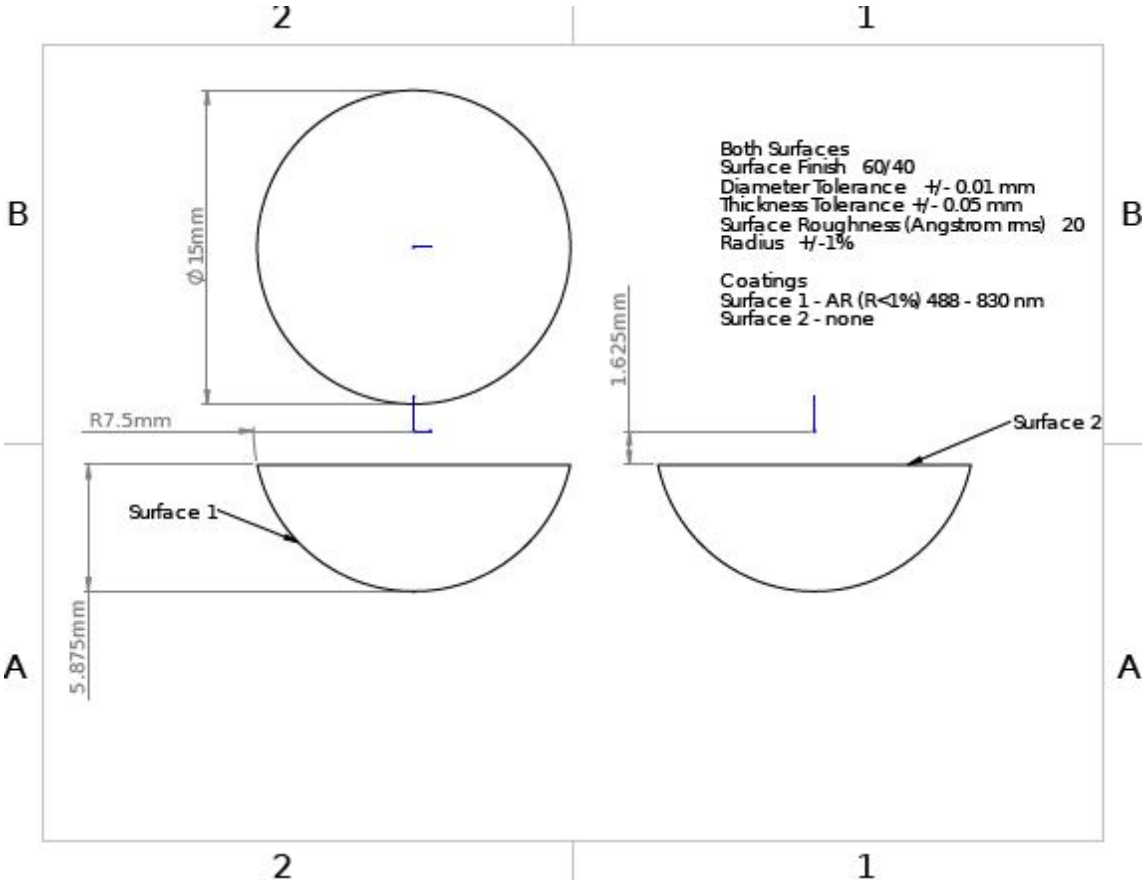

Figure 11

Near-index matching between the SIL and the cover slip is achieved with a thin layer of immersion oil (we currently use Nikon type NF/F2). This oil must be of a high viscosity to achieve the required layer thickness. A thin layer of oil is also more likely to drip down the sides of the SIL causing further aberrations. The SIL and the custom SIL holder must be cleaned thoroughly after each use, and then the oil layer should be re-applied.

4.1.10 Aperture

The adjustable iris (SM1D12D, Thorlabs) is positioned after the final beam expansion telescope (between L4 and SM4 in Figure **??**). It serves two purposes: it is a spatial filter to make a circular beam (clean edges) and it allows fine control over the numerical aperture of the illumination beam (this affects the beam waist size and in turn the axial resolution of the microscope). Remove the iris and set diameter to exactly the correct diameter ($7.6mm$) with the help of vernier calipers, but always check that this is correct by looking at the beam with respect to the shadow of the phase mask edges to make sure that they are just touching on all sides (this is visible on a fluorescing pinhole placed just before CL1 in Figure 2).

4.1.11 Wave-plate

A mounted zero order half wave plate (WPH05M-488, Thorlabs) is rotated to change the polarisation of the linearly polarised laser beam that enters the polarising beam splitter.

4.1.12 Polarising Beam Splitter

The polarised light is transmitted through the cage if it is P-polarised and deflected into a beam block if it is S-polarised (Figure 12). Rotation of the wave plate allows manual control of the laser power within the upper limit set in the Vortran software.

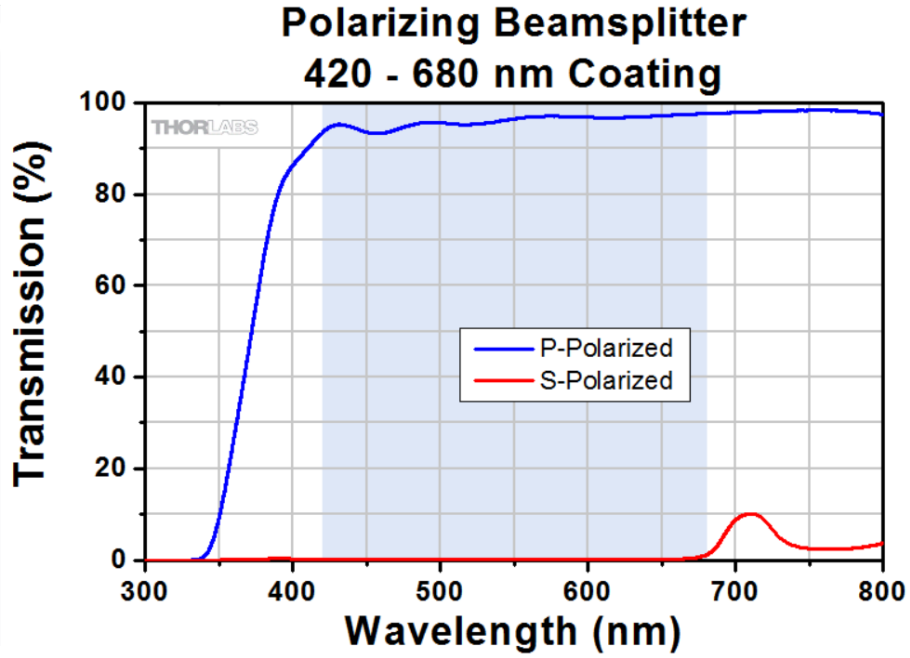

Figure 12: CCM1-PBS251/M, Thorlabs. Transmission plot.

4.1.13 Motorised Sample Stage

The sample stage is manually adjusted in y and z. The height and angular orientation of the prongs must exactly match the height and orientation of the SIL holder. Once the sample stage is perfectly aligned, samples may be mounted on top. The motorised PI actuator is controlled via the laptop. It is used to scan the sample horizontally through the diagonal (stationary) light sheet. The camera is synced with the motorised actuator so that images are taken at each sample position. The actuator is very delicate and expensive to replace. DO NOT allow the actuator to crash into anything, and please handle carefully. When mounting the actuator in its holder, take care that it is fastened tightly or the spring-loaded stage may jettison the actuator out of its holder. On the other hand, if the fastening is too tight then the actuator will not be able to scan properly and data sets may appear to be distorted. It is helpful to rotate the actuator in its holder before fastening so that the scale faces up towards the user.

4.1.14 Zoom Lens

The zoom lens allows the user to scale down the resolution of the system at the expense of the field of view (FOV). Full analysis

This component has been removed temporarily 4^{th} October 2019.

5 Alignment

5.1 Alignment Protocol (Rough Guide)

Refer to Figure 2 to find key pinhole locations.

- Before the light is aligned in the cage; the cage must be perfectly level with perfect angles at the joins
- Start at the beginning where the light comes out of the laser
- Do one arm at a time, removing optics first
- Use the steering mirrors and pinholes to get the beam straight through the first section
- Pinholes should always be pushed flush with a flat object such as a cage plate

- The brightest part of the beam should be considered to be the centre
- The beam size may be shrunk with other pinholes to make sure that the beam is exactly centred in each hole
- Precision is everything. Tiny imperfections have a huge effect on the data
- The order of this protocol is also crucial to understand where every imperfection lies
- "In front" means the side facing the incoming laser beam and "behind" means where the laser light exits the optic
- Remember to shutter the beam whilst taking optics in and out of the cage, and also put temporary beam block on the sample stage
- Every alignment is iterative; once you are reasonably happy go back a step and repeat the previous movement until you are happy, then do the next part again and keep going until you have got the best alignment that you can possibly have
- Misalignments are difficult to see close to the incorrectly positioned optic. It is often necessary to align with respect to a pinhole some distance away
- Distances between lenses should be measured using a ruler/tape measure however fine alignments should be done using a wave-front sensor
- Check the alignment everywhere before touching anything. It may be that nothing moved that much in transit and only slight adjustments are required

Step by step: illumination pathway

- Place beam block in Airy pathway
- Remove L1 and L2 from their mounts
- Place 3 pinholes in front of 0.5λWP, L1 mount and between L2 mount and SM3 mount
- Use SM1 and SM2 to perfectly align the beam through this cage section. Remove the centre pinhole for checks if necessary (in theory, if a beam passes directly though two well-placed pinholes then it is well-centred in the cage)
- Note that the beam shape is highly irregular so it may be difficult to tell where the centre is
- Remove L3 and L4. Leave pinhole in front of SM3. Place a pinhole behind L3 mount and one next to a cage plate in the arm. Move SM3 until beam is directly centred through both of these pinholes **and** the contracted iris at the end of the arm. If this does not work, then we may assume that the alignment through the first arm was not perfect so repeat the alignment there and then try again
- Check that the brightest part of the beam is in the centre of the iris. Repeat the alignment iteratively in the two cage arms until the bright part is centred and the beam is straight everywhere
- Replace L1. Check the alignment in front of L2 mount, in front of SM3 mount, at a cage plate after L3 and at the iris. Tweak the x-y position of L1 until the beam is well-aligned with the brightest part in the centre of the iris
- Replace L2 and align the x-y position of L2 with respect to SM3 mount, a cage plate after L3 mount and the mostly-closed iris behind L4 mount. Distance between L1 and L2 should be 150mm
- With L1 and L2 correctly positioned, now place two pinholes in arm 4 (the one containing BS1 and BS2). One pinhole should go in between BS1 and BS2 (rods not pictured) and one should go against CL1 (take care to make sure the pinhole is straight). Place one pinhole in arm 3 against SM5. Move SM4 until beam goes straight through first pinhole. Remove arm 3 pinhole and move SM5 until beam is straight through arm 4. Replace arm 3 pinhole and repeat
- Flip pinhole before CL1 to expose white fluorescent pad to the incoming beam. Make sure that the bright part is still in the centre

- When you are happy with this, replace L3 and align lens in x-y with respect to arm 3 pinhole, pinhole at beam splitters and CL1 pinhole too
- Repeat with L4, remembering that irregularities may only be visible quite a distance away from the initial fault. Distance between L3 and L4 should be 300mm
- Align the Gaussian pathway completely before doing the Airy pathway to match
- Remove L7 and align through arm 5 using SM8. The beam is now a line. Rotate the line continually during the alignment to make sure that the centre of the line is always centred
- Once straight through arm 5, remove L8 and align through arm 6 as well
- Check that the beam goes directly through the centre of the SIL holder, but do not touch the SIL holder unless explicitly discussed with Sephie or Stella
- Replace L7 and check that the distance between CL1 and L7 is 225mm Check
- Align L7 in x-y, again checking that the line is aligned in the final illumination arm for all possible rotations of CL1
- Align L8 in x-y as best as possible with the limited space available, again checking all rotations
- Add in part about using L7 and L8 to relay focal point through SIL

Step by step: Airy section

- Now, shutter the Gaussian beam to check that the Airy beam is roughly centred
-

Step by step: SIL
The solid immersion lens and the camera are the two most difficult parts to align correctly.
Step by step: detection pathway

- Use a planar mirror on top of the (level) SIL holder to align the detection pathway with respect to the illumination pathway
-

5.2 Ideal "Unaberrated" Beads

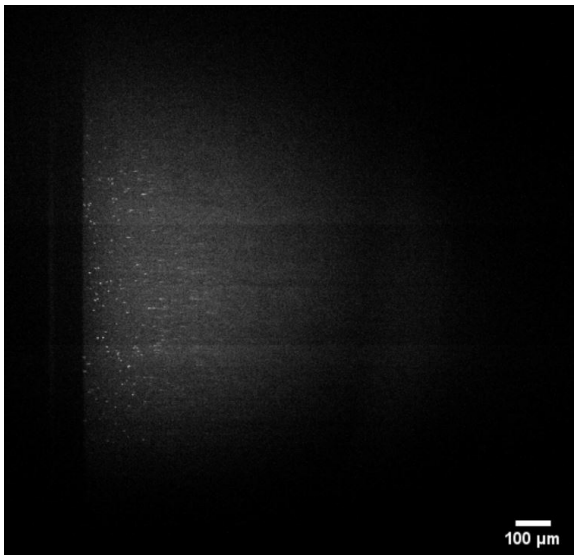

Figure 13: Relatively unaberrated $0.2\mu m$ fluorescent green polymer bead sample. The "tails" are straight out to the right. The beads close to the cover slip are well-focused. The focused beads look regular and circular. There is no doubling effect at the cover slip.

5.3 Test Samples

For alignment, calibration and testing of the CLSM you will require the following samples:

- Planar mirror for aligning with respect to the detection pathway
- Planar mirror to confirm that the phase mask is correctly orientated
- Fluorescein droplet on cover slip to check beam angle, focal position, objective focus, camera angle, beam profile (for corrections later), Gaussian and Airy beam comparisons, general alignment (Figure 15)
- $0.2\mu m$ fluorescent green polymer beads fixed in agarose gel to check alignment of system. "Beads show all sins of the microscope". These beads are sub-diffraction-limited and so that may be used to measure the point spread function across the field of view and the beam waist (axial resolution)
- $4.8\mu m$ fluorescent green polymer beads fixed in agarose gel to check the Airy "comet tails" for clarity, strength, direction etc (be aware that these beads may look irregular due to microscopic lensing effect)
- Beef stained with acridine orange to substitute human tissue during test phases. Can also be used to confirm correct light-sheet focus and estimate the field of view in turbid tissue
- $10\mu m$ graticule calibration target from Thorlabs to experimentally measure the pixel-limited lateral resolution of the CLSM
- Lens cleaning tissue (stained or autofluorescent) provides an interesting target to adjust focus and check detection pathway optics on their own using ambient light (Figure 16)
- Satsuma pieces are an interesting test target with high autofluorescence under blue laser light 17

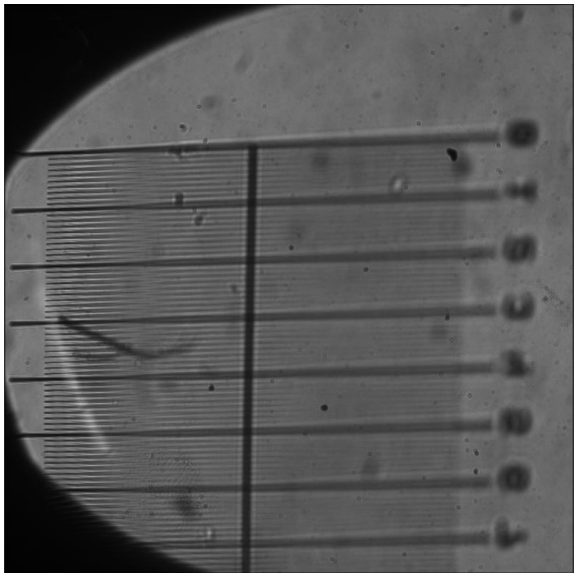

Figure 14

Figure 15: Light-sheet tilted onto its side and imaged in a fluorescein droplet. The line is sharp and quite straight across the pixel array. The Airy and Gaussian beams may both be viewed at once with this orientation to check their relative positions.

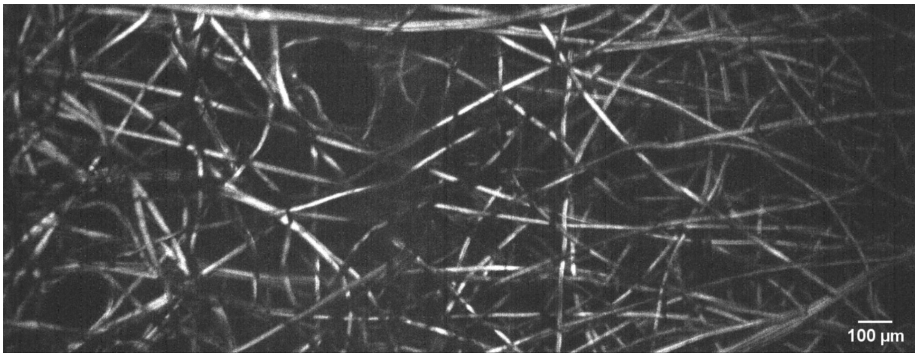

Figure 16: Lens cleaning tissue stained with acridine orange shows up sharply on the microscope. This can be useful to test the

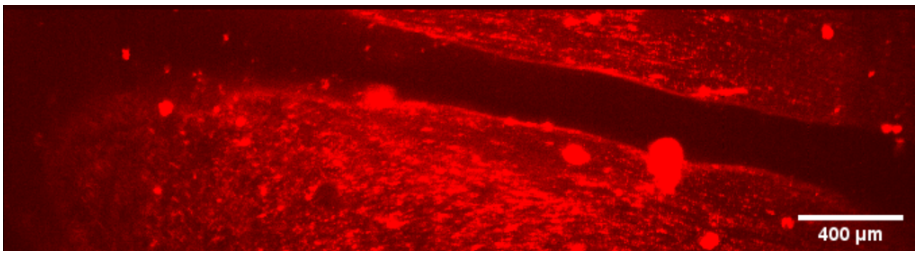

Figure 17

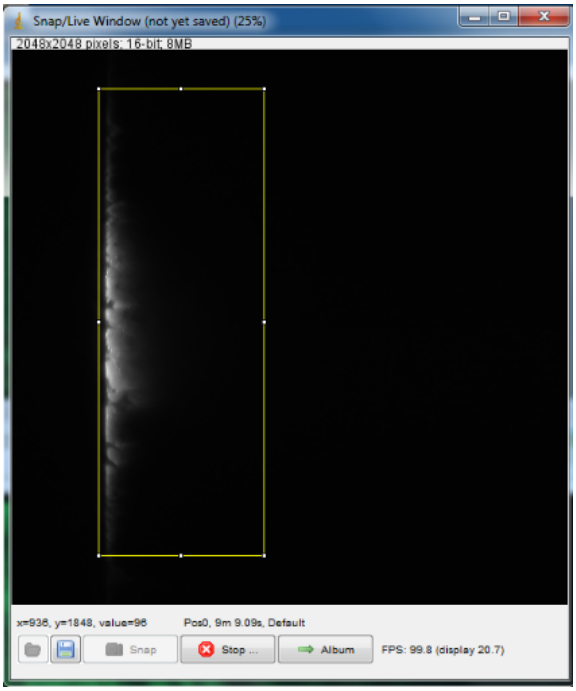

Figure 18

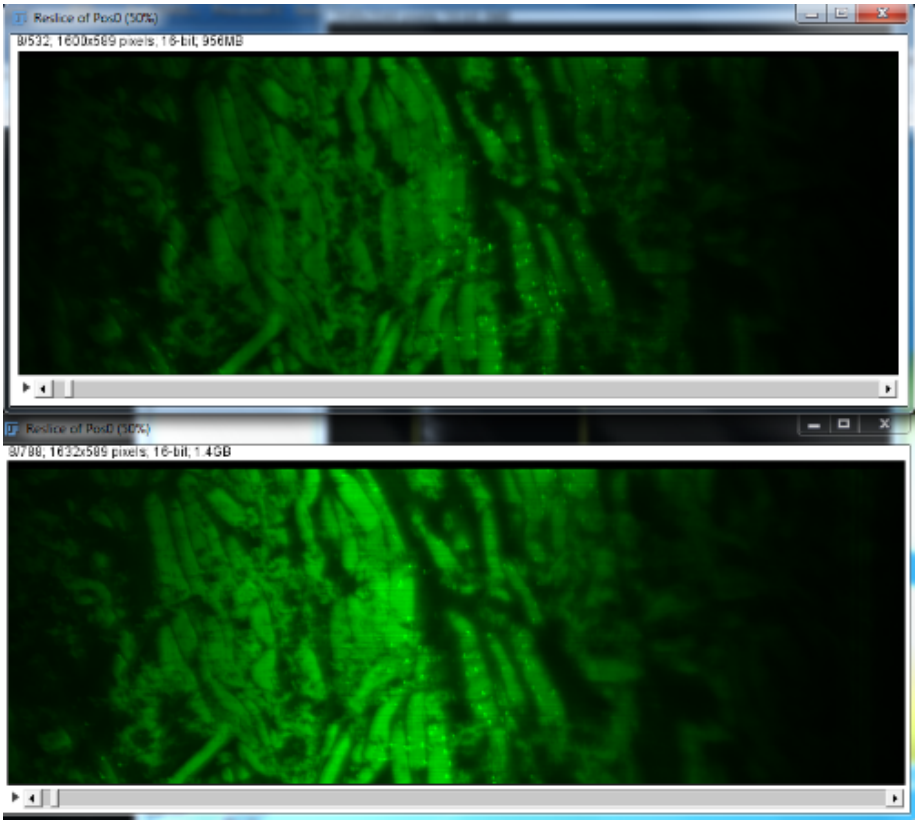

Figure 19

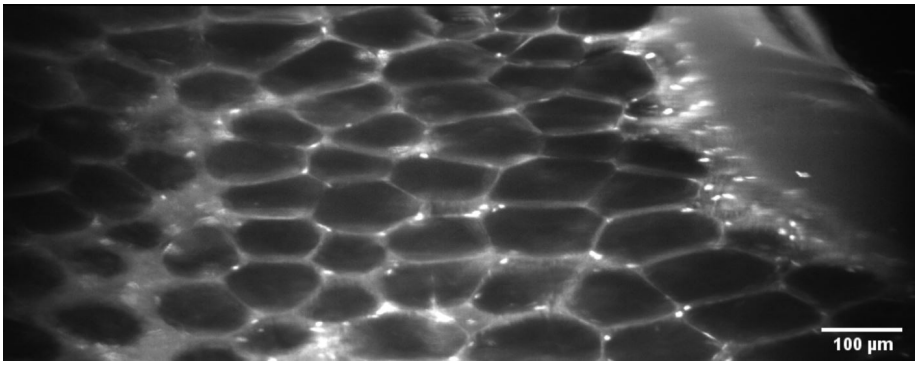

Figure 20

Figure 21

6 Potential Imperfections

With this system, it can be difficult to tell which anomalies are due to a poor samples, and which are due to system imperfections. The main overriding potential for imperfection comes from misalignment. The following list of points to be aware of is not exhaustive.

6.1 Spherical Aberration

This aberration is often linked to short focal length optics (f=50mm is considered short). Figure 22 shows how a highly curved optic may smear out the focal plane so that the focal "point" can no longer be defined.

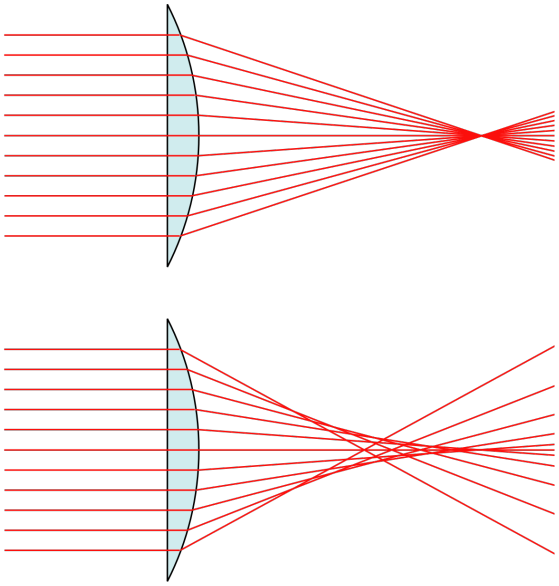

Figure 22: Taken from Wikipedia. Spherical aberrations often arise from highly curved optics. They result in a smeared-out focal plane and blurring.

6.2 Astigmatism

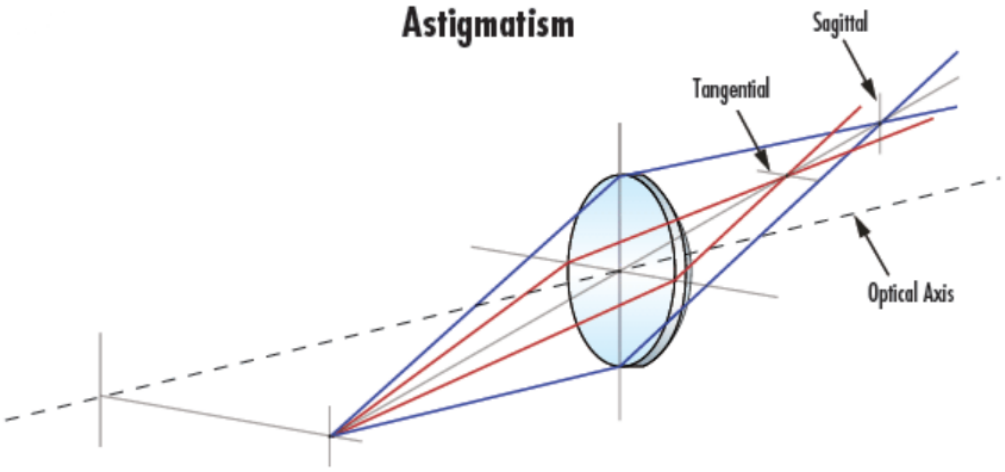

Figure 23: Figure from Edmund Optics. This aberration often arises from off-centre optics. The focus in the horizontal direction lies in a different plane to the focus in the vertical direction.

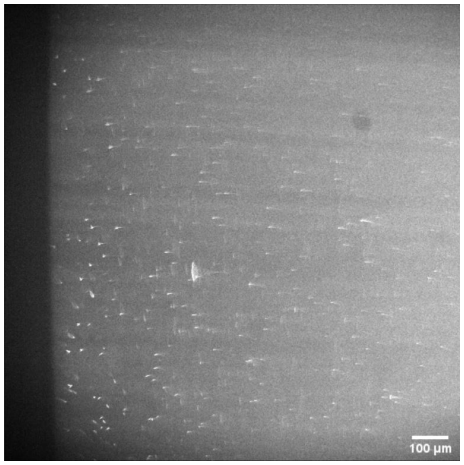

Figure 24: These beads are affected by astigmatism. Changing the focus of the objective results in an elongated point spread function first smeared in one direction and then in the other. This image is indicative of a misalignment elsewhere in the system.

6.3 Coma

This aberration is associated with tilted optics. It produces "comet tail"-like aberrations at the focus. Figure 25 shows a ray diagram illustrating how the rays do not meet up at the same position in the focal plane.

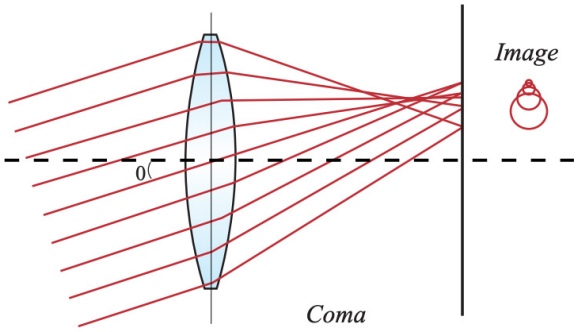

Figure 25: This image from Edmund Optics illustrates how a tilted lens can produce multiple images ("comet tails") at the focus. Coma aberrations are difficult to correct for without alteration of the design itself.

6.4 Incorrect Oil Layer Thickness

This is difficult to get right. Many immersion oils have a viscosity which is very dependent on the ambient temperature. Some oils can become more "sticky" over time, and when this happens the scanning is no longer smooth and images will be distorted. It is also possible for runny oil to slowly drip down the sides of the solid immersion lens. This results in further refractive index mismatch and irregular edges, both of which will corrupt the illumination and the fluorescence signal. Here is some general advice for avoiding these issues.

- Clean everything, including the SIL holder, thoroughly with ethanol before mounting each sample.
- The SIL must always be perfectly spotless before each measurement. This may take several attempts.
- We recommend Nikon type NF/F2 immersion oil. These oils have low background fluorescence and a moderately high viscosity.
- Two to three drops of Nikon type NF/F2 oil should be placed on top of the clean, mounted SIL.

- Use a clean dropper bottle and take care to avoid bubbles as far as possible.
- Gently drop the cover slip on top of the oil layer. Lower one edge first to try and avoid trapping air bubbles under the glass.
- Now that the cover slip is in place, check that the oil covers the entire area in between the lens and the cover slip. If gaps remain, gently nudge the SIL from underneath with a gloved finger to encourage the two glass surfaces to sit flush with one another. If this does not work, more immersion oil may be required. However, oil should be used as sparingy as possible.
- With the exception of bead samples, it is often easier to place the cover slip first and then mount the sample on top. This also reduces the risk of contaminants leaking onto the rest of the system.

6.5 Scanning Errors

The SIL holder and the sample holder must be individually perfectly level with respect to the bench, and also perfectly flush with each other. If they are not, the depth of focus will drift over time and the overall image quality may also be affected. To check this, a spirit level should be used. This part is one of the most difficult to align; any slight errors must be taken seriously. It may be necessary to make fine adjustments to the way that the stages are bolted, however this should not be attempted by anyone who is not an expert.

6.6 Dirty Lens

Dirt on the SIL often appears as "bright smudges" that cross the cover slip boundary (Figure 26). This lens becomes dirty every time you use it; it is the most likely suspect if there is dirt affecting your measurements. If the dirt has been introduced elsewhere, it can be harder to spot. Spilt fluorescein can appear as background fluorescence in your images. Specks of dirt can alter the beam profile or produce diffraction effects. Dirt can easily become trapped around the cover slip - look out for shadows in the light-sheet along the direction of propagation, particularly when imaging the profile in fluorescein.

Figure 26

6.7 Illumination Beam Not Focussed at the Surface

$0.2\mu m$ beads will look at their smallest when the system is well-aligned, clean, and the light-sheet beam is exactly focused on them. The image quality degrades at depth, and so to optimise the best part of the image, the light-sheet should be *just* focused inside the sample, right next to the cover slip. There are a few places where this may be adjusted, but the easiest way to make fine adjustments is to move the cylindrical lens ever-so-slightly along the optical axis. Another way to check where the focus is is to rotate the light-sheet to get a line on the camera (use a fluorescein droplet or a piece of stained tis

6.8 Twisted Camera

Due to the 90° rotations in this system, the camera must be mounted at 45° to the bench (direction matters - ADD IMAGE). Measure this angle using a spirit level (check bench level for reference). If the camera is twisted, the line where the light-sheet meets the cover slip will not line up with the vertical direction as seen on screen. This makes analysis difficult. Note that the light-sheet also rotates; make sure the cylindrical lens is in the correct position before making your assessment. You can use FIJI to check that the lines match up - draw a line in the reference vertical direction whilst holding down the Shift button on the keyboard.

6.9 Hanging Camera

The camera is a heavy component that puts stress on the mounting. This slight dip misaligns the pixel array introducing a "doubling effect", particularly at the cover slip. Imaging $0.2\mu m$ beads and $4.8\mu m$ beads makes it evident if you have this problem. Check the level of the bench using a spirit level, and see if if the camera matches this level along the axis of propagation. It is likely to be tilted downwards at the back of the camera. To remedy this, gently support from below using a post (or proper 45° mount if space is available on the bench).

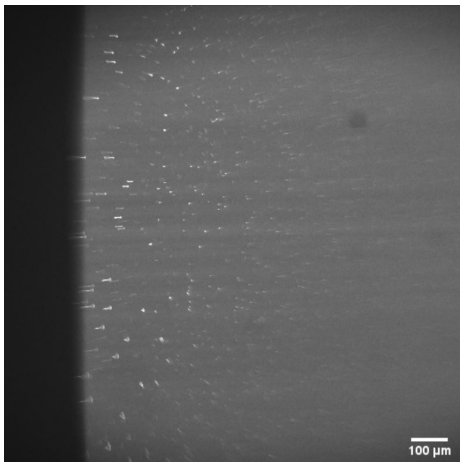

Figure 27: This image shows out of focus, doubled beads at the cover slip boundary. This aberration is very reduced when the camera is attached with an extra mount to reduce the load that directly hangs on the cage mount.

6.10 Objective Not Focussed

The objective must be focussed on each sample individually when it is placed on the stage. There will always be very small changes to the thickness of the oil layer. For some samples (particularly 4.8μm fluorescent beads, it is very difficult to tell when you have focussed correctly as these structures are large enough to span many planes that are parallel to the light sheet. The 4.8μm beads also act like tiny lenses for the focused laser light. The spheres appear to be distorted, with half of the bead often brighter than the other half as the light is further focussed through the bead.

7 Software

The Orca camera, Stradus laser and PI actuator all have their own software that should be installed separately before the parts are added to the μ-Manager configuration. Jonny and Sephie have access to the program installers in a shared OneDrive folder; they are available on request. Alternatively they may be found directly from the component suppliers. μ-Manager is used to co-ordinate the camera, laser and actuator for remote system control. FIJI and Matlab are currently used for image analysis.

7.1 Vortran Stradus

Here is where the maximum laser output can be set to anywhere between 0 and 150mW. It is not recommended to operate the laser below 15mW or above 80mW. If the laser is operated at a low power there may be instabilities in the beam. The heat sink is not fully flush with the supporting breadboard at present, so laser powers above 80mW run the risk of overheating the laser. If this happens, the laser beam may cut out unexpectedly and the heat sink and laser will be hot to the touch.

7.2 PI MikroMove

This is an important step. Before opening μ-Manager, set the positive and negative limits for stage control using this program to avoid seriously damaging the actuator. Add details.

7.3 HC Image Live

This software should be downloaded in order to run the Orca sCMOS camera. HC Image Live may be used to check that the camera is connected and working as expected before the camera is set up in μ-Manager. Once this has been done, close the program and open μ-Manager. Nothing else is required.

7.4 μ-Manager

7.4.1 Connecting External Hardware

Figure 28: USB configuration for pre-written μ-Manager file ("MMConfigdemotEST5.cfg"). 1: Laptop docking station power supply. 2: USB 3.0 A to back of Orca sCMOS camera (USB 3.0 B) port. 3: USB 3.0 to "6" on StarTech USB 3.0 10 port hub. 4: Mouse. 5: Monitor. 6: USB 3.0 connection to laptop docking station ("3"). 7: Power supply for StarTech USB 3.0 10 port hub. 8: USB 3.0 to RS232 laser power control box. 9: USB 3.0 to micro USB for PI actuator control box. 10: USB 3.0 to micro USB back of Vortran Stradus diode laser. 11: Keyboard.

The hardware configuration setup wizard in μ-Manager contains information about the comport for each piece of hardware connected to the laptop. Swapping a physical USB port connection around can mean that you configuration file will need to be updated. This can take time as it's a "trial-and-error" process. There is a "master file" which should not be altered, and the physical connections that go with that file are shown here. ADD

7.4.2 Live

This window shows us light collected from the sample as seen by the camera. It is often where we notice misalignments and it is a reference point to find appropriate exposure times and interesting parts of the sample (control of changes to the sample position is done using software).

This window also allows us to select a region of interest from the full field of view. Use the rectangle tool from the ImageJ task bar to indicate the region. Press the "ROI" button in the main μ-Manager window to crop the recorded region down. To undo this selection, press the button next to it with 4 green arrows pointing outwards.

7.4.3 Stage Control

Plugins > Device Control > Stage Control You should have already set up the positive and negative limits for actuator control in the PI MikroMove program. This will automatically prevent the stage from crashing when it is controlled by μ-Manager. Set the fine control and coarse control values in the pop-up window and scroll through the allowed range to get an idea of where the interesting feature in the sample might be. For a longer scan, make sure that the entire intended range contains useful signal before beginning the scan. Make a note of the starting position.

7.4.4 Crop

Often, it is not necessary to capture the entire field of view. This is especially true for very opaque tissue. In this case, you may crop the field of view in "live" mode to get the region you want, and then this region will be saved into the memory. When you go on to take the 3-D scan, uninteresting areas will be ignored. This is a straightforward way to cut down on memory usage and required processing power for your data.

7.4.5 Multi-D Acquisition

Tools > $Multi - DimensionalAcquisition...$

- Before making a 3-D scan, check that your intended range does indeed contain useful signal. Manually set the stage to the starting position using "Stage Control".
- Make sure that the laser power and camera exposure are correct (no saturation), then stop the camera live feed.
- Open the Multi-Dimensional Acquisition window (Figure 29).
- Use the z-stack section as shown in Figure 29.
- Set the z-step size to equal the pixel size ($1.7\mu m$ without the zoom lens).
- Set the range that you have already scouted out using the live window.
- Keep shutter open.
- Save images using a pre-established and sensible filing system. For example; include your name, the date, sample identifier, sample locattion, beam type, exposure time, laser power, staining method etc. It may be easier to save the data in groups of like data, for example make a new folder each day and separate based on sample within that folder.

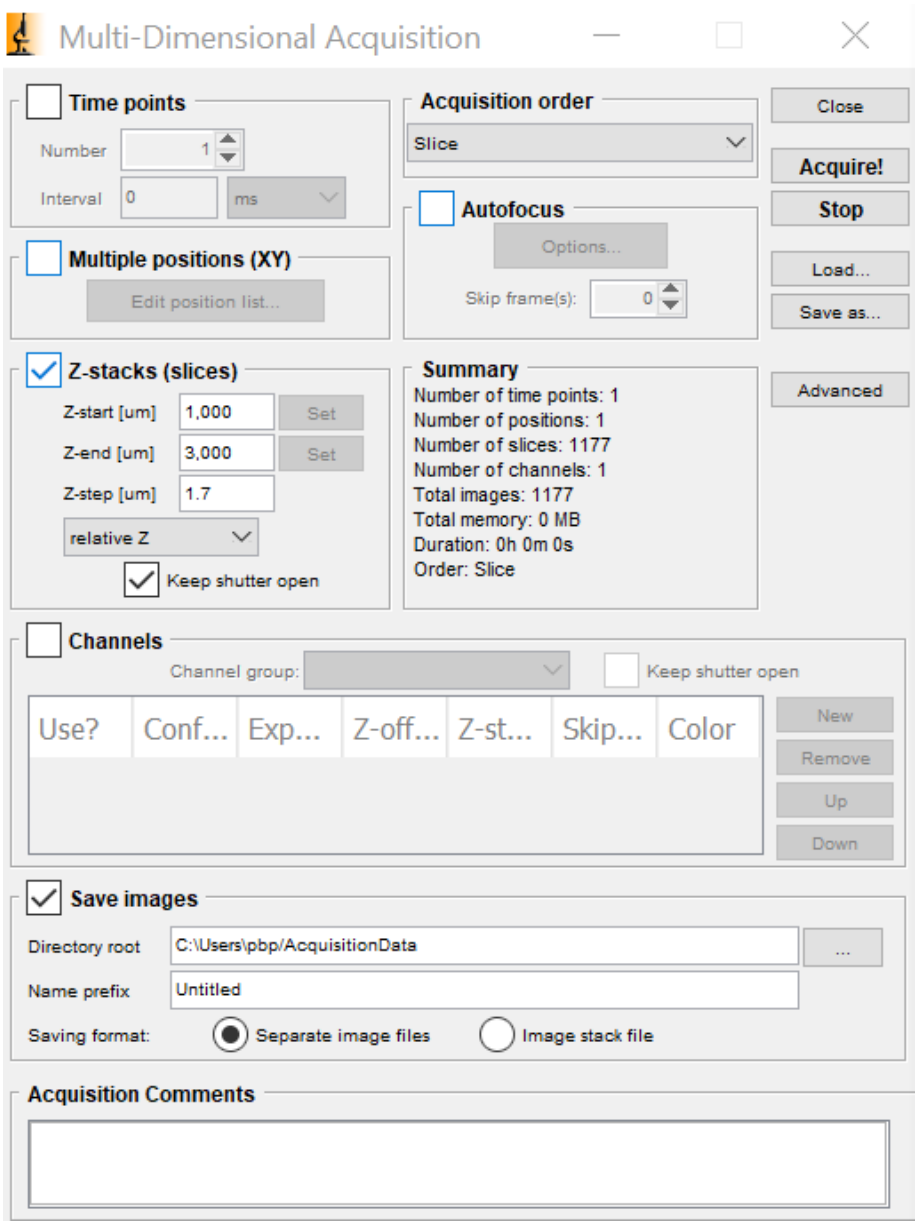

Figure 29: Making a 3-D acquisition in μ-Manager.

7.4.6 Creating a New ".cfg" File

If the pre-built configuration file is corrupted or does not work, you can make a new one using the following steps.

- Before opening micromanager, check that PI stage, camera and laser are all functioning normally within their own software (PI Mikromove, HCImageLive and Vortran respectively)
- Open Micromanager program
- Open blank configuration or demo
- Go to Tools > Hardware Configuration Wizard
- Create new configuration
- Core controller is already added

- Scroll through the list of available devices and find HamamatsuHam (the properties are automatically added by the DCAM driver for this one). Click “add”
- Find “VLTStradus” under “Stradus” and click “add”. For this one the following settings should be used

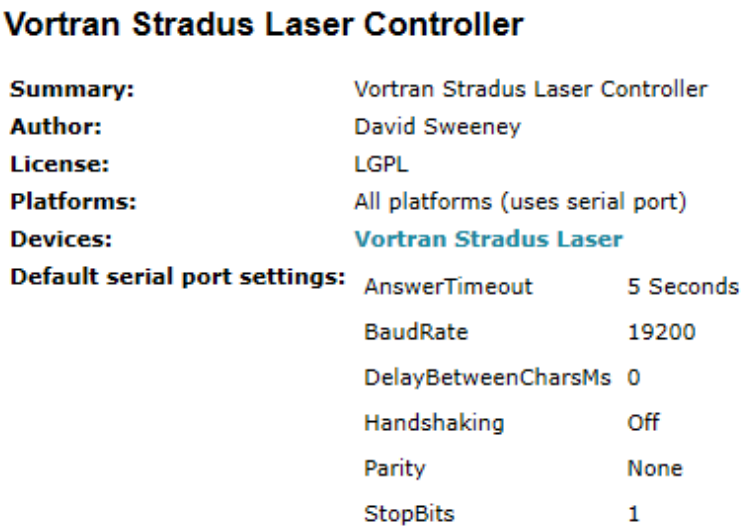

Figure 30

- • It will take some trial and error to find the correct serial port. See attached section (to be written) with prewritten config file for set USB attachment configuration
- The PI actuator and stage require the addition of two devices to your configuration file; “PIGCS” and “PIGCS2”
- These devices use the same serial port
- The controller that we use is “C-863-11” https://micro-manager.org/wiki/PI_GCS_2
- Each actuator requires different control box settings. Check which ones your actuator needs, change the buttons on the box accordingly and then use the correct serial port settings to match that (Figure 31)
- For our actuator (10mm), we require switch 5 OFF and switch 6 ON
- To check the baud rate that this relates to, open the PIMikroMove software and look at the pop up for the C-863 controller

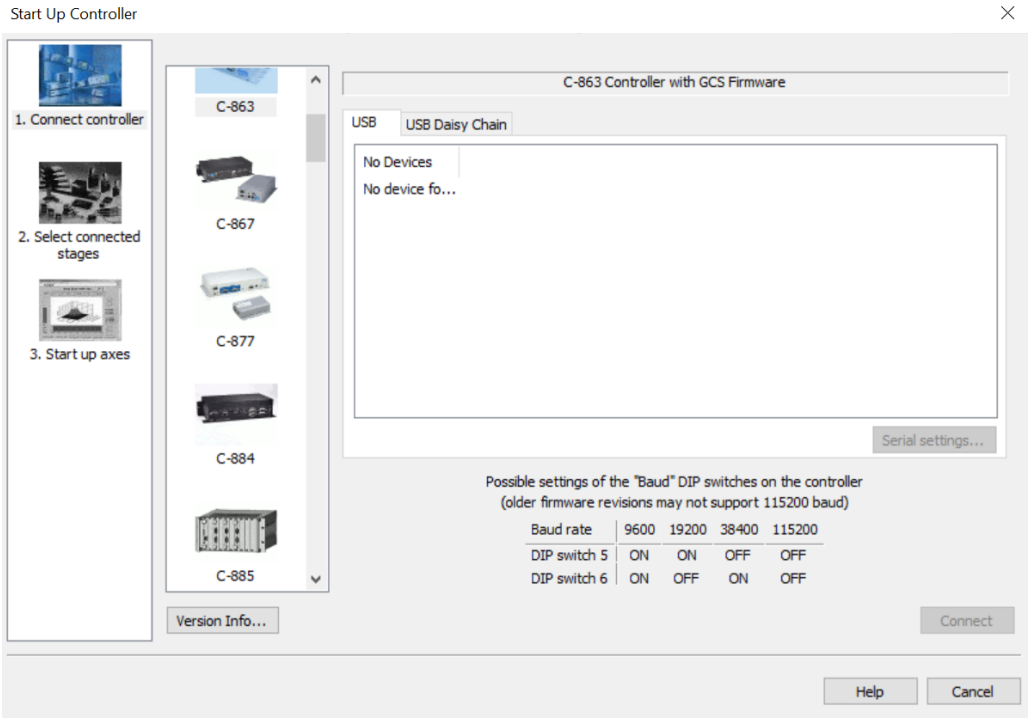

Figure 31

7.5 FIJI (Is Just ImageJ)

This is free software that can be found on the FIJI website. There are regular updates; be sure to keep up with the automatic prompts to stay updated.

7.5.1 Brightness Contrast

Image > Adjust > Brightness/Contrast

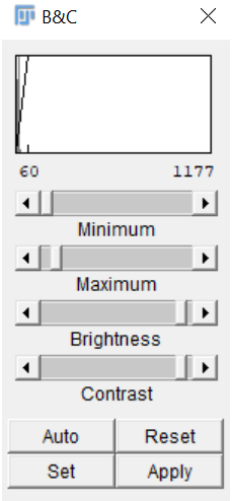

Figure 32: Setting the brightness and contrast in FIJI.

Be careful doing data comparisons as the automatic brightness and contrast settings can be deceptive. Maximum and minimum values can be set manually using the "set" button (Figure 32).

7.5.2 Re-slicing

Image > Stacks > Reslice []...

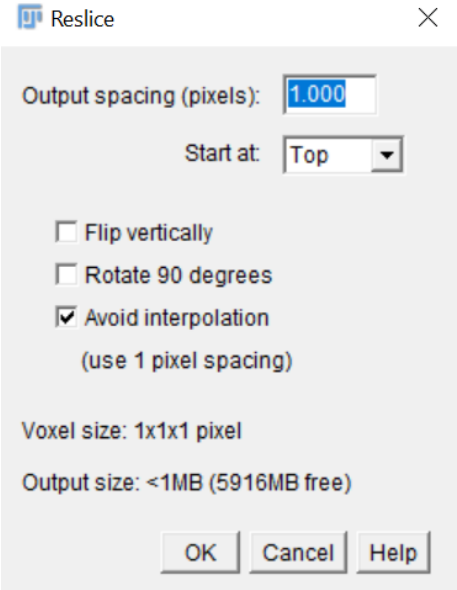

Figure 33: Re-slicing data in FIJI.

FIJI may be used to "re-slice" a data set so that it can be viewed from any orientation (Figure 33). Each image is originally captured in the plane of the light-sheet. Each snapshot contains an angled image which crosses the surface boundary and penetrates into the sample. Once a full stack has been collected, use this function ("from the left") to view layers of tissue in the plane of the cover slip (and the surface). Scan to look closer to the surface or deeper into the sample. To check on the light-sheet point spread function, re-slice fluorescent bead data (0.2μm, green) "from the top". In this orientation, 4.8μ beads produce enough signal to check on the comet tails produced in Airy mode.

7.5.3 Set Scale

Analyze > Set Scale...

The scale refers to the physical size represented by each pixel in our image. Figure 34 shows how the scale should be set for the CLSM with no zoom lens. The step-size for multi-dimensional measurements is set to match the pixel dimensions in x and y, which are identical and measured using a 10μm graticule scale (R1L3S2P, Thorlabs). The compact LSM has a measured pixel-limited lateral resolution of 1.7μm. Occasionally the scale is forgotten in between data sets- always make sure that the scale is set correctly.

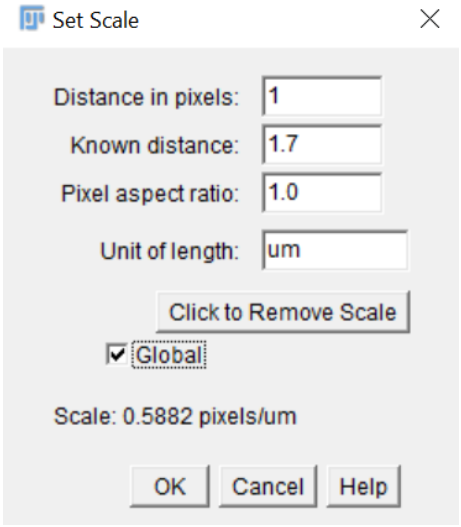

Figure 34: Setting the scale in FIJI. With no zoom lens attached, these parameters should be used.

7.5.4 Scale Bar

Analyze > Tools > Scale Bar...

It is useful to add a scale bar to the image stack (Figure 35). Remember to label all slices. You may prefer to analyse the data first and "shear" it to transform the data cube into the physical parallelopiped that it represents.

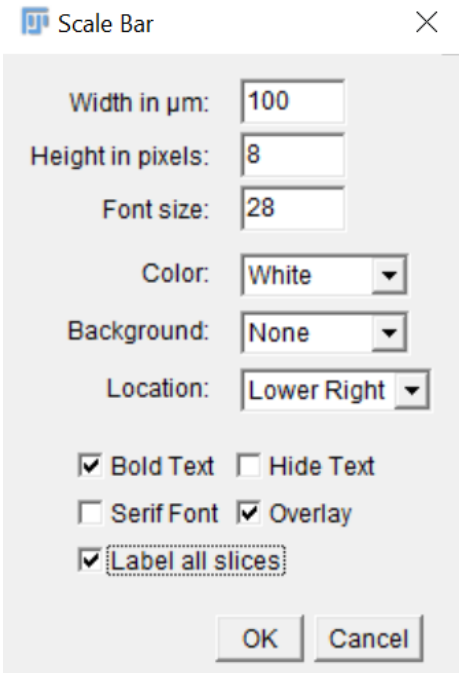

Figure 35: Adding a scale bar to the image stack in FIJI. Size, colour and position may be adjusted as appropriate.

7.5.5 Z Project

Image > Stacks > Z Project...

This option may be used to quickly assess a volume of data. By choosing the maximum intensity option (Figure 36), you can project the brightest parts of each frame into a single 2-D snapshot. This is

particularly useful for looking at scarcely populated bead samples. Beads should be re-sliced from the top first and then projected to get an idea of the point spread function across the entire field of view. Project few frames if the sample is densely populated or if it is a large scan.

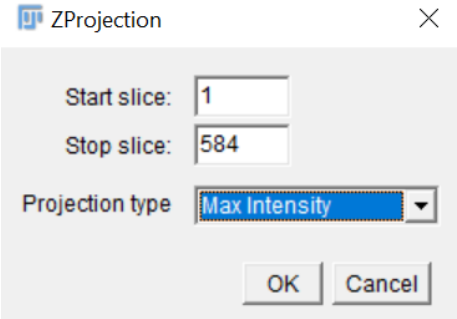

Figure 36: Projecting an image stack in FIJI. Choose a region from the data stack using “start slice” and “stop slice”.

7.5.6 Crop

- Use rectangle tool to select a region of interest from your data set.
- Image > Crop (or use Ctrl+Shift+X)

Cropping is useful when you are only interested in a smaller part of a large data set (Figure 37). ”Crop” removes data outside the region of interest in every frame above and below the current selection (inclusive). Once the data has been removed, the data set is smaller and FIJI can work faster through any adjustments that you make.

N.B. Be aware that once a data set is opened in FIJI, all of the memory required is ”reserved” by FIJI even after the data set is closed but FIJI remains open. Only open a small number at a time, and crop each data set as appropriate before adding anything else to the memory. The memory becomes unreserved again after FIJI has been closed.

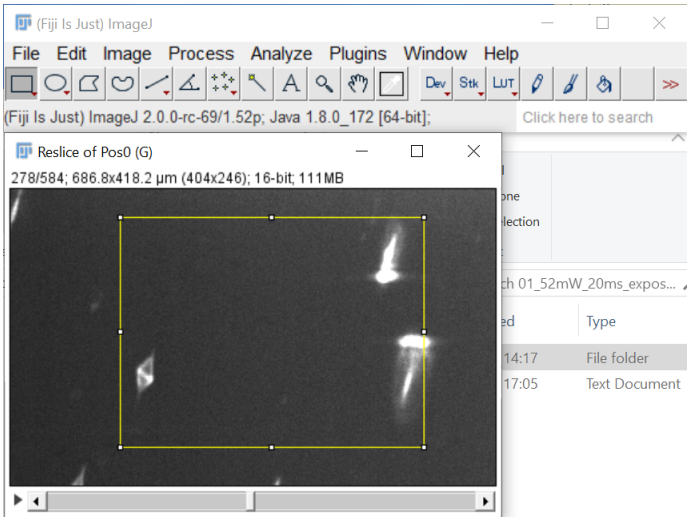

Figure 37: Cropping to a region of interest in FIJI.

7.5.7 Transform

Image > Transform > (Choose transformation from drop down list)

Occasionally it is helpful to transform the entire data set; e.g. flip it left to right or the other way up. This should not be necessary except for Matlab testing or if the camera orientation does not match the

direction expected by the current version of the code. (For our purposes, the image on the screen should show the cover slip boundary as a vertical line on the left hand side of the field of view. To the right of this, we expect to see the sample surface and then deeper into the sample).

7.5.8 Scale...

Image > Scale...

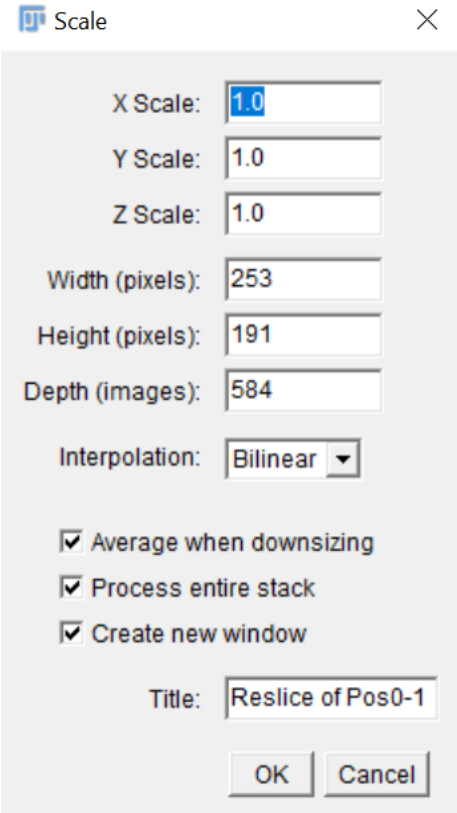

Figure 38: Setting the scale of voxels in a data set in FIJI.

As the voxels are not, in reality, cubic, some versions of the shearing code require the scale to be reset using this function. The scanning direction (z) contains steps of $1.7\mu m$. Some shearing codes may require these steps to be rescaled by dividing this number by $\sqrt{2}$. This may be done using the window shown in Figure 38.

7.5.9 Lookup Tables

Image > Lookup Tables > (Choose colour scheme from drop down list)

FIJI has a variety of in-built lookup tables which may help to make the grey-scale more visible. Green and Cyan are often well-suited to our eyes. Rainbow lookup tables should never be used as our eyes favour the green parts of the spectrum and this may affect conclusions.

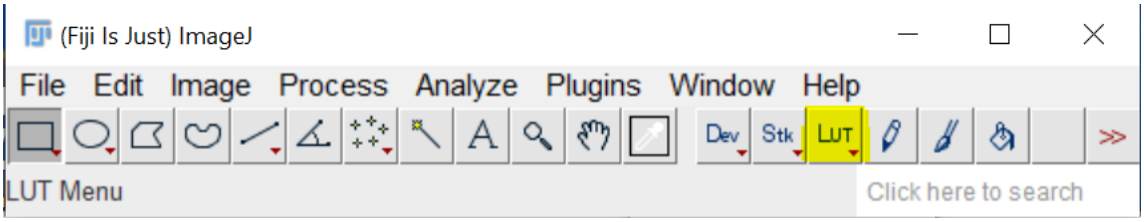

Figure 39: Look up tables. Button highlighted in yellow gives a drop down menu of colour scheme options.

7.5.10 Plot Profile

Analyze > Plot Profile

To draw a line, use the line tool (Figure 40) on an image. Hold down "Shift" as you draw the line to make it perfectly horizontal, straight or at 45°. Next, press "Ctrl+K" to get a plot pf the profile, or use "Analyze > Plot Profile". To get a live plot, press the red "Live" button in the profile window (Figure 41). This allows you to redraw your line or drag it around the image. You may take multiple plots for comparisons.

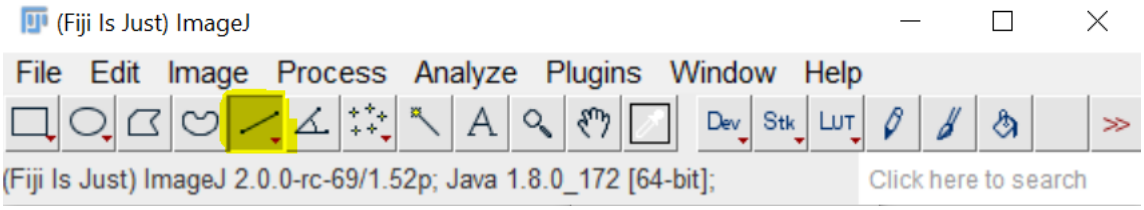

Figure 40: Drawing a line in FIJI. Press the button highlighted in yellow.

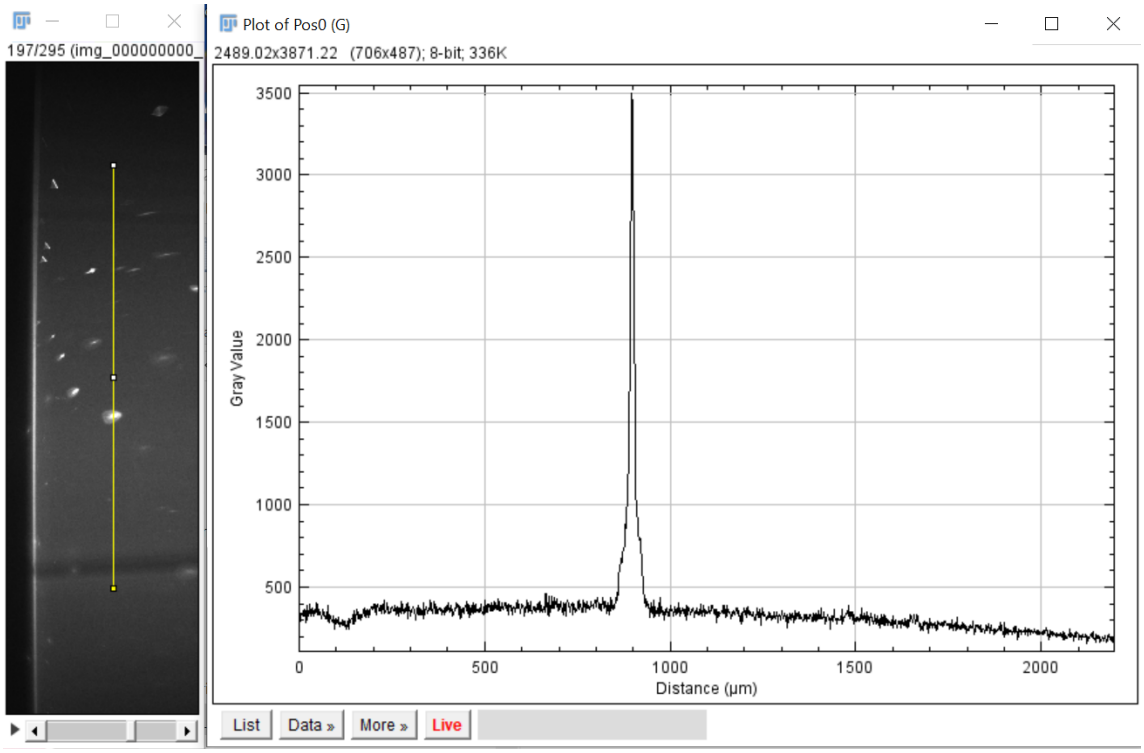

Figure 41: Plotting a line profile in FIJI.

7.5.11 Measure

Analyze > Measure

This function measures whatever you have selected. This may be the length of a line that has been drawn, for example. If nothing has been selected, then "Measure" gives you a summary of the frame.

7.5.12 Synchronize Windows

Analyze > Tools > Synchronize Windows

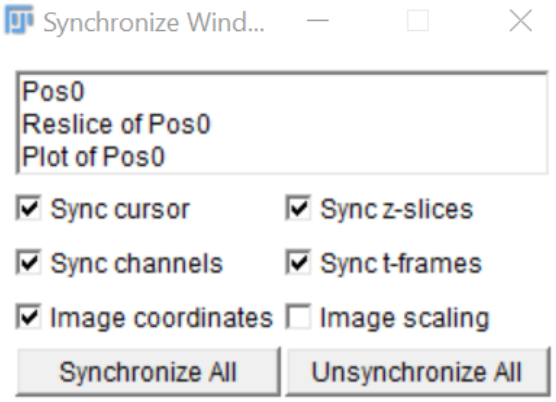

Figure 42: Syncronizing windows in FIJI. Make choices from live menu of all open windows.

This is useful to compare specific beads in a sample after differing image processing. Choose which windows you would like to synchronize from the live menu (Figure 42). Now identically sized data sets may have equivalent line profiles plotted across a particular bead in the re-processed sample.

7.5.13 Shear

Plugins > TransformJ > TranformJ Affine

FIJI has a fast alternative for the custom shearing code written in Matlab. Large data sets will require this to be done on a high-spec computer.

- Set scale as appropriate (probably x=1.7μm, y=1.7μm, z=1.7μm).
- Open TransformJ Affine (Figure 43).
- "Create".
- Click "Shear" in TransformJ: Matrix (Figure 44).
- Set values as shown in Figure 45.
- Come back to Figure 44 and set the value highlighted in yellow. This accounts for the tilt of the shear. 0.5 is a perfect 45° angle. In one recent data set we found that 0.7 is closer to the truth (this is trial and error).
- Save your TransformJ: Matrix to a safe place and give it a sensible name.
- Come back to TransformJ: Affine window (Figure 43). Load your newly saved shearing matrix file and choose background and interpolation. Click "OK".
- To check if your angle is correct, flip a bead sample test so that the cover slip boundary is a vertical line on the right hand side of the field of view. Shear the data. When you scroll through the frames, beads should now appear to be in the same place in each frame. Alternatively, re-slice the bead data from the top and check that comet tails/alternative point spread functions go straight down (can be certain with the line tool whilst holding down "Shift").

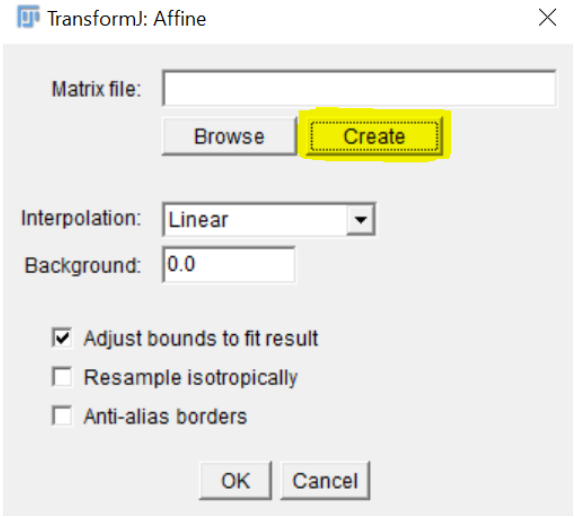

Figure 43

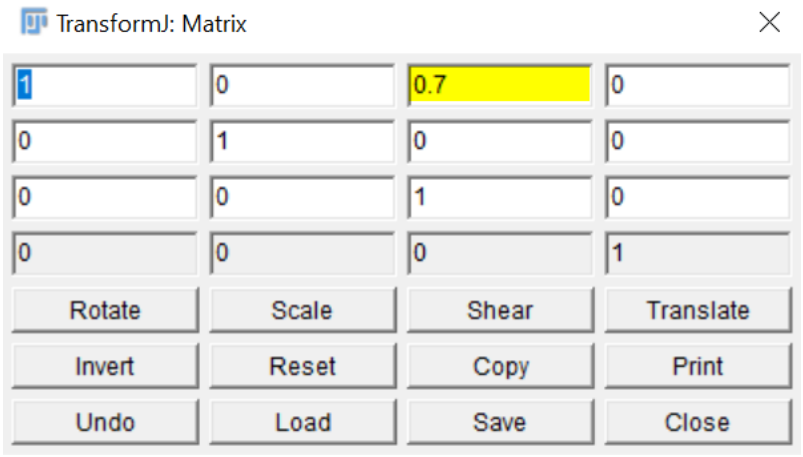

Figure 44

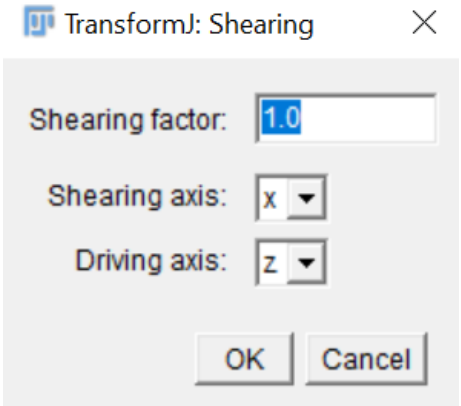

Figure 45

Add in later

7.5.14 ClearVolume

Plugins > ClearVolume This FIJI plugin could be useful for looking at cleared tissue samples. The scan can be rotated to see the morphology of 3-dimensional structures. We have run into memory issues when trying to use the software with larger scans.

8 Sample Preparation

8.1 1% Agarose Gel

Label the eppendorfs that the agarose gel will be stored in. Measure out agarose powder and pure water into a Erlenmeyer flask with a ratio of 1:99. There should be *plenty* of room in the top of the flask - it should be mostly empty. Stir the mixture vigorously with a clean stirrer. Put the flask in a microwave and heat for about a minute at 700W watching continuously. It can be helpful to stop every 10 seconds or so to stir and check that the mixture is not bubbling. We want a clear liquid which, when warm, can be easily pippeted into eppendorfs. There is a very fine margin between undissolved agarose gel and a big puddle in the microwave dish. Although the quantities may be measured out exactly, this process always causes a little evaporation and so your final concentration will be slightly higher than what you have measured. Pipette small quantities into labelled eppendorfs very quickly as the agarose sets within 10-20 minutes.

8.2 Fluorescent Beads

Bead samples are highly sensitive to fluorescent contamination. Small beads become faint to the point of being invisible if the background fluorescence is too high. The lifetime of the bead samples as described is normally a couple of hours (more if evaporation is slowed by placing the slides in a draught-proof container). Always make fresh samples at the beginning of the day (this goes for tissue samples too). The final image quality is highly dependent on the quality of the samples.

8.2.1 0.2μm

The purchased bead mixture is 1% solids. As the beads are only $0.2\mu m$ in diameter, there are many beads per unit volume. The dilution used for the $0.2\mu m$ beads should be adapted when larger beads are required.

Heat the 1% agarose gel inside an eppendorf for around 30 minutes in a dry bath. The dry bath has a reduced risk of evaporating the water compared to microwave heating. Meanwhile, dilute the bead mixture from the bottle (gently invert the bottle a few times for a uniform concentration) 10,000$\times$ in pure 5MΩ water. This mixture should be placed in a sonicator for 20 minutes to remove clumps. When the beads and the agarose gel are ready, they are mixed with a ratio of 1:10 beads to agarose gel. This mixture is shaken in a vortex for 30 seconds and then pipetted out onto a clean cover slip before the gel begins to set. The droplet should be a couple of millimetres high and roughly the diameter of the solid immersion lens (15mm). The cover slips with the fixed beads on top should be left to set for a couple of minutes before moving then=m to the microscope.

8.2.2 4.8μm

Beads larger than the pixel-limited resolution tend to look much less regular under the microscope. This may be due to a lensing effect within the spherical beads. It appears as though the laser light (and therefore the fluorescent response) is stronger where the light exits the bead, presumably where the light is more focused. The protocol for preparation of these beads is almost identical to that of the $0.2\mu m$ beads, however the concentration of the bead mixture should be increased as desired to give a more populated sample.

8.2.3 9.9μm

These beads are not often used, however they can be useful for when the zoom lens is in operation and you would like to characterise the field of view when fully zoomed out. Again, use the same protocol with a higher concentration of bead mixture to agarose gel as desired.

8.3 Fluorescein

Fluorescein powder should be diluted in water to produce a transparent yellow liquid. This colour is excited by the blue laser to produce a green glow which passes through the filters in the detection arm. The exact concentration is not extremely important; there just needs to be enough fluorescence to show the light-sheet and not so much that the signal is saturated (the exposure time for the camera may also be adjusted in μ-Manager to avoid saturated pixels). The surface tension of the diluted fluorescein is sufficient for a droplet (1cm in diameter) to hold itself on top of a pre-mounted cover slip. If any fluorescein gets onto any of the lenses, they will have to be cleaned. Stray fluorescein produces very strong artefacts. The liquid may be dropped onto the cover slip and removed directly from the cover slip using a pasteur pipette to avoid spillages.

8.4 Tissue Samples

General notes:

- Always carry out a risk assessment first
- Some chemicals used are hazardous. Follow local rules
- Observe local rules for waste disposal and safety with biohazardous materials
- Do not leave tissue in liquid for extended periods of time as this can cause morphological damage to the tissue structures

Cut a small piece of tissue using a sharp blade (clean edges are important). Make sure that the tissue is defrosted first if using flash-frozen tissues. For colon: soak in phosphate buffered saline (PBS) solution for 5 minutes. Submerge in acridine orange for 40 seconds. Rinse again in PBS for 30 seconds to a minute - acridine orange should not visibly pool on the surface. The stain takes a few minutes to permeate though the sample; this normally coincides with the time taken to move to the optics lab and mount the sample on the microscope. If storing the sample for more than 10 minutes before imaging, put a very small drop of PBS on the sample and keep in a small, closed container to avoid drying. Always image within a couple of hours of staining. For beef muscle: this tissue tends to be more dense and opaque than human colon tissue. Extend the acridine orange step from 40 seconds to around a minute.

8.5 Other Samples (e.g. cleared)

As of yet, our collaborators have provided all cleared tissue samples for us. This section will be updated if clearing methods are established within our group at the University of St Andrews.

9 SIL Cleaning Protocol

Carefully lift the SIL out of its holder (wearing gloves). Put the lens in a clean ethanol bath and leave it there for a few minutes so that the immersion oil is soaked away. Take the lens out of the bath and polish with a dry optics cleaning tissue. Inspect for residue. If any streaks or oil remain, repeat the bath a polishing steps. *Finally, wash with isopropanol and polish lens dry again.

10 Taking Measurements

For alignment and testing it is often sufficient to take a single snapshot image using μ-Manager, or simply watch the live feed. To check that the motorised stage is performing correctly, take a short multi-dimensional acquisition with the μ-Manager software. A power meter may be used to measure the illumination laser power. A spectrometer has been used to check the illumination spectrum. A wave-front sensor has been used to check the alignment of the beam expansion section.

- Ensure vibrations are minimised as much as possible
- The laser safety box also acts to remove background light that may effect measurements
- Check on samples in between measurements - make sure that tissue has not dried out

- Do not leave the system unattended, particularly in non-laser designated areas. A responsible, trained member of staff should always keep the laser power supply key close by
- Keep an eye on the monitor - sample may have shifted or the exposure time may have become unsuitable for a particular region (avoid saturating pixels)
- Do not give the computer other memory-intensive tasks whilst μ-Manager is acquiring data
- Remember to clear space on the laptop (using an external hard drive or alternative) after each imaging session
- See section on using μ-Manager for details on which parameters to use for acquisitions
- Use a pre-established labelling system for your data and be consistent

10.1 Fine-tuning the Focus

This is particularly important for changing between sample types (e.g. cleared to uncleared transitions). Alter the z position of the cylindrical lens very slightly to move the focus to just inside the bottom surface of the tissue (in cleared tissue, there is a change in refractive index so the position of this focus may move). Make the focus sharper by changing the position of the SIL in the y direction as illustrated below in Figure 46. This is a very subtle movement.

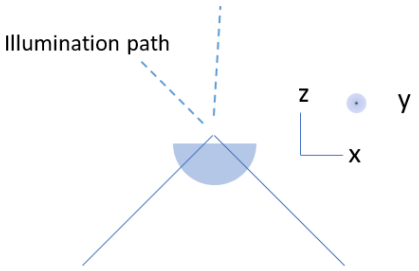

Figure 46

N.B. Tissue samples sit slightly higher above the cover slip compared to beads – this means that beads next to the cover slip will appear slightly out of focus if the system is set up for tissue. Tissue is what should be used to make final adjustments before tissue measurements.

10.2 Example Human Tissue

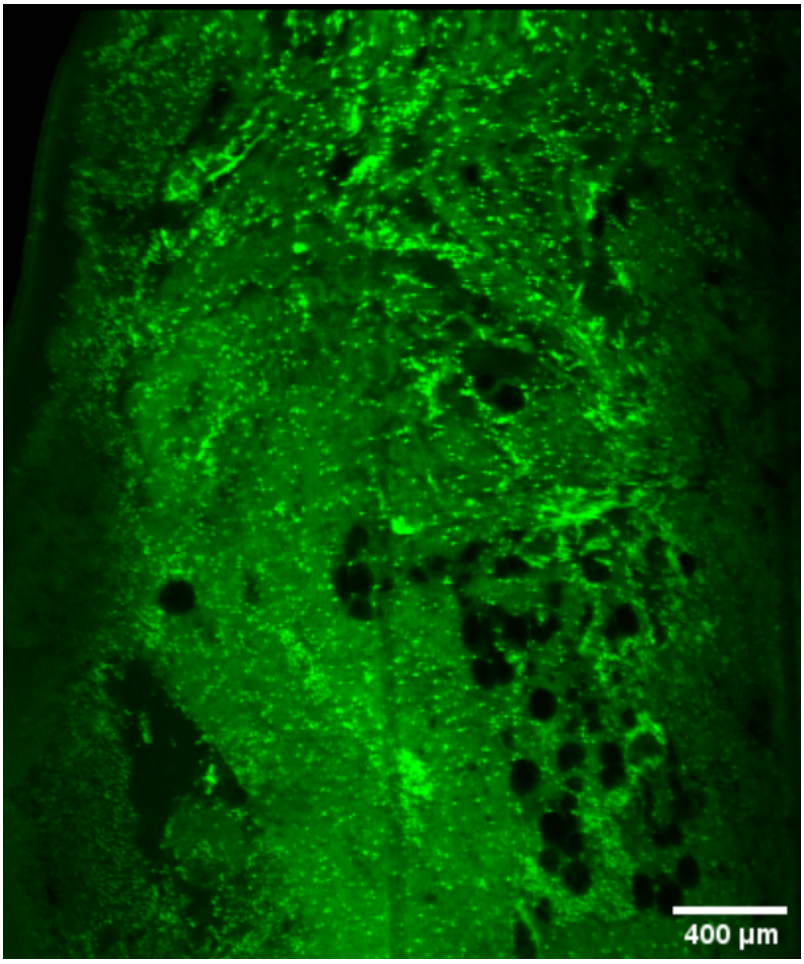

Figure 47

11 Calibration

It is important to measure the lateral resolution, axial resolution and the point spread function (this varies throughout the field of view), the field of view in the camera, the depth of penetration in various samples, the width of the light-sheet, the Airy beam profile, and the time taken for each step from tissue removal to diagnostic evidence. This is not an exhaustive list of important measurements to make, however these ones should be re-evaluated every time something changes in the system. For the following analysis, note that both the numerical aperture and the magnification calculations acquire an extra factor equal to the refractive index of the solid immersion lens (1.46).

11.1 Pixel Size (Lateral Resolution)

Measure the pixel size (which defines the lateral resolution as without the zoom lens this system is pixel-limited) using a graticule (eg R1L3S2P, Thorlabs) in the sample plane (place a cover slip underneath to avoid significant refocusing of the objective). The graticule should be illuminated using diffuse white light through the illumination arm (place a small torch in the cage). The shadow of the graticule could also be measured by back-lighting the graticule in line with the detection pathway. In FIJI, calculate the distance per pixel. In the plane of the light-sheet the aspect ratio is 1:1. The gratings should point to the detection arm and illumination arm, not towards the sample stage. Always measure the part of the grating that is in focus. Take several measurements and then do an average.

To theoretically calculate the pixel size of the system, use the expression given in Equation 1.

$$Pixel\ Limited\ Resolution = \frac{Physical\ Pixel\ Width}{M_{objective} \times \frac{f_{tube,intended}}{f_{tube,actual}} \times n_{SIL}} \tag{1}$$

Equation 1: The pixel-limited resolution of the CLSM. The physical pixel width of the Orca sCMOS camera is $6.5\mu m$. $M_{objective}$ is $4\times$. $\frac{f_{tube,intended}}{f_{tube,actual}} = \frac{3}{4}$. $n_{SIL} = 1.46$.

In our case, this gives a theoretical pixel size of $1.48\mu m$ and we measure the pixel size experimentally as $1.7\mu m$. The discrepancy is to be expected; optical systems are never perfect. Imperfect optics, misalignments and other factors may give rise to a larger resolution.

11.2 Point Spread Function (PSF) in the Plane of the Light-Sheet (Axial resolution)

To measure the axial resolution, prepare a (0.2μm) fluorescent bead sample and take a 3-D scan. Shear the data so that the frames are stored in the correct position relative to one another. Next, re-slice the data in FIJI "from the top" to view the beads in a frame that is perpendicular to the light-sheet. Approximations such as the full width half maximum may be used to measure the axial resolution of the system. Use the "line" tool on FIJI and plot the profile. Theorectically, the axial resolution is given by the thickness of the light-sheet. From the side, a focused light-sheet has a Gaussian profile (Figure 48). The beam waist diameter is described by Equation 2. The general numerical aperture expression is defined in 3.

$$Beam\ Diameter\ at\ Waist = \frac{2 \times \lambda_{illum} \times Focal\ length\ of\ optic}{\pi \times Diameter\ of\ collimated\ beam\ prior\ to\ focus \times NA_{SIL}} \tag{2}$$

Equation 2: This is the beam waist diameter measured at $\frac{1}{e^2}$ of the maximum intensity.

$$NA = n \times sin(\theta) \tag{3}$$

Equation 3: n is the refractive index of the medium and θ is the angle that the beam converges at.

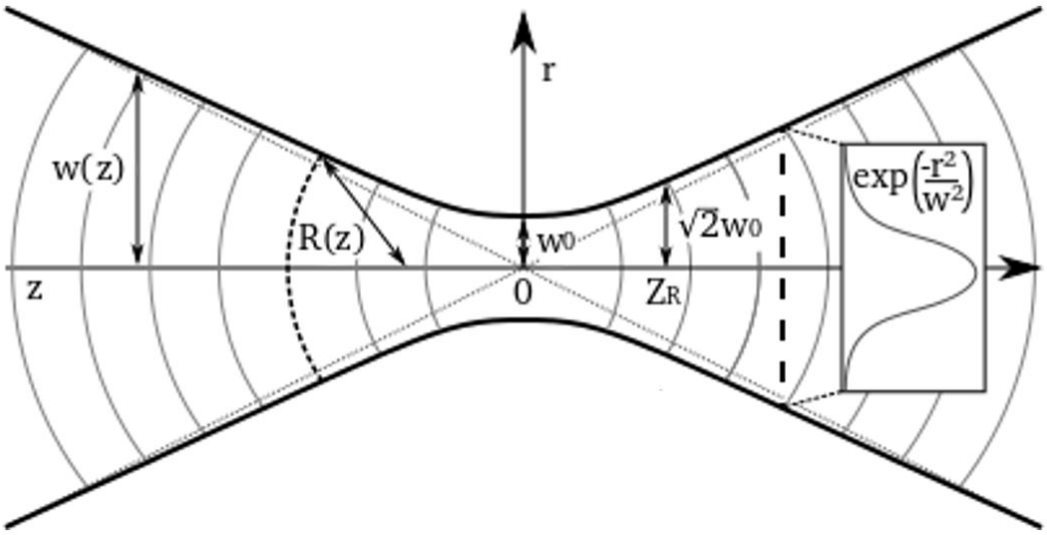

Figure 48: Some useful parameters for a Gaussian beam. w(z): beam radius. R(z): radius of curvature of wave-fronts. w_0: beam waist radius. Z_R: Rayleigh range.

The theoretical axial resolution of the system is around $2.8\mu m$ from approximation in Equation 2. Add in the measured value too.

11.3 Field of View and Width of the Light-Sheet

The field of view collected by the camera depends on the number of pixels in the array, the dimensions of each pixel and the total magnification in the detection arm (which is measured experimentally). This does not really change (unless the zoom lens is added). For the CLSM, the camera field of view has been measured to be almost $3.5mm^2$. This field of view differs from the field of view in the sample, which is confined by off-centre aberrations, depth of penetration, Rayleigh range, the sample, and the light-sheet width etc. The light-sheet width may be calculated by considering the light-sheet cross section in the direction that has not been focused by the cylindrical lens.

11.4 Depth of Penetration in Various Samples

The image quality is always highly dependent on the quality and opacity of the sample. There are two main parameters that affect the depth from which information is accessible: 1. attenuation of light in the sample, and 2. depth of penetration of the fluorescent dye (this is not the case for auto-fluorescent or GFP-modified samples). To measure the depth of usable information, the assessor must make a judgement call about where features become indistinguishable. This may depend on the requirements of the end-user as well. Various frames throughout a 3-D stack should be assessed. Several samples of the same type should be assessed and an average depth should be measured for that particular kind of sample. The "line" tool and "Measure" function in FIJI may be used.

Assuming no aberrations, the theoretical distance over which the sample will be in focus is equal to the Rayleigh range (Equation 4), or half of the confocal parameter. The expression given in Equation 4 applies for the Gaussian beam only. Theoretical calculation of the Airy beam requires a more complex expression (see Vettenberg paper).

$$z_R = \frac{\pi \omega_0^2}{\lambda} \tag{4}$$

11.5 Airy Profile (for Deconvolution)

It is important to experimentally define the Airy profile of the light-sheet so that Airy data may be deconvolved. To do this, prepare a $4.8\mu m$ bead sample and take a 3-D scan. As with the Gaussian PSF measurement, the data must be sheared and then resliced "from the top". $4.8\mu m$ beads are used as the signal from $0.2\mu m$ beads is not strong enough to see the full Airy comet tail. Note the position of the focus relative to the centre of the (cropped?) image and the angle of the comet tails as displaced (anticlockwise?) from a perfect 45° angle CHECK. Then a "parameter sweep" through different deconvolutions is performed. The parameter set that produces the best reduction of the side lobes ("comet tails") is considered to contain the most accurate information about the Airy light-sheet profile.

12 Image Processing

12.1 Shearing

The object plane is the sample is relayed onto the pixel array in the camera. Successive frames are stored in an images stack, which is automatically interpreted as a cube. To see the data in its correct geometry (parallelopiped), the data is "sheared". This may be done with a tailor-made Matlab code. It is important to note the angle of the tilted planes (found by studying the point spread function). The physical step size between successive planes must also be considered.

12.2 Deconvolution (For Airy Data Only)

The current version of the deconvolution code for this system has not yet been perfected. This deconvolution is a 1-D solution, however a 2-D or 3-D deconvolution would be more suited to the 3-D curved light-sheet. We are working with our industrial collaborators at M^2 Life to adapt some existing 3-D deconvolution code for this purpose. In the mean time, the 1-D code may be used to obtain reasonable deconvolved data for close to the surface only.

13 Saving Data

Each data set can easily take up a couple of gigabytes. We recommend external hard drives as a storage solution (this makes data easier to transfer). However, processing files from an external drive takes additional time. It is sometimes preferable to process the data and then save only the processed files, or a region of interest from a particular set. Each group should set up their own data saving protocol. Some institutions with large online storage spaces may prefer to store data online. Before data is taken, a methodology for file naming etc. should be established. Issues like patient confidentiality should be dealt with separately and conditions of ethical approval must be respected.

14 Everyday Use

For more detailed protocol, please see the rest of the document.

- Warn others in the room that there will be laser radiation present. Put on safety goggles.
- Prepare samples
- Check that interlock switches are free/nothing in the way
- Turn on laptop, camera and laser (which will remain shuttered)
- Open μ-Manager
- Check that SIL holder is roughly in the middle of sample holder. Move using μ-Manager stage control if not
- Check that the Airy beam pathway is shuttered
- Make sure that SIL and SIL holder are perfectly clean
- Put SIL in holder

- Put 2-3 drops of immersion oil on SIL
- Place a clean cover slip on SIL, clamp down at sides being careful to avoid air bubbles under cover slip
- Put sample in the centre of the SIL above cover slip
- Replace lid, closing interlock. Laser shutter may now open
- Look at image in live feed. Use μ-Manager to control position. Use this time to crop region of interest as desired, change exposure time as necessary. Check the region that you would like to scan on live feed
- Move stage to starting position for scan
- Stop live feed
- Take scan, remembering to include the necessary parameters and the correct file name and pathway for saving
- When scan is finished, check that laser emission is off in μ-Manager and open the lid. Switch shutter to Gaussian pathway if taking Airy scan
- Repeat scan with new beam, same step size etc.
- Every time the sample is changed, clean the SIL and SIL holder thoroughly and use a clean cover slip
- Empty data from laptop onto external hard drive once at lunchtime and again at the end of the day
- At the end of the day, clean the work space and make sure all waste is disposed of correctly (although this should be done as you go anyway)
- Close μ-Manager, turn the laser and the camera off, and leave the data to download onto the hard drive. Lock laptop. Make sure that the laser power supply box key is never left unattended by the designated responsible person
- Once everything is switched off, lock the lab

15 References

References

1. Böttcher, T. From molecules to life: quantifying the complexity of chemical and biological systems in the Universe. *Journal of molecular evolution* **86,** 1–10 (2018).

2. Smith, M. J. *et al.* Real-time NMR monitoring of biological activities in complex physiological environments. *Current Opinion in Structural Biology* **32.** New constructs and expression of proteins / Sequences and topology, 39–47 (2015).

3. Henderson, R. *et al.* Biological markers in environmental health research. *Environ. Health Perspect* **7,** 3–9 (1987).

4. Lange, O. L., Nobel, P. S., Osmond, C. B. & Ziegler, H. *Physiological plant ecology III: Responses to the chemical and biological environment* (Springer Science & Business Media, 2013).

5. Twomey, J. D. *et al.* COVID-19 update: The race to therapeutic development. *Drug Resistance Updates* **53,** 100733 (2020).

6. Isomaa, B. A major health hazard: the metabolic syndrome. *Life Sciences* **73,** 2395–2411 (2003).

7. Webster, J. P., Molyneux, D. H., Hotez, P. J. & Fenwick, A. The contribution of mass drug administration to global health: past, present and future. *Philosophical Transactions of the Royal Society B: Biological Sciences* **369,** 20130434 (2014).

8. Balunas, M. J. & Kinghorn, A. D. Drug discovery from medicinal plants. *Life Sciences* **78,** 431–441 (2005).

9. Green, B. Use of the Hippocratic or other professional oaths in UK medical schools in 2017: practice, perception of benefit and principlism. *BMC research notes* **10,** 1–4 (2017).

10. Krishnamurthy, S., Brown, J. Q., Iftimia, N., Levenson, R. M. & Rajadhyaksha, M. Ex Vivo Microscopy: A Promising Next-Generation Digital Microscopy Tool for Surgical Pathology Practice. *Archives of pathology & laboratory medicine* **143** (2019).

11. Andreucci, M., Solomon, R. & Tasanarong, A. Side effects of radiographic contrast media: pathogenesis, risk factors, and prevention. *BioMed research international* **2014** (2014).

12. Turchin, I. V. Methods of biomedical optical imaging: from subcellular structures to tissues and organs. *Physics-Uspekhi* **59,** 487 (2016).

13. Yoon, S. *et al.* Deep optical imaging within complex scattering media. *Nature Reviews Physics* **2,** 141–158 (2020).

14. Rodríguez, C. *et al.* multiphoton imaging in vivo. **18** (2021).

15. McMullan, D. Scanning electron microscopy 1928–1965. *Scanning* **17,** 175–185 (1995).

16. Vernon-Parry, K. Scanning electron microscopy: an introduction. *III-Vs Review* **13,** 40–44 (2000).

17. Leamy, H. Charge collection scanning electron microscopy. *Journal of Applied Physics* **53,** R51–R80 (1982).

18. Zhou, W., Apkarian, R., Wang, Z. L. & Joy, D. in *Scanning microscopy for nanotechnology* 1–40 (Springer, 2006).

19. Bennett, A. E. *et al.* Ion-abrasion scanning electron microscopy reveals surface-connected tubular conduits in HIV-infected macrophages. *PLoS Pathogens* **5,** e1000591 (2009).

20. Crewe, A. & Wall, J. A scanning microscope with 5 Å resolution. *Journal of Molecular Biology* **48,** 375–393 (1970).

21. Pease, R. & Nixon, W. High resolution scanning electron microscopy. *Journal of Scientific Instruments* **42,** 81 (1965).

22. Titze, B. & Genoud, C. Volume scanning electron microscopy for imaging biological ultrastructure. *Biology of the Cell* **108,** 307–323 (2016).

23. Kherlopian, A. R. *et al.* A review of imaging techniques for systems biology. *BMC Systems Biology* **18,** 1–18 (2008).

24. Farkas, D. L. Biomedical Applications of Translational Optical Imaging: From Molecules to Humans. *Molecules* **26** (2021).

25. Applegate, M. B., Istfan, R. E., Spink, S., Tank, A. & Roblyer, D. Recent advances in high speed diffuse optical imaging in biomedicine. *APL Photonics* **5,** 040802 (2020).

26. Marchesini, R., Bertoni, A., Andreola, S., Melloni, E. & Sichirollo, A. Extinction and absorption coefficients and scattering phase functions of human tissues in vitro. *Applied Optics* **28,** 2318–2324 (1989).

27. *Blue Sky, Hyperphysics* Accessed on 19.09.2022. http://hyperphysics.phy-astr.gsu.edu/hbase/atmos/blusky.html.

28. Shirley, J. W. An early experimental determination of Snell's law. *American Journal of Physics* **19,** 507–508 (1951).

29. Becker, F. & Richardson, R. Critical-Angle Reflectivity. *The Journal of the Acoustical Society of America* **45,** 793–794 (1969).

30. Marcatili, E. Extrapolation of Snell's law to optical fibers. *JOSA* **63,** 1372–1373 (1973).

31. Lichtman, J. W. & Conchello, J.-A. Fluorescence microscopy. *Nature Methods* **2,** 910–919 (2005).

32. Marchesini, R., Bertoni, A., Andreola, S., Melloni, E. & Sichirollo, A. E. Extinction and absorption coefficients and scattering phase functions of human tissues in vitro. *Appl. Opt.* **28,** 2318–2324 (1989).

33. Alabugin, A. Near-IR Photochemistry for Biology: Exploiting the Optical Window of Tissue. *Photochemistry and Photobiology* **95,** 722–732 (2019).

34. Anderson, R. R. & Parrish, J. A. The optics of human skin. *Journal of investigative dermatology* **77,** 13–19 (1981).

35. Chen, G. *et al.* Advanced Near-Infrared Light for Monitoring and Modulating the Spatiotemporal Dynamics of Cell Functions in Living Systems. *Advanced Science* **7,** 1903783 (2020).

36. Curcio, J. A. & Petty, C. C. The Near Infrared Absorption Spectrum of Liquid Water. *J. Opt. Soc. Am.* **41,** 302–304 (1951).

37. Sordillo, L. A. *et al. Third therapeutic spectral window for deep tissue imaging* in *Optical Biopsy XII* (eds Alfano, R. R. & Demos, S. G.) **8940** (SPIE, 2014), 128–134.

38. James, F. A. J. L., Jones, R. V. & Paton, W. D. M. The conservation of energy, theories of absorption and resonating molecules, 1851-1854: G. G. Stokes, A. J. Ångström and W. Thomson. *Notes and Records of the Royal Society of London* **38,** 79–107 (1983).

39. Herman, B. *Fluorescence microscopy* (Garland Science, 2020).

40. Renz, M. Fluorescence microscopy—A historical and technical perspective. *Cytometry Part A* **83,** 767–779 (2013).

41. Shashkova, S. & Leake, M. C. Single-molecule fluorescence microscopy review: shedding new light on old problems. *Bioscience Reports* **37** (2017).

42. Walker, D. A fluorescence technique for measurement of concentration in mixing liquids. *Journal of Physics E: Scientific Instruments* **20,** 217 (1987).

43. *Jablonski Diagrams* Accessed on 19.09.2022. https://en.wikipedia.org/wiki/Jablonski_diagram#/media/File:Jablonski_Diagram_of_Fluorescence_Only-en.svg.

44. Einstein, A. Über einen die Erzeugung und Verwandlung des Lichtes betreffenden heuristischen Gesichtspunkt. *Annalen der Physik* **322,** 132–148 (1905).

45. Rumi, M. & Perry, J. W. Two-photon absorption: an overview of measurements and principles. *Adv. Opt. Photon.* **2,** 451–518 (2010).

46. Signorini, R. *et al.* Effective Two-Photon Absorption Cross Section of Heteroaromatic Quadrupolar Dyes : Dependence on Measurement Technique and Laser Pulse Characteristics, 4224–4234 (2008).

47. Xu, C. & Webb, W. W. in *Topics in fluorescence spectroscopy* 471–540 (Springer, 2002).

48. Cheng, L.-C., Horton, N. G., Wang, K., Chen, S.-J. & Xu, C. Measurements of multiphoton action cross sections for multiphoton microscopy. *Biomedical Optics Express* **5,** 3427–3433 (2014).

49. Parravicini, J. *et al.* Practical two-photon-absorption cross sections and spectra of eosin and hematoxylin. *Journal of Biophotonics* **13,** e202000141 (2020).

50. Cheng, L.-c., Horton, N. G., Wang, K., Chen, S.-j. & Xu, C. Measurements of multiphoton action cross sections for multiphoton microscopy. **5,** 855–859 (2014).

51. Xu, C., Zipfel, W., Shear, J. B., Williams, R. M. & Webb, W. W. Multiphoton fluorescence excitation : New spectral windows for biological nonlinear microscopy. **93,** 10763–10768 (1996).

52. Kumar, S., Singh, A., Singh, V. R., George, J. B. & Balaji, J. Saturation Dynamics Measures Absolute Cross Section and Generates Contrast within a Neuron. *Biophysj* **111,** 1328–1336 (2016).

53. Ragazzi, M. *et al.* Fluorescence confocal microscopy for pathologists, 460–471 (2014).

54. Wang, M. *et al.* High-Resolution Rapid Diagnostic Imaging of Whole Prostate Biopsies Using Video-Rate Fluorescence Structured Illumination Microscopy. **75,** 4032–4042 (2015).

55. Xiong, B., Han, X., Wu, J., Xie, H. & Dai, Q. Improving axial resolution of Bessel beam light-sheet fluorescence microscopy by photobleaching imprinting. *Opt. Express* **28,** 9464–9476 (2020).

56. Glaser, A. K. *et al.* Light-sheet microscopy for slide-free non-destructive pathology of large clinical specimens. *Nature Biomedical Engineering* **1** (2017).

57. Corsetti, S., Gunn-Moore, F. & Dholakia, K. Light sheet fluorescence microscopy for neuroscience. *Journal of Neuroscience Methods* **319.** Methods and Models in Alzheimer's Disease Research, 16–27 (2019).

58. Corsetti, S. *et al.* Widefield light sheet microscopy using an Airy beam combined with deep-learning super-resolution. *OSA Continuum* **3,** 1068–1083 (2020).

59. Gustafsson, M. G. *et al.* Three-dimensional resolution doubling in wide-field fluorescence microscopy by structured illumination. *Biophysical Journal* **94,** 4957–4970 (2008).

60. Rao, J., Dragulescu-Andrasi, A. & Yao, H. Fluorescence imaging in vivo: recent advances. *Current opinion in biotechnology* **18,** 17–25 (2007).

61. Song, L., Hennink, E., Young, I. & Tanke, H. Photobleaching kinetics of fluorescein in quantitative fluorescence microscopy. *Biophysical Journal* **68,** 2588–2600 (1995).

62. Szendi-Szatmári, T., Szabó, Á., Szöllősi, J. & Nagy, P. Reducing the Detrimental Effects of Saturation Phenomena in FRET Microscopy. *Analytical Chemistry* **91,** 6378–6382 (2019).

63. Fu, Y., Wang, H., Shi, R. & Cheng, J.-X. Characterization of photodamage in coherent anti-Stokes Raman scattering microscopy. *Opt. Express* **14,** 3942–3951 (2006).

64. Soeller, C. & Cannell, M. Construction of a two-photon microscope and optimisation of illumination pulse duration. *Pflügers Archiv* **432,** 555–561 (1996).

65. Smith, A. W. & Landon, A. J. Mode-locked laser pulse shapes. *Applied Physics Letters* **17,** 340–343 (1970).

66. Diels, J.-C. M., Fontaine, J. J., McMichael, I. C. & Simoni, F. Control and measurement of ultrashort pulse shapes (in amplitude and phase) with femtosecond accuracy. *Appl. Opt.* **24,** 1270–1282 (1985).

67. Gao, A., Qin, W., Liu, W. & Cai, C. *Lorentzian function curve fitting of longitudinal mode of pulsed laser based on LabVIEW* in *Fourth International Conference on Experimental Mechanics* **7522** (2010), 1838–1843.

68. Lefort, C. A review of biomedical multiphoton microscopy and its laser sources. *Journal of physics D: Applied physics* **50,** 423001 (2017).

69. Royon, R., Lhermite, J., Sarger, L. & Cormier, E. High power, continuous-wave ytterbium-doped fiber laser tunable from 976 to 1120 nm. *Optics Express* **21,** 13818–13823 (2013).

70. Stolen, R. H. & Lin, C. Self-phase-modulation in silica optical fibers. *Phys. Rev. A* **17,** 1448–1453 (4 1978).

71. Tai, S.-P. *et al.* Two-photon fluorescence microscope with a hollow-core photonic crystal fiber. *Opt. Express* **12,** 6122–6128 (2004).

72. Pinault, S. C. & Potasek, M. Frequency broadening by self-phase modulation in optical fibers. *JOSA B* **2,** 1318–1319 (1985).

73. Stolen, R. & Ashkin, A. Optical Kerr effect in glass waveguide. *Applied Physics Letters* **22,** 294–296 (1973).

74. Onishi, M., Kanamori, H., Kato, T. & Nishimura, M. *Optimization of dispersion-compensating fibers considering self-phase modulation suppression* in *Optical Fiber Communications, OFC.* (1996), 200–201.

75. Boyraz, O., Indukuri, T. & Jalali, B. Self-phase-modulation induced spectral broadening in silicon waveguides. *Optics Express* **12,** 829–834 (2004).

76. Moses, J., Malomed, B. A. & Wise, F. W. Self-steepening of ultrashort optical pulses without self-phase-modulation. *Physical Review A* **76,** 021802 (2007).

77. DeMartini, F., Townes, C., Gustafson, T. & Kelley, P. Self-steepening of light pulses. *Physical Review* **164,** 312 (1967).

78. Suydam, B. in *The Supercontinuum Laser Source* 295–317 (Springer, 2006).

79. Bird, D. & Gu, M. Resolution improvement in two-photon fluorescence microscopy with a single-mode fiber. *Applied Optics* **41,** 1852–1857 (2002).

80. Tang, J., Ren, J. & Han, K. Y. Fluorescence imaging with tailored light. *Nanophotonics* **8,** 2111–2128 (2019).

81. Klein, E. *Notes on underwater sound research and applications before 1939* (Department of the Navy, Office of Naval Research, 1967).

82. Abbe, E. Beiträge zur Theorie des Mikroskops und der mikroskopischen Wahrnehmung. *Archiv für mikroskopische Anatomie* **9,** 413–468 (1873).

83. Lauterbach, M. A. Finding, defining and breaking the diffraction barrier in microscopy–a historical perspective. *Optical Nanoscopy* **1,** 1–8 (2012).

84. Gustafsson, M. Surpassing the lateral resolution limit by a factor of two using structured illumination microscopy. *Journal of Microscopy* **198,** 82–7 (2000).

85. Siegerist, F. *et al.* Structured illumination microscopy and automatized image processing as a rapid diagnostic tool for podocyte effacement. *Scientific Reports* **7,** 1–11 (2017).

86. Saxena, M., Eluru, G. & Gorthi, S. S. Structured illumination microscopy. *Adv. Opt. Photon.* **7,** 241–275 (2015).

87. Li, D. *et al.* Extended-resolution structured illumination imaging of endocytic and cytoskeletal dynamics. *Science* **349,** aab3500 (2015).

88. Gustafsson, N. *et al.* Fast live-cell conventional fluorophore nanoscopy with ImageJ through super-resolution radial fluctuations. *Nature Communications* **7,** 1–9 (2016).

89. Komis, G. *et al.* Superresolution live imaging of plant cells using structured illumination microscopy. *Nature Protocols* **10,** 1248–1263 (2015).

90. Kipnis, A., Goldsmith, A. J., Eldar, Y. C. & Weissman, T. Distortion Rate Function of Sub-Nyquist Sampled Gaussian Sources. *IEEE Transactions on Information Theory* **62,** 401–429 (2016).

91. Lévesque, L. Nyquist sampling theorem: understanding the illusion of a spinning wheel captured with a video camera. *Physics Education* **49,** 697 (2014).

92. Kino, G. S. & Corle, T. R. *Confocal scanning optical microscopy and related imaging systems* (Academic Press, 1996).

93. Williams, C. S. & Becklund, O. A. *Introduction to the optical transfer function* (SPIE Press, 2002).

94. Khooa, V. S. *et al.* Magnetic resonance imaging (MRI): considerations and applications in radiotherapy treatment planning. *Radiotherapy and oncology* **42,** 1–15 (1997).

95. Pooley, R. A. Fundamental Physics of MR Imaging. *RadioGraphics* **25,** 1087–1099 (2005).

96. Jog, A., Carass, A. & Prince, J. L. *Improving magnetic resonance resolution with supervised learning* in *2014 IEEE 11th International Symposium on Biomedical Imaging (ISBI)* (2014), 987–990.

97. Ciobanu, L. & Pennington, C. 3D micron-scale MRI of single biological cells. *Solid State Nuclear Magnetic Resonance* **25.** 31st Congress Ampere, Magnetic Resonance and Related Phenomena, 138–141 (2004).

98. Weissleder, R. Weissleder, R. Scaling down imaging: molecular mapping of cancer in mice. Nat Rev Cancer 2: 11-18. *Nature reviews. Cancer* **2,** 11–8 (Feb. 2002).

99. Grover, V. P. *et al.* Magnetic Resonance Imaging: Principles and Techniques: Lessons for Clinicians. *Journal of Clinical and Experimental Hepatology* **5,** 246–255 (2015).

100. *MRI scan* Apr. 2022. https://www.nhs.uk/conditions/mri-scan/what-happens/.

101. https://www.nhs.uk/conditions/mri-scan/what-happens/.

102. Yeh, B. M. *et al.* Opportunities for new CT contrast agents to maximize the diagnostic potential of emerging spectral CT technologies. *Advanced drug delivery reviews* **113,** 201–222 (2017).

103. Lin, E. & Alessio, A. What are the basic concepts of temporal, contrast, and spatial resolution in cardiac CT? *Journal of Cardiovascular Computed Tomography* **3,** 403–408 (2009).

104. Wang, J. & Fleischmann, D. Improving Spatial Resolution at CT: Development, Benefits, and Pitfalls. *Radiology* **289,** 261–262 (2018).

105. Carovac, A., Smajlovic, F. & Junuzovic, D. Application of ultrasound in medicine. *Acta Informatica Medica* **19,** 168 (2011).

106. Bennett, G. L. & Balthazar, E. J. Ultrasound and CT evaluation of emergent gallbladder pathology. *Radiologic Clinics* **41,** 1203–1216 (2003).

107. D'amico, A. & Pittenger, R. *A brief history of active sonar* tech. rep. (SPACE and NAVAL WARFARE SYSTEMS CENTER SAN DIEGO CA, 2009).

108. Tsai, T.-H., Fujimoto, J. G. & Mashimo, H. Endoscopic Optical Coherence Tomography for Clinical Gastroenterology. *Diagnostics* **4,** 57–93 (2014).

109. Von Ramm, O. T. & Smith, S. W. *Prospects And Limitations Of Diagnostic Ultrasound* in *Recent and Future Developments in Medical Imaging II* **0206** (SPIE, 1979), 6–18.

110. Maier, A., Steidl, S., Christlein, V. & Hornegger, J. Medical imaging systems: An introductory guide (2018).

111. Mohammed, A. & Abdullah, A. *Scanning electron microscopy (SEM): A review* in *Proceedings of the 2018 International Conference on Hydraulics and Pneumatics—HERVEX, Băile Govora, Romania* (2018), 7–9.

112. Golding, C. G., Lamboo, L. L., Beniac, D. R. & Booth, T. F. The scanning electron microscope in microbiology and diagnosis of infectious disease. *Scientific Reports* **6,** 1–8 (2016).

113. Ackermann, H.-W. & Heldal, M. Basic electron microscopy of aquatic viruses. *Manual of aquatic viral ecology* **18,** 182–192 (2010).

114. Haddad, G. *et al.* Rapid scanning electron microscopy detection and sequencing of severe acute respiratory syndrome Coronavirus 2 and other respiratory viruses. *Frontiers in Microbiology* **11,** 596180 (2020).

115. Huang, B., Wu, M., Wang, W., De Camilli, P. & Zhuang, X. Three-dimensional Superresolution Fluorescence Microscopy and Its Application to Clathrin Mediated Endocytosis. *Biophysical Journal* **96,** 16a (2009).

116. Boyde, A. & Wood, C. Preparation of animal tissues for surface-scanning electron microscopy. *Journal of Microscopy* **90,** 221–249 (1969).

117. Iftimia, N. *et al. Optical coherence tomography imaging for cancer diagnosis and therapy guidance* in *2009 Annual International Conference of the IEEE Engineering in Medicine and Biology Society* (2009), 4067–4069.

118. Cahill, R. A. *et al.* Intraperitoneal virtual biopsy by fibered optical coherence tomography (OCT) at natural orifice transluminal endoscopic surgery. *Journal of Gastrointestinal Surgery* **14,** 732–738 (2010).

119. Drexler, W. *et al. In vivo ultrahlgh-resolution, functional optical coherence tomography* in *Conference on Lasers and Electro-Optics* (2000), CThF4.

120. Lee, A. M. D. *et al.* Wide-field in vivo oral OCT imaging. *Biomed. Opt. Express* **6,** 2664–2674 (2015).

121. Xu, J., Pokorny, J. & Smith, V. C. Optical density of the human lens. *J. Opt. Soc. Am. A* **14,** 953–960 (1997).

122. Matenaers, C., Popper, B., Rieger, A., Wanke, R. & Blutke, A. Practicable methods for histological section thickness measurement in quantitative stereological analyses. *PloS One* **13,** e0192879 (2018).

123. Pullman, J. private communication. Oct. 2019.

124. Taqi, S. A., Sami, S. A., Sami, L. B. & Zaki, S. A. A review of artifacts in histopathology (2018).

125. Irshad, H., Member, S., Veillard, A., Roux, L. & Racoceanu, D. Methods for Nuclei Detection , Segmentation , and Classification in Digital Histopathology : A Review — Current Status and Future Potential. *IEEE Reviews in Biomedical Engineering* **7,** 97–114 (2014).

126. Titford, M. A Short History of Histopathology Technique. *Journal of Histotechnology* **29,** 99–110 (2006).

127. Chen, Y. *et al.* Rapid pathology of lumpectomy margins with open-top light-sheet (OTLS) microscopy. *Biomed. Opt. Express* **10,** 1257–1272 (2019).

128. Fereidouni, F., Mitra, A. D., Demos, S. & Levenson, R. Microscopy with UV Surface Excitation (MUSE) for slide-free histology and pathology imaging. *Optical Biopsy XIII: Toward Real-Time Spectroscopic Imaging and Diagnosis* **9318,** 46–51 (2015).

129. Qorbani, A. *et al.* Microscopy with ultraviolet surface excitation (MUSE): A novel approach to real-time inexpensive slide-free dermatopathology. *Journal of Cutaneous Pathology* **45,** 498–503 (2018).

130. Xie, W. *et al. Microscopy with Ultraviolet Surface Excitation (MUSE) for Rapid Intraoperative Pathology of Breast Surgical Margins* in *Biophotonics Congress: Optics in the Life Sciences Congress 2019 (BODA,BRAIN,NTM,OMA,OMP)* (Optical Society of America, 2019), JW4C.3.

131. Fereidouni, F. *et al.* Microscopy with ultraviolet surface excitation for rapid slide-free histology. *Nature Biomedical Engineering* **1,** 957–966 (2017).

132. Kopp, K., Demos, S. G. & Kosc, T. Z. *Microscopy with ultraviolet surface excitation (MUSE) enables translation of optical biopsy principles to enhance life science education* in *Optical Biopsy XVII: Toward Real-Time Spectroscopic Imaging and Diagnosis* **10873** (2019), 190–197.

133. Shortis, M. R., Seager, J. W., Harvey, E. S. & Robson, S. *Influence of Bayer filters on the quality of photogrammetric measurement* in *Videometrics VIII* (eds Beraldin, J.-A., El-Hakim, S. F., Gruen, A. & Walton, J. S.) **5665** (SPIE, 2005), 164–171.

134. Yoshitake, T. *et al.* Rapid histopathological imaging of skin and breast cancer surgical specimens using immersion microscopy with ultraviolet surface excitation. *Scientific Reports* **8,** 1–12 (2018).

135. Fouquet, C. *et al.* Improving axial resolution in confocal microscopy with new high refractive index mounting media. *PloS One* **10,** e0121096 (2015).

136. Clendenon, S. G., Young, P. A., Ferkowicz, M., Phillips, C. & Dunn, K. W. Deep tissue fluorescent imaging in scattering specimens using confocal microscopy. *Microscopy and Microanalysis* **17,** 614–617 (2011).

137. Bruce, M. A. & Butte, M. J. Real-time GPU-based 3D Deconvolution. *Opt. Express* **21,** 4766–4773 (2013).

138. Nylk, J. *et al. Structured illumination microscopy as a diagnostic tool for nephrotic disease* in *Advanced Biomedical and Clinical Diagnostic and Surgical Guidance Systems XV* **10054** (2017), 158–164.

139. Ma, Y. *et al.* Recent advances in structured illumination microscopy. *Journal of Physics: Photonics* **3,** 024009 (2021).

140. Super-resolution optical imaging: A comparison. *Micro and Nano Engineering* **2,** 7–28 (2019).

141. Wicker, K., Mandula, O., Best, G., Fiolka, R. & Heintzmann, R. Phase optimisation for structured illumination microscopy. *Optics Express* **21,** 2032–2049 (2013).

142. Neil, M., Juškaitis, R. & Wilson, T. Real time 3D fluorescence microscopy by two beam interference illumination. *Optics Communications* **153,** 1–4 (1998).

143. York, A. G. *et al.* Resolution doubling in live, multicellular organisms via multifocal structured illumination microscopy. *Nature Methods* **9,** 749–754 (2012).

144. Wang, M. *et al.* Gigapixel surface imaging of radical prostatectomy specimens for comprehensive detection of cancer- positive surgical margins using structured illumination microscopy. *Nature Publishing Group,* 1–16 (2016).

145. Schlichenmeyer, T. C., Wang, M., Elfer, K. N. & Brown, J. Q. Video-rate structured illumination microscopy for high-throughput imaging of large tissue areas. *Biomed. Opt. Express* **5,** 366–377 (2014).

146. Wang, M. *et al.* Partial nephrectomy margin imaging using structured illumination microscopy, 1–9 (2018).

147. Johnson, K. A. & Hagen, G. M. Artifact-free whole-slide imaging with structured illumination microscopy and Bayesian image reconstruction. *GigaScience* **9** (2020).

148. Mertz, J. Optical sectioning microscopy with planar or structured illumination. *Nature Methods* **8,** 811–819 (2011).

149. Chang, B.-J., Perez Meza, V. D. & Stelzer, E. H. K. csiLSFM combines light-sheet fluorescence microscopy and coherent structured illumination for a lateral resolution below 100 nm. *Proceedings of the National Academy of Sciences* **114,** 4869–4874 (2017).

150. Escobet-Montalbán, A. *et al.* Wide-field multiphoton imaging through scattering media without correction. *Science Advances* **4,** eaau1338 (2018).

151. Piksarv, P. *et al.* Integrated single-and two-photon light sheet microscopy using accelerating beams. *Scientific Reports* **7,** 1–8 (2017).

152. Veettikazhy, M. *et al.* Multi-photon attenuation-compensated light-sheet fluorescence microscopy. *Scientific Reports* **10,** 1–10 (2020).

153. Veettikazhy, M. Towards Multi-photon Light-sheet Microscopy through a Fiber (2021).

154. Purnapatra, S. B. & Pratim Mondal, P. Generation of extended light-sheets for single and multi-photon fluorescence microscopy. *Applied Physics Letters* **103,** 043701 (2013).

155. Siedentopf, H. & Zsigmondy, R. Uber Sichtbarmachung und Größenbestimmung ultramikoskopischer Teilchen, mit besonderer Anwendung auf Goldrubingläser. *Annalen der Physik* **315,** 1–39 (1902).

156. Voie, A. H., Burns, D. & Spelman, F. Orthogonal-plane fluorescence optical sectioning: Three-dimensional imaging of macroscopic biological specimens. *Journal of Microscopy* **170,** 229–236 (1993).

157. Wohland, T., Shi, X., Sankaran, J. & Stelzer, E. H. Single Plane Illumination Fluorescence Correlation Spectroscopy (SPIM-FCS) probes inhomogeneous three-dimensional environments. *Opt. Express* **18,** 10627–10641 (2010).

158. Poola, P. K., Afzal, M. I., Yoo, Y., Kim, K. H. & Chung, E. Light sheet microscopy for histopathology applications. *Biomedical Engineering Letters* **9,** 279–291 (2019).

159. Barner, L. A., Glaser, A. K., True, L. D., Reder, N. P. & Liu, J. T. C. Solid immersion meniscus lens (SIMlens) for open-top light-sheet microscopy. *Opt. Lett.* **44,** 4451–4454 (2019).

160. Olarte, O. E., Andilla, J., Gualda, E. J. & Loza-Alvarez, P. Light-sheet microscopy: a tutorial. *Adv. Opt. Photon.* **10,** 111–179 (2018).

161. Power, R. M. & Huisken, J. A guide to light-sheet fluorescence microscopy for multi-scale imaging. *Nature Methods* **14,** 360–373 (2017).

162. Reichmann, J., Eguren, M., Lin, Y., Schneider, I. & Ellenberg, J. *Live imaging of cell division in preimplantation mouse embryos using inverted light-sheet microscopy* 1st ed., 279–292 (Elsevier Inc., 2018).

163. Royer, L. A. *et al.* correspondEnce ClearVolume : open-source live 3D visualization for light-sheet microscopy BigDataViewer : visualization and processing for large image data sets. *Nature Publishing Group* **12,** 3–4 (2015).

164. Plöschner, M. *et al.* Multimode fibre : Light-sheet microscopy at the tip of a needle. *Nature Publishing Group,* 1–7 (2015).

165. Power, R. M. & Huisken, J. Adaptable , illumination patterning light sheet microscopy. *Scientific Reports,* 1–11 (2018).

166. Vettenburg, T. *et al.* Light-sheet microscopy using an Airy beam. *Nature Methods* **11,** 541–544 (2014).

167. Kumar, A. *et al.* Dual-view plane illumination microscopy for rapid and spatially isotropic imaging. *Nature Protocols* **9,** 2555–2573 (2014).

168. Reynaud, E. G., Peychl, J., Huisken, J. & Tomancak, P. Guide to light-sheet microscopy for adventurous biologists. *Nature Methods* **12,** 30–34 (2015).

169. Pitrone, P. G. *et al.* OpenSPIM: an open-access light-sheet microscopy platform. *Nature Methods* **10,** 598–599 (2013).

170. Vladimirov, N. *et al.* Light-sheet functional imaging in fictively behaving zebrafish. *Nature Methods* **11,** 883–884 (2014).

171. Wolf, S. *et al.* Whole-brain functional imaging with two-photon light-sheet microscopy. *Nature Methods* **12,** 379–380 (2015).

172. Royer, L. A., Lemon, W. C., Chhetri, R. K. & Keller, P. J. A practical guide to adaptive light-sheet microscopy. *Nature Protocols* **13,** 2462–2500 (2018).

173. Voigt, F. F. *et al.* The mesoSPIM initiative: open-source light-sheet microscopes for imaging cleared tissue. *Nature Methods* **16,** 1105–1108 (2019).

174. Glaser, A. K. *et al.* Multi-immersion open-top light-sheet microscope for high-throughput imaging of cleared tissues. *Nature Communications,* 1–8.

175. Ritter, J. G., Spille, J.-H., Kaminski, T. & Kubitscheck, U. A cylindrical zoom lens unit for adjustable optical sectioning in light sheet microscopy. *Biomed. Opt. Express* **2,** 185–193 (2011).

176. Yang, Z., Haslehurst, P., Scott, S., Emptage, N. & Dholakia, K. A compact light-sheet microscope for the study of the mammalian central nervous system. *Scientific Reports* **6,** 1–7 (2016).

177. Zhao, M. *et al.* Cellular imaging of deep organ using two-photon Bessel light-sheet nonlinear structured illumination microscopy. **5,** 3242–3247 (2014).

178. Fereidouni, F., Mitra, A. D., Demos, S. & Levenson, R. *Microscopy with UV Surface Excitation (MUSE) for slide-free histology and pathology imaging* in *Optical Biopsy XIII: Toward Real-Time Spectroscopic Imaging and Diagnosis* (eds Alfano, R. R. & Demos, S. G.) **9318** (SPIE, 2015), 46–51.

179. Liu, Y., Rollins, A. M., Levenson, R. M., Fereidouni, F. & Jenkins, M. W. Pocket MUSE: an affordable, versatile and high-performance fluorescence microscope using a smartphone. *Communications Biology* **4,** 1–14 (2021).

180. Siviloglou, G., Broky, J., Dogariu, A. & Christodoulides, D. Observation of accelerating Airy beams. *Physical Review Letters* **99,** 213901 (2007).

181. Siviloglou, G. A. & Christodoulides, D. N. Accelerating finite energy Airy beams. *Optics Letters* **32,** 979–981 (2007).

182. Langer, R. E. On the connection formulas and the solutions of the wave equation. *Physical Review* **51,** 669 (1937).

183. Weisstein, E. W. Airy functions. *https://mathworld. wolfram. com/* (2002).

184. Qin, S. Image reconstruction for large FOV Airy beam light-sheet microscopy by a 3D deconvolution approach. *Opt. Lett.* **45,** 2804–2807 (2020).

185. Galué, L. A generalized Bessel function. *Integral Transforms and Special Functions* **14,** 395–401 (2003).

186. Schreiber, B., Elsayad, K. & Heinze, K. G. Axicon-based Bessel beams for flat-field illumination in total internal reflection fluorescence microscopy. *Optics Letters* **42,** 3880–3883 (2017).

187. Dufour, P., Piché, M., De Koninck, Y. & McCarthy, N. Two-photon excitation fluorescence microscopy with a high depth of field using an axicon. *Applied Optics* **45,** 9246–9252 (2006).

188. Lin, P.-Y., Hwang, S.-P. L., Lee, C.-H. & Chen, B.-C. Two-photon scanned light sheet fluorescence microscopy with axicon imaging for fast volumetric imaging. *Journal of Biomedical Optics* **26,** 116503 (2021).

189. Li, S. *et al.* Self-reconstructing Bessel beam created by two-photon-polymerized micro-axicon for light-sheet fluorescence microscopy. *Results in Physics* **24,** 104111 (2021).

190. Slaoui, M. & Fiette, L. in *Drug Safety Evaluation: Methods and Protocols* (ed Gautier, J.-C.) 69–82 (Humana Press, Totowa, NJ, 2011).

191. Delahunt, B., Miller, R. J., Srigley, J. R., Evans, A. J. & Samaratunga, H. Gleason grading: past, present and future. *Histopathology* **60,** 75–86 (2012).

192. Montironi, R., van der Kwast, T., Boccon-Gibod, L., Bono, A. V. & Boccon-Gibod, L. Handling and pathology reporting of radical prostatectomy specimens. *European Urology* **44,** 626–636 (2003).

193. Montironi, R., Mazzucchelli, R. & van der Kwast, T. Morphological assessment of radical prostatectomy specimens. A protocol with clinical relevance. *Virchows Archiv* **442,** 211–217 (2003).

194. Titford, M. & Bowman, B. What May the Future Hold for Histotechnologists ? Who Will Be Affected ? What Will Drive the Change ?, 5–10 (2012).

195. Slaoui, M., Bauchet, A.-L. & Fiette, L. in *Drug safety evaluation* 101–114 (Springer, 2017).

196. Underwood, J. The impact on histopathology practice of new human tissue legislation in the UK. *Histopathology* **49,** 221–228 (2006).

197. Demichelis, F., Della Mea, V., Forti, S., Palma, P. D. & Beltrami, C. A. Digital storage of glass slides for quality assurance in histopathology and cytopathology. *Journal of Telemedicine and Telecare* **8,** 138–142 (2002).

198. Zhang, Y. *et al.* Digital synthesis of histological stains using micro-structured and multiplexed virtual staining of label-free tissue. *Light: Science & Applications* **9,** 1–13 (2020).

199. Bancroft, J. D. & Layton, C. The hematoxylins and eosin. *Bancroft's theory and practice of histological techniques,* 173–186 (2012).

200. Kumar, N. *et al.* A dataset and a technique for generalized nuclear segmentation for computational pathology. *IEEE transactions on medical imaging* **36,** 1550–1560 (2017).

201. Kather, J. N. *et al.* New colors for histology: optimized bivariate color maps increase perceptual contrast in histological images. *PloS One* **10,** e0145572 (2015).

202. Gareau, D. S. Feasibility of digitally stained multimodal confocal mosaics to simulate histopathology. *Journal of Biomedical Optics* **14,** 1–5 (2009).

203. Hu, B., Bolus, D. & Brown, J. Q. Improved contrast in inverted selective plane illumination microscopy of thick tissues using confocal detection and structured illumination. *Biomed. Opt. Express* **8,** 5546–5559 (2017).

204. Jaafar, H. Intra-operative frozen section consultation: concepts, applications and limitations. *The Malaysian journal of medical sciences: MJMS* **13,** 4 (2006).

205. Cheah, P.-L., Looi, L. M. & Horton, S. Cost Analysis of Operating an Anatomic Pathology Laboratory in a Middle-Income Country. *American Journal of Clinical Pathology* **149,** 1–7 (2017).

206. *Acridine orange* https://www.thermofisher.com/order/catalog/product/A1301.

207. Rigler, R. Acridine orange in nucleic acid analysis. *Annals of the New York Academy of Sciences* **157,** 211–224 (1969).

208. Kino, G. S. *Applications and theory of the solid immersion lens* in *Optical Pulse and Beam Propagation* **3609** (1999), 56–66.

209. Pokusaev, B. *et al.* The effect of bioresorbable additives and micro-bioobjects on gel formation, stabilization and thermophysical properties. *Thermal Science* **23,** 1297–1310 (2019).

210. Matiatou, M. *et al.* Data on the refractive index of freshly-excised human tissues in the visible and near-infrared spectral range. *Results in Physics* **22,** 103833 (2021).

211. Wang, H. *et al.* Deep learning enables cross-modality super-resolution in fluorescence microscopy. *Nature Methods* **16,** 103–110 (2019).

212. Schindelin, J. *et al.* Fiji : an open-source platform for biological-image analysis. **9** (2019).

213. Nishimura, T., Hattori, A. & Takahashi, K. Structural changes in intramuscular connective tissue during the fattening of Japanese black cattle: effect of marbling on beef tenderization. *Journal of Animal Science* **77,** 93–104 (1999).

214. Steu, S. *et al.* A procedure for tissue freezing and processing applicable to both intra-operative frozen section diagnosis and tissue banking in surgical pathology. *Virchows Archiv* **452,** 305–312 (2008).

215. Nylk, J., McCluskey, K., Aggarwal, S., Tello, J. A. & Dholakia, K. Enhancement of image quality and imaging depth with Airy light-sheet microscopy in cleared and non-cleared neural tissue. *Biomedical Optics Express* **7,** 4021–4033 (2016).

216. Araki, K. & Ogata, T. Three-dimensional configuration of crypts of different types of colorectal adenomas. *Scanning Microscopy* **9,** 10 (1995).

217. Humphrey, P. A. Histopathology of prostate cancer. *Cold Spring Harbor Perspectives in Medicine* **7,** a030411 (2017).

218. Garra, B. S. *et al.* Improving the distinction between benign and malignant breast lesions: the value of sonographic texture analysis. *Ultrasonic Imaging* **15,** 267–285 (1993).

219. Pilewskie, M. & Morrow, M. Margins in breast cancer: How much is enough? *Cancer* **124,** 1335–1341 (2018).

220. Kiesslich, R. *et al.* Diagnosing Helicobacter pylori in vivo by confocal laser endoscopy. *Gastroenterology* **128,** 2119–2123 (2005).

221. Thiberville, L. *et al.* In vivo imaging of the bronchial wall microstructure using fibered confocal fluorescence microscopy. *American journal of respiratory and critical care medicine* **175,** 22–31 (2007).

222. Mueller, J. L. *et al.* Rapid staining and imaging of subnuclear features to differentiate between malignant and benign breast tissues at a point-of-care setting. *Journal of cancer research and clinical oncology* **142,** 1475–1486 (2016).

223. Renier, N. *et al.* iDISCO: a simple, rapid method to immunolabel large tissue samples for volume imaging. *Cell* **159,** 896–910 (2014).

224. Renier, N. *et al.* Mapping of brain activity by automated volume analysis of immediate early genes. *Cell* **165,** 1789–1802 (2016).

225. Ueda, H. R. *et al.* Whole-brain profiling of cells and circuits in mammals by tissue clearing and light-sheet microscopy. *Neuron* **106,** 369–387 (2020).

226. Stefaniuk, M. *et al.* Light-sheet microscopy imaging of a whole cleared rat brain with Thy1-GFP transgene. *Scientific Reports* **6,** 1–9 (2016).

227. Chakraborty, T. *et al.* Light-sheet microscopy of cleared tissues with isotropic, subcellular resolution. *Nature Methods* **16,** 1109–1113 (2019).

228. Stelzer, E. H. *et al.* Light sheet fluorescence microscopy. *Nature Reviews Methods Primers* **1,** 1–25 (2021).

229. Glaser, A. K., Bishop, K. W., Barner, L. A., Serafin, R. B. & Liu, J. T. A hybrid open-top light-sheet microscope for multi-scale imaging of cleared tissues. *BioRxiv* (2020).

230. Hillebrand, S., Schwarz, M. & Winterhalter, P. Characterization of anthocyanins and pyranoanthocyanins from blood orange [Citrus sinensis (L.) Osbeck] juice. *Journal of Agricultural and Food Chemistry* **52,** 7331–7338 (2004).

231. Lee, H. S. Characterization of major anthocyanins and the color of red-fleshed Budd Blood orange (Citrus sinensis). *Journal of Agricultural and Food Chemistry* **50,** 1243–1246 (2002).

232. Singh, V. & Mishra, A. K. White light emission from vegetable extracts. *Scientific Reports* **5,** 1–9 (2015).

233. Garcıa-Plazaola, J. I. *et al.* Autofluorescence: biological functions and technical applications. *Plant Science* **236,** 136–145 (2015).

234. Larson, A. & Chin, M. T. A method for cryopreservation and single nucleus RNA-sequencing of normal adult human interventricular septum heart tissue reveals cellular diversity and function. *BMC Medical Genomics* **14,** 1–8 (2021).

235. Alberts, B. *et al.* Garland Science. *Molecular Biology of the Cell,* 197 (2002).

236. Gumbs, A. A., Gagner, M., Dakin, G. & Pomp, A. Sleeve gastrectomy for morbid obesity. *Obesity Surgery* **17,** 962–969 (2007).

237. Kerr, J. B. *Gastrointestinal tract* 1999.

238. Rashid, F. & Haque, A. U. Nuclear morphological and morphometric features of reactive versus neoplastic gastric mucosa. *Int J Pathol* **7,** 66–72 (2009).

239. Chakraborty, M. & Panda, A. K. Spectral behaviour of eosin Y in different solvents and aqueous surfactant media. *Spectrochimica Acta Part A: Molecular and Biomolecular Spectroscopy* **81,** 458–465 (2011).

240. Wijesinghe, P. *et al.* Learned deconvolution using physics priors for structured light-sheet microscopy. *bioRxiv* (2021).

241. Elfer, K. N. *et al.* DRAQ5 and eosin ('D&E') as an analog to hematoxylin and eosin for rapid fluorescence histology of fresh tissues. *PLoS One* **11,** e0165530 (2016).

242. *Fluorescence spectraviewer, acridine orange and eosin absorption and emission spectra* https://www.thermofisher.com/order/fluorescence-spectraviewer?SID=srch-svtool&UID=1301dna#!/.

243. Photometrics, T. private communication. Aug. 2020.

244. Hamamatsu. private communication. Aug. 2020.

245. Browne, A. W. *et al.* Deep learning to enable color vision in the dark. *PloS One* **17,** e0265185 (2022).

246. Rivenson, Y. *et al.* Virtual histological staining of unlabelled tissue-autofluorescence images via deep learning. *Nature Biomedical Engineering* **3,** 466–477 (2019).

247. Wu, Z. *et al.* Multi-photon microscopy in cardiovascular research. *Methods* **130,** 79–89 (2017).

248. Cahill, L. C. *et al.* Rapid virtual hematoxylin and eosin histology of breast tissue specimens using a compact fluorescence nonlinear microscope. *Laboratory Investigation* **98,** 150–160 (2018).

249. König, T. T., Goedeke, J. & Muensterer, O. J. Multiphoton microscopy in surgical oncology-a systematic review and guide for clinical translatability. *Surgical Oncology* **31,** 119–131 (2019).

250. Rogart, J. N. *et al.* Multiphoton imaging can be used for microscopic examination of intact human gastrointestinal mucosa ex vivo. *Clinical Gastroenterology and Hepatology* **6,** 95–101 (2008).

251. Jain, M. *et al.* Multiphoton microscopy in the evaluation of human bladder biopsies. *Archives of pathology & laboratory medicine* **136,** 517–526 (2012).

252. Pena, A.-M. *et al.* Three-dimensional investigation and scoring of extracellular matrix remodeling during lung fibrosis using multiphoton microscopy. *Microscopy Research and Technique* **70,** 162–170 (2007).

253. Yan, J. *et al.* A pilot study of using multiphoton microscopy to diagnose gastric cancer. *Surgical Endoscopy* **25,** 1425–1430 (2011).

254. Zipfel, W. R. *et al.* Live tissue intrinsic emission microscopy using multiphoton-excited native fluorescence and second harmonic generation. *Proceedings of the National Academy of Sciences* **100,** 7075–7080 (2003).

255. Bhawalkar, J. D., He, G. S. & Prasad, P. N. Nonlinear multiphoton processes in organic and polymeric materials. *Reports on Progress in Physics* **59,** 1041–1070 (1996).

256. Dunn, K. W. & Young, P. A. Principles of multiphoton microscopy. *Nephron Experimental Nephrology* **103,** e33–e40 (2006).

257. Mignani, A. G. & Baldini, F. Fibre-optic sensors in health care. *Physics in Medicine & Biology* **42,** 967 (1997).

258. Correia, R., James, S., Lee, S., Morgan, S. & Korposh, S. Biomedical application of optical fibre sensors. *Journal of Optics* **20,** 073003 (2018).

259. Socorro, A. & Dıaz, S. in *Fiber Optic Sensors* 115–147 (Springer, 2017).

260. Di Domenico, G., Ruocco, G., Colosi, C., DelRe, E. & Antonacci, G. Cancellation of Bessel beam side lobes for high-contrast light sheet microscopy. *Scientific Reports* **8,** 1–7 (2018).

261. Dharmavarapu, R., Ng, S. H., Eftekhari, F., Juodkazis, S. & Bhattacharya, S. MetaOptics: Opensource software for designing metasurface optical element GDSII layouts. *Optics Express* **28,** 3505–3516 (2020).

262. Genevet, P., Capasso, F., Aieta, F., Khorasaninejad, M. & Devlin, R. Recent advances in planar optics: from plasmonic to dielectric metasurfaces. *Optica* **4,** 139–152 (2017).

263. Yu, N. & Capasso, F. Flat optics with designer metasurfaces. *Nature Materials* **13,** 139–150 (2014).

264. Chen, H.-T., Taylor, A. J. & Yu, N. A review of metasurfaces: physics and applications. *Reports on Progress in Physics* **79,** 076401 (2016).

265. Staude, I. *et al.* Tailoring directional scattering through magnetic and electric resonances in subwavelength silicon nanodisks. *ACS Nano* **7,** 7824–7832 (2013).

266. Chong, K. E. *et al.* Efficient polarization-insensitive complex wavefront control using Huygens' metasurfaces based on dielectric resonant meta-atoms. *ACS Photonics* **3,** 514–519 (2016).

267. S4 : A free electromagnetic solver for layered periodic structures. *Computer Physics Communications* **183,** 2233–2244 (2012).

268. Lin, D., Fan, P., Hasman, E. & Brongersma, M. L. Dielectric gradient metasurface optical elements. *Science* **345,** 298–302 (2014).

269. Lee, S. R. *et al.* All-silica fiber Bessel-like beam generator and its applications in longitudinal optical trapping and transport of multiple dielectric particles. *Opt. Express* **18,** 25299–25305 (2010).

270. McGloin, D. & Dholakia, K. Bessel beams: diffraction in a new light. *Contemporary Physics* **46,** 15–28 (2005).

271. Baz, A., Bigot, L., Bouwmans, G. & Quiquempois, Y. Single-mode, large mode area, solid-core photonic bandgap fiber with hetero-structured cladding. *Journal of Lightwave Technology* **31,** 830–835 (2013).

272. Sudo, S. & Itoh, H. Efficient non-linear optical fibres and their applications. *Optical and Quantum Electronics* **22,** 187–212 (1990).

273. Pochechuev, M. *et al.* Two-photon imaging of fiber-coupled neurons. *Journal of Biophotonics* **11,** e201600203 (2018).

274. Ozbay, B. N. *et al.* Three dimensional two-photon brain imaging in freely moving mice using a miniature fiber coupled microscope with active axial-scanning. *Scientific Reports* **8,** 1–14 (2018).

275. Karpf, S. *et al.* Two-photon microscopy using fiber-based nanosecond excitation. *Biomedical Optics Express* **7,** 2432–2440 (2016).

276. Morales-Delgado, E. E., Psaltis, D. & Moser, C. Two-photon imaging through a multimode fiber. *Optics Express* **23,** 32158–32170 (2015).

277. Diddams, S. A., Eaton, H. K., Zozulya, A. A. & Clement, T. S. *Full-field characterization of femtosecond pulses after nonlinear propagation* in *Technical Digest. Summaries of Papers Presented at the Conference on Lasers and Electro-Optics. Conference Edition. 1998 Technical Digest Series, Vol. 6 (IEEE Cat. No. 98CH36178)* (1998), 519.

278. Agrawal, G. P. in *Nonlinear Science at the Dawn of the 21st Century* 195–211 (Springer, 2000).

279. Olarte, O. E. *et al.* Image formation by linear and nonlinear digital scanned light-sheet fluorescence microscopy with Gaussian and Bessel beam profiles. *Biomedical Optics Express* **3,** 1492–1505 (2012).

280. Li, S. *et al.* Self-reconstructing Bessel beam created by two-photon-polymerized microaxicon for light-sheet fluorescence microscopy. *Results in Physics* **24,** 104111 (2021).

281. Deng, S. *et al.* Sidelobe suppression in light-sheet fluorescence microscopy with Bessel beam plane illumination using subtractive imaging. *Chinese Optics Letters* **16,** 111801 (2018).

282. Escobet-Montalbán, A. *et al.* Three-photon light-sheet fluorescence microscopy. *Opt. Lett.* **43,** 5484–5487 (2018).

283. Bird, D. & Gu, M. Fibre-optic two-photon scanning fluorescence microscopy. *Journal of Microscopy* **208,** 35–48 (2002).

284. Bird, D. & Gu, M. Compact two-photon fluorescence microscope based on a single-mode fiber coupler. *Optics Letters* **27,** 1031–1033 (2002).